UNIVERSITY OF SOUTHAMPTON

FACULTY OF NATURAL AND ENVIRONMENTAL SCIENCES

School of Chemistry

A Study on the Estimating DPV Surface Coverages for Chemically Modified Electrodes

By

HAIRUL HISHAM BIN HAMZAH

Thesis for the degree of Doctor of Philosophy

April 2017

Table of Contents

UNIVERSITY OF SOUTHAMPTON

ABSTRACT

FACULTY OF NATURAL AND ENVIRONMENTAL SCIENCES

School of Chemistry

Thesis for the degree of Doctor of Philosophy

A STUDY ON THE ESTIMATING DPV SURFACE COVERAGES FOR CHEMICALLY MODIFIED ELECTRODES

Hairul Hisham Bin Hamzah

This thesis is about estimating the surface coverages (Γ) of immobilised redox molecules at modified electrode surfaces using differential pulse voltammetry (DPV). The cyclic voltammetry (CV) technique less sensitive than DPV technique because of the background current that can obscure the Faradaic current of the attached redox molecules. As a result, CV technique less sensitive for measurements of low surface concentrations of immobilised redox species. This is not the case for DPV. Currently, there is no specific agreed procedure to determine the surface coverages by DPV. Thus to establish the method to determine the surface coverages of immobilised redox molecules at the surface of the electrode by DPV measurement was a prime interest in this research. Secondary to that point, exploring a new strategy in preparing chemically modified electrodes in order to obtain a better surface coverages of covalently immobilised redox molecules at electrode surfaces was also an aim of this thesis.

Enhanced DPV currents were obtained when an external resistance *(R_{ext})* of suitable magnitude was added in the DPV cell circuit for electrode modified with either for organic, DNA labelled or inorganic redox systems. This motivated us to develop an experimental model for estimating the DPV surface coverages ($\Gamma_{DPV,\ exp}$) of attached redox molecules at electrode surfaces at suitable R_{ext}. Moreover, a simple equation for estimating the $\Gamma_{DPV,\ exp}$ based on DPV parameters is presented in this study and shown to work well, given several underlying assumptions. Our approach makes use of an additional R_{ext} in the DPV cell circuit and several non-adjustable DPV parameters. Subsequently, the $\Gamma_{DPV,\ exp}$ of immobilised redox probes can be estimated by integrating the area under the oxidation peak of the differential pulse voltammograms (DPVs) at a suitable R_{ext}. The experimental approach was verified by numerical modelling using a specially developed DPV simulation in MATLAB. The electrochemical parameters used for the DPV simulation, such as uncompensated solution resistance in an electrochemical cell (R_u), double layer capacitance (C_{dl}) and electrode kinetics (k_s and α) were obtained from cyclic voltammetry (CV), chronoamperometry and electrochemical impedance spectroscopy (EIS) measurements

made on the modified electrodes. Good agreement was obtained between the experimental DPV and the simulations.

The second part of this thesis was focused on extracting thermodynamic and kinetic parameters such as the standard potential ($E°$), the diffusion coefficient (D_o), surface coverages, the rate constant for adsorption (k_A), the rate constant for homogenous reaction (k_H), the rate of electron transfer (k_s), and the transfer coefficient (α) for the electrochemical grafting of primary amine linkers onto GC electrode surfaces by numerical simulation. These parameters are impossible to access by experimental approaches. The grafting process was performed in two different solvents; by electrochemical grafting from neat ACN and by electrochemical grafting in a mixed solvent of ACN and sodium hydrogen carbonate ($NaHCO_3$). In the case of the mixed-solution method, the ratio of ACN to $NaHCO_3$ was 4:1. The primary amine of the EDA-Boc molecule was studied as an experimental model in this work. Using a specially developed CV simulation for inhibiting species at the surface of the electrode, the experimental CVs for the electrochemical grafting of EDA-Boc in the two solutions were simulated. Good agreement between experimental CV and the simulated CV was obtained. Moreover, this simulation allows us to extract the aforementioned parameters, which are not electrochemically accessible. To investigate the effect of the presence of $NaHCO_3$ on immobilised EDA-Boc at the surface of GC electrodes, the anthraquinone (AQ) was covalently coupled to the grafted EDA (after removal of the Boc group). The CV and DPV surface coverages of covalently attached AQ on the EDA linker based on the two methods of electrografting were compared. The developed DPV simulation was also employed in this work in order to show the utility and flexibility. A good agreement between experimental and simulated DPV was achieved.

DECLARATION OF AUTHORSHIP

I, Hairul Hisham Bin Hamzah

declare that this thesis and the work presented in it are my own and has been generated by me as the result of my own original research.

A STUDY ON THE ESTIMATING DPV SURFACE COVERAGES FOR CHEMICALLY MODIFIED ELECTRODES

I confirm that:

1. This work was done wholly or mainly while in candidature for a research degree at this University;
2. Where any part of this thesis has previously been submitted for a degree or any other qualification at this University or any other institution, this has been clearly stated;
3. Where I have consulted the published work of others, this is always clearly attributed;
4. Where I have quoted from the work of others, the source is always given. With the exception of such quotations, this thesis is entirely my own work;
5. I have acknowledged all main sources of help;
6. Where the thesis is based on work done by myself jointly with others, I have made clear exactly what was done by others and what I have contributed myself;
7. Parts of this work have been published as:

H. Hisham; D. Guy, B. Philip, P. Aleksandra, K. Jeremy; Electrografting of mono-N-Boc-etehylenediamine from an acetonitirile/aquesous $NaHCO_3$ mixture. Journal of Electrochemistry, Xiamen University, China, 2017, 23(2), 130-140.

Signed:.....

Date: .....

Acknowledgements

I would like to express my highest gratitude and appreciation to my supervisor, Professor Philip Bartlett for his continuous guidance, passions as well as his valuable commitment to me and my work. I am extremely lucky and enjoy working with Professor Philip Bartlett. He had never failed to respond to every questions and necessity regarding my work. All his efforts for the past four years has been a tremendously motivational, striving me to achieve the level that I am now. Thank you very much again, Prof. Phil.

Also, I would like to express my appreciation to Associate Professor Guy Denuault for developing DPV and CV simulations on MATLAB programme. The programmes have been fundamental for my work and I could not imagine completing my work without your brilliant and innovative programmes. Not forgetting, I would like to thank him for his kind guidance and ideas for my work. Also, I would like to thank my advisor, Dr Peter Berkin.

I am so grateful for given a chance to collaborate with many brilliant researchers and scholars from the University of Southampton and the Queen Mary University of London. Massive thanks to Professor Jeremy Kilburn and his research group for their valuable inputs and their expertise particularly, Dr. Jessica Gropi, for preparing the Os and AQ-Os modified GC electrodes. I would also like to thank Dr. Alexsandra for introducing me to her works on covalent attachment of modified electrodes. Not forgetting, many thanks also goes to Mrs. Rachel Gao for her superb sharing of her works on a self-assembled monolayer of ssDNA at the surface of the gold electrode.

Thanks to the brilliant Bartlett's group, especially to Mr. Eugene, Dr. David, Dr. Eva, Dr. Charlie, Dr. Gabriela, Dr. Jack and Dr. Peter for helping me out whenever I was struggling in the lab. To my lab buddies, Dr. Izzet, Martha and Firas thanks for being there for me. The lab would be so empty and dull without you guys.

Thanks to my lovely Skylaris group members; Jolly, Max, Valerio and Lucas for being attentive and accommodative. I always remember our very best moments, laughter, joy and also our usual complimentary coffee treat at The Bridge on every Thursday. To my charming office mates; Turgut, Saiful, David, Danai and Ana, thank you for your unfailing love and friendships.

Special thanks also to my family members and friends in the UK and in Malaysia, for their endless encouragement, thoughts, support, advice, understanding, prayers and love. To the utmost, to my mum. You have been there for me since, even though there was a time when you were not physically well and was admitted to the hospital while I was away in the UK last year. Mum, this valuable works is dedicated for you. You have been my inspiration, you have shown me how important is to be a courage and dedicated individual.

Definitions and Abbreviations

General symbols

ACN ; Acetonenitrile
AQ ; Anthraquinone
Au ; Gold
Boc-EDA ; *N*-Boc-ethylenediamine
Boc-HDA ; *N*-Boc-1,6-hexanediamine
C_{dl} ; Double layer capacitance
CMEs : Chemically modified electrodes
CV ; Cylic voltammetry
CVs ; Cylic voltammograms
D_o ; Diffusion coefficient
DBU ; 1,8-Diazabicycloundec-7-ene,
DsDNA ; Double stranded DNA
DPV ; Differential pulse voltammetry
DPVs ; Differential pulse voltammograms
ΔE_P ; Modulation amplitude for DPV
ΔE_s ; Potential step for DPV
EDC ; *N*-(3-Dimethylaminopropyl)-*N′*-ethylcarbodiimide
EIS ; Electrochemical impedance spectroscopy
GC ; Glassy carbon
k_A; Rate constant for adsorption
k_H; Rate constant for homogenous reaction
k_s ; Rate of electron transfer
NHS ; N-Hydroxysuccinimide ester
Os; Osmium
RC ; Time constant
R_{ext} ; Added external resistance
$R_{ext,\ max}$; Added external resistance at the maximum DPV peak current
R_l ; Adlayer resistance
R_t ; Total uncompensated resistance in an electrochemical cell ($R_u + R_{ext}$)
$R_{t,\ max}$; Total uncompensated resistance in an electrochemical cell ($R_u + R_{ext}$) at the maximum DPV peak current.
R_u ; Unknown uncompensated solution resistance
SAMs ; Self-assembled monolayers
ssDNA ; Single stranded DNA
TBATFB; Tetrabutylammonium tetrafluoroborate
TFA; Trifluoroacetic acid
V_{ap} ; Applied voltage
V_{pa} ; Voltage across in the parallel circuit

Greek symbols

α ; Transfer coefficient
η; Overpotential (E_p-E_{mid})
Γ ; Surface coverage
$\Gamma_{CV,\ exp}$; Surface coverage measured from CV experiment
$\Gamma_{DPV,\ exp}$; Surface coverage measured from DPV experiment
$\Gamma_{DPV,\ sim}$; Surface coverage extracted from DPV simulation
τ_p ; Modulation time for DPV
τ_i ; Interval time for DPV

Chapter 1: Introduction

1.1 Chemically modified electrodes (CMEs)

Chemically modified electrodes (CMEs) can be produced by the modification of the bare electrode surfaces, leading to an electrode suited for a particular function by immobilising a suitable reagent onto a surface. This leads to increase the sensitivity, selectivity, specificity and stability compared to the bare electrode surface[1]. Basically, CMEs can have molecular layers either monolayer or multilayer[2], coated on the electrode surface which changes the chemical, physical, electrochemical, optical and electrical properties[3].

The selection of electrode substrate in producing the CMEs determines not only display appropriate electrochemical characteristics but also be suitable for the method of attachment to be employed and maintenance. Appropriate electrochemical characteristics include a wide potential window either in acidic and basic solutions, high signal-to-noise ratio, high electrical conductivity and surface reproducibility. In the early days of electrochemistry most of the work was done on solid electrodes like platinum and gold, but when polarography was introduced in 1922 by Professor Heyrovsky[4], the liquid mercury electrode soon became the dominating electrode material due to its unique properties. However, in the 1960s, several new solid and film electrodes have been developed in order to replace liquid mercury. This is due to the fact that the mercury electrode could not be used for the oxidation of many organic molecules because of its limited anodic potential range and its toxicity. In addition, solid electrode substrates have the advantages of being more mechanically stable[5]. Also, the handling of solid electrodes is much easier such that they may readily be applied in flow streams due to their mechanical stability and hardness. Many different solid substrates can be used as working electrodes in order to produce the CMEs.

In terms of the substrates used for producing CMEs by various researchers, glassy carbon (GC)[6], graphene[7], basal plane pyrolytic graphite[8], diamond[9], gold, copper[10], platinum[11], indium tin oxide[12] and many more other substrates have been extensively studied in the literature. In addition, electrode substrates can be prepared in several forms and dimensions such as tubular, ring, planar, macro and micro-sized[13]. Nevertheless, two different electrode substrates were used during conducting this research, these were GC and gold electrodes. The GC electrode was the main electrode type used in this research because of its high electrical conductivity, impermeability to gases, reasonable mechanical and dimensional stability and high chemical resistance[14]. It also has a wide potential range which is suitable for utilising in acid and basic media from about -0.8 to +1.2 V and -1.6 to +1.2 V *vs* S.C.E in acid and base respectively[15]. In contrast, the gold electrode is one the most inert metal electrodes and less prone to the formation of stable oxide films or surface contamination[16]. This is due to the nature of the properties of gold as a noble metal with high density and high electrical conductivity. Additionally, the gold electrode has low over the

potential for the hydrogen evolution reaction (HER) and the reaction starts at -200 to -300 mV *vs* SHE[17].

The earliest works of the modification of electrode substrates were reported by Lane and Hubbard[18,19] in these they discussed in detail electrode reactions at a metallic surface deliberately coated with organic substances. In other early work, Miller and co-workers[20] were able to attach optically active amino-acids to a graphite surface. In the same year (1975) Murray and co-workers[21] expanded their report on surface modified electrodes by attaching hydrolysis-sensitive trialkoxy or trichlorosilane to a SnO_2 electrode by reaction with surface hydroxy-groups. Such a procedure had previously been used to modify chromatographic supports and glass slides for use in trace metal analysis.

Originally, when CMEs were pioneered by Lane and Hubbard, the CME was merely studied for its electrochemical behaviour, but nowadays, they provide a route for other purposes such as chemical and biochemical sensing, energy conversion corrosion protection, developing molecular electronics and electrochromic devices[22]. On the basis of the above, to fulfil the desire for tailor-made electrodes by creating a robust surface of a modified electrode for a specific application, the electrochemist attempts to find new methods of electrode modification with the ability to produce a stable, selective and reproducible surface.

Essentially, CMEs can be achieved in several ways such as the addition of a variety of reactants to the electrode surface by physical adsorption, self-assembly of thiol monolayers, covalent attachment of electroactive organic molecules through a linker, redox polymer coatings (uniform), heterogeneous multilayers (non-uniform)[23] and several more. Figure 1.1, depicts the common approaches used in the literature for producing CMEs. In this thesis, a variety of modifications of the electrode surfaces with electroactive molecules employing different strategies for generating monolayer, mixed-monolayer and multilayer structures were carried out.

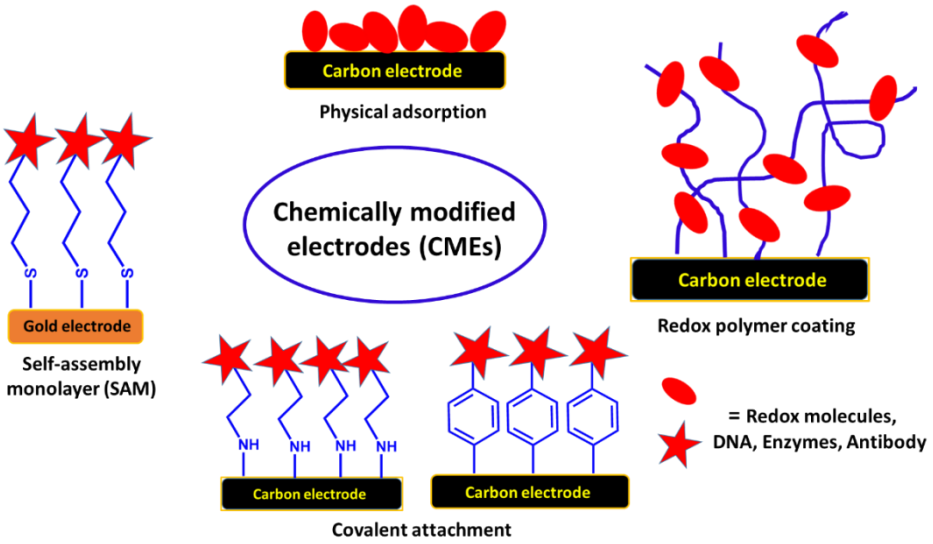

Figure 1.1; Some general approaches commonly used for creating chemically modified electrodes (CMEs).

1.2 Methods for chemically modifying electrodes

As mentioned earlier, various possible strategies can be found in the literature for the preparing CMEs. The choice of method depends on the need to make the modification processes simple, quick, or robust for a particular use. Moreover, layer structures of material presents on the electrode surface are also considered in modifying the surface of the electrodes either the monolayer or multilayer structures. There are three popular methods that can be found in the literature, employed for creating a wide of variety surface of modified electrodes, these are physical adsorption, self-assembled monolayers and covalent attachment. These methods were employed during this research.

1.3 Physical adsorption

The simplest method for obtaining a CME is physical adsorption. For instance, physisorption of aromatic species[24], olefins and long chain aliphatic onto carbon has been used for multi purposes studies[25]. The basis of physisorption of redox molecules at the surface of the electrode is the weak non-physical forces such as Van der Waal's electrostatic and/or hydrophobic interactions[26]. These types of interaction are not that strong so that make the adsorbed molecules are not so stable as to be confined at the surface of electrodes for longer periods. Thus, the desorption of adsorbed molecules from the surface may occur when conducting voltammetric mesurements[27]. In addition, monolayer coverage of the film is difficult to obtain as unspecific multilayers of adsorbed redox molecules may form[28]. This leads to the disadvantage that the electron transfer between redox active sites must propagate through the multilayer film[2], probably leading different electron

transfer kinetics and/or thermodynamic due to lateral interactions between the adjacent adsorbed redox molecules. However, the simplicity and speed of preparation for immobilising redox molecules onto the electrode surface is a significant advantage of this technique[29].

Biljana *et al*.[30] demonstrated a rapid procedure to produce CMEs by physically adsorbing quinone redox active molecules onto the cleaned GC electrode surface in order to study the catalytic activity of absorbed quinones for oxygen reduction and the production of hydrogen peroxide. In preparation of the CMEs based on physisorbed in their work, the quinone solution was left to evaporate for a few minutes in order to obtain quinone modified GC electrodes.

Another interesting example was reported by Annamalai and Puchakayala in 2011[31]. In their work, they produced CMEs by mixing anthraquinone (AQ) with carbon nanotubes, employing a drop coating technique. However, before physically immobilising AQ on carbon nanotube (CNT), the CNT powders were initially coated on the cleaned GC electrode. In their work, they reported that this procedure does not involve synthetic steps, which means the time consumed in preparing the CMEs was avoided.

1.4 Self-assembled monolayers (SAMs)

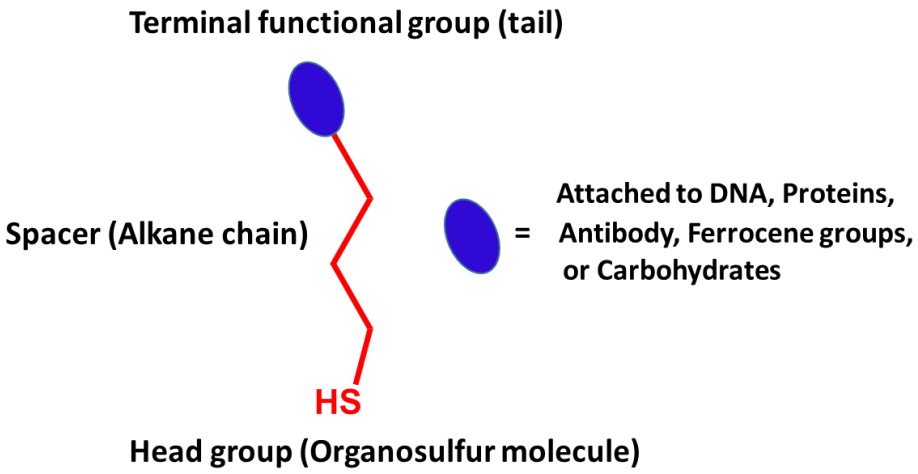

Figure 1.2; Structural features of n-alkyl thiols for spontaneous chemisorption to the surface of metal electrodes to form self-assembled monolayers. (SAMs).

Self-assembled monolayers (SAMs) are organic molecular assemblies formed on metal electrode surfaces spontaneously by adsorption of organosulfur molecules. SAMs are generated by the chemisorption of thiols having a sulphur head group, backbone and an end group[32].

Thus, this type of adsorption is more stable than physical adsorption. In terms of the head group, the molecule has a high affinity for the substrate. The backbones, such as alkyl chain or aromatic

ring, play an important role in the formation of the different packed monolayers due to steric effects. In contrast, the terminal end group (tail) is generally attached to various redox molecules, DNA, protein, or antibody[33] as depicted in Figure 1.2.

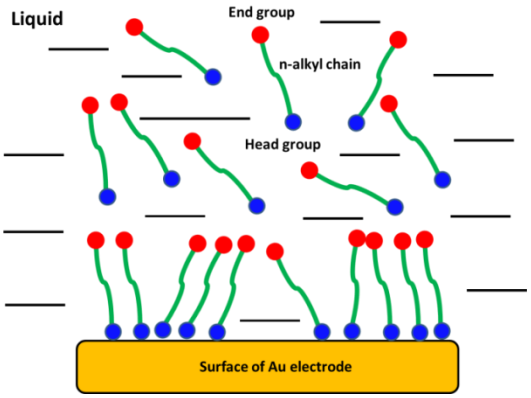

Figure 1.3; Schematic representation of the formation of a self-assembled monolayer at a surface of the gold electrode.

SAMs are easily prepared by immersing the surface of the electrode in a solution containing the SAM molecules as illustrated in Figure 1.3. Since it was introduced 1986 by Porter and co-workers[34], the SAM technique have been employed research in many scientific areas such as material science, molecular biology and medicine and particularly in the development of genosensors.

SAMs based on thiol groups are an attractive approach for creating a surface modified electrode for many reasons including the stability of these monolayers due to the strong chemisorption of the head group towards the surface of the electrode. The interactions between the thiols group with the surface of the electrode may include van der Waals interactions, hydrophobic interactions, hydrogen bonds and semi-covalent interaction between sulphur and substrate[35]. As demonstrated in the literature, the thiol group can form monolayers of organosulphur species onto the surface of gold[16,34], silver[36], copper[37], iron[38] and platinum[39] metals. However, the formation of SAMs is more favourable onto gold electrodes as the surface of gold does not require a stable surface oxide and does not undergo unusual reaction (e.g; corrosion)[16,40].

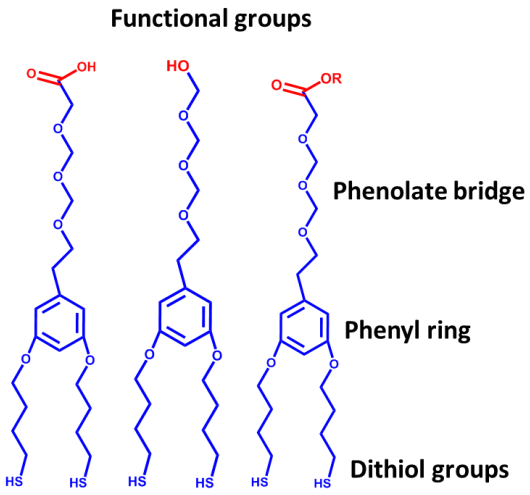

Figure 1.4; General structures of dithiols with different functional groups for the spontaneous chemisorption to the surface of metal electrodes to form self-assembled monolayers (SAMs).

Building on previous studies, SAMs based on dithiol groups have been used as supports for the immobilisation of antibodies and oligonucleotide probes. Essentially, the organosulfur molecules contain two identical alkythiol substituents attached to the phenyl ring through a phenolate bridge that provides two attachment points on the metallic surface as illustrated in Figure 1.4[41–44]. It can, therefore, be anticipated that these molecules will generate more stable SAMs than monothiols due to a multivalent mechanism of interaction. It also provides an adequate spacing for an immobilised biomolecule, thus allowing an improved mobility and flexibility at the recognition terminus.

Recently, our group has demonstrated the self-assembled of 30-mer single-stranded DNA probes at the gold sphere segment void (Au SSV) surface by the dithiol linker for monitoring the hybridization of ssDNA to double-stranded DNA (dsDNA) by electrochemically driven melting[45]. The main reason to use this type of attachment at the Au SSV was to suppress desorption of the ssDNA probe at negative potentials.

Although the chemisorption of the SAM molecules at gold electrode surfaces is easy to achieve, the resulting SAMs have been demonstrated to have a lack of stability as the Au-S bond energy is only moderately strong, around 43 kcal/mol[46]. Consequently, the bonds between Au-S are susceptible to cleavage or rearrangement on the surface[47].

1.5 Covalent attachment

As an alternative to overcome the drawbacks SAMs, stronger attachment to the electrode surface can be accomplished by covalent linking. In addition, immobilisation of redox molecules, enzymes or DNA by covalent attachment offers great advantages such as a well-defined organisation of the modified electrodes surfaces, formation of densely-packed monolayer structures, the flexibility for attachment of various functional electroactive groups and highly efficient electron transfer from redox centres to the electrode surface[48,49].

Essentially, chemical reactions can be carried out to form a covalent bond between the electrode surface and a molecule of interest. This type of strategy was first developed by Murray and co-workers[50] in the mid to late 1970s. In their work, the oxidised surface of metal and carbon electrodes was silanized by reaction with an organosilane compounds and then reacted with another molecule of interest as illustrated in Figure 1.5.

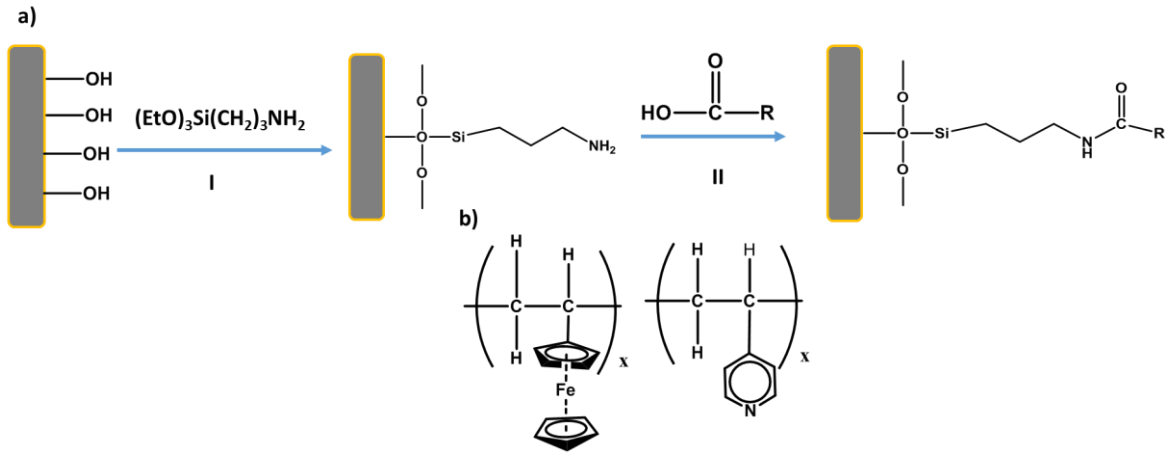

Figure 1.5; a) General reaction scheme for the original covalent attachment to an electrode surface to produce a chemically modified electrode, developed by Murray and co-workers. Treatment I; Oxidized carbon or metal electrode is treated with ϒ-aminopropyltriethoxysilane. Treatment II; the silanized electrode is treated with a compound containing the desired group to be attached (R). b) Structures of the compounds of R.

As shown in Treatment I, the silane served as a glue for fixing the molecule to the surface of the electrode. One might expect that from this technique, a monolayer of silane at the surface of the electrode would be obtained. Nevertheless, as discussed by Bard[51], the silanization reactions favour polymerization in which multilayers structures are formed. Another earlier work describing the covalent binding of molecules to the electrode surfaces was reported by Watkins and co-workers. In this case, optically active amino acids were covalently bound to substrates via an amide bond, providing a stable surface for electrochemical reactions[52].

Since it was first introduced by Murray and colleagues[50], the covalent modification of electrodes has gone through many improvements in order to tailor and design robust surfaces for modified electrodes and in particular, for the formation of monolayer structures. One of the interests in this thesis is the covalent attachment of redox molecules onto electrodes using organic linkers.

The covalent immobilisation of organic electroactive molecules on the surface of electrodes based on the use of linkers such those using electrochemical oxidation of primary amines or electrochemical reduction of diazonium salts is well established nowadays. Subsequently, the immobilisation of organic redox molecules can be achieved using classical solid-phase methodology where a bond is formed between the surface of the electrode first modified with a suitable linker either a primary amine or diazonium salt[53]. Previous studies from our group have extensively reported on the modification of electrode surfaces based upon these methods.

The covalent attachment of redox molecules onto the electrode surfaces in our group was first described by Chretien *et al.*[54], who described a new approach using a mono-Boc protected diamine (Boc-EDA) linker grafted to the carbon surfaces. The process involves electrochemical oxidation of Boc-EDA. In addition, another organic linker Boc-aminomethylphenyl (BocNH-$CH_2C_6H_4$) was also used by employing electrochemical reduction of the BocNH-$CH_2C_6H_4$ diazonium salt. The use of the mono-Boc protecting group was to prevent the formation of bridged or multilayer structures on the electrode surface. Subsequently, anthraquinone, as a redox model couple, was attached to the linkers after removal of the Boc protecting group. In this study, the combination of electrochemical attachment of Boc protected linkers and subsequent modification under the condition of solid-phase synthesis provides a very versatile methodology for tailoring a wide range of organic functional arrangements on the glassy carbon surface.

In further work from our group, Ghanem *et al.*[55] reported on covalent modification of glassy carbon with organic redox probes through diamine linkers using electrochemical and solid-phase synthesis methodologies. In this work, the anthraquinone and nitrobenzene probes were coupled to the various mono-Boc-protected diamine linkers after covalently grafting to glassy carbon electrodes through electrochemical oxidation of the diamine. From this study, it was concluded that the anthraquinone surface coverages were found to decrease as the chain length of the alkyl diamine linker increased and the electron transfer kinetics were found to be faster for the lower coverage and the longer, more flexible linkers. On the contrary, in the case of nitrobenzene, when the length of linker increased, only a slight change in surface coverage was reported.

In another significant contribution to the covalent attachment method for preparing the CMEs, Boland and co-workers[56] have electrografted aryldiazonium salt of 3-(4-aminophenyl)propionic acid at the surface of GC electrodes by electrochemical reduction. The surface carboxylic acid generated was then bonded to an osmium complex to provide a covalently bound redox-active

monolayer. The grafted layer was stable to pH, temperature and on storage, retaining the electroactivity of the immobilised osmium complex for at least 6 months.

In a different study, Lita *et al*.[57] reported the formation of a mixed monolayer by electrografted an aryldiazonium salt, followed by an arylhydrazine at the surface of a GC electrode. At the beginning of the modification process, a 4((triisopropylsilyl)ethynyl)phenyl film was electrografted to the surface, followed by removal of the triisopropylsilyl protecting group to give a submonolayer of phenylethylene. They employed two strategies in order to fill in the sparse monolayer with a second modifier. In the first step, nitrophenyl groups were grafted to the phenylethylene-modified surface by the oxidation of 4-nitrophenylhydrazine. Ferrocene was then covalently coupled to the terminal alkyne groups on the surface via a click reaction with azidomethylferrocene.

In other cases, electrochemists have attempted to improve the efficiency of electrochemical grafting for covalent attachment of redox molecules at the surface of electrodes by using mixed solvents. The main motivation for this type of strategy was to improve the surface coverages of the grafted redox molecules. Buriez *et al*.[58] demonstrated the electrochemical grafting of the π-conjugated amino-ferrocifen complex at gold surfaces under two different conditions; in methanol with lithium perchlorate supporting electrolyte and in methanol-lithium perchlorate in the presence of a base (collidine (2,4,6-trimethypyridine)). The results showed that the covalent grafting of the amino-ferrocifen complex in the presence of collidine significantly altered the CV feature of the grafted complex. However, the surface coverages of the grafted amino-ferrocifen complex for the two different grafting conditions were equal. Thus, it was concluded that there was no significant change in surface coverages of the immobilised complex despite the fact that grafting of the complex was significantly enhanced in the presence of a base. In other work, Tanaka and co-workers showed the grafting of amines bearing ferrocene derivatives as a redox active groups in the presence of pyridine base also shown that the presence of collidine did not increase of surface coverages of ferrocene. As mentioned generally in this paragraph, it is one of the interests of the studies in this thesis to investigate to the covalent grafting of primary amines linker in a mixed solvent. The aim of this was to improve the grafting efficiency and promote better surface coverages of immobilised redox molecules. This will be discussed in detail in Chapter 6.

1.6 Electrochemical behaviours for ideal and non-ideal immobilised reactants

As already explained in detail in Sections 1.3, 1.4, and 1.5, when dealing with the immobilisation of redox species at the electrode surface, the electrochemical response for the electrode reaction is significantly affected by the behaviour of the electroactive species attached. Generally, when the electroactive species is strongly attached to the electrode surface, the contribution of dissolved or desorbed species in the bulk electrolyte can be negligible[59,60]. However, an adsorption isotherm of attached species to the electrode surface and the interactions behaviour among the immobilised redox species need to be considered[59].

In late 1979, Laviron[59] reported on the use of linear potential sweep voltammetry for the surface study of the electrochemical reactions for the strongly adsorbed system by irreversible adsorption, covalent binding and polymer coating. Also, Laviron[59] showed that the voltammetric response is influenced by interactions between the attached molecules. In his model, Laviron[59] showed that the ideal voltammograms are obtained when there are no interactions among the attached molecules, the electrode surface is homogenous and the electrochemical reaction is at equilibrium. The equilibrium electrochemical reactions are achieved when scan rate (v)/ rate of the electrochemical reaction (k_s) tends towards to zero ($vnF/RTk_s \sim 0$). In contrast, the non-ideal response is obtained when the interactions among attached molecules are considered, resulting in a shift of E_p as well as a change of the shape of curves. In addition, the heterogeneity of the electrode surface gives similar effects as shown by the electrochemical response for the interactions between the molecules. As observed by Laviron *et al.*[59,61], when the ratio vnF/RTk_s is increased, differences between the oxidation and reduction peaks of the voltammograms appeared. This allows k_s to be calculated.

As mentioned generally in the paragraph above, the ideal system for strongly adsorbed molecules will be obtained when all the adsorption sites are equivalent and there are no interactions among immobilised molecules. Ideally, this condition follows a Langmuir isotherm[59,60,62]. It can be assumed that the area occupied by one molecule of the O or R forms is the same. Hence the first expression for the total surface concentration of adsorbed O and R forms is constant and equal to Γ_T as shown in Equation 1.1[59]. Thus, the maximal concentration of the adsorbed O and R forms is designated as Γ_m.

$$\theta_O + \theta_R = \theta_T \qquad \textbf{Eq. 1.1}$$

The coverages of θ_O, θ_R and θ_T are defined by $\theta_O = \Gamma_O/\Gamma_m$, $\theta_R = \Gamma_R/\Gamma_m$ and $\theta_t = \Gamma_T/\Gamma_m$.

By assuming that the surface coverages of O and R forms follow the Langmuir model, the second expression is obtained by writing that the current is proportional to the variation of Γ_O and Γ_R.

Cathodic current is considered as positive. The equations are expressed in Equation 1.2 and 1.3, respectively.

$$i_c = nFA\Gamma_m \frac{\delta\theta_R}{\delta t} \quad \textbf{Eq. 1.2}$$

$$i_a = -nFA\Gamma_m \frac{\delta\theta_O}{\delta t} \quad \textbf{Eq. 1.3}$$

Where *n* is the number of electrons transferred, *F* is the Faraday constant and *A* is the electrode area. In addition, by assuming the electrode surface is homogenous, the Langmuir model can be used which means that the homogenous surface is likely to ensure that the adsorption sites are equivalent. In this case, superficial concentrations tend towards zero and any interactions that exist among the immobilised molecules become negligible[59]. Thus, a surface standard potential ($E^{o'}$) can be defined as shown in Equation 1.4.

$$E^{o\prime} = E^o - \left(\frac{RT}{nF}\right) \ln\left(\frac{b_O}{b_R}\right) \quad \textbf{Eq. 1.4}$$

Where $E^{o'}$ is the standard potential of the species in solution, b_o and b_R are the adsorption coefficients of O and R forms. Essentially, b_O and b_R are assumed to be independent of the potential. Thus the equilibrium adsorption of O and R forms can be related to the standard free energy (ΔG) and can be written as expressed in Equations 1.5 and 1.6, respectively.

$$b_o = \exp(\frac{\Delta G_o}{RT}) \quad \textbf{Eq. 1.5}$$

$$b_R = \exp(\frac{\Delta G_R}{RT}) \quad \textbf{Eq. 1.6}$$

Based on Equations 1.5 and 1.6, Equation 1.4 can be written as expressed in Equation .1.7

$$nF(E^{o'} - E^o) = \Delta G_o - \Delta G_R \quad \textbf{Eq. 1.7}$$

Equation 1.7 shows that the increase, or decrease, of the electrical energy which has to be spent during the reduction and oxidation process is equal to the difference in the standard free energies of adsorption of O and R forms. If the oxidised (O) form is strongly adsorbed, ΔG_O decreases, thus $E^{o'}$ becomes more negative than E^o. In this case, more electrical energy has to be spent in order to compensate the energy lost by the molecules during the adsorption process.

Hence, the surface concentrations for Γ_O and Γ_R of O and R forms obey a surface Nernst equation as shown in Equation 1.8.

$$\frac{\Gamma_O}{\Gamma_R} = \exp\left[\left(\frac{nF}{RT}\right)(E - E^{O\prime})\right] \qquad \textbf{Eq. 1.8}$$

For an ideal system under the Langmuir isotherm conditions[59,62], in the voltammograms the peak potential E' is equal to E^{O}', the potentials for anodic and cathodic peaks are equal (E_{pa}= E_{pc}) and the full width at half maximum (FWHM) is equal to 90.6/n at 25 °C as already given in Equation 1.4. As a result, the oxidation and reduction peaks are symmetrical as shown in Figure 1.6.

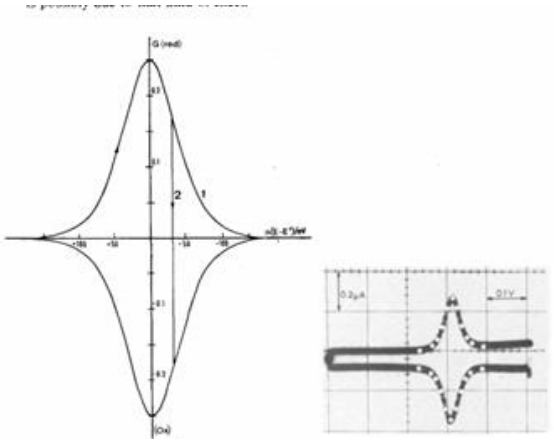

Figure 1.6; Theoretical adsorption for anodic and cathodic peaks (on the left) from ideal system when the electrochemical reactions follow a Langmuir isotherm. Experimental adsorption (on the right) for benzoquinoline at pH 11 in water-ethanol (9:1). A scan rate of 0.25 V s^{-1} was employed and the area of the electrode was 0.0136 cm^2. (Adapted from E. Laviron with permission)[62].

In terms of the kinetics of electron transfer at the surface of the electrode for the immobilised redox system without interactions between molecules, the *i-E* response curve (Figure 1.6) can be described by Equation 1.9 and follows a Langmuir isotherm[59]

$$i = nFAk_s(\Gamma_O\eta^{-\alpha} + \Gamma_R\eta^{1-\alpha}) \qquad \textbf{Eq. 1.9}$$

where k_s is the rate of the surface reaction in s^{-1} and α is the transfer coefficient. As theoretically pointed out by Laviron[59], when vnF/RTk_s tends towards zero, ideally, symmetric anodic and cathodic peaks can be obtained. In contrast, when vnF/RTk_s increases, the shapes of the peaks change and the difference for ΔE_p (E_{pa}-E_{pc}) between the cathodic and anodic peaks increase. Thus, the rate constant k_s can be calculated from the experimental values of ΔE_p and v[59,61].

In contrast, Laviron *et al.*[59,60] also discussed non-ideality for the immobilised case where it is caused by interactions among immobilised O and R forms in the film. As already shown in Figure 1.6 for the voltammetric response for the ideal case, in the non-ideal case the shape of the *i-E*

curve depends upon the energies of the interactions of O with O, R with R, and O with R. As a result, the interactions between molecules can be taken into account by considering the Frumkin isotherm and by assuming that the rate of electron transfer (k_s) is independent to the surface coverages[59,60]. In the case of the Frumkin isotherm, a random distribution of O and R sites in the film is assumed. Thus, the *i-E* curve can be expressed as shown in Equation 1.10[59,63]

$$exp\left[\frac{nF}{RT}(E - E^{o\prime})\right] = \frac{\theta_o}{\theta_R} exp\lfloor 2v\theta_o(a_{OR} - a_O) + 2v\theta_R(a_R + a_{OR})\rfloor \qquad \text{Eq. 1.10}$$

where a_{OR}, a_O, and a_R are the interaction coefficients for expressing O-R, O-O, and R-R interactions. Where $a>0$ and $a<0$, define an attractive interaction and a repulsive attraction, respectively. All the coefficients are assumed to be independent of the potential. In addition, the interactions parameters are assumed to vary linearly with the coverage of O and R. v is the number of water molecules displaced from the surface by adsorption of one O and R. θ_O and θ_R are the fractional coverages of O and R, respectively. For the non-ideal case, when the reaction is reversible, i.e; vnF/RTk_s tends towards ∞, the shape and the width of the voltammetric peak is governed by the parameters $vg\theta_T$. As discussed by Bard[63], from Eq. 1.10 the *i-E* curve can be expressed based on Equation 1.11

$$i = \frac{n^2 F^2 Av\Gamma_O^*}{RT}\left[\frac{\theta_R(1-\theta_R)}{1-2vg\theta_T\theta_R(1-\theta_R)}\right] \qquad \textbf{Eq. 1.11}$$

where $\theta_T = (\theta_O + \theta_R)$, $g = a_O + a_R - 2a_{OR}$, and $\Gamma_o^* = \Gamma_O + \Gamma_R$. The potential variation in Eq. 1.11 arises through the variation of θ_R with E, via Equation 1.8. As a result, the *i-E* response is governed by the interaction parameter $vg\theta_T$. When $vg\theta_T = 0$, the *i-E* curve follows Langmuir isotherm as already shown in Figure 1.6. When $vg\theta_T < 0$, the voltammetric peak will be broader and flatter than the Lagmuirian peak. On the contrary, the peak will be narrower and shaper when $vg\theta_T > 0$. These effects can clearly be seen as shown in Figure 1.7.

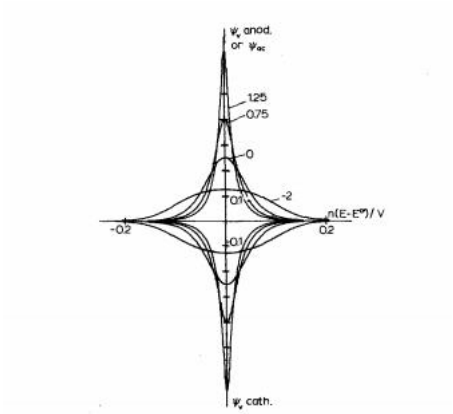

Figure 1.7; Equilibrium linear potential sweep voltammetry peaks that were obtained when a Frumkin isotherm is considered. The height and width of the anodic and cathodic peaks were obtained when $vg\theta_T$ values were varied from 1.25 to -2. At $vg\theta_T$ = 0, the voltammetric peak follows the Langmuir isotherm, as a result, the ideal behaviour is obtained. (Adapted from E. Laviron with permission)[59].

In terms of the kinetic surface reaction for the non-ideal system, Laviron and co-workers[59,60] assumed that k_s is independent with the surface coverages. This is because when the surface coverage increases, the orientation of immobilised molecules may vary, as a result, k_s will change. Thus they expressed an equation as shown below.

$$i = -nFAk_s\Gamma_m[\theta_o\eta^{-\alpha}\, exp(-\beta\theta_O - \Upsilon\theta_R) - \theta_R\eta^{1-\alpha}\, exp(-\lambda\theta_R - \mu\theta_O)] \qquad \textbf{Eq. 1.12}$$

At equilibrium, when i = 0, a similar expression as previously shown in Eq.1.10 was found. Thus, as stated by Laviron *et al.*[59,60] Equation 1.12 is compatible with a Frumkin isotherm, thus, the determination of k_s is difficult and it can be very different from the actual value of k_s as the interactions parameters (β, Y, λ and μ) are unknown.

Anson and Brown[64] also discussed the non-ideal behaviour of the Nernst equation for the attached redox molecules. In their model, by including the activity coefficients in the theoretical investigation of immobilised redox molecules, the peak height and wave shapes of the *i-E* curve from the experiments can theoretically be studied. The experimental CV from the adsorbed 9,10-Phenantherenequinone (9,10-PQ) system was fitted with the theoretical CV using Equation 1.13. This equation is assumed for the ideal system of the surface-bound reactant.

$$i = \frac{n^2F^2\Gamma_T v}{RT}\frac{\xi}{(1+\xi)^2} \qquad \textbf{Eq. 1.13}$$

Where Γ_T is the total amount of Q initially present on the electrode surface, v is the potential scan rate, and ξ= exp[(nF/RT)/(E-$E^{o'}$)]. As it is an ideal response, the *i-E* curve follows the Langmuir isotherm in which E_{pa} and E_{pc} appear at the same potential. In addition, the equal magnitude of peak currents (I_{pa} and I_{pc}) are given by Equation 1.14.

$$i_p = \frac{n^2F^2\Gamma_T v}{4RT} \qquad \textbf{Eq. 1.14}$$

The theoretical CV curve (dashed line) that was calculated using Eq. 1.13, does not give a good quantitative match to experimental CV (solid line) as shown in Figure 1.8.

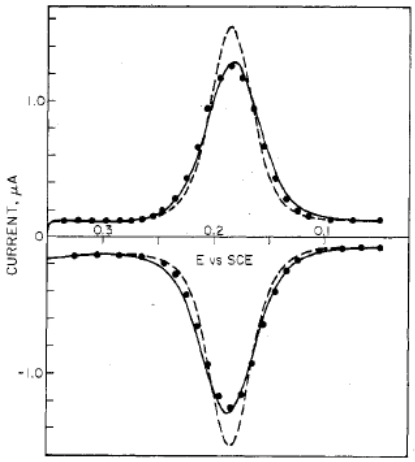

Figure 1.8; Experimental (solid line) and theoretical voltammograms reported by Brown and Anson for physically adsorbed phenanthrenequinone (9,10-PQ) at graphite electrodes. The theoretical voltammograms were generated by considering with (dotted line) and without (dashed line) non-ideality parameter interactions of attached molecules (*r*). (Adapted from Brown and Anson[64] with permission).

However, after taking into account the perturbation parameter (*r*) for the immobilised molecules (non-ideality parameters), the agreement of the theoretical CV current to the experimental voltammogram was improved significantly. Thus, after considering the *r* parameter in their numerical analyses, the theoretical CV currents (dotted line) produced a quantitative match to the experimental CV (solid line) as displayed in Figure 1.8. To account for the non-ideal behaviour surface activities, Equations 1.15 to 1.19 were employed in their model.

$$\xi = \frac{a_o}{a_R} = \frac{\gamma_O\Gamma_O}{\gamma_R\Gamma_R} \qquad \textbf{Eq.1.15}$$

Where α, Y, and Γ are the surface activities, activity coefficients and surface coverages, respectively. The subscript indicates the oxidised and reduced forms of the adsorbate. The activity coefficients of O and R forms are exponentially dependent on their surface concentrations, expressed as shown in Equation 1.16 and 1.17.

$$\gamma_O = exp - (r_{OO}\Gamma_O + r_{OR}\Gamma_R) \qquad \textbf{Eq. 1.16}$$

$$\gamma_R = exp - (r_{RR}\Gamma_R + r_{OR}\Gamma_O) \qquad \textbf{Eq. 1.17}$$

Where r_{OO} and r_{OR} are parameters that describe the interactions between attached oxidant due to the presence of the other attached oxidant and reductant molecules respectively. r_{RR} and r_{OR} are similar parameters for attached molecules but in the reduced form. As in the Laviron model, the Anson and Brown[64] model also assumes that the interaction parameters are not dependent upon the potential.

By substituting Eq. 1.16 and 1.17 in Eq. 1.15 and introducing the fraction (*f*) of the oxidised form on the surface of the electrodes, Equation 1.18 is obtained.

$$\xi = \frac{f}{1-f} exp - \{\Gamma_T[f(r_O + r_R) - r_R]\} \qquad \textbf{Eq. 1.18}$$

where $r_O = r_{OO} - r_{OR}$ and $r_R = r_{RR} - r_{RO}$

A further equation was obtained (Equation 1.19) by employing Eq. 1.18 in the Nernst equation (Eq 1.13). Thus Eq. 1.19 was used to get the *i-E* curve for cyclic voltammetry by relating the potential and the parameter *f*.

$$i = \frac{n^2F^2v\Gamma_T v f(1-f)}{RT[1-f\Gamma_T(r_O+r_R)(1-f)]} \qquad \textbf{Eq. 1.19}$$

However, when $r_O = r_R = 0$, as expected, Eq.1.19 reduces to Eq 1.14. As reported by Anson and Brown, Eq. 1.19 predicts that the anodic and cathodic peak currents will have an equal magnitude as given by Equation 1.20.

$$i_p = \frac{n^2F^2v\Gamma_T v}{RT[4-\Gamma_T(r_O+r_R)]} \qquad \textbf{Eq. 1.20}$$

Thus, the peak potentials for anodic and cathodic currents are given by Equation 1.21

$$E_{pa} = E_{pc} = E'_{O,R} - \frac{RT\Gamma_T(r_O-r_R)}{2nF} \qquad \textbf{Eq. 1.21}$$

where $E'_{O,R}$ is the formal potential for the attached couple. Equation 1.21 predicts that the two peak potentials will shift along the potential axis as a function of the concentration of attached reactant. However, $E_{pa} = E_{pc}$ remains constant when $r_O = r_R$.

As the voltammetric response from the non-ideal system is also affected by heterogeneity of the solid electrode surface, Laviron *et al.*[59,60] also discussed that the non-homogenous nature of the surface has to be taken into account. They considered that the coefficients of the Temkin isotherm can be described at the equilibrium reaction of the adsorbed molecules. Essentially, the Temkin isotherm describes adsorption that involves multiple interactions between the adsorbed molecule and surface. This can be explained when the adsorption of molecules to the surface sites involving

multivalent contacts that can be achieved by two contributions. Firstly, a favourable energy from the specific electrode surface-to-molecule contacts (intrinsic binding energy). Secondly, an unfavourable energy is required to match each binding site and molecules to make these contacts (rearrangement energy). However, at that time, no theory for the application of the Temkin isotherm voltammetry had been developed and Laviron[59] only makes some qualitative predictions. In his predictions, he considered that the reduction of the oxidised form will give a reduced form on the same site, particularly at the low coverages. As a result, the distance between the adsorbed molecules is large. If the coefficients of the Temkin isotherm for O and R forms are equal, and the effects of the surface heterogeneity on O and R forms are the same, the voltammetry peak may follow the ideal shape. This is because the difference in binding energy between O and R forms is constant. In contrast, if the coefficients are different, the reduction of O form will first take place on the sites that have the lowest difference in energy between O and R. Afterwards, the reaction will gradually occur on the sites that have higher difference in energy. Consequently, a very large magnitude electrical energy has to be used as compared to the ideal case. Thus, the peak will get wider and flatter. Comparing the voltammetric peak obtained with the Frumkin Isotherm to the peak based on the Temkin isotherm, Laviron[59] pointed out that the voltammetric shape is practically indistinguishable although their mathematical expressions are different. However, similarly, the derivations of both isotherms assume that the energy of the molecules varies linearly with the surface coverages.

1.7 Electrochemical techniques for estimating the surface coverages of immobilised reactants

The properties of modified electrodes are typically characterised using various electrochemical techniques in order to find out the amount of material attached to the surface, the redox chemistry of the attached material, and the redox potential of the attached species. Last but not least, the electrochemical kinetics of attached species such as the transfer coefficient and rate of electron transfer to/from the redox species to the surface of the electrode are also considered. The amount of attached material at the surface of the electrode can be very small, therefore sensitive electroanalytical techniques are required. The measurements of the amount of immobilised redox active species at the surface of the electrode is a major focus in this thesis.

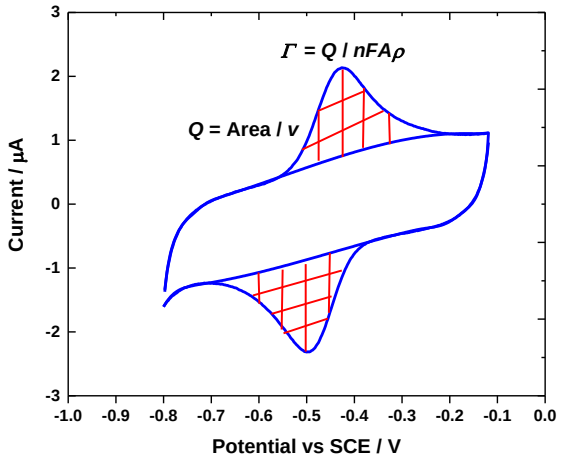

Figure 1.9; Cyclic voltammetric behaviour for a surface layer on an electrode. The amount of reactant on the electrode (Γ), can be obtained from the area under the oxidation or reduction peaks by calculating the Faradaic charge. The charge can be calculated by dividing the area under redox peak to the scan rate. The cyclic voltammogram was taken from Chapter 4 of this thesis.

The basic protocol for determining the surface coverages of immobilised redox species is the technique of cyclic voltammetry[51,65]. The general equation employed to determine the surface coverages of the attached redox molecules is expressed in Equation 1.22.

$$\Gamma = \frac{Q}{nFA} \qquad \textbf{Eq. 1.22}$$

Equation 1.22 is based on Faraday's law where Q is the charge passed for the oxidation or the reduction process. Q can be extracted by integrating the area under the voltammetry peaks and dividing the integrated area by the scan rate as shown in Figure 1.9. In addition, n, F, and A have

their usual meaning where *n* is the number of electrons transferred, *F* is the Faraday constant and *A* is the electrode area.

By contrast, numerous reports in the literature have extensively used a different approach by considering the microscopic roughness factor (ρ) of the cleaned electrode surface. Thus, the surface coverage is calculated using Equation 1.23.

$$\Gamma = \frac{Q}{nFA\rho} \qquad \textbf{Eq. 1.23}$$

Q, *n*, *F* and *A* have the same meaning as mentioned above, *p* is the roughness factor and it can be determined by calculating the ratio of the real area to the geometric area ($\rho = A_{real}/ A_{geometry}$). The scale of roughness for a cleaned electrode surface is completely dependent on the physical treatments of the surface such as polishing, washing, utrasonicating and cleaning solvent used, either aqueous or non-aqueous. Generally, the roughness scales that were experimentally determined and reported in the literature range between 1.2 to 3 for solid electrodes of the gold[66], bare ITO[67], silver, platinum[68] and screen printed carbon electrode[69]. The determined ρ values can than be used in Equation 1.23.

In comparing the two equations, Eq. 1.22 offers a simpler approach in which the expression assumes that the real area is similar to the geometrical area. Thus the roughness factor can be assumed as 1 ($\rho = 1$). Eq.1.22 has been extensively employed in most of the literature in order to calculate the surface coverages of the surface-confined redox species. In addition, the big advantage of these approaches that they apply for both the ideal or non-ideal CV responses, as discussed in Section 1.6, as we only need the integrated areas of the oxidation and reduction peaks, which directly allows us to calculate the surface coverage of attached redox molecule by estimating the Faradaic charge from the redox reaction.

In some cases, Equation 1.24 is also used. Thus, to calculate the surface coverage based on CV, Eq. 1.24 can be rewritten as shown in Equation 1.25.

$$i_p = \left(\frac{n^2F^2}{4RT}\right)\Gamma A v \qquad \textbf{Eq. 1.24}$$

$$\Gamma = \left(\frac{i_p 4RTAv}{n^2F^2}\right) \qquad \textbf{Eq. 1.25}$$

Where i_p is the anodic or cathodic current peak, *n* is the number of electrons transferred, *F* is the Faraday constant, *R* is the gas constant, *T* is the temperature in Kelvin, *A* is the electrode area, and *v* is the scan rate. This expression was first introduced by Sharp and co-workers in 1979[70]. The main feature of this equation is the dependence of the anodic and the cathodic current peaks on the scan rates (*v*). Thus, a linear relationship of *i* vs *v* should be obtained to confirm the presence

of the surface-confined redox couple. This linear relationship allows the surface coverage of immobilised redox species to be calculated. This calculation is based on a few assumptions. Firstly, an electrochemical process of the surface-confined redox species must be reversible with fast electron transfer kinetics. The immobilised redox layer must be stable and should produce the same height in the i_a and i_c. Secondly, this equation is only valid when the redox couple follows the Langmuir model. These topics have been discussed in detail in Section 1.6. However, i_p for anodic and cathodic currents depend on various factors such as the kinetic dispersion, the lateral electron transfer, the thermodynamic inhomogeneity, the desorption of the redox species from the film and the ohmic drop effect that may lead to broad or narrow the CV peaks. These complications give an inaccurate value for estimating the surface coverages of the attached redox molecules. Thus, this expression is seldom used in extracting the surface coverage.

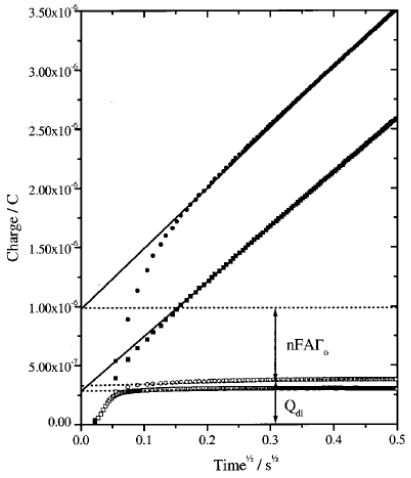

Figure 1.10; Chrono-coulometry response curves for estimating the density of immobilised DNA probes on the gold electrode, developed by Steel and colleagues in 1998. In the first step, the chronocoulometric measurements were performed in the background electrolyte, a buffer solution of 10 mM TRIS buffer, pH 7.4 in order to extract Q_{Buffer}. Then the solution was changed to 50 µM of $[Ru(NH_3)_6^{3+}]$ in TRIS buffer, pH 7.4 in order to determine the amount of the immobilised DNA probes (reprinted with the permission from ref 71)[71].

In dealing with chemically modified electrodes involving self-assembled DNA sequences either single-stranded DNA (ssDNA) or double-stranded DNA (dsDNA) at surface modified gold electrodes, Steel et al. developed[71] a procedure employing chroncoulometry that can be used to estimate the coverage of immobilised ssDNA and hybridised dsDNA. In this experiment, the probe DNA coverages at the surface of the gold electrode were calculated from the number of cationic redox molecules electrostatically associated with the anionic DNA backbone. The $[Ru(NH_3)_6]^{3+}$ cations charge to compensate the anionic phosphate groups in the DNA. An attractive protocol for the chronocoulometry was introduced by Steel in which the double layer charge in the buffer solution and the charge due to the reaction of $[Ru(NH_3)_6]^{3+}$ diffusing to the electrode surface can be differentiated from electrostatically bound $[Ru(NH_3)_6]^{3+}$ compensating

the anionic charge of the phosphate groups in DNA. The integrated current or charge (Q) as a function of time ($t^{1/2}$) in the chronoamperometry experiment was expressed based on the integrated Cottrell equation. The following expression is then obtained where the first term describes the diffusional contribution to the total change (Q) as shown in Equation 1.26.

$$Q = \frac{2nFD_o^{1/2}C_o}{\pi^{1/2}}t^{1/2} + Q_{dl} + nFA\Gamma_o \qquad \textbf{Eq. 1.26}$$

In this expression n is the number of electrons transferred, F is the Faraday constant, A is the electrode area, D_o is the diffusion coefficient, C_o is the bulk concentration, Q_{dl} is the capacitive charge and $nFA\Gamma$ is the charge from the reduction of the electrostatically bound $[Ru(NH_3)_6]^{3+}$ ions. Since it was introduced in 1998, Steel's procedure[71] has been a useful technique to determine the density of immobilised DNA at the surface of electrodes. As found in the literature, making a plot of Q against $t^{1/2}$, chronocoulomteric intercepts at $t = 0$ give Q_{buffer} and Q_{RuHex}, respectively. In general, Eq. 1.26 has been simplified as shown in Equation 1.27.

$$\Gamma_o = \frac{Q_{RuHex} - Q_{buffer}}{nFA} \qquad \textbf{Eq. 1.27}$$

where Q_{RuHex} is the charge in the presence of $[Ru(NH_3)_6]^{3+}$ analyte in the buffer solution and Q_{buffer} is the charge in the absence of $[Ru(NH_3)_6]^{3+}$ analyte, n is the number of electrons transferred per reduction event ($1e^-$), F is the Faraday constant and A is the electrode area. Under saturating conditions assuming that the anionic charge of the phosphate groups is entirely compensated by $[Ru(NH_3)_6]^{3+}$ in which one $[Ru(NH_3)_6]^{3+}$ ion electrostatically binds for every three nucleotide phosphate groups. Thus the density of DNA bound at the gold surface can be determined.

Another interesting technique for determining the surface coverages is differential pulse voltammetry (DPV). To date, and to the best of our knowledge, there is no specific protocol for extracting the surface coverages of the immobilised reactant using DPV. However, initial publications indicating the capability of DPV for estimating the surface concentration of the attached redox reactant was reported by Brown and Anson[64] in 1977 and Koval and Anson in 1978[72]. In their experiments, they added an external resistor (R_{ext}) to the DPV cell circuit when monitoring the coverage of the immobilised reactants. In particular, the advantage of employing an R_{ext} is that the sensitivity of the DPV technique can be enhanced as discussed by James and co-workers[64] in early 1977. Eight months later, from the same group, Brown and Anson[64] reported the first paper using DPV to measure the surface coverages of adsorbed reactants. In their work, they investigated the relationship of the DPV peak currents and the amount of R_{ext} added. This provided an approximate method based on a simple equivalent circuit (Figure 1.11) for measuring the Γ_{DPV} of the immobilised redox species.

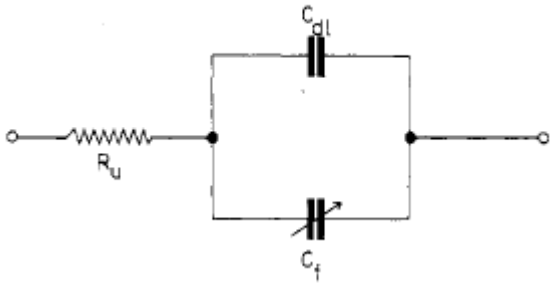

Figure 1.11; Simple equivalent circuit used by Anson *et al*. for approximation method in estimating DPV surface coverage (reprinted with the permission from ref. 64)[64].

$$i = \frac{\Delta E_p}{R_u} \exp - [\frac{t}{R_u(C_{dl}+C_f)}] \qquad \textbf{Eq. 1.28}$$

Where ΔE_p is the magnitude of each potential pulse, t is the pulse time and R_u is an unknown uncompensated solution resistance in the electrochemical cell. By adding the R_{ext} in the cell circuit, they found that the maximum DPV peak current was generated at a specific R_{ext} added. Differentiating Eq. 1.28 with respect to R_u predicts that the specific R_u can generate a maximum current ($i_{p,max}$) at a fixed sampling time. The differentiation of Eq. 1.28 can be expressed as follows;

$$\nabla = -\frac{\Delta E_p}{R_u}\ exp - \left[\frac{t}{R_u(C_{dl}+C_f)}\right] + \frac{\Delta E_p}{R_u}\frac{t}{C_{dl}+C_f R_u^2}\ exp - \left[\frac{t}{R_u(C_{dl}+C_f)}\right]$$

$$\nabla = \frac{\Delta E_p}{R_u^2}\ exp - \left[\frac{t}{R_u(C_{dl}+C_f)}\right]\left\{-1 + \frac{t}{(C_{dl}+C_f)R_u}\right\} \qquad \textbf{Eq. 1.29}$$

And set to 0, so maximum occurs for

$$\nabla = 0 = \frac{\Delta E_p}{R_u^2}\ exp - \left[\frac{t}{R_u(C_{dl}+C_f)}\right]\left\{-1 + \frac{t}{(C_{dl}+C_f)R_u}\right\}$$

$$0 = -1 + \frac{t}{(C_{dl}+C_f)R_u}$$

$$1 = \frac{t}{(C_{dl}+C_f)R_u}$$

$$R_{u,max} = \frac{t}{(C_{dl}+C_f)} \qquad \textbf{Eq. 1.30}$$

Again, they assumed that the Faradaic pseudocapacitance (C_f) at this $R_{u,max}$ condition is constant throughout the duration of the potential pulse. Thus, from their approximation method based on Eq. 1.28, substituting Eq. 1.30 to Eq. 1.28, they concluded that the maximum DPV peak current ($i_{p,max}$) at a specific R_{ext} added is given by Equation 1.31.

$$i_{p,max} = \frac{\Delta E_p (C_{dl}+C_f)}{\tau e} \qquad \textbf{Eq. 1.31}$$

Where ΔE_p is the magnitude of the potential pulse, C_f is the Faradaic pseudocapacitance at the peak potential, τ is the time after the pulse application when the current is measured, and e is a factor of 2.718. In addition, they assumed that the maximum fraction (f) of the oxidised molecular form attached at the electrode surface is 0.5. The nonideal parameter (r) from the interactions of between attached molecules is also considered. This point has specifically been discussed in Section 1.6 and it can be found from Eq. 1.15 to Eq. 1.21. Thus, the magnitude of the C_f corresponds to f from Equation 1.32.

$$C_f \; at \; i_{p,max} = \frac{n^2 F^2 \Gamma}{2RT(2-r\Gamma)} \qquad \textbf{Eq. 1.32}$$

Where n is the number of electrons transferred, F is the Faraday constant, Γ is the surface coverage, R is the gas constant, r is the non-ideal interaction parameter among the immobilised molecules and T is the temperature in K. As they found in their experimental study of the adsorbed 9,10-PQ system C_f was much larger than C_{dl}, by combining Equations 1.31 and 1.32 yield Equation 1.33, they gave the following equation to estimate the surface coverage from the DPV current.

$$\boldsymbol{\Gamma = \frac{2\,(i_p)_{max}}{r(i_p)_{max} + \frac{n^2F^2\Delta E_p}{2RT\tau e}}} \qquad \textbf{Eq. 1.33}$$

Where R, T, n, F, r, ΔE_p, τ and e = 2.718 have their usual meanings and as already mentioned above whilst $i_{p,max}$ is the maximum DPV peak current at $R_{ext,max}$ (Eq. 1.32). $R_{ext,max}$ is the specific R_{ext} added in the DPV cell circuit that generated the maximum DPV peak current. Note that in Brown and Anson's paper, we noticed that there is a typographical error in Equation 19. Thus Eq. 1.33 is the correctted equation for the approximation for Γ using DPV.

A year later, Koval and Anson[72] proposed a new mathematical expression for determining $\Gamma_{DPV,\ exp.}$ In this approach, they assumed that the immobilised redox system the pentamineruthenium (II) complex, follows ideal Nernstian behaviour as expressed in Equation 1.34.

$$C_f\ at\ i_{p,max} = \frac{n^2F^2A\Gamma}{4RT} \qquad \textbf{Eq. 1.34}$$

By substituting Eq. 1.30 in the Nernstian reactant expression (Equation 1.34). Thus, the substitution of Eq. 1.30 into Eq. 1.34 gives

$$\Gamma = \frac{4RT}{n^2F^2A}\ (\frac{t}{Ru_{max}} - C_{dl}\ ) \qquad \textbf{Eq. 1.35}$$

where R is the gas constant, T is the temperature in Kelvin, n is the total number of electrons transferred, F is the Faraday constant, A is the area of the electrode, t is the fixed time at which the DPV current is sampled, $R_{u,max}$ is the value of the R_u added that gives the maximum DPV peak current, and C_{dl} is the double layer capacitance. Again, we noticed that there is a typographical error in Equation 5 from their paper. Thus, Eq. 1.35 shown herein is the correctted mathematical expression.

Nevertheless, as discussed by Blaedel and Mabbot[65], the mathematical model equations proposed by Brown and Anson[64,72] for the reaction mechanisms in response to the DPV waveforms are very complex for the surface-redox reactions. Apart from Blaedel and Mabbot's work, to date, no further reports have appeared the another use of the equations by Anson and co-workers for determining the surface coverages of attached reactants by DPV. Even though the proposed equations by Anson *et al.*[64,72] for estimating the DPV surface coverages are not widely used, however, the papers published by Anson and colleagues[64,72] on the effects of the presence of external resistance (R_{ext}) in estimating the DPV surface coverages of the attached redox molecules has motivated a lot of interest in this area of research.

1.8 Why use DPV?

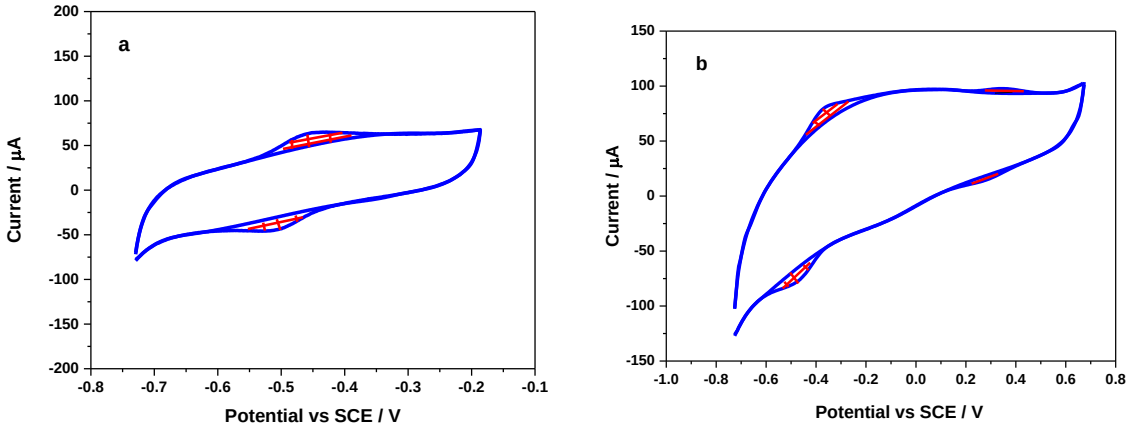

Figure 1.12; Cyclic voltammograms for immobilised redox molecules at the surface of the electrode. a) CV behaviour for a small concentration of immobilised reactant. b) CV behaviour for mixed-layer of immobilised redox molecules. The CVs were taken from Chapters 4 and 5 of this thesis.

The most common method used for determining the surface coverages of immobilised redox molecules on modified electrodes is estimating the charge under the oxidation and reduction peaks in cyclic voltammetry (CV)[65]. Nevertheless, CV is not very sensitive at low coverages of surface modified species as depicted in Figure 1.12a due to the background charging current, which obscures the Faradaic signal[72,73]. Hence, the detection limit is around 10^{-5} M[74]. In addition, modification of electrode surfaces with immobilised mixed layers either employing two different redox groups[75,76] or one redox molecule with an inactive long alkyl chain (dilution procedure)[77,78] is one of the strategies for chemically modified electrodes[79]. However, it can be challenging to measure the surface coverages by CV because the final composition may produce a low surface concentration of the redox molecules (Figure 1.12b). Moreover, the shape of the cyclic voltammogram tends to become less ideal for mixed layers[33,77]. This is the main motivation to explore differential pulse voltammetry (DPV) measurement for estimating the surface coverages of immobilised redox species.

1.9 Differential Pulse Voltammetry (DPV)

Pulse voltammetric was introduced by Barker and Jenkin[80], their motivation was to lower the detection limits of voltammetric measurements. With the intention of increasing the ratio between the Faradaic and non-Faradaic currents, such techniques permit convenient quantitation down to the 10^{-8} M level. Due to the great improvement in detection limit, modern pulse techniques have

largely supplanted classical polarography in the analytical laboratory. In the late 1950s, a pulse polarographic instrument, based on the Barker design, was manufactured in England and sold, at least in the United States, for about $25,000; a princely sum in those days[81]. The first development of pulse techniques was made with the dropping mercury electrode. The objective was to synchronise the pulses with drop growth and reduce the capacitive current contribution by current sampling at the end of drop life. After applying a pulse of potential, the capacitive current decays away faster than the faradaic current and the current is measured at the end of the pulse. Therefore, this technique has the advantage of an increase in sensitivity and better characteristics for analytical applications[82]. Though in fact, the dropping mercury electrode has an excellent cathodic range, its anodic range is very limited. Therefore, pulse voltammetry at stationary solid electrodes is an alternative approach in order to achieve highly sensitive determination of oxidised substrates[5].

The early studies of pulse voltammetry at solid electrodes showed that sensitive and reproducible results can be obtained for reductions from aqueous media or hydrofluoric acid solvent. Sokol *et al.*[83] discussed utilising platinum electrodes for DPV in order to study the reversible oxidation of 9,10-diphenylanthracene and irreversible oxidation of 2,4,6-tri-tert-butylphenol, m-anisaldehyde, and isobutyraldehyde at a range of potentials from +1.2 to +2.9 V *vs* SCE. They reported that the background current produced by platinum electrodes at positive potentials was dramatically suppressed. The results show an improvement in the signal-to-background ratio for samples that were oxidised at potentials more positive than about +1.5 V *vs* SCE. However, only m-anisaldehyde and isobutyraldehyde gave about a 5-fold increase in the signal-to-background ratio.

In principle, there are three commonly used techniques of pulse voltammetry that are widely discussed in text books and articles. They are the normal pulse voltammetry (NPV), differential pulse voltammetry (DPV), and square wave voltammetry (SWV). As discussed by Hussam[74], DPV and SWV have similar advantages and give a lower detection limit of 10^{-8} M. On the other hand, NPV can easily be used to measure concentration down is 10^{-5} M with a detection limit of 10^{-6} M. However, our major focus is on utilising DPV in order to determine surface coverage of immobilised reactants at the surface of the electrode. This is because DPV is more suitable and sensitive than a normal pulse and derivative normal pulse[84] in this application.

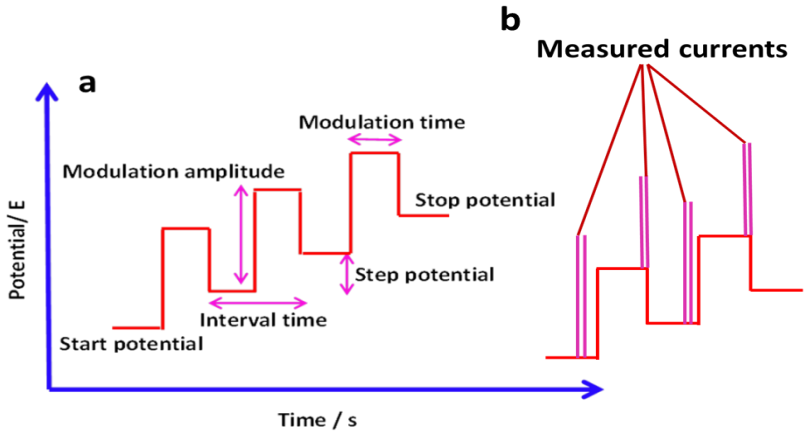

Figure 1.13; The common feature of the DPV waveform that can normally be found in literature. The potential waveform of DPV consists of small pulses (constant amplitude) superimposed upon a staircase waveform. b) Enlargement of two different pulses where the current is sampled twice in each pulse period (once before the pulse and at the end of the pulse). Then, the difference between these two current values is recorded and displayed.

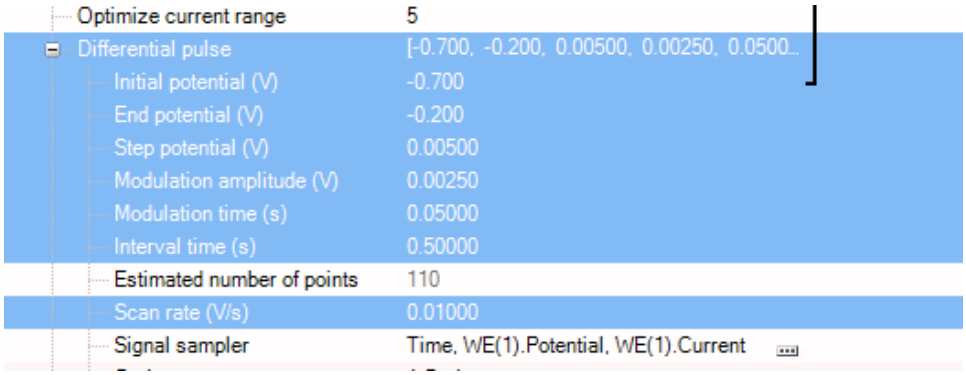

Figure 1.14; Screen shot from the Nova software shows four different of DPV parameters need to be set up before starting a DPV measurement; step potential (ΔE_s), modulation time (τ_p), modulation amplitude (ΔE_p), and interval time (τ_i). In contrast, the scan rate of DPV can be obtained by dividing the step potential to interval time.

Differential pulse voltammetry is based upon the application of successive double potential pulses which produce a peak-shaped response for which the non-Faradaic contribution and the Ohmic drop effect are significantly reduced. As shown in Figures 1.13(a) and 1.13(b), the current is measured at the end of each pulse, and the difference between the two current samples [$\Delta I = I_2 - I_1$)] is plotted versus a potential (x-axis)[85]. The arithmetic average of both potential values [$E_{1,2} = (E_1 + E_2)/2$] is selected as the x-axis potential[86]. In DPV, the duration of the second pulse is often much shorter than the duration of the first pulse[86]. Figure 1.14 shows the four different DPV parameters that need to be set up in Nova software before running the DPV measurements.

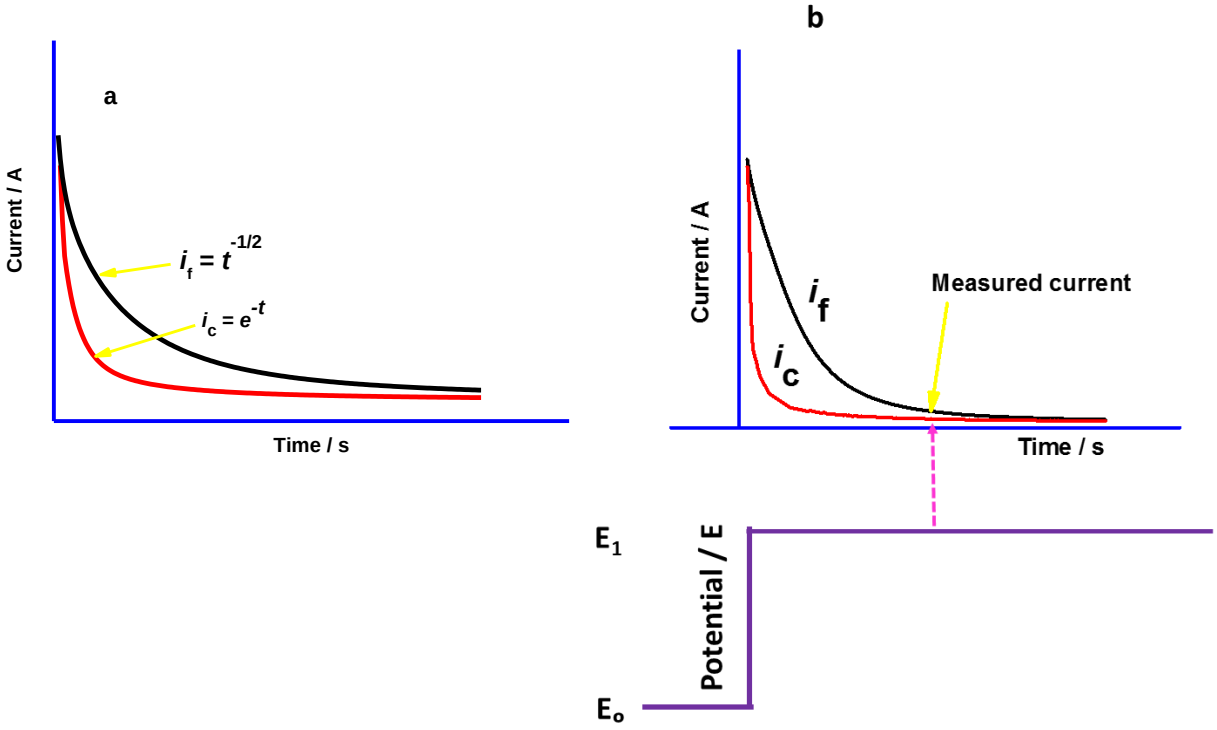

Figure 1.15; a) Two contribution to the DPV currents (the capacitive and Faradaic currents) when measuring DPV for redox species in solution. The capacitive current decays exponentialy whereas the Faradaic current decays with the square root of time. b) The decay of the capacitive and Faradaic current for the case of immobilised redox species, where both DPV current decay contributions exponentialy.

The basis of all pulse techniques used for the study of electroactive species in homogeneous solutions is the difference in the rate of decay of the charging current and the Faradaic current following a potential step[87] as illustrated in Figure 1.15a. The charging current decays exponentially, whereas the Faradaic current associated with the rate of solution-phase diffusion decays as a function of 1/(time$^{1/2}$). Thus the rate of decay of the charging current is considerably faster than the rate of decay of the Faradaic current[88]. As a result, measuring the current at the end of the potential pulse, it is possible to discriminate the Faradaic current over the charging current. However, for surface bound reactants, in the absence of any diffusing reactants, this is no longer the case. The Faradaic current decays faster following the potential step than in the homogeneous solution case[87]. In that case, the Faradaic current also decays exponential, as displayed in Figure 1.15b. Despite this, DPV still remains a more sensitive technique than CV for the study of low coverages of attached species. In order to increase the sensitivity of DPV for immobilised redox species, a suitable additional external resistance (R_{ext}) can be added to the working electrode and the system ground[64,72,87,89]. In our work, this has been employed to study the electrochemical redox

behaviours of redox molecules confined at the surface of modified electrodes in order to produce a well-resolved DPV peak signals, especially when using very small coverage of redox molecules.

There are extensive publications on the determination of surface coverages of immobilised redox species for chemically modified electrodes using CV, however, the study of modified electrodes using DPV has not received much attention. To the best of our knowledge, only a few papers have reported on measuring surface coverages by the DPV technique[12,64,72,90]. These papers have their own protocols and specifically offered different equations in order to calculate the surface coverages from the DPV measurement. Comparison between their methods is summarised in Table 1.1. We are interested in the proposed method for determining Γ_{DPV} for low-level adsorbed and covalently attached reactants that was reported by Brown and Anson[64] in 1977 and Koval and Anson in 1978[72]. Therefore, the main aim of this study was to conduct experimental and theoretical DPV study using our chemically modified electrodes in order to estimate the number of attached molecules at the surface of the modified electrodes.

Table 1.1- Survey of the literature on DPV surface coverages measurements.

Title	Immobilised reactants	DPV surface coverages equations	References
Development of new localised surface plasmon resonance on gold nanostructures sandwiched between tin-doped indium oxide films	- The surface of ITO electrode was treated with gold nanostructure and a thin ITO film. -Ethynyl ferrocene was coupled to the azide-terminated ITO/Au NSs/ITO surface, using click chemistry. - The ferrocene modified ITO/Au NSs/ITO was measured using DPV *vs* Ag/AgCl	-The DPV surface coverages of ferrocene were estimated from the current intensity of DPV peak, employing Equation 1.36. $I_{pa} = \frac{(1-\alpha)nn_aF^2Av}{2.718RT}\,\Gamma$ **Eq. 1.36** -Where i_{pa} is the anodic peak current, α is charge transfer coefficient, n is the total number of electron, n_a is the total number of electrons involves in the rate-determining step, F is the Faraday constant and v is the scan rate. -DPV parameters used; Unreported	Joaana *et al*., 2009[12]
Adsorption behaviour of dinucleotides on bare and Ru-modified carbon electrode surfaces	-Physically adsorbed FAD at GC electrode.	-The area under DPV peak represents the charge, employing Eq. 1.37. $Q = nFA\Gamma$ **Eq. 1.37** -Where Q is the charge, n is the number of electrons involved in the redox reaction, F is the Faraday constant, A is the surface area of the electrode, Γ is the FAD surface concentration. -The equilibrium surface concentration of FAD on GC electrode was calculated by integrating DPV peaks after the baseline correction. -DPV parameters used; Modulation amplitude = 50 mV, Modulation time = 0.07 s, Interval time = 0.25 s, Step potential = 0.015 V and Scan rate DPV = 7.5 mV /s.	Wei *et al*., 2008[90]

Table 1.1- Survey of the literature on DPV surface coverages measurements (continued).

Title	Immobilised reactants	DPV surface coverages equation	Reference
Electrochemistry of the Ruthenium (3^+, 2^+) couple attached to graphite electrodes	- Physically adsorbed and covalently immobilised pyridinepentaaamineruthenium (II) complexes at the graphite electrodes.	-By adding the external resistance in series to the working electrode, the optimum DPV peak current at a specific R_{ext} was obtained. $$\Gamma = \frac{4RT}{n^2F^2A}\left(\frac{t}{Ru_{max}} - C_{dl}\right)$$ -By employing equation above (Equation from Eq. 1.35) the Γ_{DPV} was calculated. -Where R is the gas constant, T is the temperature in Kelvin, n is the total number of electron, , F is the Faraday constant, A is the area of electrode, t is the fixed time at which DPV current is sampled, Ru_{max} is the value of R_u at a maximum DPV peak current, C_{dl} is the double layer capacitance. -DPV parameters used; Modulation amplitude = 5 mV, Modulation time = 0.048 s, Interval time = Unreported, Step potential = Unreported and Scan rate DPV = Unreported.	Koval and Anson, 1978[72]

Table 1.1- Survey of the literature on DPV surface coverages measurements (continued).

Title	Immobilised reactant	DPV surface coverages equations	Reference
Cyclic and differential pulse voltammetry behaviour of reactants confined to the electrode surface.	-Physically adsorbed 9,10-phenanthrenequinone at basal plane pyrolytic graphite.	-By adding the external resistance in series to the working electrode, the optimum DPV peak current at a specific R_{ext} was obtained. -A nonideal parameter from the CV is needed, which is *r*. -*r* is the perturbing influence experienced by a given molecule of attached. $$\Gamma = \frac{2(i_p)_{max}}{r(i_p)_{max} + \frac{n^2F^2\Delta E_p}{2RT\tau e}}$$ -By employing equation above (Equation from Eq. 1.33) the Γ_{DPV} was calculated. -Where *R* is the gas constant, *T* is the temperature in Kelvin, *n* is the total number of electron, *F* is the Faraday constant, i_{pmax} is the optimum DPV peak current at Ru_{max}, ΔE is the magnitude of the potential pulse, τ is the time after the pulse application when the current is measured and e = 2.718. -DPV parameters used; Modulation amplitude = 5 mV, Modulation time = 0.048 s, Interval time = Unreported, Step potential = Unreported and Scan rate DPV = Unreported.	Brown and Anson 1977[64]

1.10 Voltammetric simulations

Electrochemical simulations are widely used for voltammetry and it is a common electrochemical practice to validate experimental using simulation. Generally, the voltammetric waveform is dependent on thermodynamic and kinetic parameters including the formal potential of redox species, double layer capacitance, diffusion coefficient, surface coverages of immobilised redox species, the rate of electron transfer, transfer coefficient and several more. Therefore, by performing voltammetric simulations, the simulation data can be helpful in obtaining more information about electrochemical processes. This means that the electrochemical parameters that could not be accessed by experiments could be obtained by simulations. Essentially, the voltammograms can be modelled by digital simulation, mathematical analysis, and numerical algorithms. However, the distinctions between them are not always clear cut[91].

Digital simulation programs such as DigiElch and Digisim, designed by specialists are wider used nowadays, particularly to study the theoretical responses for system voltammetry. This a versatile and powerful technique. However, the voltammetric simulations that we wanted to employ here are not offered by DigiElch or Digisim software. In this project, voltammetric simulation programs were written in the MATLAB environment. MATLAB is one of the most popular scientific computation programs and allows an easy implementation for numerical computation, visualisation and programming. The basic data element is a matrix, and problems and solutions are expressed in familiar mathematical notation.

In this thesis, the simulations were carried out in collaboration with Associate Professor Guy Denuault. Two different types of voltammetry simulation have been developed during the work of this research using numerical techniques in order to mimic the physicochemical properties of the electrode process. The first simulation was developed for the DPV experiment on immobilised redox molecules at the surface of modified electrodes. In contrast, the second simulation was specifically developed for CV experiments on the electrochemical grafting of primary amine linkers to the surface of GC electrodes as mentioned generally in Section 1.5. Details of the simulations for each case will be explained in Chapters 4 and 6 of this thesis.

1.11 Research objective and overview

This thesis demonstrates general methods for preparing the chemically modified electrodes such as physical adsorption, self-assembly monolayers and covalent attachment in order to produce the different variety of chemically modified electrodes (CMEs). In addition, various redox molecules such as 9,10-phenanthrequinone, 2-anthraquinone carboxylic acid, osmium bipyridine complex were immobilised at the surface of modified electrodes either by direct attachment to the surface of electrodes, by organic linkers and or by attachment of the redox molecule to the DNA chain.

Generally, every electrochemist who is interested in chemically modified electrodes could prepare these CMEs. However, the main goal of this research is to estimate the amount of immobilised redox species at the surface electrode by using the DPV technique. This research was carried out to seek a new perspective on determining surface coverages of redox molecules by DPV rather than relying on CV measurements. Therefore, an experimental model has been developed in this work. Accompanying the experimental model, the DPV simulation was also developed in order to verify the experimental approach.

The second concern in this work was to improve the efficiency of electrochemical grafting of primary amine linkers to the surface of GC electrodes using a new strategy, as well as to obtain better surface coverages of immobilised molecules. Our established method for grafting the EDA-Boc linker to the surface of carbon electrodes was first introduced in 2008. Since it was reported in 2008, the details of the electrochemical reaction during attachment of EDA-Boc to the surface of carbon electrodes have not been explored. In this thesis, the theoretical responses on the electrochemical grafting of EDA-Boc to the surface of GC electrodes was investigated.

Chapter 2 provides the details of the chemicals, materials, equipment, and methods for the preparation and characterisation of the chemically modified electrodes. In addition, the procedures for integrating the area under DPV peak using Origin 9.1 software were also given.

Chapter 3 demonstrates the simple procedure for producing a CME where the physical adsorption of quinone onto the surface of GC electrode was adopted. 9,10-PQ was drop cast onto the surface of GC electrodes for preliminary experiments to estimate surface coverages by DPV measurements. The Γ_{DPV} equation from Anson's group[64,72] has been employed in this work. The general characterisations on 9,10-PQ modified electrodes by CV and chronocoulometry were made in order to extract the electrochemical parameters such as surface coverages by CV, transfer coefficient, the rate of electron transfer and double layer capacitance. In addition, the layer structure of adsorbed 9,10-PQ was also investigated using EIS measurements.

Chapter 4 generally shows that the established method in our group for covalently immobilising redox species. The 2-AQ-carboxylic acid was covalently coupled at the surface of GC electrodes through an EDA linker. The initial work was to show that the CME produced from the covalent attachment gives robust a modified surface in terms of stability and well-behaved quinone redox system. From the stable modified surfaces of AQ immobilised through EDA linker, an experimental model for estimating the surface coverages of immobilised AQ by DPV measurement was introduced. In addition to the experimental model, the DPV simulation was developed in order to mimic the electrode process, where the experimental approach was verified.

Chapter 5 was done as part of a collaboration with a group at Queen Marry, University of London led by Professor Jeremy Kilburn. The two main aims in this Chapter were to test and demonstrate the utility and flexibility of our experimental and simulation models for estimating DPV surface coverages on different schemes for covalent attachment of redox molecules to the GC electrodes. Thus, in this work, an osmium bipyridine complex was covalently attached to the surface of the GC electrode through a hexadiamine (HDA) linker. Further, a more complex modified surface was made by covalent grafting of two redox molecules at the surface of the GC electrodes in order to create a mixed-monolayer structure. Os-AQ modified GC electrodes were produced and was tested experimentally and with simulation model in order to demonstrate the utility and flexibility of our developed models.

Chapter 6 concentrates on electrochemical grafting of the EDA-boc linker to the surface of GC electrodes by employing two different methods. The first method was based on a general method for grafting EDA-Boc linker in neat acetonitrile in the presence of the supporting electrolyte tetrabutylammonium tetrafluoroborate (TBATFB). The second method was based on a new electrochemical grafting of EDA-Boc in a mixed solvent of acetonitrile and sodium hydrogen bicarbonate (weak base) in a ratio of 4:1, again with TBATFB electrolyte. Since the first method was introduced in 2008 in our group, the details of electrochemical reaction during attachment of EDA-Boc to the surface of the carbon electrode, signalled by CV has not been given much attention. Thus in this chapter, the CV simulation program for electrochemical grafting of EDA-Boc was developed in order to study the theoretical response for grafting EDA-Boc. The same approach was also performed on electrochemical grafting of EDA-Boc in mixed solvents of acetonitrile and $NaHCO_3$. By performing CV simulation in this work, several electrochemical parameters that could not be accessed directly through experiments such as $E°$, k_A, k_H, α, and Γ, could be obtained.

Chapter 7 focuses on the preparation of a CME by using the self-assembly monolayer technique for immobilising a 24-mer single-stranded DNA labelled with AQ at the 3' to the surface of a gold electrode. The self-assembly monolayer technique is less stable than covalent attachment for immobilised redox molecules, but the main aim of this work to test the application of our models on a different type of electrode and attachment of the redox species.

Chapter 8 presents recommendations for future work in order to extend our work either for experimental or simulations models. Further experiments are recommended that could give insight on the surface of the modified electrodes. In addition, further research is needed to apply the developed models to a wider variety of chemically modified electrodes.

Chapter 2: Material and methods

2.1 General procedures

The experimental and simulation procedures presented in this chapter are a general description of the methods used. Details of specific experimental and simulation conditions can be found in the results and discussion for each experimental chapter of this thesis.

2.2 Chemicals

All chemicals used in this research are listed in Table 2.1. The reagents were used without further purification. Deionised water (resistivity 18 MΩ cm) from a Purite select water purifying system was used throughout for solution preparation.

Table 2.1; List of chemicals and materials used in this thesis

Chemical	Purity	Supplier
9,10-phenanthrenequinone	≥ 99 %	Sigma-Aldrich
Methanol	99.9 %	Fisher Scientific
Sodium ferricyanide	99 %	Fissons
Sodium ferrocyanide	99.99 %	Fissons
Sodium phosphate monobasic	98 %	Sigma-Aldrich
Sodium phosphate dibasic	99 %	ACROS
Hydrochloric acid	37 %	Fisher Scientific
Potassium chloride	99.6 %	Fisher Scientific
1.0 µm alumina polishing powder	-	BUEHLER
0.3 µm alumina polishing powder	-	BUEHLER
Acetic acid	99.8 %	Analar
Sodium acetate	≥ 99.0 %	Sigma Aldrich
Ammonia	35 %	Fisher Scientific
Ammonium chloride	98.8 %	Analar
Sodium chloride	≥ 99.5 %	Sigma-Aldrich
Sodium hydroxide	≥ 98 %	Sigma-Aldrich
Acetonitrile	HPLC	Fisher Scientific
N-Boc-ethylenediamine	≥ 98.0 %	Sigma-Aldrich
1,4-Dioxane	≥ 98.0 %	Fisher Scientific
1-ethyl-3-(3-dimethylaminopropyl) carbodiimide	≥ 97 %	Sigma-Aldrich
N-hydroxysuccinimide	98 %	Sigma-Aldrich
Anthrquinone-2-carboxylic acid	> 99.0 %	TCI Chemicals
Sodium hydrogen bicarbonate	99 %	Sigma-Aldrich
1,8-diazabicycloundec-7-ene	98 %	Sigma-Aldrich
Trifluoro acetic acid	99 %	Sigma-Aldrich
Tetrabutylammonium tetrafluoroborate	> 99.0 %	Sigma-Aldrich
Dimethylformamide	HPLC	Fisher Scientific

2.3 GC electrodes

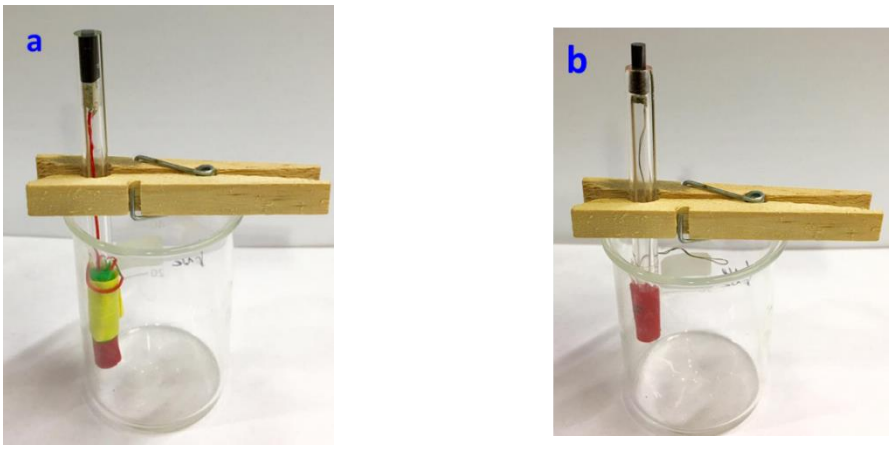

Figure 2.1; Two different designs of GC electrode used. a) The old design of GC electrode. b) The new design of GC electrode.

For the experimental work on adsorbed 9,10-PQ at the surface of GC electrode, the old design of GC electrode as shown in Figure 2.1a was used. In contrast to the experimental work on covalently immobilised AQ and Osmium complex using amine linkers, a new design of GC electrode was used (Figure 2.1b) in order to use the meniscus contact method described below.

2.4 Fabrication of an old design of GC electrode

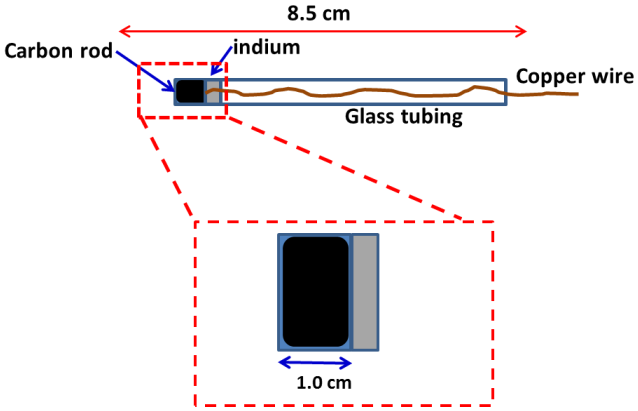

Figure 2.2; Schematic representation of an old design GC electrode.

8.5 cm long of glassy carbon electrodes with a surface area of 0.071 cm^2 were fabricated as shown in Figure 2.2. A 1 cm length of carbon rod was sealed inside of the glass tube. A copper wire was permanently connected to the carbon rod using melted indium (Aldrich).

2.5 Fabrication of a new design of GC electrode

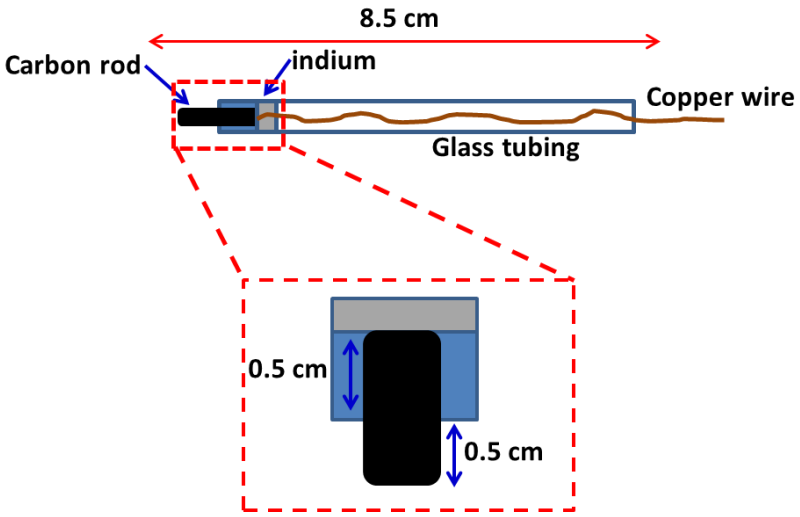

Figure 2.3; Schematic representation of a new design GC electrode.

8.5 cm long of glassy carbon electrode with a surface area of 0.071 cm^2 were fabricated as shown in Figure 2.3. A 0.5 cm length of carbon rod was left protruding from the glass whilst another 0.5 cm was sealed inside of the glass tubing. The fabrication of this type of glassy carbon electrode was due to sensitive a meniscus measurement of our modified electrodes. A copper wire was permanently connected to the carbon rod using melted indium (Aldrich). The setup for the working electrode was chosen to be able to apply the meniscus configuration during the electrochemical experiments. This technique allowed us to characterise the modified surface avoiding any contributions to the electrochemical signal from material adsorbed on the sides of the GC rod.

2.6 Cleaning surface of the GC electrode

Before the modification procedure, the glassy carbon electrodes were polished using silicon carbide polishing paper (grade 1200) followed by a 5 micron lapping film. Then, the glassy carbon electrodes were polished with 1 and 0.3 µM of alumina slurries on polishing cloth pads (Buehler). The polished electrodes were sonicated with deionized water (DI) for 7 min and were dried in air. Then, they were sonicated again in ethanol for 10 min and dried in air. The cleaned surface GC electrodes were covered with pipette tips when they were not in use.

2.7 Electrochemical cell design for meniscus experiment set up

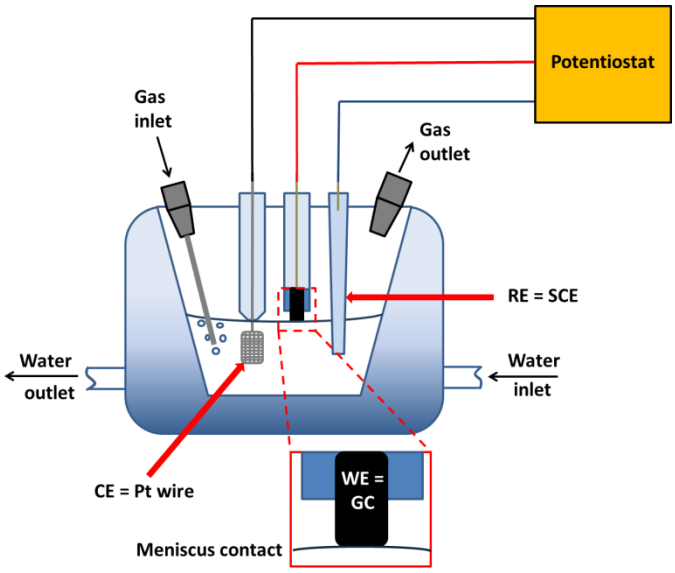

Figure 2.4; Experiment set up for meniscus measurements at modified GC electrodes. A homemade electrochemical cell was obtained from the blowing glass workshop, University of Southampton.

For the meniscus contact measurements on our modified glassy carbon electrodes, a suitable electrochemical cell was designed. The meniscus contact was achieved by slowly lowering the modified electrode towards the electrolyte surface until the meniscus contact was determined by eye. The cell has five necks, three for the working, counter and reference electrodes, the other two necks were used for gas inlet and outlet. A frit was used for purging the electrolyte solution with argon gas. The buffer was purged for 20 min prior to electrochemical measurements by CV, DPV and EIS, respectively. During the experiment, the frit was pulled up manually and a flow of argon gas at a slow rate was maintained above the electrolyte. The oxygen outlet was closed with a rubber stopper.

2.8 Why use meniscus contact method?

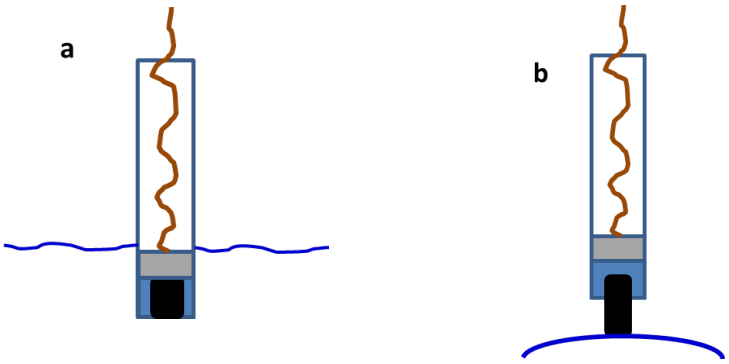

Figure 2.5; Working electrode set up for electrochemical experiments. The old set up (a) and the meniscus contact set up (b).

Figure 2.5a shows the old set up with the working electrode inside the electrolyte solution. We know from experience of former group members that this type of set up presents the problem of contamination from materials trapped between the glass holder and the carbon, due to leakages caused by differential thermal expansion of the glass and GC. As a result, contaminated materials could also contribute in part to the signal detected by CV. Therefore, we decided to employ the meniscus contact set up as shown in Figure 2.5b. In the meniscus configuration, only the bottom surface of the GC electrode is in contact with the buffer solution through the meniscus. This can avoid any contribution to the detected signals from the sides of the carbon rod.

2.9 Electrochemical instruments

Electrochemical measurements (cyclic voltammetry, differential pulse voltammetry and chronoamperometry) were carried out by using an Autolab PGSTAT30 Potentiostat/Galvanostat (Ecochemie). Electrochemical impedance spectroscopy (EIS) measurements for determining uncompensated solution resistance (R_u) in the electrochemical cell and double layer capacitance (C_{dl}) of modified electrodes were performed on an Autolab PGSTAT30 Potentiostat/Galvanostat (Ecochemie). All the measurements were made using a three-electrode system which was placed in a Faraday cage. The three-electrode system consists of a working electrode (modified GC electrode), a reference electrode (saturated calomel electrode, SCE) and a counter electrode (platinum gauze, 1 cm x 0.5 cm). A resistor box (RS component) was added in the electrochemical cell circuit, (via the working electrode) to provide a series of different magnitudes of external resistance for the DPV experiments. In addition, the resistor box was also used in chronoamperometry and EIS measurements in order to obtain different R_{ext} conditions in the electrochemical cell.

2.10 Homemade Dummy cell for the *RC* equivalent circuit

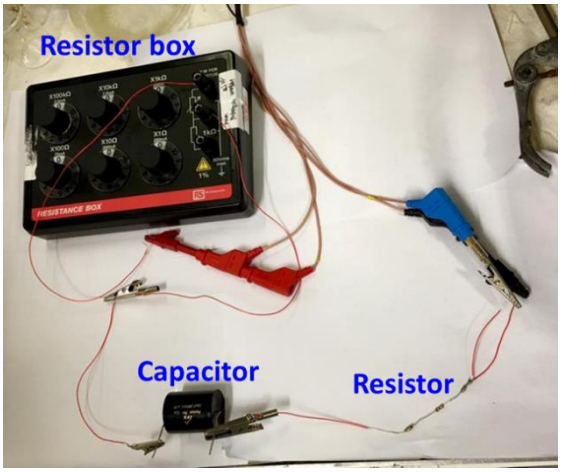

Figure 2.6; Homemade dummy cell for the *RC* equivalent circuit connects to a resistor box.

A homemade dummy cell for the *RC* equivalent circuit was made by constructing the circuit using a fixed resistance value of 180 ± 5 Ω and connecting to a capacitor as shown in Figure 2.6. Two different capacitor values were used in the EIS measurements, which were at 18 ± 3 µF and 20 ± 3 µF, respectively. The resistor component with a 5% tolerance was bought from NOVA and the capacitor components were bought from the JB capacitors company.

2.11 Experimental

2.11.1 Reagents

2.11.1.1 Preparation of 0.1 M buffer solutions (pH 1-13)

Solutions with pH values from pH 1-13 were prepared by employing the two solutions method, with the two solutions were having the same buffer concentration (0.1 M). To obtain the desired pH, two different solutions were well-mixture while monitoring the required pH with a pH meter as detailed in Table 2.2. Each solution (0.1 M) such as hydrochloric acid, sodium phosphate monobasic, sodium phosphate dibasic, sodium acetate, acetic acid, potassium chloride, ammonium chloride, ammonia and sodium hydroxide were prepared as stock solutions in volumetric flasks of 250 mL.

Table 2.2; Preparation of 0.1 M buffer solutions for pH 1-13 based upon the two solutions method.

pH	Buffer composition (0.1 M)
1.0	Hydrochloric acid (HCl) + Pottasium Chloride (KCl)
2.0	Hydrochloric acid (HCl) + Pottasium Chloride (KCl)
3.0	Acetic acid (CH_3COOH) + Sodium acetate ($C_2H_3NaO_2$)
4.0	Acetic acid (CH_3COOH) + Sodium acetate ($C_2H_3NaO_2$)
5.0	Acetic acid (CH_3COOH) + Sodium acetate ($C_2H_3NaO_2$)
6.0	Sodium phosphate monobasic (NaH_2PO_4) + Sodium phosphate dibasic (Na_2HPO_4)
7.0	Sodium phosphate monobasic (NaH_2PO_4) + Sodium phosphate dibasic (Na_2HPO_4)
8.0	Sodium phosphate monobasic (NaH_2PO_4) + Sodium phosphate dibasic (Na_2HPO_4)
9.0	Ammonia (NH_3) + Ammonium Chloride (NH_4Cl)
10	Ammonia (NH_3) + Ammonium Chloride (NH_4Cl)
11	Ammonia (NH_3) + Ammonium Chloride (NH_4Cl)
12	Sodium Hydroxide (NaOH) + Sodium phosphate dibasic (Na_2HPO_4)
13	Sodium Hydroxide (NaOH) + Sodium Chloride (NaCl)

2.11.1.2 Preparation of 0.01 M $Fe(CN)_6^{-3/-4}$ redox couple solution

0.329 g of ferricyanide $K_3[Fe(CN)_6]$ and 0.368 g of ferrocyanide $K_4[Fe(CN)_6]$ were dissolved in 0.1 M phosphate buffer solution. The solution of was used in EIS measurement for investigating the blocking effect of the immobilised films.

2.11.2 Procedures for Chapter 3

2.11.2.1 Reagent solutions

0.052 g of 9,10-Phenantherenequinone (Sigma) was dissolved in 100 mL methanol solution (HPLC grade/ Merck), 0.1 M phosphate buffer (pH 7) was prepared with a mixture of NaH_2PO_4 and Na_2HPO_4, used as a supporting electrolyte in an electrochemical cell.

2.11.3 Modification of the cleaned GC electrodes with 9,10-PQ

The 9,10-PQ modified glassy carbon (GC) electrode was prepared by drop casting 3 μL of a solution of 1 mM 9,10-PQ onto the cleaned surface of GC as illustrated in Figure 2.7. Then, the 9,10-PQ modified GC electrode was dried for 3-min at room temperature. Phosphate buffer (pH 7) solution was deoxygenated by purging with Ar gas for at least 20 min prior to electrochemical measurements. All the electrochemical experiments on the 9,10-PQ modified GC electrode were conducted using three different modified GC electrodes in order to the reproducibility.

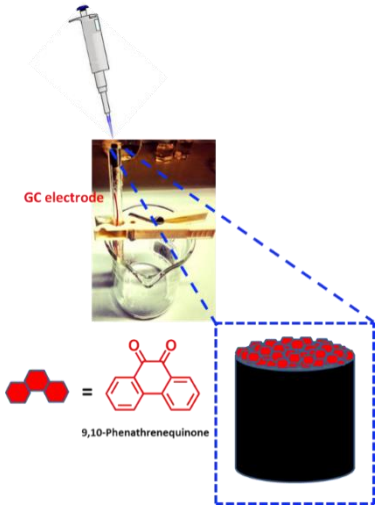

Figure 2.7; Experimental set up for modification of glassy carbon electrodes with 9,10-PQ based upon a drop casting method.

2.11.4 Characterisation of the 9,10-PQ modified GC electrodes

2.11.4.1 pH study of the 9,10-PQ modified GC electrodes

Cyclic voltammetry measurements for 9,10-PQ modified glassy carbon electrodes were carried out in 0.1 M buffers, pH values (pH1-13). The pH values were adjusted to pH 1-13 by using the two solution method, which the two solutions are having the same buffer concentration (0.1 M). To obtain the desired pH, 2 different solutions were well mixed while monitoring the pH with a pH meter. The compounds used are listed in Table 2.2. Buffer solutions were deoxygenated by purging with Ar gas for at least 20 min prior to electrochemical measurements by CV. All CV experiments for the 9,10-PQ modified GCE were conducted in triplicate in order to obtain reproducible half-wave potentials (E_{mid}) at a scan rate of 50 mV/s.

2.11.4.2 Varying R_{ext} in the DPV cell circuit for determining the DPV surface coverages

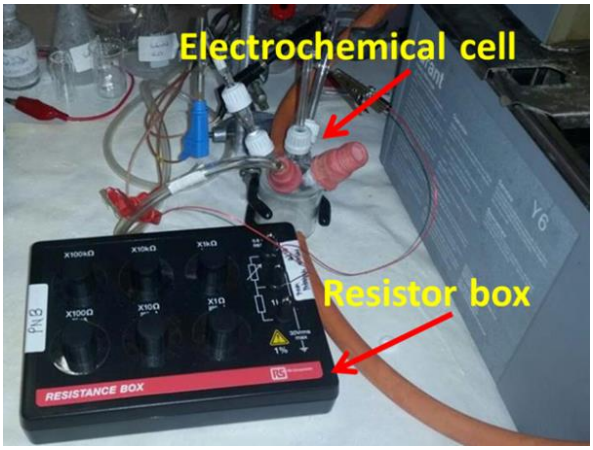

Figure 2.8; An adjustable resistor box was added in the cell circuit for external resistance (R_{ext}).

The adjustable resistor box was added to the cell circuit and was connected with a 9,10-PQ modified GC electrode as displayed in Figure 2.8 in order to obtain different magnitudes of R_{ext} for the DPV measurements. In contrast, the general circuit as illustrated in Figure 2.9 shows the R_{ext} added in series with the working electrode in the electrochemical system of our modified electrodes. The connection of a resistor box to the working electrode was also used for EIS and chronoamperometry measurements.

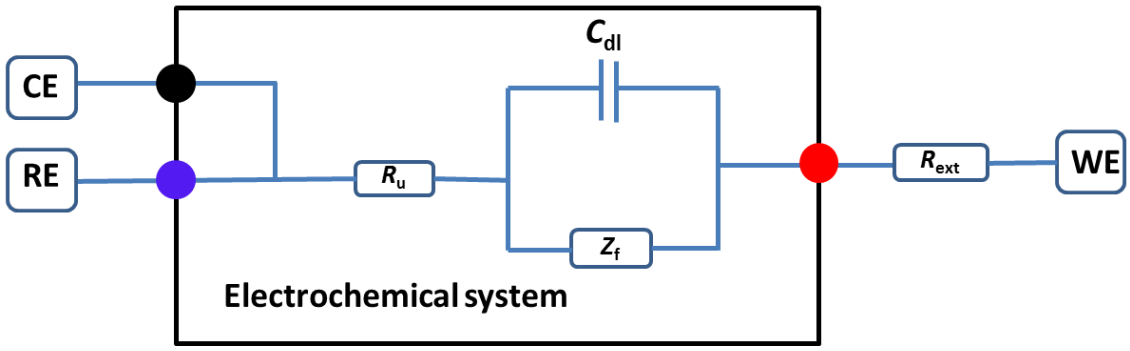

Figure 2.9; The external resistor (R_{ext}) with schematic of the general Randles equivalent circuit for the electrochemical system model. R_u is the solution resistance, C_{dl} is the double layer capacitance and Z_f is the Faradaic impedance.

Care was taken to hold the conditions constant in the electrochemical cell for the DPV measurements, especially in the position of the working electrode between a counter electrode and a reference electrode. A potential scan at -0.5 V to -0.08 V *vs* SCE was used and the temperature of 25 ± 0.5 º C in the electrochemical cell was controlled by a water bath.

2.12 Procedures for Chapter 4

2.12.1 Reagent solutions

0.024 g of N-Boc-ethylenediamine and 0.33 g tetrabutylammonium tetrafluoroborate (TBATFB) were dissolved in 10 mL acetonitrile. The concentrated hydrochloric acid (HCl) 12 M was diluted with 4 M HCl in 1,4-dioxane. 0.0378 g of anthraquinone-2-carboxyclic acid, 240 µL N-(3-dimethylaminopropyl)-N-carbodiimide (EDC), 0.0342 g N-hydroxysuccinimide (NHS) were dissolved in 3 mL dimethylformamide (DMF) solution. For the control GC electrodes, 0.0378 g of AQ was dissolved in 3 mL DMF solution.

2.12.2 Electrochemical grafting of EDA-Boc to the surface of GC Electrode

The electrochemical immobilisation of EDA-Boc linker at the surface of GC electrodes (Figure 2.10) was achieved by electrochemical oxidation from a solution containing 0.024 g N-Boc-EDA and 0.330 g TBATFB in 10 mL acetonitrile (15 mM). The electrode was cycled for 7 cycles within the potential window from 0 to 2 V *vs* Ag/AgCl at a scan rate of 50 mV s^{-1} using a meniscus experiment set up.

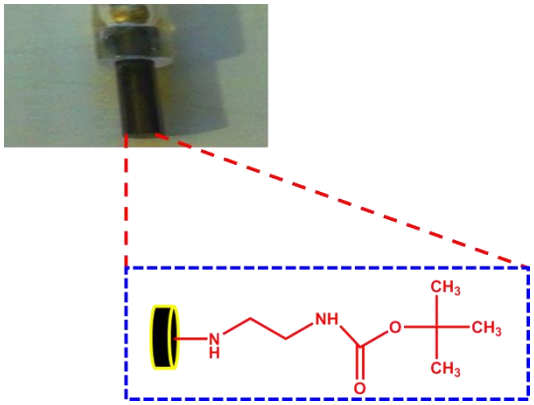

Figure 2.10; Electrochemical grafting of EDA-Boc at the surface of the GC electrode by oxidation process 15 mM EDA-Boc.

2.12.3 Removing of Boc protecting group from the grafted EDA-Boc

The GC electrodes with the grafted EDA-Boc were suspended in 4 M HCl in dioxane solution at room temperature and were stirred for 1 h. The deprotected electrodes were rinsed with deionised water, acetonitrile and then dried in air for 1 min.

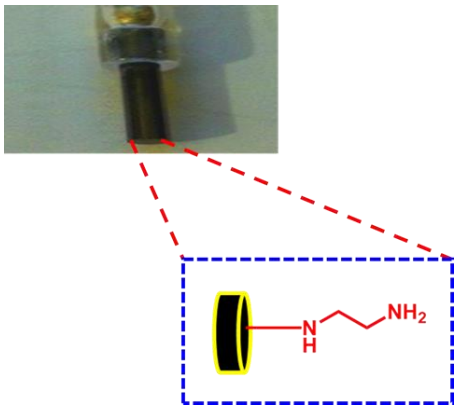

Figure 2.11; The immobilised free EDA after removal of the Boc group with 4 M HCl in 1,4-dioxane.

2.12.4 General procedures for the coupling reaction of AQ on EDA modified GC electrodes

The coupling of AQ to the EDA linker (Figure 2.11) was performed from 3 mL DMF solution containing 37.8 mg AQ, 240 µL EDC and 34.2 mg of NHS at room temperature and they were stirred using a magnetic stirrer for 16 h. The modified electrodes were then washed thoroughly with deionised water, acetonitrile and dried before electrochemical measurements. After the first check by cyclic voltammetry, the electrode was left stirring in DMF for 3 consecutive days in order to remove any adsorbed AQ at the electrode. The AQ modified GC electrodes (Fig. 2.12) were covered with pipette tips when they were not being used.

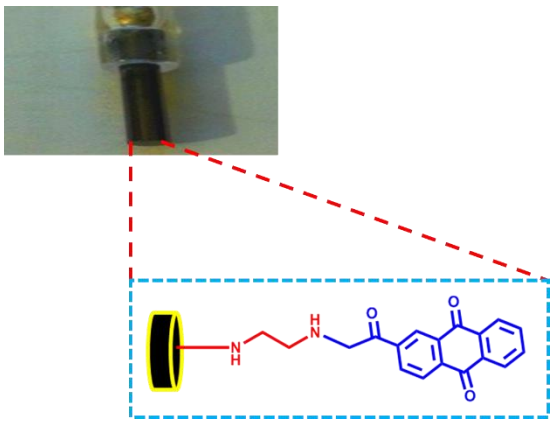

Figure 2.12; The covalently immobilised AQ-2-carboxylic acid at the surface of the GC electrode by attached via the EDA linker.

2.13 Procedures for Chapter 5

2.13.1 General procedures for covalent immobilisation of the Os bipyridine complex at the surface of GC electrode.

This work was carried out in collaboration with Professor Jeremy Kilburn and Dr. Jessica Gropi at Queen Mary, University of London. The Os modified GC electrodes were kindly prepared and provided by Dr. Jessica Gropi. The general procedures for covalently coupling the Os complex at the surface of the GC electrode is shown in Scheme 2.1. The details of the procedures are given in her PhD thesis[92] and published article[93].

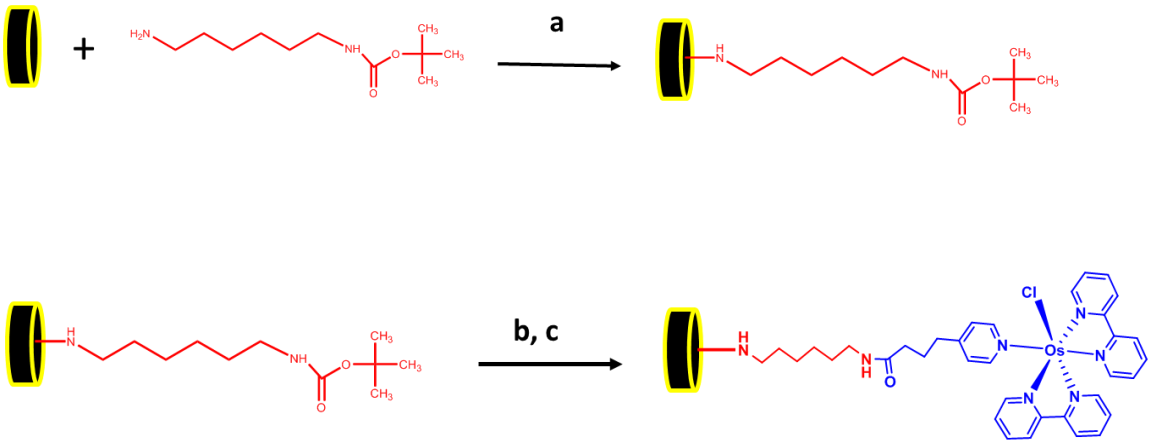

Scheme 2.1- Synthetic steps for the preparation of HDA-Os monolayer. Conditions; a) 20 mM HDA in acetonitrile with 0.1 M TBATFB, cyclic voltammetry 0-2 V, 5 cycles. b) 4 M HCl in dioxane for 1 h. c) 10 mM Osmium complex, 0.1 M EDC and 60 mM NHS in DMF for 16-h.

2.13.2 General procedures for covalent immobilisation of AQ and Os bipyridine complex at the surface of GC electrode (mixed-monolayers)

The AQ-Os modified GC electrodes were prepared and provided by Dr Jessica Gropi. The general procedures for covalently grafting AQ and Os at the surface of GC electrode can be seen in Scheme 2.2. Again, the details of the procedures could be found in her PhD thesis[92] and published article[93].

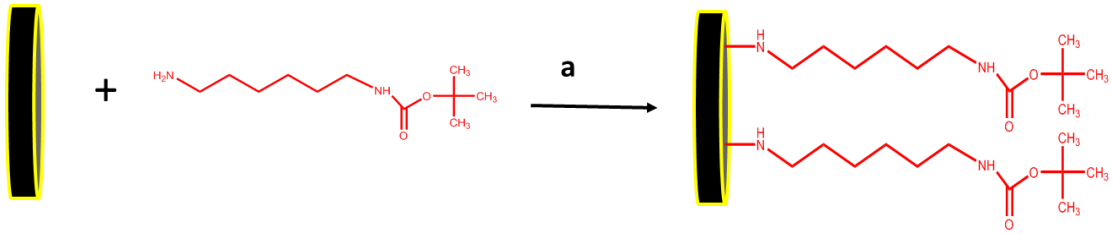

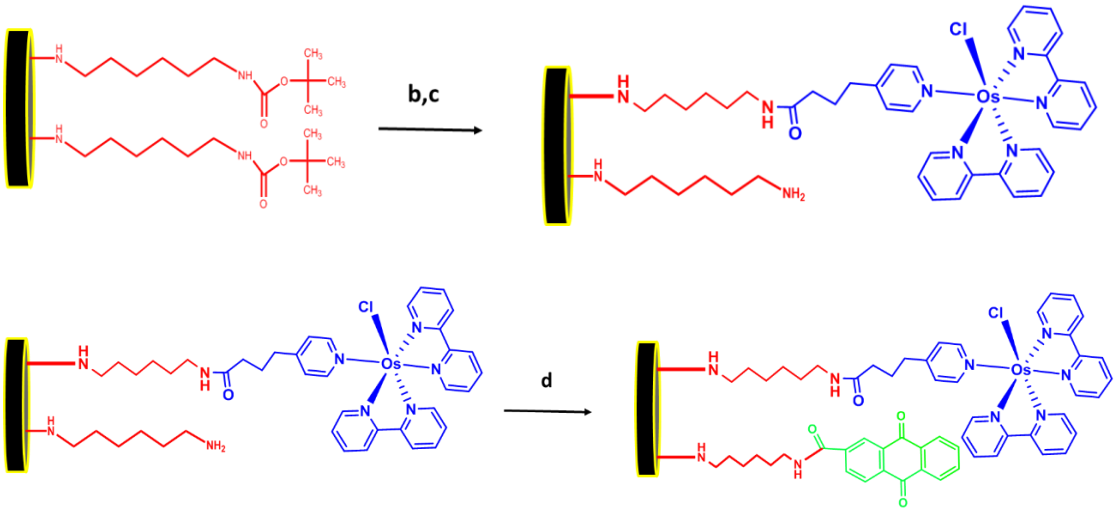

Scheme 2.2- Synthetic steps for the preparation of a HDA-Os/AQ monolayer. Conditions; a) 20 mM solutions in CH_3CN with 0.1 M TBATFB, cyclic voltammetry 0-2 V, 5 cycles. b) 4 M HCl in dioxane for 1 h. c) 10 mM osmium complex, 0.1 M EDC, 60 mM NHS in DMF for 16-h. d) 50 mM anthraquinone-2-carboxylic acid, 0.5 M EDC, and 0.3 M NHS in DMF for 16-h.

2.14 Procedures for Chapter 6

2.14.1 Reagent solutions

10 mM of the EDA-Boc solution was prepared by dissolving 0.016 g of N-Boc-EDA and 0.330 g of TBATFB in 10 ml acetonitrile. Concentrated hydrochloric acid (HCl) 12 M was diluted with 4 M HCl in 1,4-dioxane. 10 mg of anthraquinone-2-carboxyclic acid, 480 µL N-(3-dimethylaminopropyl)-N-ethylcarbimide, EDC, 0.0684 g N-hydroxysuccinimide (NHS) were dissolved in 6 mL DMF solution. The sodium hydrogen bicarbonate ($NaHCO_3$) solution (0.1 M) was prepared by dissolving a 0.84 g of $NaHCO_3$ in 100 ml of deionized water. A stock solution of 0.1 M 1,8-diazabicycloundec-7-ene (DBU) was prepared by diluting 1.49 mL of concentrate (DBU 6.69 M) in 100 ml acetonitrile. 0.1 M trifluoroacetic acid was prepared by diluting 0.77 ml of concentrated TFA acid in 100 ml of acetonitrile.

2.14.2 Electrochemical modifications of GC electrodes with EDA-Boc linker in neat acetonitrile-Method 1

The electrochemical immobilisation of Boc-EDA linker at the surface of glassy carbon electrodes was achieved by electrochemical oxidation from a solution containing 0.016 g N-Boc-EDA and 0.330 g TBATFB in 10 mL acetonitrile. The electrode was cycled for 7 cycles within the potential window from 0 to 2 V *vs* Ag/AgCl at a scan rate of 50 mV s^{-1} using the meniscus contact method.

2.14.3 Electrochemical modifications of GC electrodes with EDA-Boc linker in acetonitrile/sodium hydrogen carbonate (4:1)-Method 2

The electrochemical immobilisation of Boc-EDA linker at the surface of glassy carbon rod electrodes was achieved by electrochemical oxidation from mixed solvents containing 0.016 g N-Boc-EDA and 0.330 g TBATFB in 8 mL ACN and 2 mL of 0.1 M $NaHCO_3$. The electrode was cycled for 7 cycles within potential a window ranging from 0 to 2 V *vs* Ag/AgCl at a scan rate of 50 mV s^{-1} using the meniscus contact method

2.14.4 Deprotecting of Boc group from the grafted EDA-Boc

The Boc-protected modified glassy carbon electrodes were suspended in 4 M HCl in dioxane at room temperature and were then stirred for 1 h. The Boc-deprotected modified electrodes were washed thoroughly with water and acetonitrile and dried before further synthetic modification.

2.14.5 General procedures for the coupling reaction of AQ on EDA modified GC electrodes

The Boc-deprotected modified glassy carbon electrodes were immersed in 6 mL of DMF solution containing 10 mg AQ, 480 µL EDC and 68.4 mg of NHS at room temperature and were stirred using a magnetic stirrer for 16 h. The modified electrodes were then washed thoroughly with deionised water, and acetonitrile and dried before electrochemical measurements. After the first check by cyclic voltammetry, the AQ modified GC electrodes were stirred in DMF for three days in order to remove non-covalent of AQ at the electrode. In addition, the AQ modified GC electrodes were covered with pipette tips when they were not in used.

2.14.6 Effect of electrochemical attachment of EDA-Boc in the presence of strong organic base 1,8-diazabicycloundec-7-ene (DBU)

This study was achieved by electrochemical oxidation from mixed solvents containing 0.016 g N-Boc-EDA and 0.330 g TBATFB in 8 mL ACN and 2 mL of 0.1 M DBU. The electrode was cycled for 7 cycles within the potential window 0 to 2 V *vs* Ag/AgCl at a scan rate of 50 mV s^{-1} using the meniscus contact set up.

2.14.7 Effect of electrochemical attachment of EDA-Boc in the presence of Trifluoroacetic Acid (TFA)

This study was achieved by electrochemical oxidation from mixed solvents containing 0.016 g N-Boc-EDA and 0.330 g TBATFB in 8 mL ACN and 2 mL of 0.1 M TFA. The electrode was

cycled for 7 cycles within a potential window from 0 to 2 V *vs* Ag/AgCl at a scan rate of 50 mV s^{-1} using meniscus contact set up.

2.15 Procedures for Chapter 7

The experimental work in this chapter was done in collaboration with Rachel Gao, a PhD student under the supervision of Professor Philip Bartlett. The modified gold electrodes with AQ-single stranded DNA based on a self-assembled monolayer with mercaptohexanol treatment were kindly prepared and provided by Rachel.

2.15.1 General procedure for immobilising 24-mer single stranded DNA (ss-DNA) probes with the attached AQ at the surface of Gold electrode

A 24-mers single stranded DNA probe with the attached AQ at the 3' end was employed in this work. The sequence of the 24-mers single stranded oligonucleotide probe was 5'-linkage-GTACCGTCACCCGCAGCATCATTT3-3' (3 –Anthraquinone). The 5' end of the probe was attached to a linkage unit with one hexaethyleneglycol (HEG) spacer and three dithiol phosphoramidites. Scheme 2.3 shows the procedures, based on a self-assembled monolayer of dithiol at the surface of the gold electrode, for immobilising the 5'-linkage-GTACCGTCACCCGCAGCATCATTT3-3' (3–Anthraquinone). In the subsequent procedure, the DNA-modified electrodes were treated with 6-mercapto-1-hexanol as a capping agent to prevent non-specific binding of DNA and to reorientate the DNA strands.

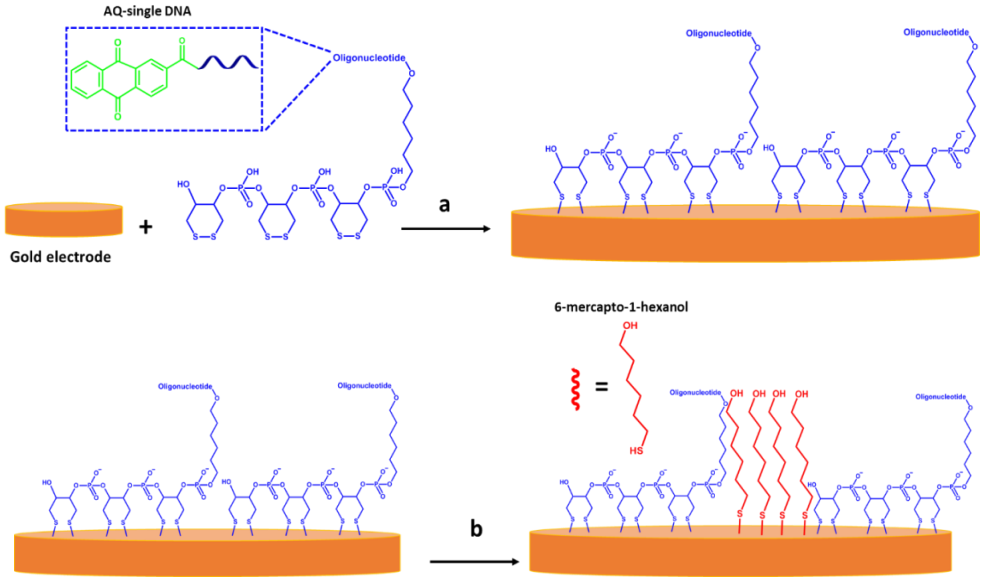

Scheme 2.3; Self-assembly monolayer steps for immobilisation of single stranded oligonucleotide-AQ probes onto the surface of gold electrodes by dithiol-gold bonds. a) 1 µM of 5' dithiol modified probe oligonucleotide in 100 µL of 0.01 M Tris buffer (pH 7.5) containing 0.5 M NaCl for 6 h at 6° C. b) 10 µM 6-mercapto-1-hexanol in 100 µl of 0.01 M Tris buffer (pH 7.5) containing 0.5 M NaCl for 4 h at 6° C.

2.16 Integrating area under DPV peak

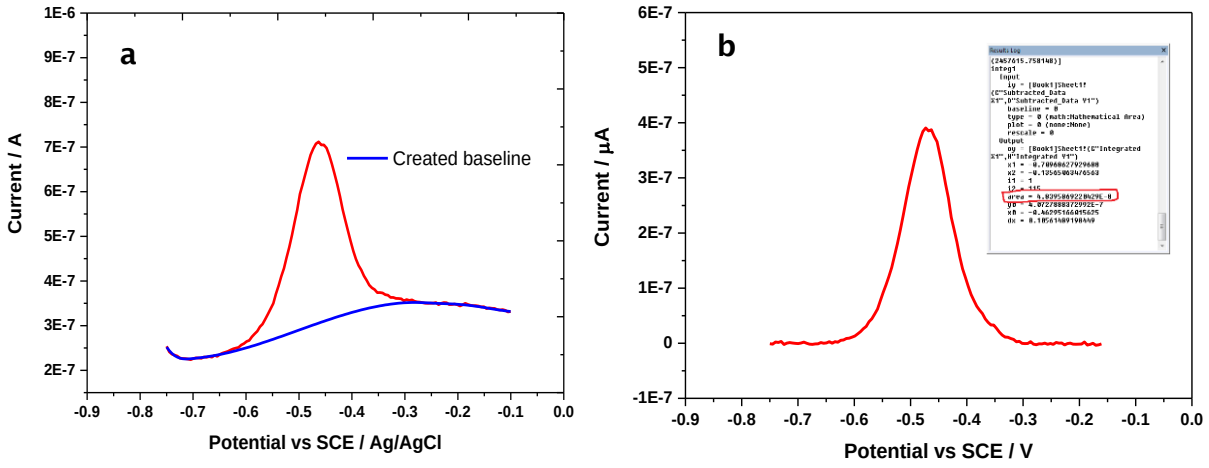

Figure 2.13; a) Created baseline for background current by using a BSpline function in Origin before performing the background subtraction. b) After background subtraction using subtract baseline functions and mathematics function for extracting the area under DPV peak.

In order to calculate the Γ_{DPV} based on our modelled equation (will be discussed further in Chapter 4), the area under the DPV peak is needed. The area can be extracted by subtracting baseline area under DPV peak employing Origin 9.1 software. In the first step, the baseline for the capacitive current was created by setting the integrate peak mode in the peak analyser function. The fourteen points were manually placed on the curve of DPV waveform, except at the potential range between the Faradaic current. Then the points were interpolated using the B-spline function to produce the baseline as shown in blue line (Figure 2.13a).

By performing the subtract baseline, the subtracted DPV peak was obtained as shown in Figure 2.13b. The final step was made by using the integrate function. Then, the integrated area under DPV peak was obtained as shown in the red circle (Figure 2.13b).

Chapter 3: Adsorbed quinone at GC electrodes as preliminary experiments for DPV surface coverages

3.1 Overview

For the initial studies, we wished to use a simple adsorption method while developing an experimental model for estimating the surface concentration of immobilised redox molecules by DPV measurement. Therefore, the initial research was focused on the modification of glassy carbon (GC) electrodes with 9,10- phenanthrenequinone (9,10-PQ) based on physical adsorption. A 1 mM 9,10-PQ solution (3 μL) was employed in the first experiments and the 9,10-PQ was drop cast onto the surface of the GC electrodes. A 1 mM 9,10-PQ was chosen because it was reported by Tashio and co-workers[94], to produce a monolayer 9,10-PQ adsorbed at the surface of a gold electrode. Despite it being a very simple method, it was found that the 9,10-PQ modified GC electrode formed by adsorption was unstable and the method had the tendency to produce multilayer adsorbed films. Therefore, this method will not be used as the approach in developing an experimental model for estimating surface coverages (Γ) by DPV technique. In addition, the monolayer of adsorbed 9,10-PQ was not easy to compose due to rapid desorption of 9,10-PQ molecules during electrochemical characterisations. Nevertheless, we have attempted to characterise its electrochemical behaviour obtaining thermodynamic and kinetic parameters such as redox potential, double layer capacitance (C_{dl}), rate of electron transfer (k_s), and transfer coefficient (α). Moreover, the surface coverages (Γ) of 9,10-PQ adsorbed by DPV measurement were calculated employing Anson's model[72]. These studies as presented in this chapter.

3.2 Physical adsorption for modification of electrode surfaces

In the initial studies in this research, the modification of electrode surfaces based on physical adsorption has been adopted. Molecular adsorption onto a solid support represents the easiest method of physical immobilisation. The adsorbate in solution is placed in contact with an electrode surface for a fixed period. The adsorption mechanisms are based on weak bonds such as Van der Waal's, electrostatic and/or hydrophobic interactions[26]. In addition, this technique does not involve any functionalization of the support and been widely used to modify electrode surfaces, particularly in biosensor-based electrochemical measurements. Although this method may give has unfavourable molecule orientation, the adsorbate is loosely bound to the surface of the electrode and decreased activity of the adsorbate, speed and simplicity are significant benefits of this immobilisation strategy[29].

The adsorption of electroactive organic species at the electrode surface is a frequent phenomenon in the electrode process and can be pivotal to the mechanisms of the electron transfer reactions. Moreover, the thermodynamic and kinetic parameters of the adsorption process obtained in electrochemical measurements not only provide information related to the adsorption properties but also allow us to understand the features of microstructure and adsorption layers of attached organic redox molecules at the surface of solid electrodes[95]. Studies of the electrochemical behaviour on various quinones (anthraquinone, naphthoquinone and phenanthrenequinone) and their derivatives adsorbed for modification of carbon electrodes have been of considerable interest during recent decades[30,96,97]. As one of the main purposes of this research is to develop experimental and theoretical models for estimating a number of immobilised redox molecules on the electrode surfaces by DPV measurement, immobilising the redox molecule of 9,10-phenantherequinone by the drop casting technique had been employed here, as illustrated in Figure 3.1.

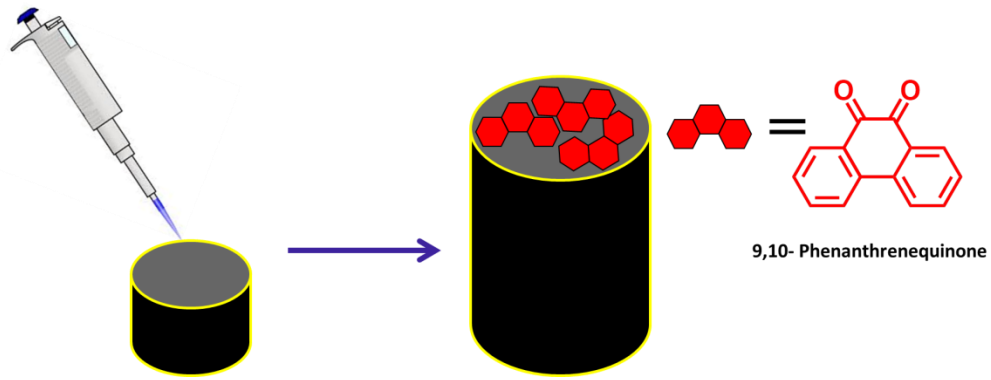

Figure 3.1; Drop casting technique for physical adsorption of 9,10-phenanthrenequinone onto GC electrode.

3.3 9,10-phenanthrenequinone as a redox model for adsorption

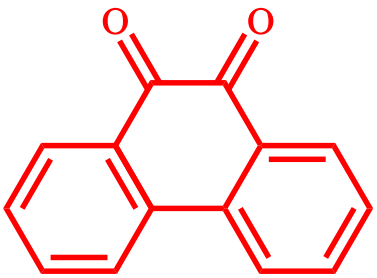

Figure 3.2; The molecular structure of 9,10-phenantherenequinone.

9,10-Phenanthrenequinone (PQ) is particularly interesting due to its photo-physical and chemical versatility (Figure 3.2). It has been investigated in applications such as for surface optical anisotropies, chromatography, pharmacology, proton transfer, modified electrodes, transition metal complexes as anticancer drugs, and photochemistry[98]. Generally, 9,10-PQ undergoes two types of reactions, namely (i) two-electron redox reactions with electron donors and (ii) aldol condensation with active methylene compounds[99]. In addition, 9,10-PQ is a specific quinone compound, containing an ortho-quinone group and two electrons will transfer during its oxidation and reduction reactions. As illustrated in Scheme 3.3, it is well established in the literature that 9,10-PQ undergoes a two-electron, two proton oxidation to 9,10-Phenanthrenehydroquinone (9,10-PQH). Hence, 9,10-PQ is a favourable organic redox compound that can be used in order to construct many molecular sensors. Despite our main interest in this work being more focused on the determining surface coverages of adsorbed 9,10-PQ by DPV, investigation of the 9,10-PQ layers structure, thermodynamic and kinetics behaviours of 9,10-PQ adsorbed at the GC electrodes surfaces was also conducted using CV, chronoamperometry and EIS techniques.

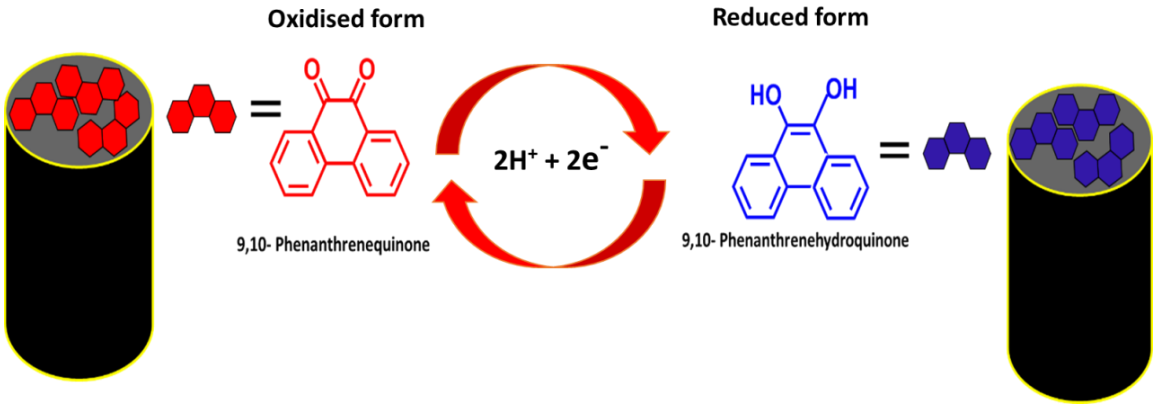

Figure 3.3; Reaction mechanism for oxidation and reduction of 9,10-phenanthrenequinone involving two electrons and two protons.

3.4 Cyclic voltammetry for 9,10-PQ modified GC electrodes

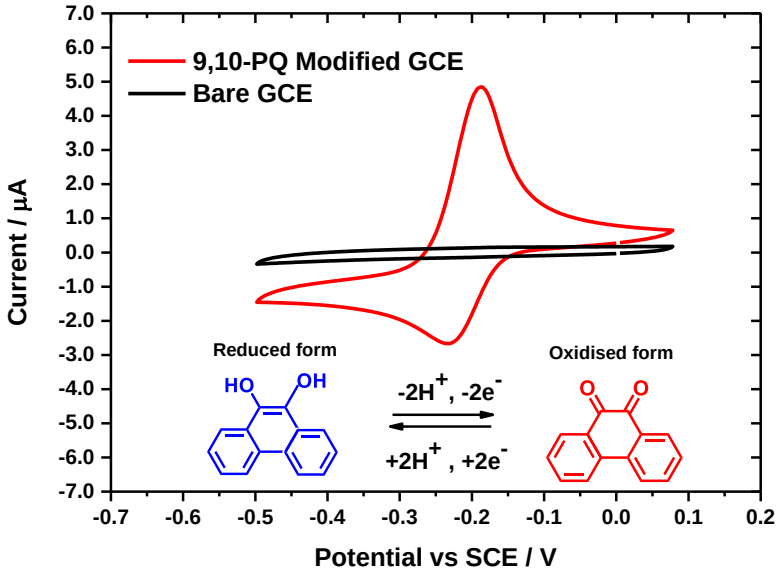

Figure 3.4; Cylic voltammograms for bare GC (black) and 9,10-PQ modified GC(red) electrodes (5th scan shown) in 0.1 M pH 7 phosphate buffer solution at a scan rate of 50 mV s^{-1}. The concentration of 9,10-PQ used was 1 mM and the electrode area is 0.071 cm^2.

Figure 3.4 shows single cyclic voltammograms of bare GC and 9,10-PQ modified GC electrodes over a potential scanned between -0.50 to +0.08 V *vs* SCE. In the case of adsorbed 9,10-PQ at the surface of GC, well-defined redox peaks for oxidation and reduction are clearly seen. However, the currents produced were unsymmetrically shaped on both the anodic and cathodic scans. The oxidation and reduction peaks of the adsorbed 9,10-PQ in phosphate buffer (pH 7) at the surface of GC appear at around ~ -0.19 V (oxidation) and ~ -0.23 V (reduction), respectively. Moreover, as can clearly be seen in Figure 3.4, the broadness of the oxidation and reduction peaks for the 9,10-PQ modified GC electrode are different. In principle, for ideal Nernstian behaviour, the oxidation and reduction peaks should be symmetrical and gaussian in shape with no peak separation. However, for the adsorbed 9,10-PQ, the asymmetry of the peak heights for oxidation and reduction was noticeable. Deviations from the ideal case are to be expected for redox-modified electrodes due to the interactions among the redox centres of immobilised molecules with the support surface. Broader and flatter peaks for the CV peak can also be caused by the heterogeneity of the surface of the working electrode[27]. Toshio and co-workers[94] have observed the asymmetry of the peak heights for oxidation and reduction of adsorbed 9,10-PQ onto the surface of the gold electrode. They discussed the origin of this asymmetry by considering factors such as the adsorption density of PQ, the adsorption strength between oxidised and reduced species, and the contribution of protons to redox reactions in an electrolyte solution. On the other hand, the thermodynamically stable redox forms and electron transfer kinetics between the

adsorbed 9,10-PQ and the electrode surface play important roles in determining the shape of the CV.

According to the electron transfer kinetics, coupled electron and proton transfers plays an important role in the electrochemistry of quinones. In order to study quinone electrochemistry either in aqueous or non-aqueous solutions, the quinone scheme, as displayed in Figure 3.5 is used.

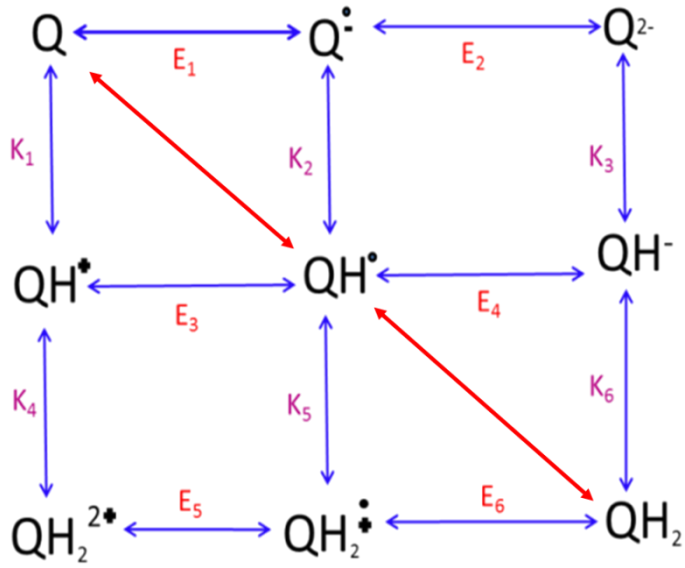

Figure 3.5; Scheme of squares for a two-electron and two-proton coupled reactions.

Therefore, we believe that the abnormality of the reduction peak is strongly related to the kinetic behaviour of 9,10-PQ. Generally, in the case of immobilised quinones, in contact with the aqueous solution, essentially, the coupled electron and proton transfer from quinone (Q) to hydroquinone (QH_2) favours the concerted mechanism as demonstrated in the red arrow. It has extensively been reported in literature[100]. However, the backwards current does not reach to zero, it shows a similar behaviour to the electrochemistry of quinone in solution where the Q favours the step wise mechanism as demonstrated by blue arrows[101,102]. This is reasonable since some 9,10-PQ molecules may desorb into the bulk solution from the 9,10-PQ film. Secondly, as the oxidation peak is bigger and higher than reduction peak, we believe that the kinetic process during reduction reaction is slower than oxidation reaction. This means that for the oxidation reaction 9,10-PQH_2 favours the concerted mechanism. In contrast, the reduction 9,10-PQ may have several possible mechanistic pathways (blue arrows). This is because the adsorbed 9,10-PQ at the GC electrode surface forms multilayers. The oxidised form of 9,10-PQ takes up two protons to undergo the reduction reaction. As can be observed, when the potential was scanned to more negative values, it is likely that the reduction process is limited by some chemical steps, contributed by propagation

of protons through multilayers film. Consequently, the abnormal kinetic behaviour for the reduction process was obtained.

Taking into account the asymmetrical redox peaks for immobilised 9,10-PQ, the Faradaic charge under oxidation and reduction peaks was determined. Essentially, the charges transferred in oxidation and reduction reactions for immobilised electroactive species should be the same if the adsorbed species is stable. Thus, the charges passed (Q) should be constant. This is due to a fixed amount of immobilised redox reactant being present at the surface of the electrodes. We found the charges transferred for adsorbed 9,10-PQ for oxidation and reduction are constant and were 8.1×10^{-6} and 9.05×10^{-6} C, respectively. The charges were obtained by integrating the areas under the oxidation and reduction peaks using Origin 9.1 software but using two different approaches. For the oxidation charge; by constructing a baseline for the charging current. In contrast, for reduction charge; by setting the baseline to be at 0 A. These procedures will be discussed in Section 3.5 when we determine the surface coverages of adsorbed 9,10-PQ at the surface of GC electrodes. Moreover, from the CV of adsorbed 9,10-PQ, the peak separation (ΔE_p) and mid-potential (E_{mid}) were also calculated. Table 3.1 summarizes the redox parameters obtained for adsorbed 9,10-PQ at the surface of the GC electrode.

Table 3.1; Redox potentials for oxidation and reduction, charges (Q), peak separation (ΔE_p) and mid-potential (ΔE_{mid}) for 9,10-PQ modified GC electrode measured at a potential scanned between -0.50 V to +0.08 V with a scan rate of 50 mV s^{-1} in 0.1 M phosphate buffer solution, pH 7.

Redox Process	Potential Redox *vs* SCE / V	Charge (Q) / C	ΔE_p *vs* SCE / V	ΔE_{mid} *vs* SCE / V
Oxidation	-0.192 ± 0.003	(8.14 ± 0.2) x 10^{-6}	-0.041 ± 0.002	-0.212 ± 0.003
Reduction	-0.233 ± 0.003	(9.35 ± 0.3) x 10^{-6}		

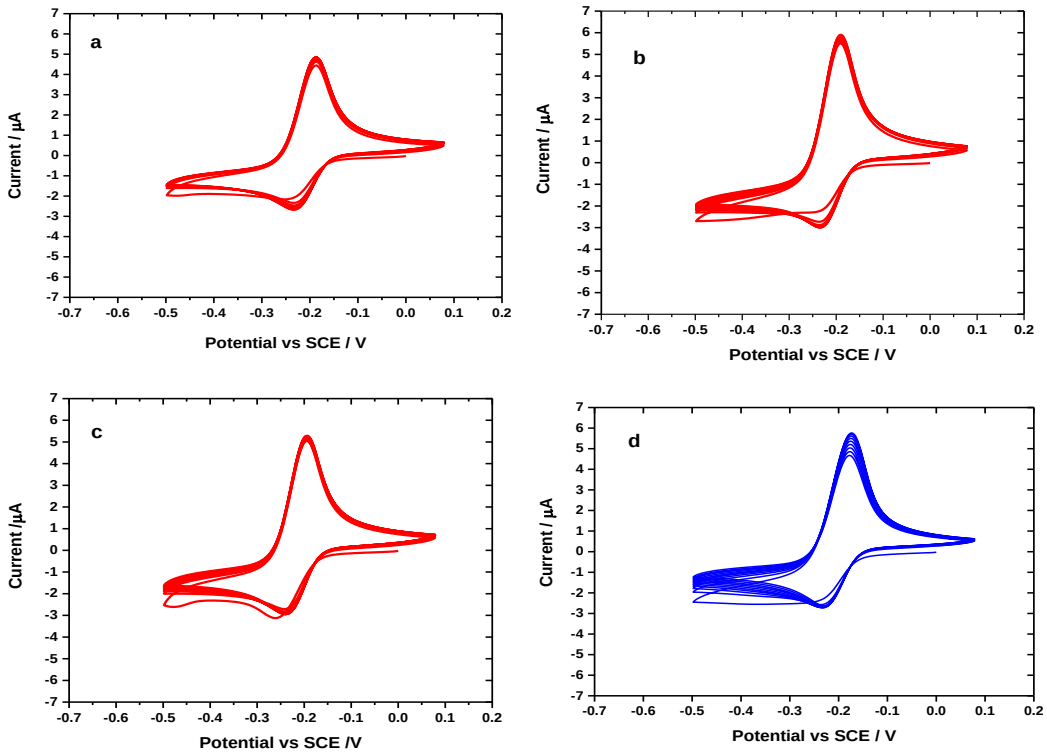

Figure 3.6; a,b,c,d) Ten cyclic voltammetry scans for four different 9,10-PQ modified GCelectrodes made by drop casting 3 µL of 1 mM 9,10-PQ, measured in 0.1 M pH 7 phosphate buffer solution. Scan rate of 50 mV s^{-1}, electrode area is 0.071 cm^2.

Repetitive cyclic voltammograms (10 cycles) for immobilised 9,10-PQ in phosphate buffer solution at pH 7 for 3 different modified electrodes are shown in Figures 3.6. In ten CV measurements for ten different 9,10-PQ modified glassy carbon electrodes (not shown) a few (2-3 CVs) produced steady currents. The other CVs, produced unstable responses as shown in Figure 3.6d. The unstable currents may be due to desorption of 9,10-PQ molecules at the surface of the GC electrode, resulting in the decreased stability of adsorbed molecules at multilayer surface coverages. This could happen because the 9,10-PQ molecules are physically confined at the surface of glassy carbon and are probably held through weak intermolecular bonds such as Van der Waal's and electrostatic forces or hydrophobic interactions[27,103]. The multilayers predicted in this work can be confirmed by estimating the surface coverages (Γ) of adsorbed 9,10 by obtaining the charge under the CV peaks, and then, calculating Γ using the Faraday law equation.

3.5 Surface coverages (Γ_{CV}) of adsorbed 9,10-PQ at GC electrodes

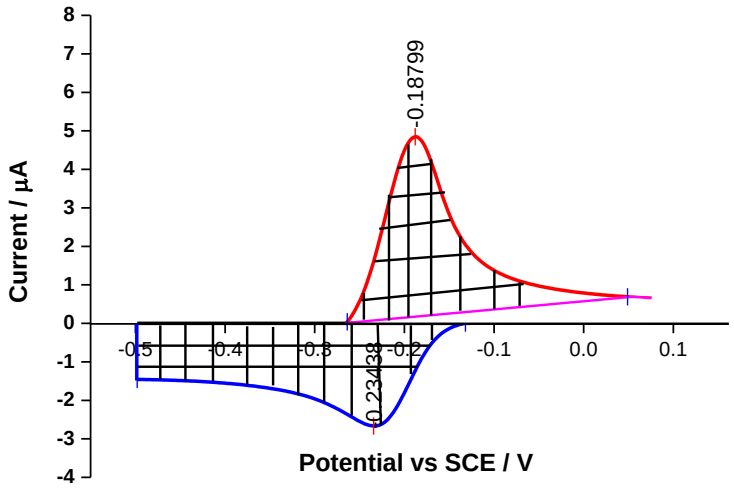

Figure 3.7; A single scan of CV for 9,10-PQ modified GC electrode from Figure 3.6 in order to show the two different approaches made in integrating the area under the oxidation and reduction peaks, respectively.

The surface coverages of the adsorbed 9,10-PQ were determined by the charges obtained through integration of the cyclic voltammograms. In this work, the initial surface concentration of adsorbed 9,10-PQ at the surface of GC electrode was determined by integrating the area of oxidation and reduction peaks as displayed in Figure 3.7. In order to integrate the area under the oxidation peak, a baseline for the capacitive current was constructed (pink line). The baseline for the capacitive current was created separately for the half cyclic voltammogram for the oxidation using Origin (version 9.1). The 4 points were manually placed on the curve of the half cyclic voltammogram, excluding at the potential range between -0.265 V and 0.04 V. Then the points were interpolated using the B-spline function to produce the baseline. By contrast, the area below the cathodic current was integrated to determine the reduction charge by setting the baseline to be at 0 A in Origin 9.1 using the peak analyser function.

Table 3.2; Surface coverages and charge of adsorbed 9,10-PQ at the surface of GC electrodes.

Potential window *vs* SCE / V	Charge (*Q*) /C	Surface coverage (Γ) / mol cm^{-2}	Average number of active immobilised molecules / molecules	Number of molecules in stock solution (theoretical) / molecules
-0.50 to +0.08	(8.74 ± 0.2) x 10^{-6}	(6.22 ± 0.3) x 10^{-10}	2.73 x 10^{13}	6.02 x 10^{14}

Table 3.2 shows the surface coverages for the adsorbed 9,10-PQ at the surface of GC electrodes setting the roughness factor for the cleaned surface of GC electrode as 1. Three replicates data from three different modified electrodes were measured. As presented in Table 3.2, the number of active adsorbed 9,10-PQ molecules based upon CV measurement can be estimated according to Faraday's law, in which the charge is directly proportional to the amount of species undergoing a loss (oxidation) and a gain (reduction) of electrons ($Q = nFe$). However, a large difference between the number of active immobilised 9,10-PQ molecules compared to the number of 9,10-PQ molecules before the adsorption process was noticed. This is probably due to the fact that the adsorbed molecules are easily lost from the surface as 9,10-PQ molecules in ethanol solution may evaporate to air during the adsorption process.

The theoretical monolayer coverage for adsorption plane parallel to the electrode surface orientation ranges for 1 x 10^{-10} to 2 x 10^{-10} mol cm^{-2} for different quinones reported[104]. The formation and properties of adsorbed monolayers depend on a number of factors, including the nature of the substrate and adsorbed molecules. Nevertheless, the values obtained in this work exceeded the theoretical value for monolayer and it can be concluded that multilayers of the 9,10-PQ adsorbed on the surface of GCE have been formed. Similarly, by employing 1 mM 9,10-PQ, Kano and Uno[105] reported on the formation of multilayers of 9,10-PQ at the surface of basal-plane pyrolytic graphite with a surface coverage of 7.1 x 10^{-10} mol/ cm^2. By contrast, in the previously discussed works of Toshio and co-workers[94], there was the formation of monolayer adsorption of 9,10-PQ onto the gold electrode when a 1 mM of 9,10-PQ was used with the surface coverages reported as 2.4 x 10^{-10} mol cm^{-2}. However, they reported that the absorption of 9,10-PQ at the surface of the gold electrode was much weaker than at the surface of the graphite electrode.

3.6 Impedance measurements for adsorbed 9,10-PQ layers

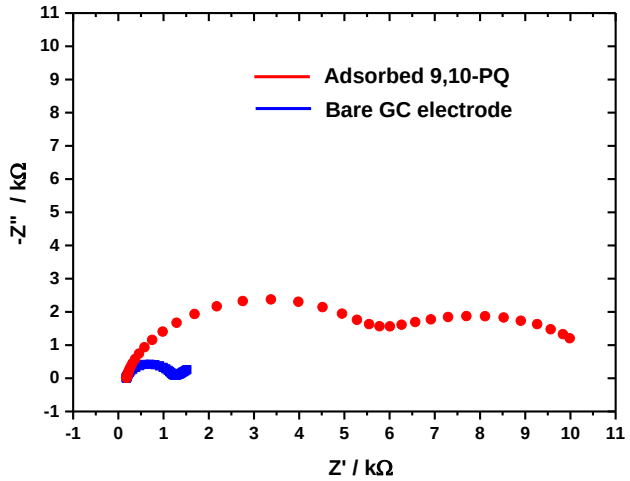

Figure 3.8; Nyquist plots from the impedance measurements of bare GC (blue) and 9,10-modified GC (red) electrodes with the presence of $Fe(CN)_6^{-3/-4}$ redox couple. Supporting electrolyte is 0.01 M solution of 1:1 $K_3[Fe(CN)_6]$/ $K_4[Fe(CN)_6]$ in 0.1 M phosphate buffer at pH 7. The frequency range is 100 kHz to 0.1 kHz at modulation amplitude of 5 mV. The impedance was measured at 0.18 V *vs* SCE.

The 9.10-PQ modified GC electrodes were also investigated using electrochemical impedance spectroscopy (EIS). This was carried out in a mixture of 0.01 M ferricyanide and ferrocyanide over a frequency range from 100 kHz to 0.1 Hz. Hence, we could investigate the interfacial charge-transfer resistance (R_{ct}) for an electron to the process $Fe(CN)_6^{-3/-4}$ couple across the adsorbed PQ layers. Figure 3.8 shows Nyquist plots for bare GC electrode (blue) and 9,10-PQ modified GC electrode (red). The blue plot shows that the typical Nyquist semicircle plot at high frequencies and the Warburg line for the unmodified electrode. Essentially, the Warburg line describes the semi-infinite diffusion of the redox solutes from the bulk solution to the electrode at low frequencies and is characterised by a 45° linear region in the Nyquist plot[106,107] .

In contrast for the 9,10-PQ modified GC electrode, a significant shifting of the real component (Z') value on the Nyquist plot as a double semicircle was obtained with the Warburg line completely absent. The double semicircle clearly indicates that the adsorbed 9,10-PQ at the GC electrode surface forms multilayers film. The significant shift of (Z') indicates that the charge transfer resistance (R_{ct}) for the ferricyanide/ferrocyanide couple has considerably increased, indicating the presence of film layers of 9,10-PQ at the surface of GC electrode suppress the rate of the electron transfer to the $Fe(CN)_6^{-3/-4}$ redox couple. EIS result is consistent with the multilayer surface coverages calculated by CV.

3.7 Effect of pH

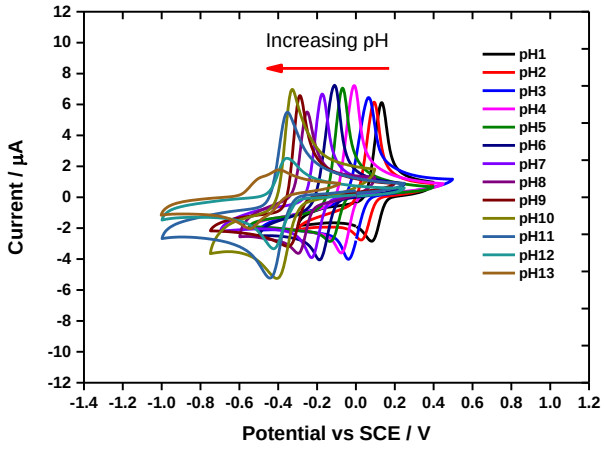

Figure 3.9; Cyclic voltammograms of the 9,10-PQ modified GC electrodes obtained (6th scan shown) at a scan rate of 50 mV/ s^{-1} in different 0.1 M buffer solutions from pH 1 to 13. A 3 µL of 9,10-PQ solution (1 mM) was drop cast onto the surface of glassy carbon. The electrode area is 0.071 cm^2.

The redox behaviour of quinone compounds is dependent on pH[108,109] Figure 3.9 shows the CVs measured in various 0.1 M buffer solutions pH (1-13) for the 9,10-PQ modified of GC electrodes.

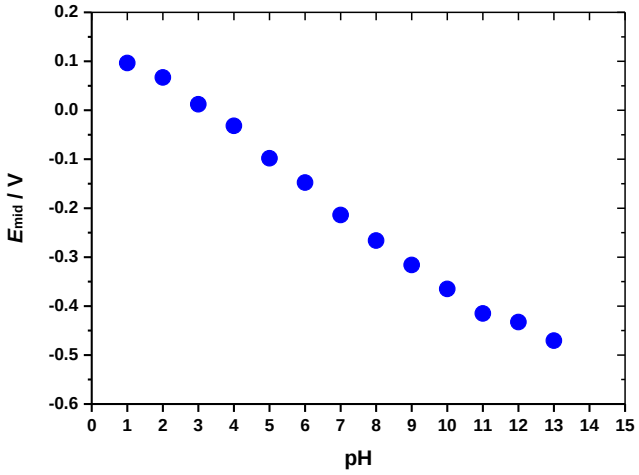

Figure 3.10; Plot of half-wave potential (E_{mid}) positions that were extracted from the cyclic voltammograms (Figure 3.9) as a function of pH. This plot will be fitted based upon a linear and a nonlinear fittings.

Clearly, with increasing pH peak potentials shift towards more negative potential and the half-wave potential ($E_{mid)}$ becomes more negative, as shown in Fig. 3.9, where E_{mid} for each pH was obtained from the E_{pa} and E_{pc} of each CV in Figure 3.9. The mid potential (E_{mid}) was obtained by using this calculation [(E_{pa} + E_{pc})/2]. In addition, cyclic voltammograms at pH 12 and 13 reveal a decrease in the anodic and cathodic currents, which is probably due to the tendency of adsorbed 9,10-PQ molecules to desorb. On the other hand, it may be due to hydrolysis of the adsorbed 9,10-PQ at high pH value[110,111]. This is similar to the work of Salimi *et al.*[112] in which for pH > 10 the

surface coverages of physically adsorbed 9,10-PQ decreased because of the desorption of 9,10-PQ molecules. Hence, it is difficult to study the electrochemical behaviour of adsorbed 9,10-PQ at alkaline buffer solutions in the pH range between 11 to 13. This is because one of the phenolic groups from the reduced form of 9,10-PQH_2 is deprotonated to form 9,10-PQ oxide anion as illustrated in Scheme 3.1.

Scheme 3.1; Deprotonation of 9,10-phenanthrene hydroquinone to 9,10-PQ oxide anion.

Furthermore, the negative charge of the 9,10PQ oxide ion will disrupt the stabilising hydrogen bonding from the second hydroxyl group by electrostatic repulsion between two negatively charged oxygen atoms[109]. Thus the 9,10-PQ oxide ion form is less stable and will desorb in basic solution at potentials more negative than the formal potential of 9,10-PQ[109,110].

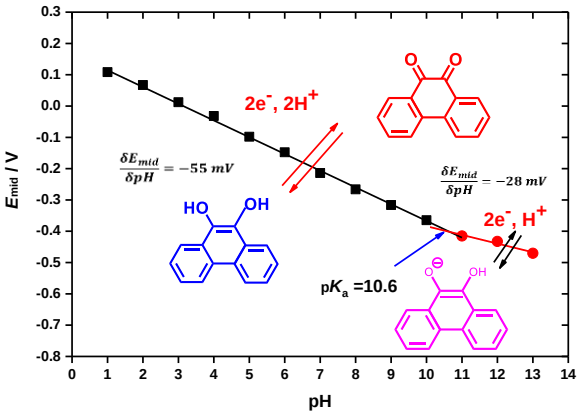

Figure 3.11; Linear fits of E_{mid} as a function of pH in different 0.1 M buffer solutions. The linear fits obtained show two different slopes at -55 and -28 mV/pH.

In addition, as illustrated in Figure 3.11, a linear fitting was made on the plot of half-potential (E_{mid}) against pH, where two different slopes were obtained for pH changes from pH 1 to 13. A linear slope (-55 mV/ pH unit) shifts to more negative half-potentials as pH increases over a range of pH 1 to 10. However, the theoretical value for the pH dependence of a 2 electrons/2 protons system is -59 mV per unit pH[113]. Henry and co-workers[114] reported that a linear shift in potential of 9,10-PQ over a pH range of 1-12 was -56.3 mV per pH unit. Work by Yang *et al.*[115] showed that the Nernstian response of a 9,10-PQ modified carbon ceramic electrode at pH 1 to 7 was -57 mV per unit pH. In contrast, in our data, a 28 mV per pH unit slope was obtained over a linear

fitting at a range pH 11 to 13. Interestingly, a slope of 28 mV per unit pH is very close to the theoretical value for 2 electrons/1 proton, which is 29 mV/ per unit pH[113]. Last but not least, by linear fitting of the 9,10-PQ data, we estimated the pK_a of adsorbed reduced 9,10-PQ to be 10.4. Taking into account the intersection between the two slopes, it can be concluded that the 9,10-PQ modified electrode surface reaction occurring at the pH <10.4 is a two-electron and two-proton process. By contrast, redox reactions at pH>10.4 are corresponded to two-electron and one proton process.

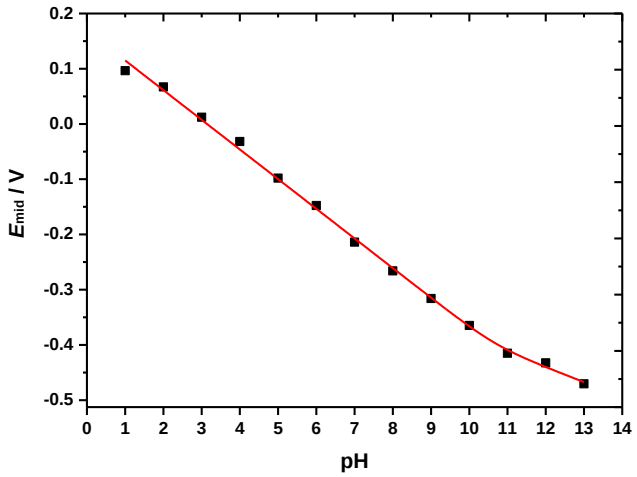

Figure 3.12; Plot of theory (solid line) based upon a nonlinear fitting and experimental data (filled squares) for the mid potential (E_{mid}) vs the pH for 9,10-PQ modified GC electrodes in 0.1 M buffer solutions at pH 1 to 13. The solid line represents a nonlinear fitting to Equation 3.1.

In order to gain more quantitative information of pK_a obtained from the mid potential (E_{mid}) of the experiment, it is better to compare the pK_a value from an experiment and a theory of pH reduction. This was achieved through a nonlinear fitting for E_{mid} to Equation 3.1[116].

$$E_{mid} = E^{\circ\prime} + \frac{RT}{2F}\ln\left([H^+]^2 + K_1[H^+]\right) \qquad \textbf{Eq. 3.1}$$

Where E_{mid} is the mid potential, $E^{\circ\prime}$ is the formal potential, T is the temperature in K, R is the gas constant, F is the Faraday constant, $[H^+]$ is the hydrogen concentration and K_1 is the dissociation constant. The best fit was obtained through minimising the root mean squared difference between the experimental and nonlinear fitted curve. Figure 3.12 shows a nonlinear fitting of mid potential (E_{mid}) as a function of pH for redox behaviour of 9,10-PQ modified GC electrodes in the different pH. As depicted clearly in Fig. 3.12, the theory (solid line) closely fits the E_{mid} data obtained from the experiment (filled squares). From the nonlinear fitting, we obtained a pK_a of 9.7. This is a slightly different to the pK_a obtained from the experiment data based on a linear regression (Figure 3.11), which was 10.6. A slight deviation of pK_a value between a nonlinear fitting and a linear

fitting was expected (Table 3.3). Despite the linear regression being an easy method for dealing with curved relationships into a straight line, the result is not statistically optimal[117]. In the case of linear fitting, the data plots of E_{mid} vs pH were fitted into two straight lines rather than by plotting a curve over the nonlinear regression fitting. Nevertheless, both of the obtained pK_a values are well in agreement with the expected pK_a for hydroquinone, which is 9-10 as quoted by Ishioka *et al.*[94] in their work on the analysis of redox behaviour adsorbed 9,10-PQ at a surface gold electrode.

Table 3.3; pH dependence of 9,10-PQ redox reaction a) The pK_a value obtained from a linear fitting at the intersection point of two linear segments. b) The pK_a value obtained from a nonlinear fitting with employing the equation 3.1.

Redox Reaction	pK_a (linear fitting)[(a)]	pK_a (nonlinear fitting)[(b)]
$Q + 2e^- + 2H^+ \leftrightarrow QH_2$ (pH 1-10) $Q + 2e^- + H^+ \leftrightarrow QH^-$ (pH 11-13)	10.6 ± 0.38	9.7 ± 0.25

3.8 Kinetics of adsorbed 9,10-PQ oxidation and reduction

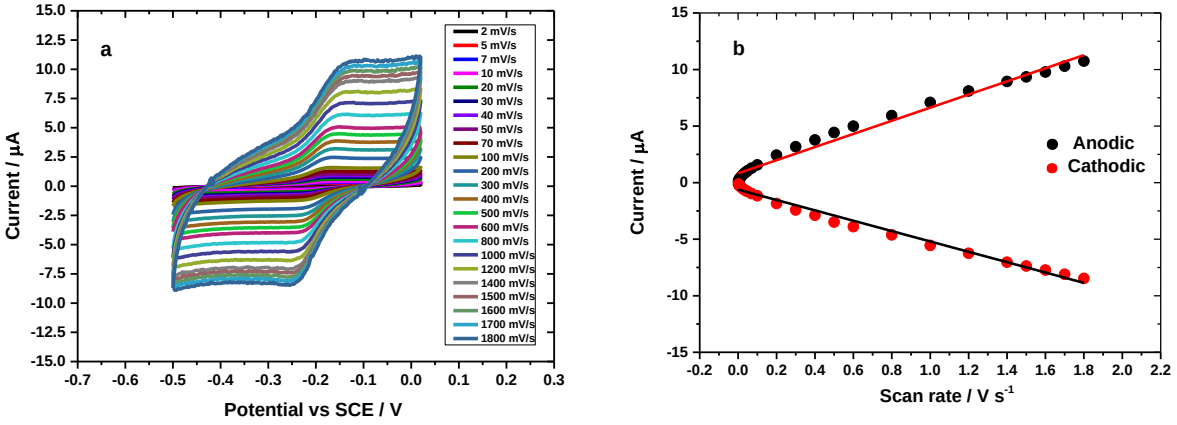

Figure 3.13; a) Cyclic voltammograms of 9,10-PQ modified GC electrodes in 0.1 M phosphate buffer of pH 7 at a series of different scan rates (0.002 to 1.8 V s^{-1}). b) Plots of I_p for anodic and cathodic currents (without background subtraction) vs scan rate (v). The measurements were conducted over a potential cycle between -0.5 to -0.08 V vs SCE as well as a controlled temperature from a water bath at 25 ± 0.5 ºC.

A series cyclic voltammograms at different scan rates in phosphate buffer solution, pH 7 for 9,10-PQ modified GC electrode are shown in Figure 3.13a. It was scanned from 0.002 V/s up to 1.8 V/s. As a result, it is clear that the anodic and cathodic currents increase linearly with scan rate. This is shown by plotting of the raw peak currents (i_p) against the scan rate. Figure 3.13b, the linear relationship indicates that the redox reactions of 9,10-PQ were confined at the surface of the GC electrode and anodic and cathodic currents are diffusionless controlled. However, a slight deviation of peak currents for anodic and cathodic at the lower scan rates between 2 and 15 mV/s was noticed. The fact that multilayer adsorbed 9,10-PQ molecules were physically trapped at the surface of the GC electrode and are restrained through weak intermolecular bonds such as Van der Waals forces, resulted in a continuous desorbing from the multilayer organisation. In contrast, at faster scan rates (shorter time scale experiment), there was less time for desorbing or leaking molecules to occur.

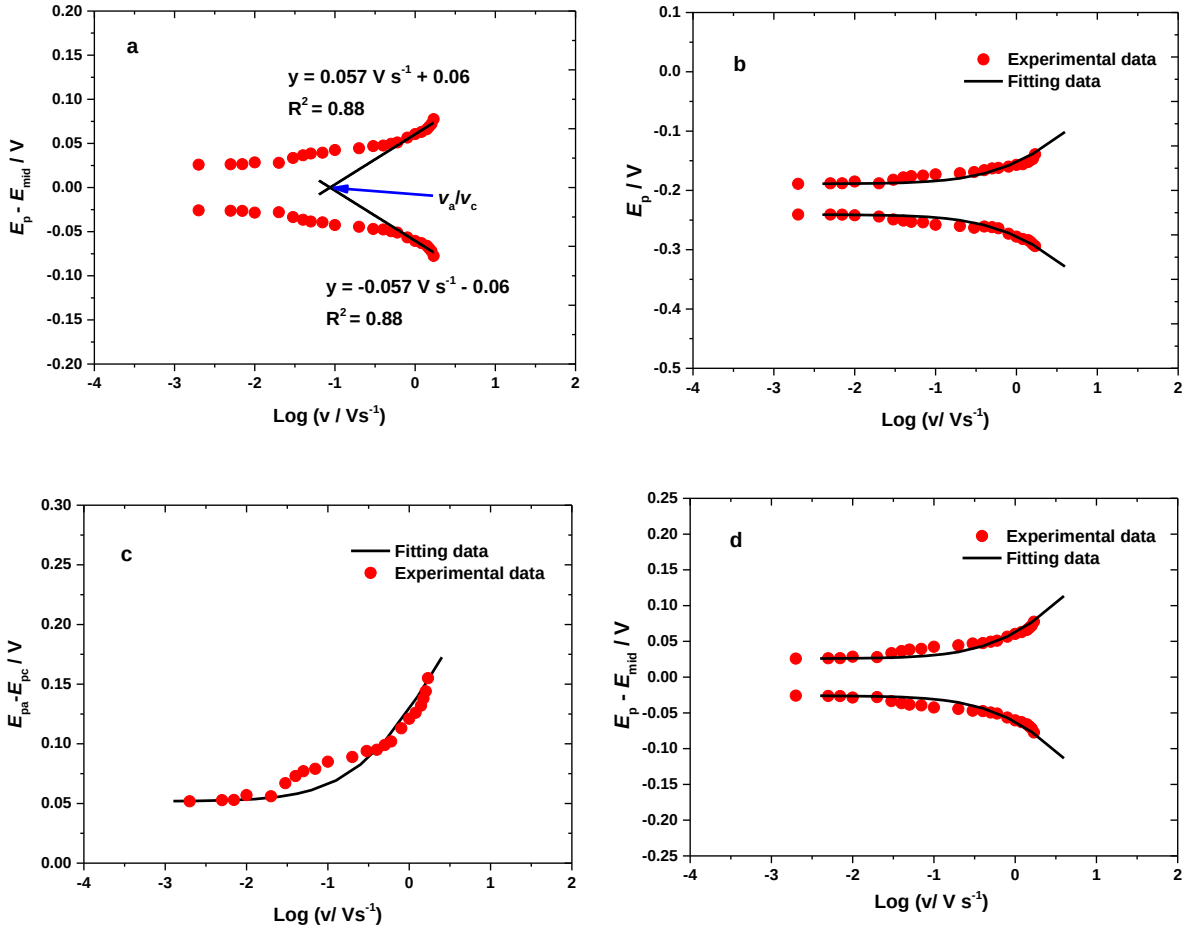

Figure 3.14; a) Laviron plots for experimental data for the variation of $E_{pa/pc}$-E_{mid} (overpotential) *vs* the logarithm of the scan rate (v) and the linear best fits over the of anodic and cathodic branches in order to determine the experimental α and k_s values. b) Plots show the influence of cyclic voltammetry scan rates on peaks of potential redox for oxidation and reduction (filled cycles) for 9,10-PQ modified GC electrode at various scan rates (0.002 to 1.8 V s^{-1}), the theoretical (solid lines) were obtained from the best fitting to the Laviron theoretical plot using the working curve for α = 0.5. c) Plot of experimental data and Laviron theory based on working curve for α = 0.5 for the peak separation (E_{peak}). d) The best fit for experimental data of $E_{pa/pc}$-E_{mid} (overpotential) to the Laviron theory by employing α = 0.5 for anodic and cathodic curves respectively.

In order to calculate the standard rate constant for electron transfer (k_s) for immobilised 9,10-PQ as well as the anodic (α_a) and cathodic (α_c) transfer coefficient, the Laviron formalism for the potential redox with scan rates response in the case of surface-confined electroactive species has been employed[61]. Theoretically, the Laviron method is based on the classical Butler-Volmer approach and the experimental data required to use this method is only the overpotential (E_p - E_{mid})[118]. In the Butler-Volmer equation, α is specifically expressed for one electron transfer process in which $\alpha_a + \alpha_c = 1$. As the Laviron model was derived from the Butler-Volmer expressions, in the case of α for 2 electrons transfer for 9,10-PQ, thus the α for anodic and cathodic branches does not add to 1 as they might refer to different transition states. In most cases α lies

between 0.3 to 0.7 and can often be approximated as 0.5 for all overpotentials, however, in many cases, α deviates from 0.5[63].

Therefore, determination of α is crucial to estimate the apparent rate constant (k_s). To determine α, the peaks E_p - E_{mid} are separately plotted vs log v to give two branches. Hence, a Laviron plot of ($E_{pa/pc}$ - E_{mid}) vs log scan rate (v) and linear fits to the anodic and cathodic branches will yield two straight lines. Both of the linear fits for each branch must be obtained for $\Delta E_{peak} > 200/n$ mV, where n is the number of electrons exchanged. In this way, we can determine α_a and α_c using Equations 3.2 and 3.3, respectively.

$$Anodic\ slope = \frac{2.3\ RT}{(1-\alpha_a)nF} \qquad \textbf{Eq. 3.2}$$

$$Cathodic\ slope = \frac{-2.3\ RT}{\alpha_c\ nF} \qquad \textbf{Eq. 3.3}$$

Where R is the gas constant, T is the temperature in Kelvin (K), n = 2 is the number of electrons transferred, F is the Faraday constant, α_c and α_a are the anodic and cathodic transfer coefficient, respectively. Furthermore, after obtaining the α_a and α_c values, the k_s value can be calculated using Equation 3.4 and 3.5, respectively.

$$k_S = (1 - \alpha_a)\frac{nFv_a}{RT} \qquad \textbf{Eq. 3.4}$$

$$k_S = \frac{\alpha_c nFv_c}{RT} \qquad \textbf{Eq. 3.5}$$

Where v_a and v_c at zero overpotential is the point of interception the extrapolated lines for the anodic and cathodic branches, respectively.

As shown in Figure 3.14c (experimental data), scan rates of 1.2 V s^{-1} to 1.8 V s^{-1} gave the peak separations $\Delta E_{peak} > 200/n$ mV or 100 mV. However, as can be observed from Figure 3.13a, the maximum scan employed is 1.8 V / s and clearly, at high scan rate, *IR* drop potential could distort the voltammograms. This leads to a limitation of the Laviron method in estimating the kinetic parameters. Using the 9,10-PQ redox molecule as our model, we assume that the 9,10-PQ involves the transfer of two electrons and two protons which are able to transfer in stepwise proton and electrons or concerted mechanism[119]. We have shown in the pH study (Section 3.7) for 9,10-

PQ modified GC electrodes in 0.1 M phosphate buffer, that 9,10-PQ occurs by a two electron ($2e^-$) two proton ($2H^+$) process.

Figure 3.14a shows in greater detail that the behaviours of E_{pa}-E_{mid} and E_{pc}-E_{mid} with Log (v) used to determine the α and k_s. It can be clearly seen that when the scan rates were gradually increased from 1200 to 1800 mV s^{-1}, anodic and cathodic branches were produced. This significantly increased ΔE_p due to a limitation in the kinetics of the charge transfer[120]. This occurs because the time scale of CV measurements over increasing scan rates decreased to become comparable to the electron transfer rate, requiring a large magnitude of overpotential to be applied to keep a sufficient flux of electrons to be transferred at the electrode[121].

Subsequently, k_s can be determined by the extrapolation of the linear part of anodic and cathodic branches on the plot of (E_p - E_{mid}) vs log v using equations 3.4 and 3.5. Therefore, the k_s value was found to be 3.71 cm s^{-1}. An important assumption of the Laviron model is the ability of the anodic and cathodic branches to be linearised over (E_p - E_{mid}) *vs* log v at high potential scan rates, consistent with the applicability of the Butler-Volmer model[120]. Table 3.3 presents the electron transfer coefficients of anodic (α_a), cathodic (α_c) and rate constant of electron transfer (k_s). From the Laviron plot on Figure 3.14a, the symmetry of anodic curve and the cathodic curve over E_p - E_{mid} *vs* log v was obtained and it can be confirmed that the transfer coefficient for anodic and cathodic are α_a, α_c = ~0.5.

Table 3.3; Electron transfer coefficient (α) and rate of electron transfer (k_s) for adsorbed 9,10-PQ at the surface of GC electrodes.

Modified GC electrode	Anodic transfer coefficient (α_a)	Cathodic transfer coefficient(α_c)	Rate constant (k_s) / s^{-1}
Adsorbed AQ	0.48 ± 0.032	0.52 ± 0.025	3.71

In contrast, from Figure 3.14d, at the scan rates of 2 to 10 mV s^{-1}, there is a non-zero peak separation of about 40 mV as observed in many redox reactions of immobilised quinones. In addition, the system is complex due to the high density of immobilised 9,10-PQ molecules and the different possible mechanistic pathways of 9,10-PQ for the two electron/two proton transfers as represented in Figure 3.5 (quinone square scheme)[122,123].

Although the reduction and oxidation of quinones is a two-step electron transfer reaction, in aqueous media only one voltammetric wave is observed due to the fast protonation steps and the similarity of the redox potentials of the quinone/semiquinone and semiquinone/quinol reactions[124]. The three oxidation states oxidised (Q), semiquinone (Q•) and hydroquinone (Q^{2-})

can also exist in three possible ionisation states, giving a total of nine separate species. Each electron transfer reaction step is characterised by a reduction potential (E'), and each protonation step is characterised by an acid dissociation constant (K). For two electrons to be transferred in a single step (n=2), the reduction potential for the first electron transfer step must be more negative than the reduction potential for the second electron transfer step. The addition of the second electron is more thermodynamically favourable than the addition of the first electron. Thus, the transfer of two electrons occurs in a single step[125].

In order to make a better estimate of k_s, three non-linear plots (Figures 3.14b, c, and d) were fitted to the Laviron theoretical curve based on Equation 3.6[61], employing a working curve for $\alpha = 0.5$.

$$E_P = \log\frac{1}{m} = \log v + \log\frac{nF}{RTk_s} \qquad \textbf{Eq. 3.6}$$

Where m is a parameter determined by the peak separation obtained from the CVs, v is the scan rate, n is the number of electrons transferred, R is gas constant, T is the temperature in Kelvin and k_s is the rate of electrons transfer. The non-linear fits for three different datasets were performed using the Laviron template. The template was kindly provided by Dr. Ghaneem, a former postdoc under the supervision of Prof. Philip Bartlett. Overall, based on Figures 3.14b, c, and d, clearly, theoretical data are not in a good fit to the experimental data points and the shape curves are not ideally predicted by Laviron theory. This shows that something more complex process occurred. These data patterns have been expected as multilayers of adsorbed 9,10-PQ at the GC electrode surface were obtained. This leads the electron transfer between redox active sites must propagate through the multilayer film as illustrated in Figure 3.15. As a result, different electron transfer kinetics probably occur due to lateral interactions between the adjacent adsorbed 9,10-PQ molecules. In order to confirm the k_s obtained from the Laviron theory, chronoamperometry measurements were also made to estimate k_s. This approach is discussed in further detail in Section 3.12.

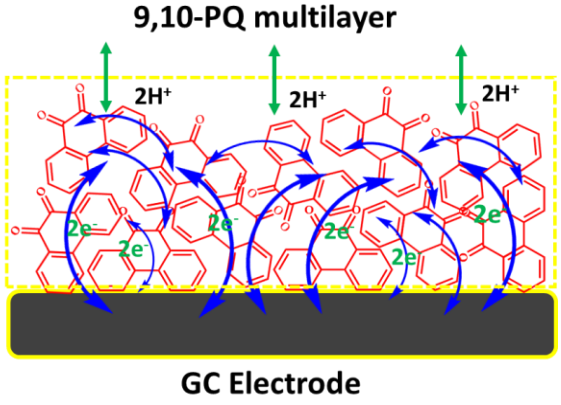

Figure 3.15; Proposed electron transfer pathways for multilayer adsorbed 9,10-PQ at the surface of GC electrode.

3.9 Differential pulse voltammograms of 9,10-PQ modified GC electrodes

According to the data from the cyclic voltammograms of the 9,10-PQ modified glassy carbon electrodes, particularly CV results that were shown in Section 3.4, there is an asymmetry in the peak heights between the oxidation and the reduction process. Clearly, the oxidation peak is broader than the reduction peak. This complication is caused by the abnormal kinetic behaviours of the multilayers of adsorbed 9,10-PQ (Figure 3.3) in which slow reduction kinetics may occur. Moreover, based on 10 cycles of the CV measurements (Figure 3.4d), it is clearly shown that the immobilising of 9,10-PQ molecules through physical adsorption is not stable enough, and it has the tendency to desorb from the multilayer structure. For these reasons, DPV measurements were scanned from negative to positive potentials (-0.6 V to 0.1 V). Thus, the analysis of the DPV signal can only be focused on the anodic current, employing it as a preliminary model to estimate the DPV surface coverages based on the Anson and Koval model[64,72].

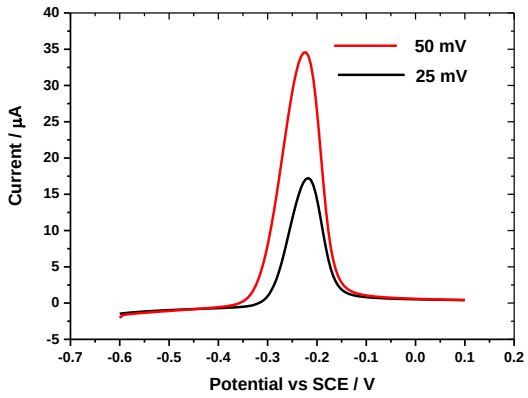

Figure 3.16; DPVs for 9,10-PQ modified GCEs in pH 7 of phosphate buffer solution at different modulation amplitudes (ΔE_p) (0.025 and 0.05 V), interval time (τ_i) = 0.5 s, modulation time (τ_p)= 0.05 s, step potential (ΔE_s)= 0.005 V and a DPV scan rate of 0.01 Vs^{-1}.

Figure 3.16 shows differential pulse voltammograms (DPVs) obtained for the two different modulation amplitude values, 25 and 50 mV respectively. They clearly show the anodic peak of the 9,10-PQ adsorbed on the surface of GCE at a redox potential (E°) of ~ -0.23 V and then the current increases when changing the pulse amplitude from 0.025 V to 0.05 V. The selection of pulse amplitude usually requires a trade-off in sensitivity, speed and resolution. Therefore, larger pulse amplitudes will give larger and broader peaks. Generally, pulse amplitudes of 0.025 or 0.05 V are commonly employed[44]. Basically, there are four different parameters that need to be considered before starting a DPV measurement, they are modulation amplitude (ΔE_p), modulation time (τ_p), interval time (τ_i) and step potential (ΔE_s). The effect of varying DPV parameters will

be discussed in more detail in Chapter 4 when we consider the covalent modification of anthraquinone-2-carboxylic acid onto the surface of GC electrodes.

3.10 Estimating DPV Surface Coverages Using Anson and co-workers' model

In the early work, the method and equation reported by Anson *et al.*[2] have been adapted to estimate the DPV surface coverages of adsorbed 9,10-PQ. In their work, they showed that the sensitivity of the DPV technique for small amounts of adsorbates can be enhanced by the intentional addition of external uncompensated resistance to the DPV circuit. Thus, varying the amount of uncompensated resistance in the DPV measurement gives a maximum peak current that can be used in an approximate method for obtaining surface coverage of adsorbates based upon Equation 3.7.

$$\Gamma = \frac{4RT}{n^2F^2A}\left(\frac{t}{(R_u)_{max}} - C_{dl}\right) \qquad \textbf{Eq. 3.7}$$

Where R is the gas constant, T is the temperature in Kelvin (K), n is the number of electrons transferred, F is the Faraday constant, A is the electrode area, t is the time at which differential pulse current is sampled, $(R_u)_{max}$ is the value of the uncompensated resistance corresponding to the maximum peak DPV current, and C_{dl} is the double layer capacitance. In addition, they used a small concentration of adsorbates at the surface of electrodes in order to evaluate signals of voltammograms between CV and DPV. In our preliminary study, we have attempted to employ a slightly higher concentration of adsorbed 9,10-PQ before carrying out this technique at different quinones and modified electrode based upon covalent attachment. We first attempted to determine the value of C_{dl} from cyclic voltammetry using equation 3.8.

$$2C_{dl} = \frac{i_a - i_c}{v} \qquad \textbf{Eq. 3.8}$$

Where i_a is the anodic current and i_c is the cathodic current for double layer charging at a potential, and v is the scan rate employed. However, an appropriate value of C_{dl} to be used in Equation 3.8 needs to be corresponded to the ratio of modulation pulse amplitude to the modulation time employed in the DPV measurement[72]. Subsequently, at suitable R_{ext}, from the experimental data, the surface coverage (Γ) based on DPV measurement can be calculated applying the Equation 3.7.

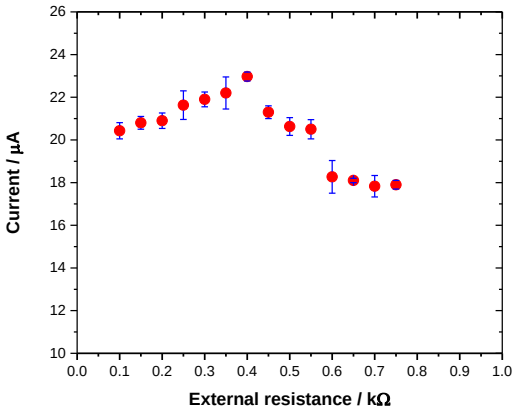

Figure 3.17; Plot of the DPV current against R_{ext} added (0.05 -0.75 kΩ) to the cell circuit for DPV measurements for 9,10-PQ modified GC electrodes in 0.1 M pH 7 phosphate buffer solution at ΔE_p = 50 mV, ΔE_s = 5 mV, τ_p = 50 ms and τ_i = 500 ms and DPV scan rate = 0.01 V s^{-1}. The measurements were carried out at potential scanned between -0.6 to -0.1 V with a controlled temperature from a water bath at 25 ± 0.5 ° C.

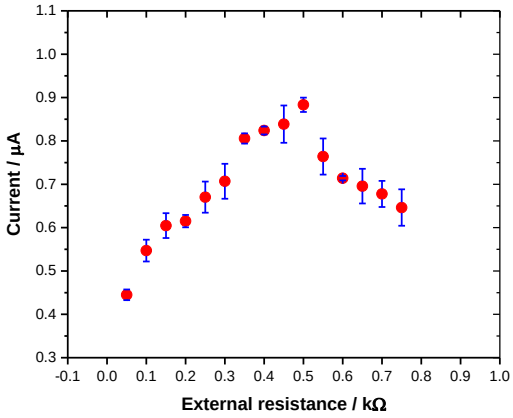

Figure 3.18; Plot of the DPV peak current against R_{ext} added (0.05 -0.75 kΩ) to the cell circuit for DPV measurements for 9,10-PQ modified GC electrodes in 0.1 M pH 7 phosphate buffer solution at ΔE_p = 2.5 mV, ΔE_s = 5 mV, τ_p = 50 ms and τ_i = 500 ms and DPV scan rate = 0.01 V s^{-1}. The measurements were carried out at potential scanned between -0.6 to -0.1 V with a controlled temperature from a water bath at 25 ± 0.5 ° C.

Figures 3.17 and 3.18 show two sets of DPV peak currents at a series of varying magnitudes R_{ext} added (50 -750 Ω), where modulation amplitudes of 50 mV and 2.5 mV and a modulation time of 50 ms were employed. Therefore, the values of C_{dl} were evaluated from the cyclic voltammograms measured at scan rates of 50 mV/50 ms = 1 V s^{-1} and 2.5 mV/50 ms = 0.05 V s^{-1} as shown in Figures 3.19a, and b and 3.20a, and b. It is noticeable that the maximum peak currents in the DPV measurement for the two datasets were obtained when R_{ext} added of 400 and 500 Ω were employed in the cell circuits, respectively. Hence, these magnitudes were used as for calculation of DPV surface coverages using Eq. 3.7.

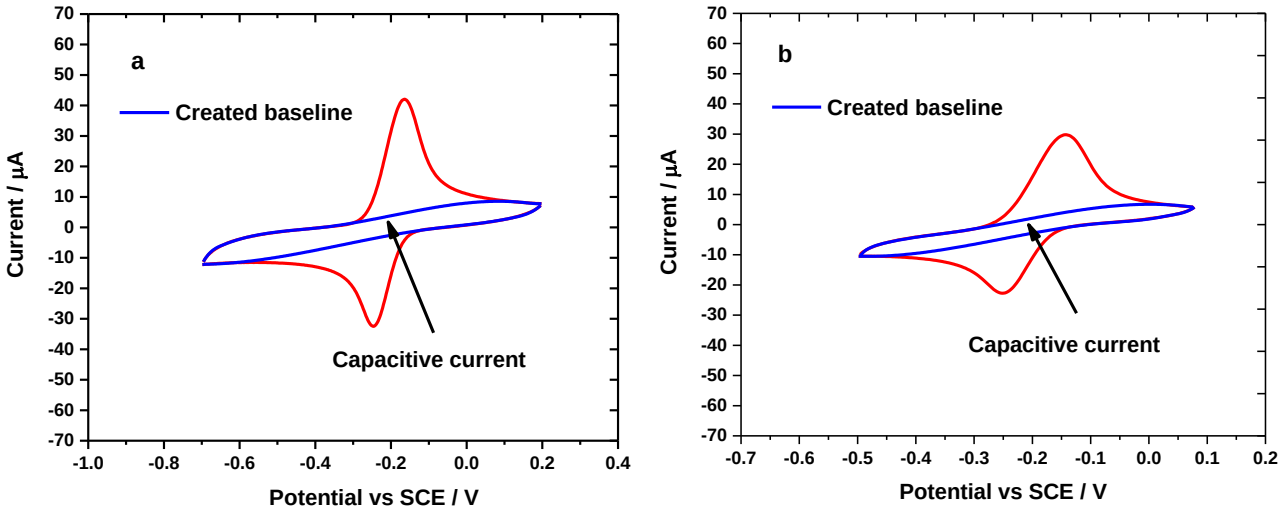

Figure 3.19; Cyclic voltammograms for 9,10-PQ modified GC electrodes in 0.1 M pH 7 phosphate buffer solution. a) Potential scanned between -0.70 to +0.2 V. b) Potential scanned between -0.50 to +0.08. All the measurements were carried out at a scan rate of 1 V s^{-1} with the electrode area is 0.071 cm^2.

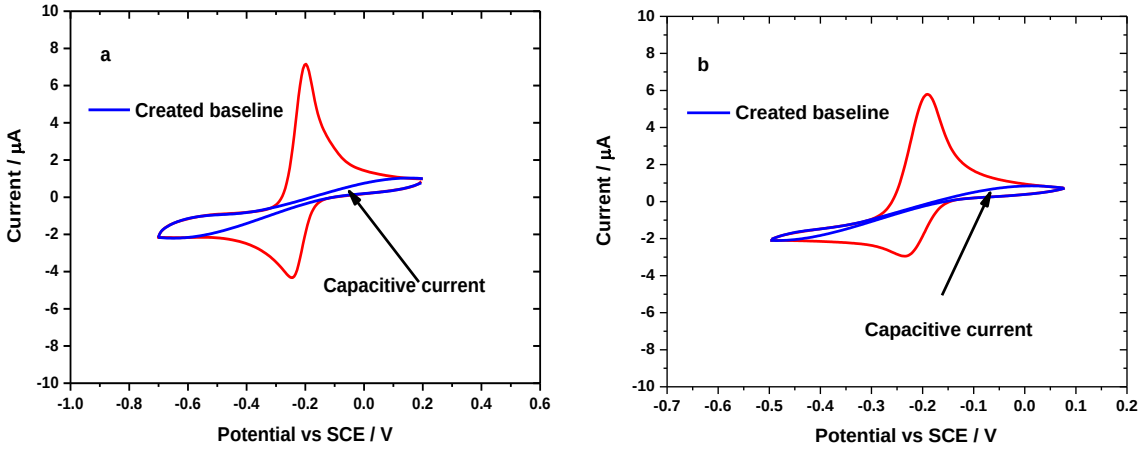

Figure 3.20; Cyclic voltammograms for 9,10-PQ modified GC electrodes in 0.1 M pH 7 phosphate buffer solution. a) Potential scanned between -0.70 to +0.2 V. b) Potential scanned between -0.50 to +0.08. All the measurements were carried out at a scan rate of 0.05 V s^{-1} with the electrode area is 0.071 cm^2.

Table 3.4; Double layer capacitance (C_{dl}) obtained for each cyclic voltammogram of 9,10-PQ modified GC electrodes at different applied potential windows in 0.1 M phosphate buffer solution, pH 7. b) Surface coverages calculated by the CV measurements at two different potential scans and a scan rate of 1 V s^{-1}. c) Surface coverages calculated from Eq. 3.7 for DPV measurements using C_{dl} and R_{ext} added at the maximum DPV current. DPV measured at ΔE_p = 50 mV, ΔE_s = 5 mV, τ_p = 50 ms and τ_i = 500 ms and DPV scan rate = 0.01 V s^{-1}.

Potential window vs SCE / V	Double layer capacitance [a](C_{dl}) / µF	Surface coverage by CV[b] / mol cm^{-2}	Surface coverage by DPV[b]/ mol cm^{-2}
-0.5 ↔ 0.08	2.15 ± 0.23	(1.89 ± 0.09) x 10^{-10}	(4.61 ± 0.005) x 10^{-10}
-0.7 ↔ 0.2	2.65 ± 0.22	(3.25 ± 0.21) x 10^{-10}	(4.59 ± 0.005) x 10^{-10}

Table 3.5; Double layer capacitance (C_{dl}) obtained for each cyclic voltammogram of 9,10-PQ modified GC electrodes at different applied potential windows in 0.1 M phosphate buffer solution, pH 7. b) Surface coverages calculated by the CV measurements at two different potential scans and a scan rate of 0.05 V s^{-1}. c) Surface coverages calculated from Eq. 3.7 for DPV measurements using a C_{dl} and R_{ext} added at the maximum DPV current. DPV measured at modulation amplitude = 2.5 mV, modulation time = 0.05 s, interval time = 0.5, step potential = 0.005 V and DPV scan rate =0.01 V s^{-1}.

Potential window/ V	Capacitance double layer [a](C_{dl}) / µF	Surface coverage by CV[b] /molcm^{-2}	Surface coverage by DPV[b]/molcm^{-2}
-0.5 ↔ 0.08	2.97 ± 0.38	(6.22 ± 0.33) x 10^{-10}	(3.64 ± 0.01) x 10^{-10}
-0.7 ↔ 0.2	5.81 ± 0.45	(1.02 ± 0.05) x 10^{-9}	(3.53 ± 0.02) x 10^{-10}

Tables 3.4 and 3.5 give the calculated surface coverage of adsorbed 9,10-PQ at the surface of GC electrodes obtained using Equation 3.7 for the DPV technique over different potential windows of CV measurements at a scan rate of 1 V s^{-1} (Figures 3.19a and b) and 0.05 V s^{-1} (Figures 3.20a and b), respectively. The reason to scan the voltammetry over the two different potential windows was because we wanted to see the effect of the potential scan on the double layer capacitance (C_{dl}) and surface coverages of AQ. Subsequently, the sensitivity of extracted C_{dl} parameters on Anson's equation can be seen. It is clear that the estimated surface coverages for both models gave very different datasets. It is noticeable that both datasets for each model consistently gave poor agreement to the surface coverages determined by CV. Based on the nature of modified electrodes, the double layer capacitance is influenced by several factors such as the type of working electrodes used the roughness of the electrode, a way of cleaning electrodes, a technique for modification, electrolyte solution, the potential of electrode and types of redox compounds

used[126]. Therefore, up to date, we believe that this model may not be applied as wide-ranging for chemically modified electrodes. It is because each modified electrode has its own electrochemical behaviour, particularly for double layer capacitance. In addition, this model was also employed on the modified GC electrode based upon covalently immobilised AQ through a monolayer of primary amine linker. This will be further discussed in Chapter 4.

3.11 Chronoamperometry for 9,10-PQ Modified GC electrodes

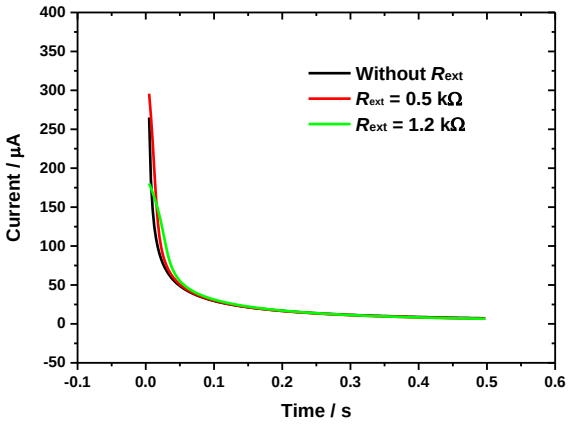

Figure 3.21; Current-time curves for 9,10-PQ modified GC electrode at three different magnitude R_{ext} using chronoamperometry by stepping the potential from -0.5 to 0.08 V vs SCE for 0.5 s. The time used here is similar to the interval time of DPV.

In order to obtain more information from adding R_{ext} to the 9,10-PQ modified GC electrode, chronoamperometry was employed. Figure 3.21 shows three chronoamperograms at different magnitudes of R_{ext} following a potential step from -0.5 V to +0.08 V vs SCE. From chronoamperograms, the time constant (RC) and rate electron transfer (k_s) of 9,10-PQ could be determined. The RC time constant is the time taken for a charging current to flow through a solution resistance (R) and capacitance (C). In addition, as we have determined the k_s for PQ modified GC electrode using Laviron formalism (as discussed in Section 3.8), the k_s calculated by the Laviron method using CV technique can be compared with k_s determined by the chronoamperometry technique.

The chronoamperograms in Figure 3.21 shows two types of current decay, corresponding to double-layer charging and Faradaic current flow, where both currents are separated by a transient time. Following the potential step in chronoamperometry, the charging current decays exponentially in time at a rate governed by RC, as expressed in Equation 3.9[127].

$$i_c = \frac{\Delta E}{R_t} exp^{\frac{-t}{RC}} \qquad \textbf{Eq. 3.9}$$

Where ΔE is the pulse amplitude, R_t is the total cell resistance and C_{dl} is double layer capacitance.

Moreover, for the electrochemical reaction involving a surface attached redox species, the Faradaic current flow also decays by a single exponential in time according to Equation 3.10[127,128].

$$i_f = k_s Q exp^{-k_s t} \qquad \textbf{Eq. 3.10}$$

Where k_s is the rate of electron transferred for the overall reaction and Q is the total charge passed in the redox transformation.

Based upon Equations 3.9 and 3.10, the RC and k_s for each R_{ext} condition can be determined by making a plot of ln i vs t[127] as displayed in Figures 3.22 a,b,c.

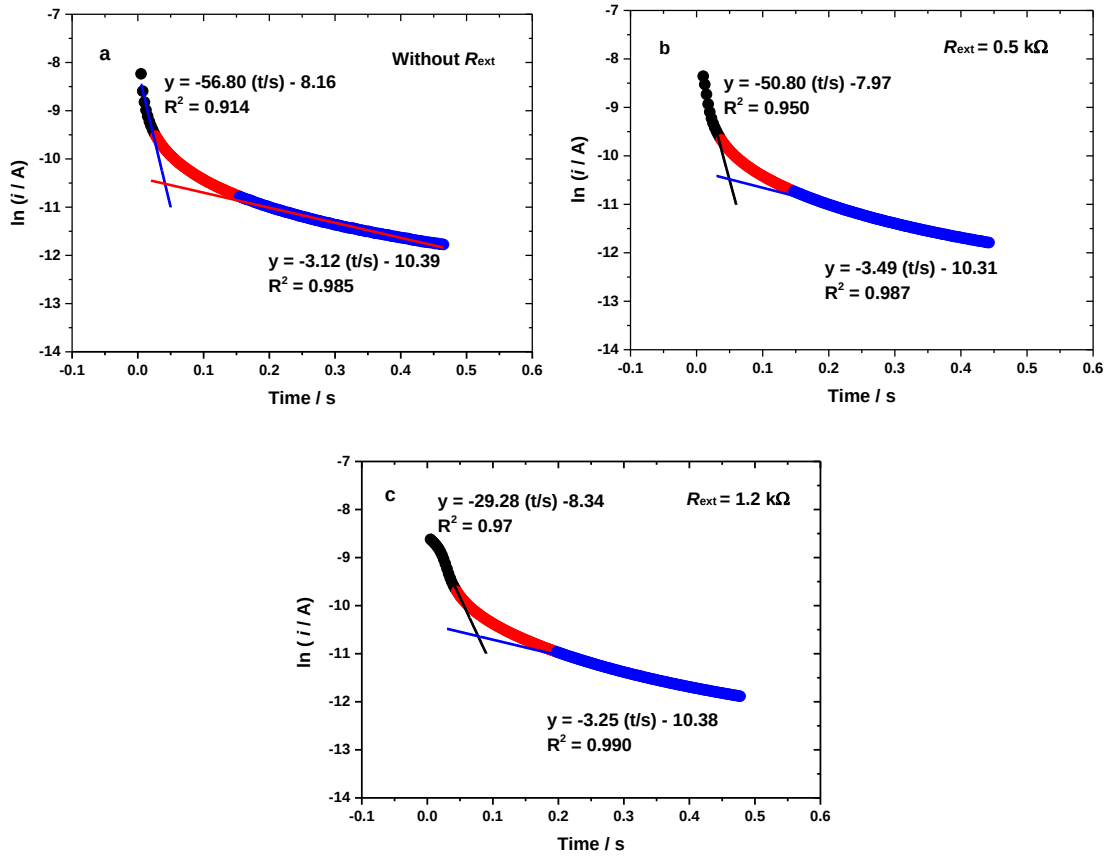

Figure 3.22; a,b and c) Based on Figure 3.21, semilog plots of ln *i vs t* for 3 different magnitudes R_{ext} were obtained in order to determine the *RC* time constant and rate of electron transfer (k_s).

As illustrated in Figure 3.22a, b, and c based on plots of ln i vs t, two linear regression lines were obtained. As indicated by Equation 3.9, a straight line equation can be expressed as ln i_c = (-1/ RC) t + 1n($\Delta E/R$), where the slope is 1/ RC. Hence, the RC value can be calculated. By contrast, k_s is determined when a straight line equation based on Equation 3.10 is presented as ln i_f = -k_s t + ln $k_s Q$, where the slope is equal to the value of k_s. Owing to the fact that the completion of

charging/discharging takes a 5*RC* time constant and the time employed here was 500 ms, analysis for k_s was performed after the 5*RC* time constant. The linear fitting was obtained by getting the linear best fit to data points as close as 0.99. Thus, the absolute slope of the linear regression line obtained gives k_s value. Both of the *RC* and k_s obtained by analysing plots of ln *i* vs *t* associated with equations 3.9 and 3.10 as shown in Figures 3.22a, b and c are presented in Table 3.6.

Table 3.6; *RC* time constant and rate of electron transfer (k_s) were obtained by two different linear fits over a plot of ln *i* vs *t*. The *RC* time constant calculated from a slope of linear best fit at short time. By contrast, the k_s was directly determined by a slope of linear best fit at long time.

R_{ext} added	Time constant (*RC*) /s	Rate of electron transfer (k_s) / s^{-1}
Without R_{ext}	0.018 ± 0.003	2.97 ± 0.15
0.5 kΩ	0.021 ± 0.002	3.35 ± 0.17
1.2 kΩ	0.037 ± 0.003	2.74 ± 0.24

As presented in Table 3.6, the value for k_s determined at R_{ext} = 0.5 kΩ is slightly higher than the determined before adding R_{ext}. Owing to the fact that in the case of immobilised 9,10-PQ, the charging and Faradaic currents exponentially decay with time, it is thought that when the *RC* time increased, the charging currents flow take a longer time to fall off, reducing the interference of the capacitive current to the Faradaic currents flow. Hence, this offers an opportunity to increase the Faradaic currents by increasing the rate of electron transfer. Thus, the k_s increased. However, the data was not consistent when R_{ext} at 1.2 kΩ was added, with the k_s decreasing. The decrease of k_s at 1.2 kΩ is most likely caused by Ohmic drop effects, where the massive *RC* time constant may obscure the Faradaic response by charging/discharging processes. This trend of results will be discussed in detail in Chapter 4 when we present experimental and theoretical data for covalently attached AQ onto GC electrode. Despite the different k_s values obtained at three different R_{ext} conditions, these values are close to the value determined using the Laviron method, particularly for R_{ext} at 0.5 kΩ. This supports our findings in varying R_{ext} on DPV measurements, showing that when an R_{ext} of 0.5 kΩ was added, the DPV current at 2.5 mV modulation amplitude is significantly amplified and produced a maximum DPV peak current when a plot of DPV current vs R_{ext} was plotted (Figure 3.18).

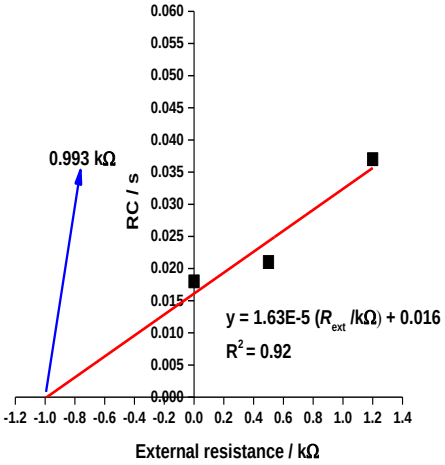

Figure 3.23; Plot of R_{ext} added in the cell circuit vs *RC* time constant data from Table 3.6.

From the *RC* times calculated as shown in Table 3.6, a plot of *RC* time constant against R_{ext} was made. It is shown in Figure 3.23. Forcing a linear fit through the data an extrapolated intercept at 0.933 kΩ was obtained. This should correspond to the solution resistance (R_u) that exists in the electrochemical cell before adding R_{ext}. However, by measuring the solution resistance at two different potentials from the capacitive current region using EIS, R_s in the electrochemical cell was obtained. The result from EIS measurements was 138 $\pm$ 6.5 Ω. Note that R_u data were directly obtained from the Nyquist plots (not shown). As expected significant deviation between the two values was noticed since Equation 3.9 is only valid for an ideal system (*RC*) but in reality, deviations from this behaviour would occur. This is because only several data points from the initial part of the curve at a short time of ln *i* vs *t* (Figure 3.22) will be linear. These linear fits may produce the results that are not statistically optimal as uncertainty to get the data points in constructing a straight line. It can be concluded that this model is too naive to describe the true behaviour at the electrode/interface-solution. In contrast, for EIS measurements the solution resistance in an electrochemical cell can be directly determined from the real part of the complex impedance (Z') based on the Nyquist plot. This point is discussed in further detail in Chapter 4 where we present our data for C_{dl} and R_u measured for covalently immobilised AQ at the surface of GC electrodes.

3.12 Varying the loadings of 9,10-PQ onto the surface of GC electrodes

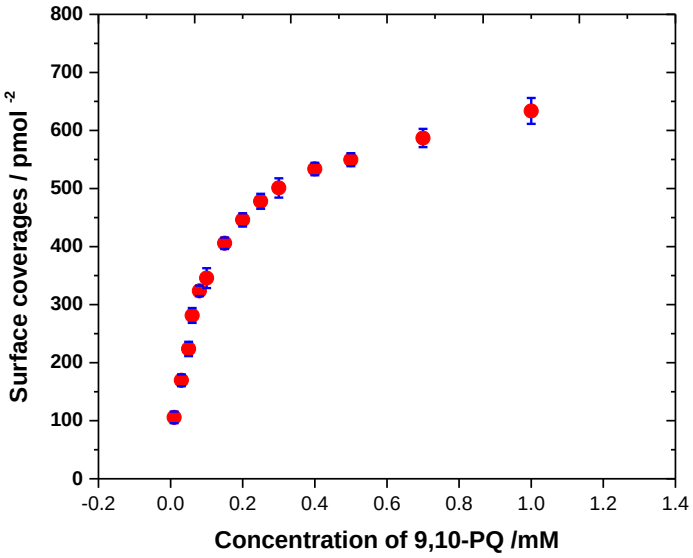

Figure 3.24; Plot for varying 9,10-PQ concentrations on the surface coverages of adsorbed 9,10-PQ at the surface of GC electrodes in 0.1 M, pH 7 phosphate buffer solution at a scan rate of 50 mV s^{-1} a potential scanned between -0.5 to +0.08 V. A 3 µL of 9,10-PQ solution was drop cast onto the surface of glassy carbon for each concentration. The electrode area is 0.071 cm^2. Three replicate data were taken for each measurement.

Different concentrations of 9,10-PQ were used in order to see the effect of loading different amounts of 9,10-PQ on the surface of on the adsorbed layers formed. As shown in Figure 3.24, the surface coverages of adsorbed 9,10-PQ molecules at the surface of GC electrodes gradually increased as the concentrations of 9,10-PQ drop casting solution increased. However, several aspects need to be considered in electrochemical measurements such as scan rate[129,130] potential window[129,130] and volume of drops of 9,10-PQ cast onto the surface of the electrode. Nevertheless, in this Section, we only employed a scan rate at 50 mV / s, a potential scan -0.5 to +0.08 V and a volume of 3 µL.

As clearly seen in Figure 3.24 when we employed a concentration of 9,10-PQ of 0.03 mM, the surface coverages of adsorbed 9,10-PQ were found to be (1.70 ± 0.10) x 10^{-10} mol/cm^2. Therefore, at these concentrations, we assumed that the adsorbed 9,10-PQ molecules may have a tendency to form a monolayer. This could be because, as theorised by Mark and Richard[131] in their work on adsorption of quinones at ordered graphite and fractured GCE, the monolayer for a flat surface and flat adsorption orientation of 9,10-PQ is 1.77 x 10^{-10} mol $cm^{-2.}$ However, from our data, this is just a speculation and there is no independent evidence to support this conclusion. In addition, from their experimental data, the surface coverage of adsorbed 9,10-PQ at the surfaces of HOPG and fractured GCE were 8.6 x 10^{-10} mol cm^{-2} and 4.7 x 10^{-10} mol cm^{-2}, respectively, although they used slightly lower concentrations of 9,10-PQ at ≤ 0.01 mM. As mentioned in Section 3.5, the

Γ_{CV} when using 1 mM of 9,10-PQ was determined to be 6.34 x 10^{-10} `mol cm^{-2}. Comparing their work on physisorbed quinones at fractured GC with our data on adsorbed 9,10-PQ at the polished GC electrode surface, similar surface coverages were noticed despite them using a lower concentration than 1 mM. This is because the fractured GC electrode is much rougher than HOPG or even polished GC electrode[131].

Table 3.7; Surface coverages of adsorbed 9,10-PQ at the surface of GC electrodes obtained based on different loadings of 9,10-PQ and number of calculated 9,10-PQ molecules for theory (before adsorption) and active molecules (after CV measurements). A 3 µL of the 9,10-PQ solution was drop cast onto the surface of GC electrodes for each concentration. The electrode area is 0.071 cm^2. The cyclic voltammetry measurements were performed at a scan rate of 50 mV/s in 0.1 M phosphate buffer at pH 7.

[9,10-PQ] / mM	Surface Coverages (Γ) measured by CV / mol cm^{-2}	Average number of active molecules based upon redox reaction	Number of molecules before adsorption (theoretical)
0.01	(1.06 ± 0.11) x 10^{-11}	4.53 x 10^{12}	6.02 x 10^{12}
0.03	(1.70 ± 0.10) x 10^{-10}	7.26 x 10^{12}	1.81 x 10^{13}
0.05	(2.24 ± 0.25) x 10^{-10}	9.57 x 10^{12}	3.01 x 10^{13}
0.06	(2.81 ± 0.13) x 10^{-10}	1.20 x 10^{13}	3.62 x 10^{13}
0.08	(3.24 ± 0.10) x 10^{-10}	1.38 x 10^{13}	4.82 x10^{13}
0.10	(3.46 ± 0.17) x 10^{-10}	1.47x 10^{13}	6.02 x10^{13}
0.15	(4.06 ± 0.10) x 10^{-10}	1.73 x 10^{13}	9.03 x10^{13}
0.20	(4.46 ± 0.12) x 10^{-10}	1.91 x 10^{13}	1.20 x 10^{14}
0.25	(4.78 ± 0.13) x 10^{-10}	2.04 x 10^{13}	1.51 x 10^{14}
0.30	(5.01 ± 0.17) x 10^{-10}	2.14 x 10^{13}	1.81 x 10^{14}
0.40	(5.34 ± 0.11) x 10^{-10}	2.28 x 10^{13}	2.41 x10^{14}
0.50	(5.50 ± 0.11) x 10^{-10}	2.35 x 10^{13}	3.01 x 10^{14}
0.70	(5.87 ± 0.18) x 10^{-10}	2.51 x 10^{13}	4.22 x10^{14}
1.00	(6.34 ± 0.33) x 10^{-10}	2.66 x 10^{13}	6.02 x10^{14}

Table 3.7 presents the variation of surface coverage obtained for adsorbed 9,10-PQ based on the different concentrations of drop casting solution. A different value in the number of active 9,10-PQ molecules compared to the theoretical number of 9,10-molecues for each concentration can clearly be seen. It can be summarised that an adsorption method for our modification of the electrode was not good enough to produce a robust modified electrode because the adsorbed molecules are only weakly bound to the support. Therefore, for this reason, we decided not to use this method in further experiments.

3.13 Conclusion

In this Chapter, we have tested Anson's model for determining surface coverages of immobilised 9,10-PQ at the surface of GC electrodes by DPV. However, DPV surface coverages data obtained for the modification of GC electrodes with adsorbed 9,10-PQ were in poor agreement when compared with CV. Characterisation of 9,10-PQ modified GC electrodes using CV and chronoamperometry were performed in order to study the thermodynamic and kinetic parameters of adsorbed 9,10-PQ. In addition, the EIS technique was employed in investigating the layers. Overall the results consistently show that the physical adsorption employed here was unstable and had a tendency to produce multilayers of adsorbed 9,10-PQ molecules. Therefore, this immobilisation method will not be used for further experiments in developing an experimental model for determining DPV surface coverages. The next experiments will focus more on the modification of GC electrodes employing the covalent attachment method

Chapter 4: Experimental and simulation modelling for the DPV surface coverages of covalently attached redox molecules

4.1 Overview

In Chapter three we investigated a simple and easy method for deposition of 9,10-PQ at GC electrodes by using the drop casting technique and studied the electrochemical behaviours. The data showed that the 9,10-PQ modified GC electrode was unstable and that is was difficult to control coverages of the adsorbed layer (tendency to produce multilayer adsorbed molecules). Therefore, in this chapter, we have covalently attached anthraquinone-2-carboxyclic acid (AQ) at monolayer ethylene diamine (EDA) linker modified GC electrodes. The covalently attached AQ at the GC electrodes was used as the main model for developing experimental and theoretical models for quantifying the surface converges of immobilised AQ. Thus, a simple equation for estimating the $\Gamma_{DPV,\,exp}$ by the experimental approach based on DPV parameters associated with a factor of e has been modelled in this work, underlying with several assumptions. The procedure makes use of additional external resistance (R_{ext}) in the DPV cell circuit associated with non-adjustable DPV parameters. Subsequently, the Γ_{DPV} of attached AQ at a suitable R_{ext} could be estimated by integrating the area under the oxidation peak from differential pulse voltammograms (DPVs). The DPVs for the immobilised redox molecules were simulated using numerical simulations developed in MATLAB software in order to verify our experimental approaches. Parameters required for DPV simulations such as electrode kinetics (k_s and α), total uncompensated resistance in the electrochemical cell (R_t) and double layer capacitance (C_{dl}), were obtained from cyclic voltammetry (CV), chronoamperometry and electrochemical impedance spectroscopy (EIS) measurements made on the modified electrodes. Good correlation was obtained between the experimental and the simulation DPVs.

4.2 Covalent immobilisation of redox molecules by employing linkers

The covalent immobilisation of electroactive molecules onto the surface of electrodes using chemical linkers such as primary amines or diazonium salts is well established[53,106]. Subsequently, the attachment of organic redox molecules can be achieved using classical solid-phase methodology when a bond is formed at a suitable linker (either primary amine or diazonium salt).

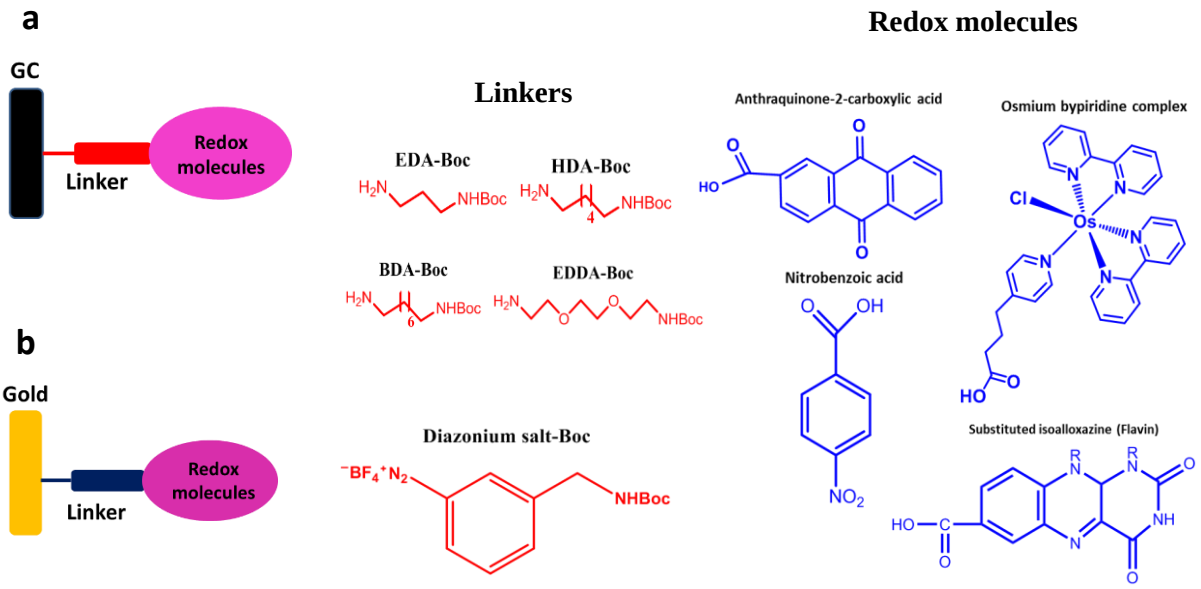

Figure 4.1; General procedure for covalent attachment of redox molecules by primary amines and diazonium salt linkers used in our group. a) Covalent attachment of redox molecules by electrochemical oxidation of primary amines onto the surface of GC electrode. b) Covalent attachment of redox molecules by electrochemical reduction of a diazonium salt onto the surface gold electrode.

From the previous work of our group (Figure 4.1), we have demonstrated in the literature results for the modification of electrodes based upon covalent immobilisation of organic redox molecules and a redox-active protein[54,55,132]. We also reported on employing electrochemical oxidation of primary amines, or electrochemical reduction of the diazonium salt, with a tert-butyloxycarbonyl (Boc)-protected amine group to carbon[54,55] and gold electrode surfaces[133]. The Boc-protected amines (Boc-EDA/HDA) or diazonium salt (Boc-$NHCH_2C_6H_4$) give two advantages. Firstly, the Boc protecting group is a bulky group and discourages the formation of polymeric layers of the grafted linkers. For instance, the Boc molecules can block the coupling of further aryl radicals at the 3 and 5 positions of aryl groups already attached to the electrode surface. Secondly, it is a very flexible method, because after removing the Boc protecting group, a wide range of redox molecules can be coupled at this reactive site by using solid-phase synthetic methodology[54,55,132]. In addition, the covalent attachment of redox probes based on organic linkers in this work might have several advantages such as well-defined organisation, the formation of densely pack

structures, and the most importantly, this type of attachment produces very stable and robust immobilised molecules at the electrode surfaces[134–136].

4.3 Covalently immobilised AQ at the surface of GC electrode

For the first model of covalent modification of redox molecules on to GC electrodes in this work, we coupled anthraquinone-2- carboxylic acid to the immobilised EDA linker (after removal of the Boc group) under solid phase conditions using the coupling reagents N-(-3-dimethylminopropyl)-N-ethylenecarbimide (EDC) and N-hydroxysuccinimide (NHS). The EDC couples the carboxyl groups to amino functions and is frequently used together with NHS. In contrast, the NHS role is to stabilise the activated ester formed as an intermediate from the carboxylic acid by EDC[137,138], increasing the coupling efficiency of AQ to EDA as shown in Figure 4.2.

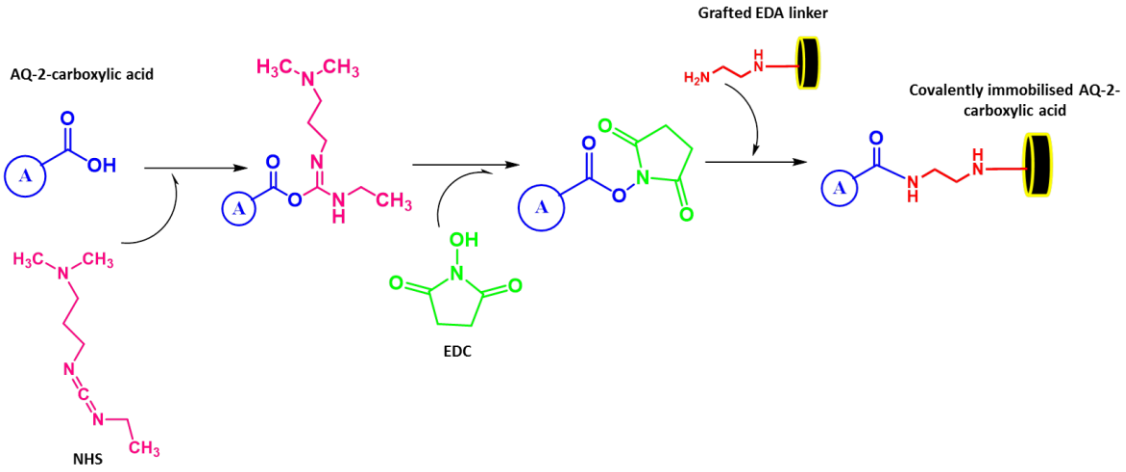

Figure 4.2; Covalent attachment of anthraquinone-2-carboxylic acid (AQ) by the formation of an amide bond with the EDA linker catalysed by coupling reagents (NHS and EDC) in DMF solution.

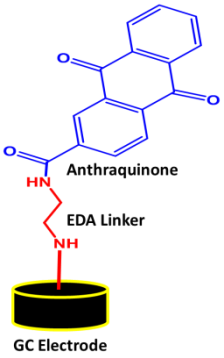

Figure 4.3; Covalent attachment of AQ using an EDA linker at the surface of GC electrode.

Figure 4.3 shows covalently immobilised AQ at the surface of GC electrode attached by the EDA linker. The AQ has been selected as the main model redox group because it is widely used in voltammetric studies due to its stable electrochemical behaviour. It is also well known that in aqueous buffer solution, the AQ molecule is characterised by a single two-electron reduction step in the presence of protons to form the hydroquinone (AQH_2)[139].

4.4 Attachment of Boc-EDA onto GC electrodes

In Chapter 3, the instability of direct immobilisation of physically adsorbed 9,10-PQ at the GC electrode surfaces has been shown. In addition, the abnormal behaviour of the redox system of adsorbed 9,10-PQ was noticed, as seen in the CV signal. This is because the multilayers adsorbed 9,10-PQ were formed, forcing the electron transfer from the multiple redox sites to the surface of electrodes through the multilayer film. Consequently, poor kinetic behaviour of the redox 9,10-PQ was obtained. Last but not least, the desorption of the attached 9,10-PQ molecules from the 9,10-PQ film was also observed. Therefore, this type of electrode modification is not favourable for employment in developing an experimental model for estimating Γ_{DPV}. In order to overcome this problem, the covalent attachment of AQ to the GC electrode surfaces, employing EDA linker was conducted in this experimental chapter.

One of the major aims of this chapter was to produce a robust surface modified electrode with monolayer immobilisation of anthraquinone (AQ) through the EDA linker in order to obtain a well-behaved redox system at the electrode/electrolyte interface. For the first step of modification, employing the established method in our group for electrochemical grafting of primary amines as mentioned in Section 4.2, the Boc-EDA linker was immobilised at the surface of the GC electrode. The process essentially involves an electrochemical oxidation of Boc-EDA with a supporting electrolyte of 0.1 M TBATFB in acetonitrile as shown in Scheme 4.1.

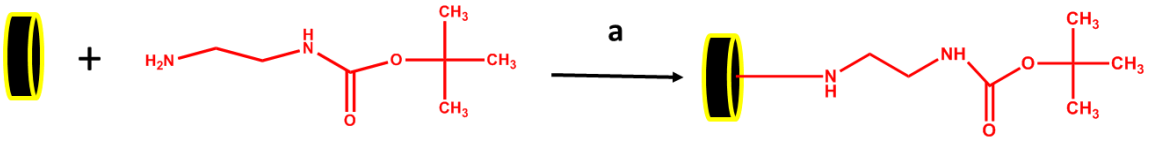

Scheme 4.1- Electrochemical immobilisation of Boc-EDA linker to the surface of GC electrode at a scan rate 50 mV s^{-1} a) A potential scanned at 0 to 2 V vs Ag/AgCl in acetonitrile containing 0.1 M TBATFB electrolyte.

.

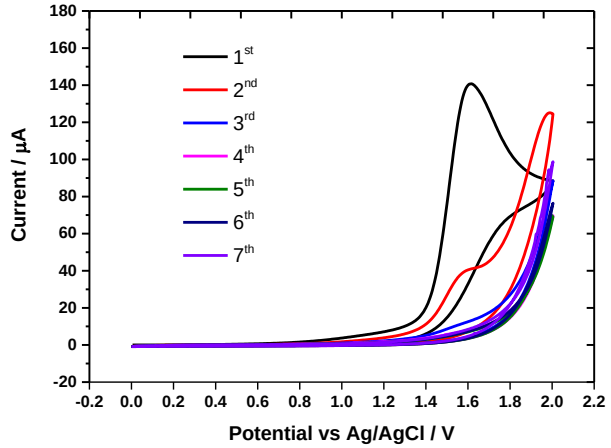

Figure 4.4; Cyclic voltammograms for electrochemical oxidation of 0.33 g (15 mM) N-Boc-EDA in 10 mL acetonitrile containing 0.1 M TBATFB electrolyte for 7 cycles recorded at a scan rate of 50 mV $s^{-1.}$ The area of GC electrode is 0.071 cm^2.

Figure 4.4 shows the first seven scans of electrochemical oxidation of Boc-EDA at the surface of the GC electrode. It can clearly be seen that the first cycle gives a broad irreversible peak for oxidation of Boc-EDA at a potential of ~ 1.60 V vs Ag/AgCl. In contrast, a drastic decrease of oxidation current for Boc-EDA on the second scan of the cyclic voltammogram can be seen. Continuing the CV scans leads to the disappearance of anodic peak after the third scan. This indicates that the GC electrode surface is completely passivated by the monolayer EDA-Boc film. The oxidation peak for the Boc-EDA corresponds to one electron oxidation of the Boc-EDA and the formation of the amine radical which bonds to the GC surface and dimerization/polymerization of Boc-EDA radicals in the bulk solution. A detailed explanation of what happens and the CV currents for the attachment of Boc-EDA will be discussed in Chapter 6.

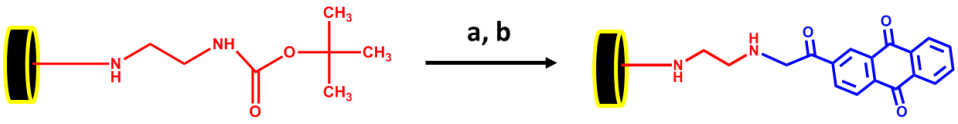

Scheme 4.2- Covalent attachment of anthraquinone-2-carboxylic acid to the surface of GC electrode through EDA linker. a) 4.0 M HCl in dioxane for 1 h. b) A mixture of anthraquinone-2-carboxylic, EDC, and NHS in DMF solution for 16 h.

Before the immobilised mono-Boc-EDA linker was covalently coupled with AQ carboxylic acid, the Boc group was removed by deprotection with 4.0 M HCl in dioxane solution for 1 h. In order to attach the deprotected mono-EDA to the AQ carboxylic acid, the mono-EDA was reacted with the AQ carboxylic acid in DMF solution with the presence of EDC and NHS as coupling reagents for 16 hours at room temperature (Scheme 4.2). The success of this modification process can be characterised by CV and other techniques such as chronoamperometry and EIS in order to determine the CV surface coverages, k_s, α, R_t and C_{dl}. Nevertheless, the DPV measurements were the focus of this work due to the main aim of this study to determine the coverages of immobilised AQ from DPV by employing the experimental and theoretical models developed in this study.

4.5 AQ modified GC and control electrodes

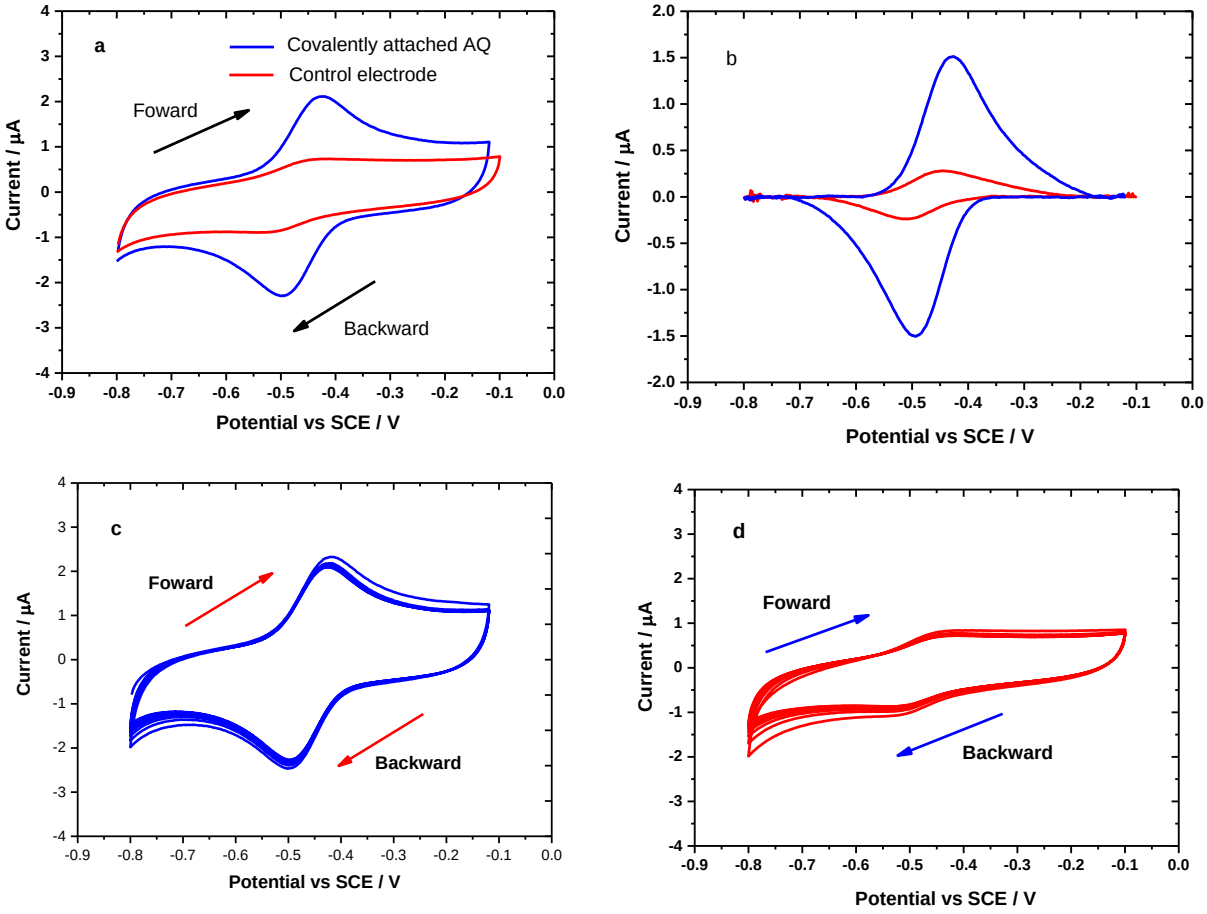

Figure 4.5; Cyclic voltammograms (CVs) for AQ modified GC electrodes based on EDA linker a) Single CVs of covalently immobilised AQ (blue) and control electrode (red). b) The anodic and cathodic currents from Figure 4.5a after performing background subtraction using Origin 9.1 software. c) Ten cycles of CV for covalently immobilised AQ. d) Ten cycles of CVs for the control electrode. All the measurements were carried out at a scan rate of 50 mV s^{-1} with a potential scan at -0.8 to -0.12 V in 0.1 M pH 7 phosphate buffer solution. The electrode area is 0.071 cm^2.

Comparing the CV signals from the physically immobilised quinone redox system as discussed previously in Chapter 3, with the covalently immobilised of quinone in this work, a stable redox system of quinone at the electrode/electrolyte interface was obtained. The modified GC electrodes for covalently immobilised AQ and control were characterised by CV in 0.1 M phosphate buffer (pH 7). Figure 4.5a (blue) shows the cyclic voltammogram of covalently attached AQ at a scan rate of 50 mV s^{-1}. In contrast, the CV in red corresponds to the control experiment. The control electrodes were obtained by dipping the GC surface in a solution only AQ with no coupling reagents of NHS and EDC. Both the modified electrodes were washed for three consecutive days in DMF in order to remove any unbonded AQ molecules. The control electrode was carried out in order to control the adsorption process of AQ at the surface of a GC electrode where there were probably some of the unbonded AQ molecules adsorbed into GC electrodes. In addition, due to leaving the immobilised EDA linker for 16-h in AQ solution, the AQ molecules may react with free EDA by uncatalysed reactions. Hence, as clearly seen in Figure 4.5a the CV still showed redox peaks of AQ despite washing the control electrode for three consecutive days in DMF.

In contrast, Figure 4.5b shows the anodic and cathodic currents of AQ modified GC electrodes after performing background subtractions from the CVs in Figure 4.5a. In order to obtain the background subtraction of anodic and cathodic currents, the subtraction was performed separately for each half cyclic voltammogram for oxidation and reduction by using Origin (version 9.1). The 35 points were manually placed on the curve of each half cyclic voltammogram, excluding at the potential range between -0.59 to -0.17 V and -0.72 to -0.35 V *vs* SCE for anodic and cathodic peaks, respectively. The remaining points were then interpolated using a subtract baseline function in order to get the subtracted anodic and cathodic currents (Figure 4.5b). In addition, after measuring the cyclic voltammogram for ten sweeps at a scan rate of 50 mV s^{-1}, the voltammogram (Figure 4.5c) shows that the AQ modified GC electrodes is favourable to produce a very stable current which it reveals good stability for the covalent immobilisation of AQ at the surface of GC. In contrast, Figure 4.5d shows ten scans of CV for the control electrode. The characteristic oxidation and reduction peaks of AQ for covalently grafted and control electrodes are clearly visible around -0.44 V and -0.51 V vs SCE. The process involves two electrons and two protons as shown in Figure 4.6. A peak separation (E_p) and a mid potential (E_{mid}) can be calculated and they were found to be 0.064 ± 0.024 V and 0.48 ± 0.015 V vs. SCE. As shown here, the covalently immobilised AQ at the GC electrode surface gave a good stability of immobilised AQ film and well-behaved of redox system at electrode/electrolyte interface, therefore, the AQ modified GC electrode was used in developing an experimental model for estimating the Γ_{DPV}. Details of the experimental model will be discussed in Section 4.12.

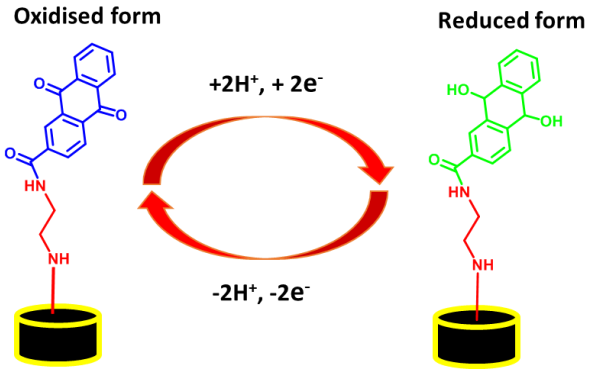

Figure 4.6; Reaction mechanism for oxidation and reduction of AQ involving two protons and two electrons.

4.6 Surface Coverages of AQ by CV Measurement

By integrating the areas under the oxidation or reduction peaks in the CV of AQ (Figure 4.7) and using the Faradaic's law (Eq. 1.2), the amount of immobilised AQ at the electrode surface can be calculated.

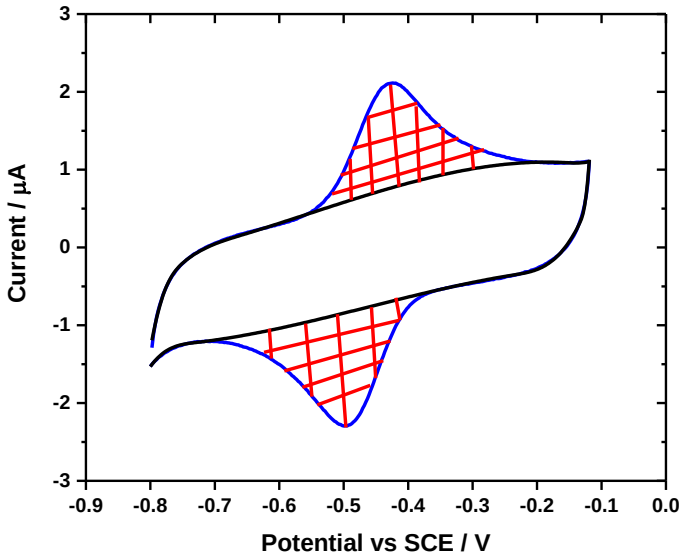

Figure 4.7; The same CV from figure 4.5a but with fitted baseline. Subsequently, the integrated area can be extracted. The fitted baseline for the capacitive current and the integrated areas were calculated using Origin software 9.1. The calculated CV surface coverages of AQ for covalently immobilised and control can be seen in Table 4.1, when assuming the roughness factor of cleaned surface of GC electrodes is 1.

Table 4.1; Calculated CV surface coverages of immobilised AQ at two different types of modified GC electrodes.

AQ modified electrode	CV surface coverages (Γ_{CV}) / pmol/cm^2
Covalently attached AQ	320 ± 9.54
Control (adsorbed AQ)	56.4 ± 9.84

Theoretically, monolayer surface coverages of AQ based on using parameterized model number 3 (PM3) calculation either for flat or perpendicular orientations are 3.3 x 10^{-10} mol cm^{-2} and 1.59 x 10^{-9} mol cm^{-2}, respectively[55]. PM_3 is a semi-empirical method for the quantum calculation of molecular electronic structure in computational chemistry. Conversely, the experimental surface coverages of covalently immobilised AQ at the surface of GC electrode were found to be 3.20 x 10^{-10} mol cm^{-2} (Table 4.1), close to the theoretical value for a monolayer with the flat orientation of AQ.

4.7 DPV for AQ Modified GC Electrodes

In order to more sensitively characterise the AQ modified GC electrodes, the modified electrodes were measured using DPV technique. As demonstrated in Section 4.5, the CV measurements of AQ modified and control electrodes were run at a scan rate of 50 mV/ s. According to the experimental model proposed by Koval and Anson[72], the relationship of CV scan rate can be related to the corresponding the DPV modulation amplitude (ΔE_p) and the modulation time (τ_p) by Equation 4.1.

$$Modulation\ amplitude\ (\Delta E_p) = CV\ scan\ rate\ (v) x\ Modulation\ time(\tau_p) \quad \textbf{Eq. 4.1}$$

Because the τ_p employed here was 50 ms, the ΔE_p was calculated to be 2.5 mV. Generally, the modulation amplitudes (ΔE_p) of 25 and 50 mV are extensively used in the literature. The magnitude of DPV current is dependent on the ΔE_p. The modulation amplitudes between 10 mV and 50 mV are often viewed as a good compromise to give a large magnitude of current and an adequate resolution. However, we are interested in the experimental approach conducted by Koval and Anson[72], in which the modulation amplitude and the modulation time of the DPV can be related to the scan rate in the CV. Thus, ΔE_p = 2.5 mV was used in our experimental design based on two reasons. Firstly, since we used CV scan rate = 50 mV/s for all CV experiments, thus, ΔE_p = 2.5 was chosen. Secondly, the advantage of using a small ΔE_p, as small as 2 mV could

improve the ratio of Faradaic-to-background current as demonstrated experimentally by Pelzer[140]. In contrast, the use of DPV parameters for the interval time (τ_i) of 500 ms and the step potential (ΔE_s) of 5 mV were generally used and reported in the literature. In order to gain more insight into the choice of DPV parameters, investigations of the DPV parameters for the AQ modified GC electrodes were conducted and the findings will be shown in Section 4.8. A set of DPV parameters employed in the DPV experiments were ΔE_p = 2.5 mV, τ_p = 50 ms, τ_i = 500 ms and ΔE_s = 5 mV. Last but not least, a DPV scan rate can be directly obtained from the Nova software. Note that, it cannot be directly changed by users. As defined by NOVA manual book, it is determined by step potential x 1/interval time as written in Equation 4.2.

$$DPV\ scan\ rate = \frac{Step\ potential\ (mV)}{Interval\ time\ (s)} \qquad \textbf{Eq. 4.2}$$

Based on Equation 4.2, a DPV scan rate can be calculated by dividing the step potential with the interval time, calculated in this case to be 0.01 V /s. However, by changing the ΔE_s or the τ_i will give a different DPV scan rate. Essentially, the interval time must be at least twice the modulation time. In our case, we used τ_p = 50 ms, thus, τ_i must be > 100 ms. In the literature τ_i = 500 ms and ΔE_s = 5 mV values are extensively used. Therefore, the parameter values mentioned above were chosen as the starting point for the experimental study.

In terms of the DPV waveform, a set of DPV parameters were employed as follows; ΔE_p = 2.5 mV, ΔE_s = 5 mV, τ_p = 50 ms and τ_i = 500 ms. Thus, we proposed the DPV waveform for the DPV experiment as shown in Figure 4.8.

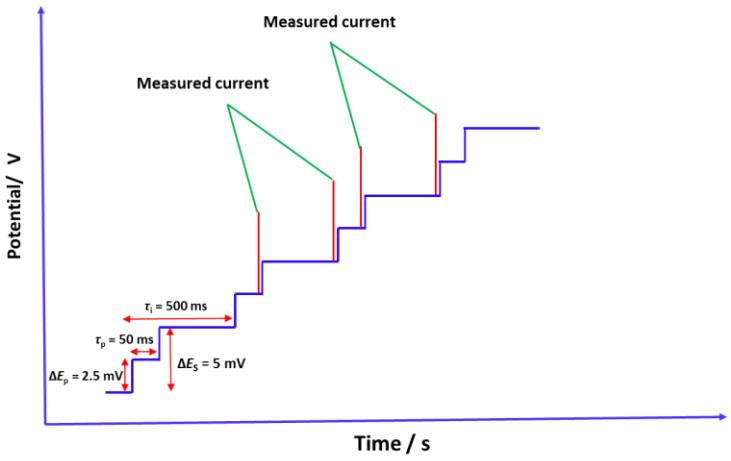

Figure 4.8; Proposed DPV waveform in our DPV experiment based on the DPV parameters that were used.

Even though our proposed waveform is not similar to the DPV waveform that we can normally be found in the Nova manual book, BASi websites, and literature but we believe that this is the DPV waveform that we employed in the DPV experiments. This is because the DPV current are still measured at before and after the pulses. Surprisingly, the definition of the DPV waveform from the NOVA manual book and the BASi website is completely different. In addition, there is some literature that give different features of DPV waveform. In order to confirm this type of waveform, we will verify it with our DPV simulation. This will look further be discussed in detail when presenting the DPV simulation in Section 4.18.

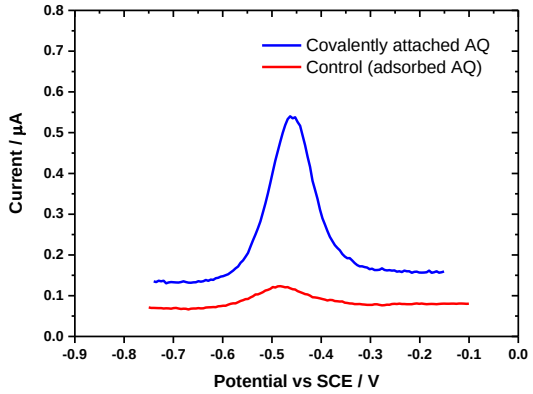

Figure 4.9; Differential pulse voltammograms (DPVs) for AQ modified GC electrode (blue) and control electrode (red). The DPVs were measured at a potential range between 0.75 V to -0.15 V vs SCE with ΔE_p = 2.5 mV, τ_p = 0.05 s, τ_i = 0.5 s, ΔE_s = 5 mV and DPV scan rate = 0.01 V s^{-1} in 0.1 M phosphate buffer solution, pH 7. The area of GC electrode is 0.071 cm^2.

Using the DPV parameters that we have modelled previously, the DPV signals for covalently coupled AQ and the control (adsorbed AQ), measured before adding any R_{ext} in the electrochemical cell circuit, are shown in Figure 4.9. Very well-defined Faradaic currents were obtained from the DPV measurements as compared to the CV measurements. The redox peak potential of immobilised AQ was found to be around -0.47 V vs SCE. Comparing to anodic and cathodic peaks potentials ($E_{pa\ and}\ E_{pc}$) and mid peak potential (E_{mid}) from CV, the E_{pa}, E_{pc} and E_{mid} were found to be -0.44 V, -0.49 V and -0.467 V vs SCE, respectively.

Another prominent feature of the DPV current above is that capacitive currents between covalently attached AQ and a control electrode (adsorbed AQ) are different from baseline. It suggests that both of the modified electrode surfaces have different film structures. This shows that the surface concentration of immobilised AQ molecules on the control electrode is somewhat lower than covalently immobilised AQ. Owing to the fact that the differential capacity of the double layer is greatly influenced by the structure of the modified electrode surfaces, clearly, the lower capacitive current for the control electrode (red) was expected.

4.8 DPV Parameters study

In this section, we systematically varied the DPV parameters while holding all others constant in order to investigate the effect on the response DPV on AQ modified GC electrode. The DPV parameters varied in these investigations are shown in Table 4.2.

Table 4.2; The DPV parameters employed for each experiment to investigate the effect DPV parameters on differential pulse voltammograms for AQ modified GC electrodes.

DPV parameter	Modulation Amplitude (ΔE_p) / mV	Modulation time (τ_p) / ms	Step potential (ΔE_s) / mV	Interval time (τ_i) / ms	DPV scan rate / mV/s
Figure 4.10a, b	1.5 to 35	50	5	500	10
Figure 4.11a, b	2.5	10 to 80	5	500	10
Figure 4.12a, b	2.5	50	5	100 to 600	50, 25, 16.7, 12.5,10 and 8.3
Figure 4.13a, b	2.5	50	1 to 5	500	2, 4, 6, 8 and 10

Figures 4.10- 4.13 show DPV currents for AQ modified GC electrode based upon the DPV parameters varied over ΔE_p, τ_p, τ_i, and ΔE_s. Overall, the anodic peaks for covalently immobilised AQ at the GC electrodes can be clearly seen with a redox potential ~ -0.47 V vs SCE.

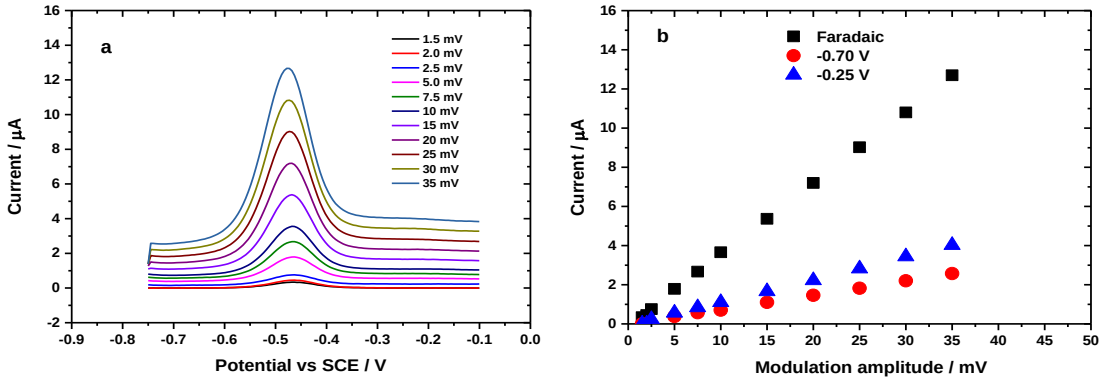

Figure 4.10; a) DPVs for AQ modified GC electrodes for various modulation amplitudes, from 1.5 mV to 35 mV at a DPV scan rate of 0.01 V s^{-1} with a potential window of -0.75 to – 0.1 V. The other DPV parameters at given in Table 4.2. b) Plots of DPV peaks and capacitive currents vs ΔE_p. The DPV peak currents were taken at the peak potential of -0.47 V. In contrast, for charging currents, the data were taken at two different potentials, -0.70 V and -0.25 V vs SCE.

Figure 4.10a shows DPVs of AQ modified GC electrodes obtained when varying the modulation amplitudes. It is clearly seen that the DPV current for the anodic peak gradually increased when changing the modulation amplitude of the pulses from 1.5 to 35 mV. In addition, the peak width and height increased when a large ΔE_p was employed. Therefore, larger pulse amplitude will give larger and broader DPV peaks. The selection of pulse amplitude usually requires an adjustment between sensitivity, speed and resolution. As shown in Figure 4.10b, a linear relationship between DPV peak and capacitive currents with modulation amplitudes at a redox potential of -0.47 V, a linear relationship for both currents with ΔE_p was obtained. Hence, it can be concluded that the DPV currents for the immobilised case are directly proportional to the pulse amplitudes.

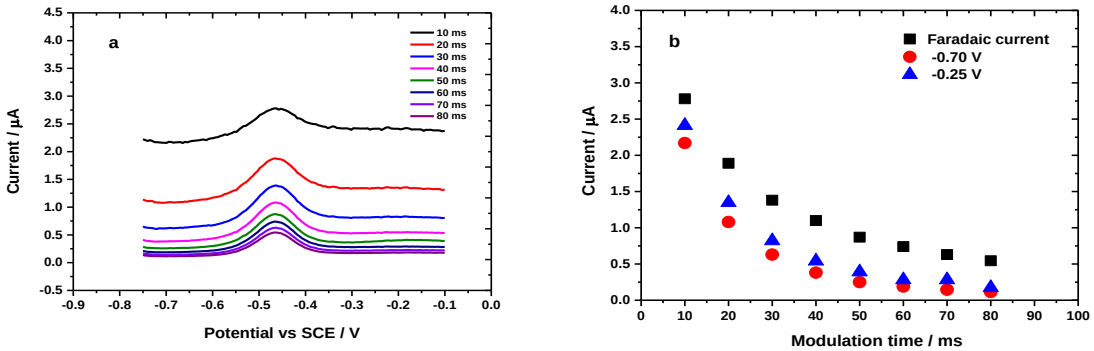

Figure 4.11; a) DPVs for AQ modified GC electrodes obtained by varying modulation times from 10 ms to 80 ms at a DPV scan rate = 0.01 V s^{-1} with a potential window of -0.75 to – 0.1 V. The other DPV parameters were presented in Table 4.2, b) Plots of DPV peak currents and capacitive currents vs modulation time. The DPV peak currents were taken at the peak potential of -0.47 V. In contrast, for charging currents, the data were taken at two different potentials, which are at -0.70 and -0.25 V vs SCE.

Secondly, when modulation times were varied (Figure 4.11a), the trend observed for DPV currents was similar to that for varying ΔE_p. However, when the shortest modulation time of 10 ms was employed, the largest, as well as the broadest DPV peak, can be observed. A plot of charging currents at two different potentials (-0.7 V and -0.25 V) and DPV peak current are shown in Figure 4.11b. The charging and Faradic currents decrease exponentially with modulation time (τ_p). In terms of the charging currents, after around 50 ms the charging current has decayed significantly and it is close to zero. In contrast, the Faradaic peak current is larger. Lovric [141] has discussed that the absolute value of capacitive current decreased when the pulse time duration increased. Moreover, as reported by Pelzer [140], choosing a long pulse duration (τ_p) and a small step modulation amplitude (ΔE_p), should improve the signal for the Faradaic current over the capacitive current. To emphasise here again, in developing our DPV experiment model for estimating DPV surface coverages, a modulation time (τ_p) of 50 ms and a small of modulation amplitude (ΔE_p) at 2.5 mV have been employed.

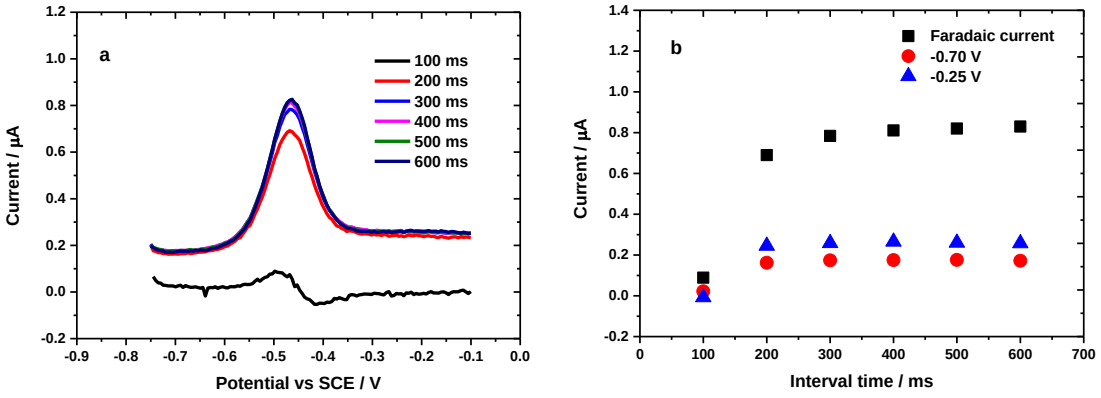

Figure 4.12; a) DPVs for AQ modified GC electrode for varying interval times from 100 ms to 600 ms at different DPV scan rates as shown in Table 4.2 with a potential window of -0.75 V to – 0.1 V. The other DPV parameters are also given in Table 4.2, b) Plots of DPV peak currents and capacitive currents vs τ_i. The DPV peak currents were taken at peak potential of -0.47 V. In contrast for charging currents, the data were taken at two different potentials, -0.70 V and -0.25 V vs SCE.

The effect of varying interval times (τ_i) was also investigated. For low modulation time (τ_p), as discussed in the preceding paragraph, the displayed DPV peak current was large and the voltammograms showed an elevated level of noise (4.11a). Conversely, the DPV peak current for 100 ms interval time gave a distorted DPV waveform when compared to DPV peaks with interval times at 300 to 600 ms (Figure 4.12a). Figure 4.12b shows that the interval time longer than 300 ms, the charging and Faradaic peak currents were constant. For a reasonable time analysis of DPV waveform measurement, the interval time (pulse period) must be at least twice the modulation time (τ_p). This is because τ_i is the time required for one potential cycle where it corresponds to the lifetime of the pulse. This can be simplified as a time measurement for two different currents which are before the pulse ($i\tau$') and at the end of the pulse ($i\tau$). Then, the time is knocked off once

the current has been measured at the end of the pulse. Therefore, the difference current ($\delta i = i\tau - i\tau'$) between two values is recorded and displayed[85]. Thus, it can be deduced that the DPV peak current at 100 ms and 200 ms showed that the interval times employed were not sufficiently to measure the difference current (δi).

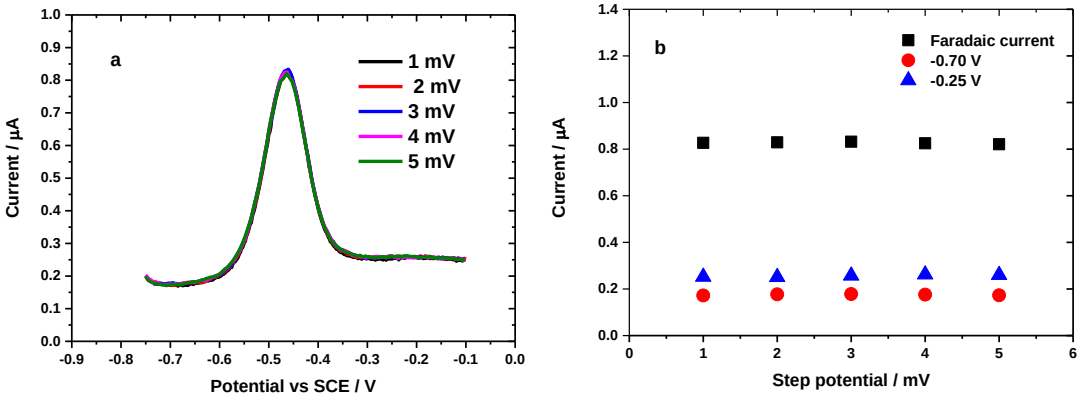

Figure 4.13; a) DPVs for AQ modified GC electrodes by varying step potentials from 1 mV to 5 Mv at different DPV scan rates as shown in Table 4.2 with a potential window of -0.75 V to 0.1 V. The other DPV parameters were also presented in Table 4.2, b) Plots of DPV peak currents and capacitive currents vs ΔE_s. The DPV peak currents were taken at peak potential of -0.47 V. In contrast, for charging currents, the data were taken at two different potentials which are at -0.70 V and -0.25 V vs SCE.

When varying ΔE_s, Figure 4.13a and 4.13b reveal that the charging currents at two different potentials and the DPV peak current are constant and the peak height and breadth are unchanged. However, as experimentally observed when conducting the DPV experiment, setting ΔE_s at 1 mV made the DPV measurement run over a longer time than for 5 mV.

To summarise, in order to get an optimal response and a well-defined peak for the DPV current, a selection of precise parameters of DPV need to be considered to produce a set of values that can lead to the best result for the current-potential response. The benefit for these investigations, a good choice of DPV scan parameters can significantly enhance the Faradaic current over the capacitive current.

Based on Eq. 4.2, by varying interval time and keeping the step potential constant, the varied DPV scan rates were obtained as shown in Figure 4.12b. In contrast, by keeping the interval time constant and varying the step potentials, the varied DPV scan rates were also obtained as shown in Figure 4.13b. Notably, as shown in Figure 4.12b and 4.13 b, by varying the scan rates on DPV measurements, the DPV current are not linear as would be observed when varying the CV scan rates for modified electrode. Therefore, the data trends show that the effect of DPV scan rates are not similar to the response of CV scan rates on the redox peak currents.

4.9 Estimating DPV charge under DPV peaks based on CV scan rates

Using the data obtained in Section 4.8, the Faradaic charge passed for each set of DPV parameters was estimated by extracting the integrated area under each DPV peak from Figures 4.10a, 4.11a, 4.12a and 4.13a, using the corresponding CV scan rate. The below histograms in Figure 4.14 shows the result.

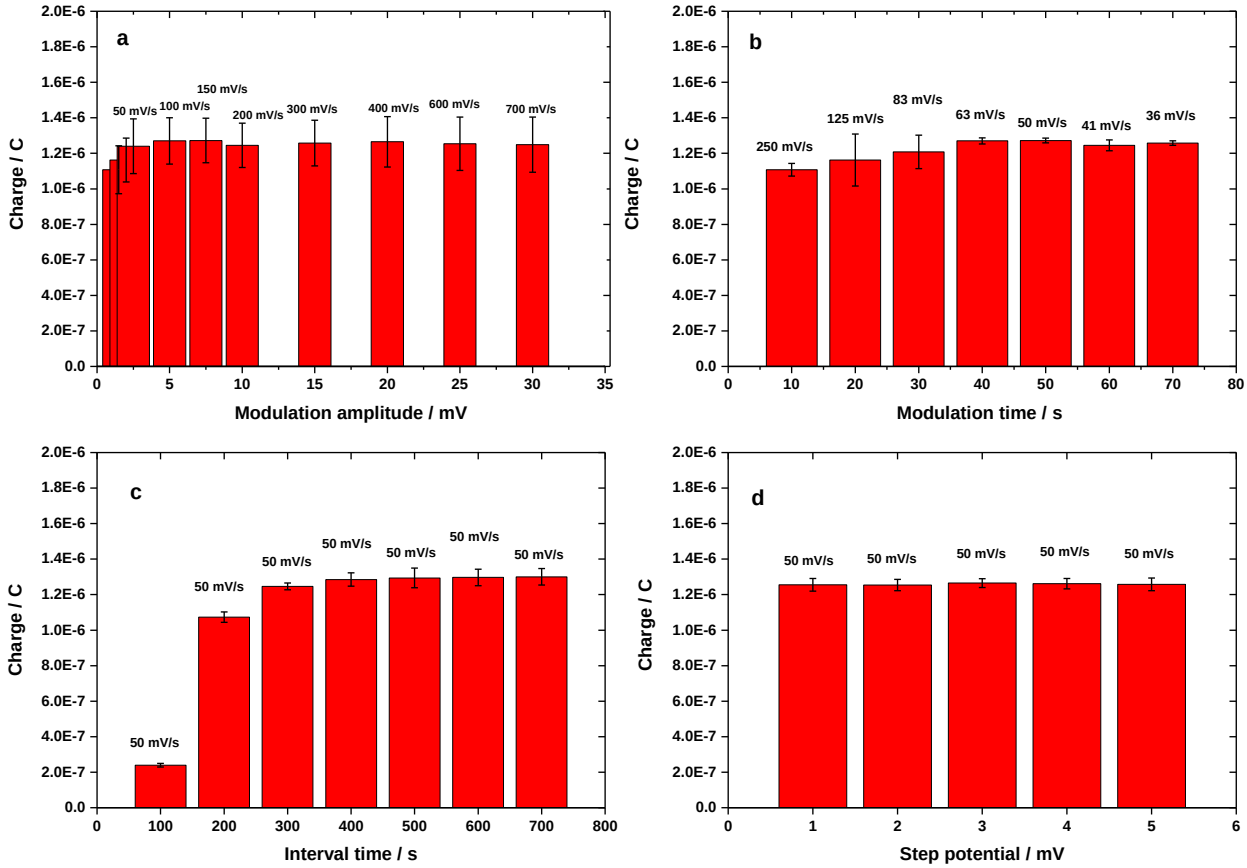

Figure 4.14; Estimated charges for AQ modified GC electrodes for the different DPV parameters based on the integrated area under the DPV peak for various a) modulation amplitudes b) modulation times c) step potentials and d) interval times. Other parameters are given in Table 4.2.

A significant conclusion based on the histograms in Figure 4.14 is that with a suitable set of DPV parameters, the DPV measurement for AQ modified GC electrode could be optimised in order to obtain a constant Faradaic process.

4.10 Effect of external resistance on DPV measurements for AQ modified GC electrodes.

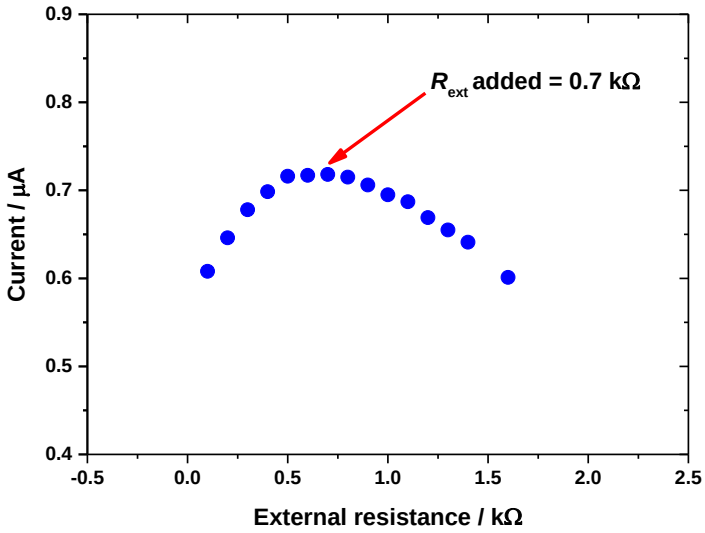

Figure 4.15; Plot of DPV peak currents before background subtraction for a series of external resistance (R_{ext}) from 0.05 to 1.6 kΩ added to the cell circuit for AQ modified GC electrode in 0.1 M pH 7 phosphate buffer, measured at ΔE_p = 2.5 mV, τ_p = 0.05 s, τ_i = 0.5 s, ΔE_s = 5 mV, and DPV scan rate = 0.01 V s^{-1}. The measurements were carried out over a potential scan between -0.75 to -0.15 V *vs* SCE with a controlled temperature of 25 ± 0.5 ° C.

The addition of an external resistance (R_{ext}) in the DPV cell circuit can produce large changes in the DPV current. Figure 4.15 shows a set of DPV peak currents for covalently attached AQ (without background subtraction) plotted against the R_{ext}. As clearly seen in Figure 4.15, the DPV peak current increased as the magnitude of R_{ext} in the cell circuit increased until it reached a maximum current at 0.7 kΩ. In contrast, a series of R_{ext} added from 0.8 kΩ to 1.6 kΩ, gave a decrease in the DPV currents.

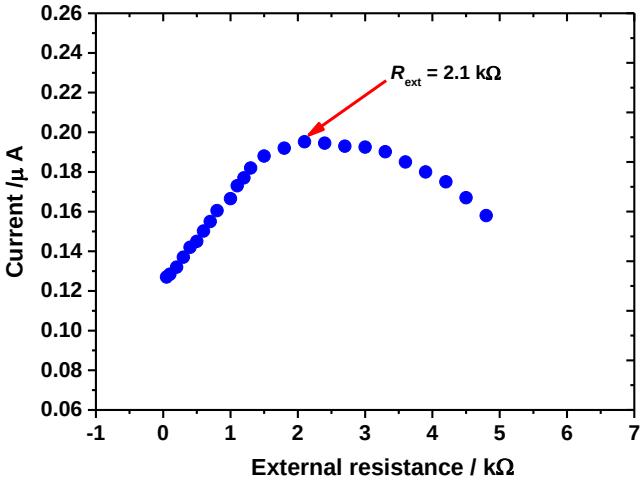

Figure 4.16; Plot of the DPV peak currents before background subtraction for a series of external resistors (R_{ext}) from 0.3 to 4.8 kΩ added to the cell circuit for a control electrode in 0.1 M pH 7 phosphate buffer, measured at ΔE_p = 2.5 mV, τ_p = 0.05 s, τ_i = 0.5 s, ΔE_s = 0.005 V, and DPV scan rate = 0.01 V s^{-1}. The measurements were carried out over a potential scan between -0.75 to -0.15 V *vs* SCE with a controlled temperature of 25 ± 0.5 ° C.

In contrast Figure 4.16 is a plot of DPV peak currents for a control GC electrode against the R_{ext} added to the working electrode. A similar trend as shown for the covalently attached AQ was obtained with the maximum DPV current found for R_{ext} of 2.1 kΩ. Beyond that value, the DPV currents start to decrease. With the presence of different magnitudes of R_{ext}, the relationship between the DPV peaks currents and R_{ext} added is not always linear. This happens because based on an approximate method provided by Anson *et al.* as already shown in Eq. 1.28, they found that the DPV current maximum will be obtained at a $R_{t,\ max}$, predicted by Eq. 1.30. Based on Equation 1.28, the rate of decay current following the application of a pulse decreases as R_{ext} increases as reflected in Figure 4.17.

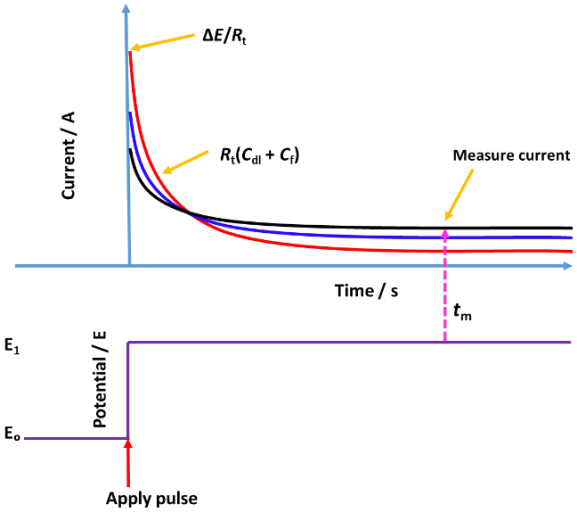

Figure 4.17; Decay of current over time for one pulse period with increasing magnitude of R_t as understood based on Equation 1.7.

However, after reaching the magnitude of $R_{t,max}$, the current is only dominated by the pre-exponential term ($i = \Delta E/R_u$) which does not depend on the concentration of the immobilised reactant[89]. When the magnitude of employed R_{ext} is larger than $R_{t,\,max}$, the ratio of t to R_t ($C_{dl} + C_f$) will be close to zero. Thus, the exponential term will be equal to one. On the other hand, the large magnitude of the Faradaic current associated with large R_{ext} may produce an ohmic drop effect which is the voltage across the parallel circuit will not reach the true/desired value of applied voltage. Hence, this effect might lead to significant errors in the kinetics electrode as shown in Equation 4.3[142,143].

$$\Delta E_t = E_R\left(1 - exp\left(\frac{-t}{R_t C_{dl}}\right)\right) \qquad \textbf{Eq. 4.3}$$

where ΔE_t is true potential, E_R is applied potential, $R_t = (R_s + R_{ext})$ is total uncompensated resistance in an electrochemical cell and C_{dl} is the double layer capacitance. For better understanding, the explanation above and the expression of Equation 4.3 could be generally thought of as shown in Figure 4.18.

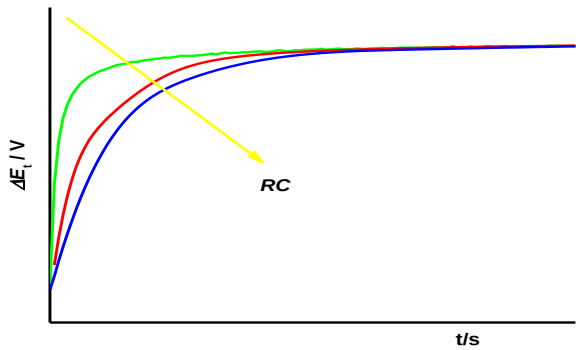

Figure 4.18; Effect of ohmic drop potential on applied potential (E_R) when the magnitude of R_u too large. This graph is based on by Equation 4.3.

4.11 Estimating surface coverages from DPV using Anson's equation

As shown in Section 4.10, R_{ext} added of 700 Ω and 2100 Ω generated the maximum DPV peak currents for AQ modified GC and control electrodes. As discussed earlier in Section 3.10 for adsorbed 9,10-PQ at the GC electrode surface, the same approach was applied in order to estimate the DPV surface coverages of AQ using Anson and co-workers's[72] Γ_{DPV} equation. The value of the double layer capacitance (C_{dl}) was evaluated from the CV measured at a scan rate of 0.05 V s^{-1} (CV scan rate = 2.5 mV/ 50 ms). Using equation 3.7, the Γ_{DPV} for AQ on the two types of modified electrodes using the results in Figures 4.15 and 4.16 were calculated to be 2.44 ± 0.2 x 10^{-10} mol cm^{-2} and 6.77 ± 0.3 x 10^{-11} mol cm^{-2}. Table 4.3 presents a comparison the Γ from CV (shown in Section 4.6) with DPV. Both datasets show that the estimated Γ for immobilised AQ from Anson's Γ_{DPV} equation is in fair agreement to the estimated coverages from CV. Also, the calculated data show that the Γ_{DPV} for covalently immobilised AQ is underestimated by the equation. In contrast, the calculated Γ_{DPV} for a control electrode is overestimated by the equation.

Table 4.3; a) Double layer capacitance (C_{dl}) obtained from cyclic voltammetry for AQ modified GC and control electrodes in 0.1 M phosphate buffer solution, pH 7 at 0.05 V s^{-1}. b) Surface coverages calculated from the CV measurements at 0.05 V s^{-1}. c) Surface coverages calculated from Eq. 3.7 for DPV measurements using C_{dl} and R_{ext} added at the maximum DPV current. DPV measured at ΔE_p = 2.5 mV, τ_p = 0.05 s, τ_i = 0.5 s, ΔE_s = 5 mV and DPV scan rate = 0.01 V s^{-1}.

Double layer capacitance estimated by CV[a] / µF	Surface coverage estimated by CV[b] / mol cm^{-2}	Surface coverage by DPV[c] / mol cm^{-2}
11.73 ± 0.7	(3.20 ± 0.65) x 10^{-10}	(2.44 ± 0.2) x 10^{-10}
5.75 ± 0.9	(5.64 ± 0.94) x 10^{-11}	(6.77 ± 0.3) x 10^{-11}

4.12 Approximation method for estimating charge and surface coverage under the DPV peak area

As stated in Chapter 1, currently, there is no any specific procedure to determine the coverage of immobilised redox species at the surface of the electrode by DPV measurement. Again, to emphasise here, one of the primary goals in conducting this study was to develop a simple experimental procedure that could determine Γ_{DPV} for immobilised redox molecules on the CMEs based on the DPV technique. Therefore, it is hoped that the findings from this study can be offered

as an alternative electrochemical technique rather than CV for estimating the surface coverages of immobilised redox species, particularly for low surface concentration.

Before proposing our approximation method in determining Γ by DPV technique, a question is raised here; how far the CV measurement could give us a true value in estimating the surface concentration of immobilised redox species. This is because, in the modern CV, the CV is generally operated by digital instruments rather than analogue CV. Thus, the digital CV mode cannot apply a true linear waveform and its naturally stepped by a staircase waveform as an approximation. For this issue, the CV measurements on AQ modified GC electrodes was conducted by attempting to run the modified electrode with different magnitudes of R_{ext} added in cell circuit. The data obtained are shown in Figure 4.19.

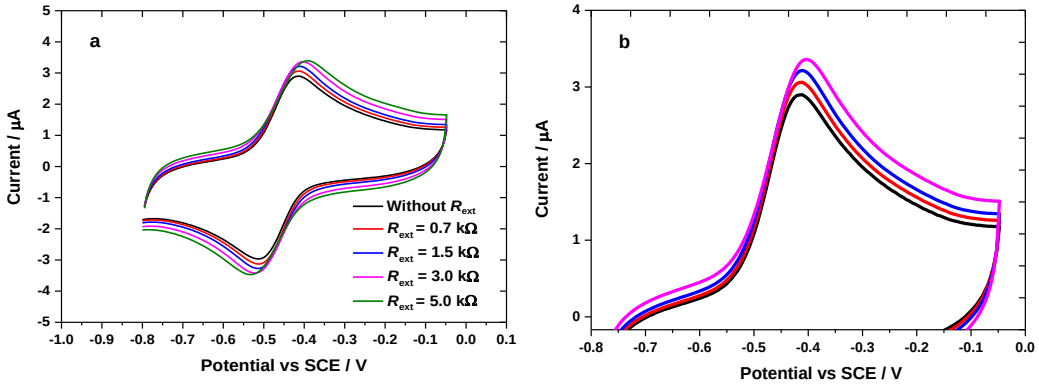

Figure 4.19; a) CVs obtained for AQ modified GC electrode after adding R_{ext} from 0.7 kΩ to 3.0 kΩ over CV measurements. The black signal is CV before adding R_{ext}. All the measurements were carried out at a scan rate of 50 mV s^{-1} with a potential scan at -0.8 to -0.12 V in 0.1 M pH 7 phosphate buffer solution. The electrode area is 0.071 cm^2. b) Enlargement of oxidation currents from Figure 4.19a.

As discussed earlier in Section 4.6, CV surface coverages were calculated to be 3.29 ± 0.94 x 10^{-10} mol cm^{-2}. However, after adding R_{ext} to the AQ modified GC electrode, unexpected amplifying CV signals were obtained (Figure 4.19b). As can be observed, the oxidation and reduction currents were enhanced by R_{ext} added. Consequently, the size of oxidation and reduction peaks get bigger. This would make the integrated area under redox peaks, as well as the calculated charge, increased. Consequently, the Γ_{CV} calculated with R_{ext} added may higher than the Γ_{CV} without R_{ext}. Nevertheless, this issue is beyond the scope of this study as our main aim is to focus more on estimating surface coverages AQ using DPV. Moreover, according to the enhancing of CV currents by R_{ext} added, this could be explained due to the fact that in the modern CV manufacturers made digital instruments with digital signal generators. Therefore, it is frequently performed based on digital mode than analogue mode (Figure 4.20), where the smooth voltage

ramp is tending to step up by very small staircase waveform (typically 0.5-5 mV)[144] as displayed in Figure 4.21.

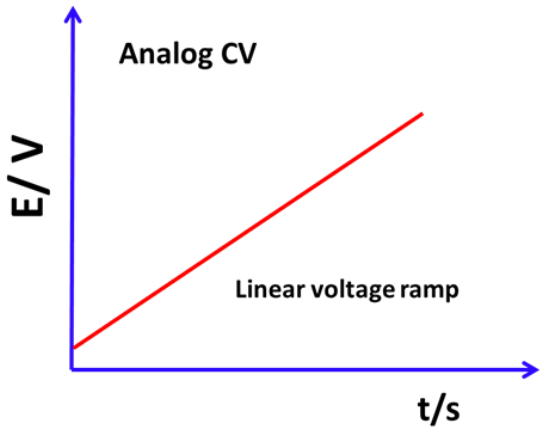

Figure 4.20; Linear voltage ramp for analog cyclic voltammetry.

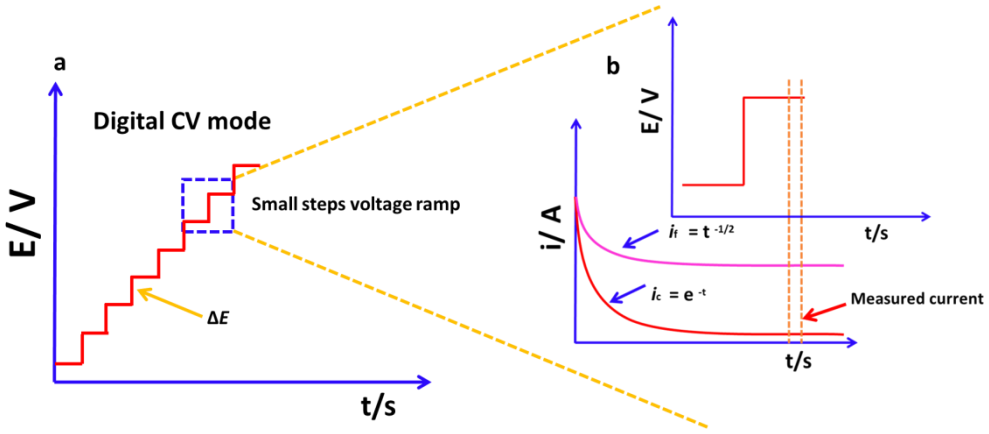

Figure 4.21; a) Step voltage ramp for the digital CV. b) Enlargement of step on digital CV to show the decay of the charging and Faradaic currents.

Despite it is naturally stepped over the voltage ramp the generated CV current is still similar to the analogue CV[144,145]. However, when the digital CV is performed on immobilised redox active at the electrode surface, it will involve with the presence of pseudocapacitance (C_f), suggesting that electron transfer kinetics of immobilised redox species strongly depends on scan rate, potential step size, and current sampling time. When involving the current sampling time on digital CV measurement, loss some charge from Faradaic reactions of adsorbed active molecules tend to occur, resulting the electroactive surface coverages can greatly differ from the true value that can be given by analogue CV[144].

Secondary to that point, as mentioned earlier in Section 1.4, the initial reports by Anson and his associates[64,72] showed that the DPV could be used to estimate the amount of immobilised redox molecules at the surface of the electrode have been a significant motivation. Moreover, an attempt of estimating the charge corresponding to CV scan rate using DPV peak area gave a constant Faradaic process, this motivated us to derive a mathematical expression for DPV charge based on the DPV parameters used in the measurement. For the initial study, we attempted to derive the mathematical expressions for the approximate total charge (Q_T) from the DPV current by integrating the area under the peak.

The approximation equations show herein follow Anson and co-workers' treatment[64] as shown in Chapter 1 (Eq. 1.28 to 1.30). From the mathematical expressions that we obtained for calculating the DPV charge, subsequently, the surface coverage of immobilised AQ can be calculated using Faraday law's ($Q = nFA\Gamma$).

In order to derive equations for the total charge (Q_T) under DPV peak, there are several assumptions;

1) We assume that the interval time (τ_i) is long enough for the transient double layer charging and Faradaic currents to decay to zero. Based on data from Figure 4.12b, we assume that a sufficient interval time is ≥ 400 ms.
2) We assume that the decay of current transients follows a simple exponential decay, note that this is not strictly true from the DPV simulation and the potential step transient DPV experiments. This is because the Faradaic process lags behind as some double layer charging needs to take place before the potential appears across the double layer to drive the electron transfer reaction based on Equation 1.28.
3) Anson *et al.*[64] reported that the largest current at the time (τ_p) occurs based on Equation 1.30.

$$R_{t,max} = \frac{t}{(C_{dl}+C_f)}$$

4) Thus, the largest current will be obtained when C_f is largest as shown in Equation 4.4.

$$i_{max} = \frac{\Delta E_1}{eR_{t,max}} \qquad \textbf{Eq. 4.4}$$

Hence, the total charge passed for the modulation pulse (ΔE_p) is obtained by integrating the current

$$\Delta q_T = \int_0^\infty i\delta t = \int_0^\infty \frac{\Delta E_1}{R_{t,max}} \exp \frac{-t}{R_t C_t} \qquad \textbf{Eq. 4.5}$$

$$\Delta q_T = \frac{\Delta E}{R_t}\left[R_t C_T exp\left(\frac{-t}{R_t C_T}\right)\right] \quad \textbf{Eq. 4.6}$$

and we have

$$\Delta q_T = \Delta E_1 C_T \quad \textbf{Eq. 4.7}$$

The differentiation is made because we don't know $R_{t,\,max}$ as well as the R_u from solution. We only know added R_{ext}.

Substituting Eq. 1.30 into Eq. 4.7 gives

$$\Delta q_{step\ pulse} = \frac{\Delta E_1 \tau}{R_{u,max}} \quad \textbf{Eq. 4.8}$$

Furthermore, substituting Eq. 4.4 into Eq. 4.8 gives Δq for each modulation amplitude

$$\Delta q_{step\ pulse} = \frac{\Delta E_1\, \tau e i_{max}}{\Delta E_1} \quad = \quad \tau e i_{max} \quad \textbf{Eq. 4.9}$$

Then, based on Equation 4.9, we sum over all the steps to obtain the total charge (Q_T) as

$$Q_T = \frac{\Delta E_2}{\Delta E_1}\sum \Delta q_{pulse} \;=\; \tau e \sum i_{max}\, \frac{\Delta E_2}{\Delta E_1} \quad \textbf{Eq. 4.10}$$

As DPV current is plotted against the potential along the potential which steps through ΔE_2 for each interval time, i_{max} is plotted against $E + \Delta E_2$, thus, a factor of $\Delta E_2/\Delta E_1$ is introduced in Equation 4.10.

In introducing the ratio $\Delta E_2/\Delta E_1$, we assume that the potential is small, hence, we can linearise the potential dependence of the coverage and double layer capacitance.

As shown in Figure 4.9, the area under the DPV curve can be expressed

$$A_{DPV} = \int i_{max}\, \delta E = \sum i_{max} \Delta E_2 \quad \textbf{Eq. 4.11}$$

Thus, Q_T under the DPV peak area is obtained as 4.12.

$$Q_T = \frac{A_{DPV}\tau e}{\Delta E_2}\;\frac{\Delta E_2}{\Delta E_1} = A_{DPV}\frac{\tau e}{\Delta E1} \quad \textbf{Eq. 4.12}$$

Since Γ = Q/nFA, thus the approximation surface coverage using peak integration is expressed as

$$\Gamma = \frac{A_{DPV}\tau e}{\Delta E_1 nFA} \quad \textbf{Eq. 4.13}$$

Where A_{DPV} is the integrated area under the DPV peak, τ is the modulation time, e is 2.718, ΔE is the modulation amplitude, n is the number of electrons transferred, F is the Faraday constant and A is the electrode area. Clearly, Eq. 4.13 shows that Γ_{DPV} is directly related to Q (DPV) and the DPV parameters. This equation should allow DPV to be used to estimate the concentration of immobilised redox species. Equation 4.13 can be simplified as shown in Equation 4.14.

$$\Gamma_{\mathrm{DPV}} = \frac{Q_T}{nFA} \qquad \textbf{Eq. 4.14}$$

In order to estimate surface coverage from DPV, we integrate the area under the DPV peak after taking away the double layer charging baseline. As mentioned earlier in Eq. 1.30, we assumed that $C_t = C_{dl} + C_f$. Therefore, using the B-spline function on Origin 9.1, the baseline for double layer charging current can be created**.**

4.13 DPV Surface Coverages for immobilised AQ based on the experiment model.

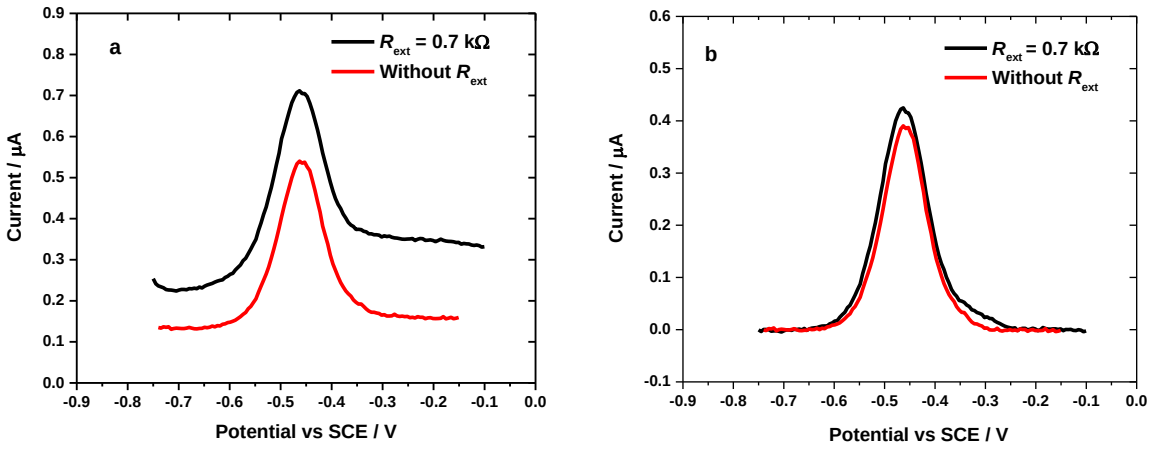

Figure 4.22; a) DPVs for AQ modified GC electrode with R_{ext} of 0.7 kΩ (black) and without the R_{ext} (red) before background subtraction. R_{ext} of 0.7 kΩ (black) gives the highest DPV current for a plot of DPV current vs R_{ext} b) The DPVs from Figure 4.22(a) after performing background subtractions using Origin 9.1 software. The DPVs were measured with ΔE_p = 2.5 mV, τ_p = 0.05 s, τ_i = 0.5 s, ΔE_s = 5 mV and a DPV scan rate of 0.01 V s^{-1} in 0.1 M phosphate buffer at pH 7 with a controlled temperature of 25 ± 0.5 ° C.

As shown in Figure 4.22a by adding a R_{ext} of 0.7 kΩ in series with the working electrode, the DPV current for the AQ modified GC electrode is amplified. Hence, it can enhance the sensitivity in the detection of surface concentration since the Faradic current from DPV is amplified. This can be clearly visualised after performing background subtraction on the DPV peaks as shown in Figure 4.22b.

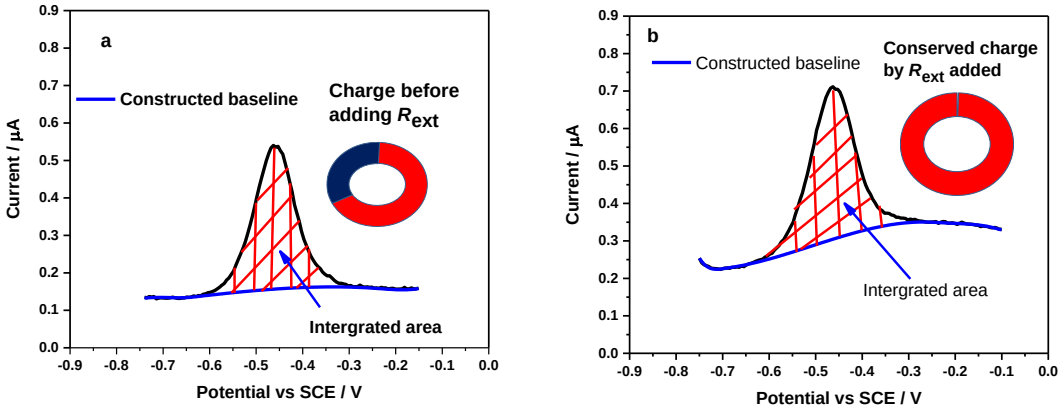

Figure 4.23; The same DPVs from Figure 4.22a but with created baseline. a) DPV before adding R_{ext}. b) DPV at R_{ext} of 0.7 kΩ corresponding to the maximum DPV peak current from the plot of DPV peak current vs R_{ext}. Subsequently, the integrated area under the DPV peak can be extracted. The created baseline for capacitive current and integrated area was obtained using Origin software 9.1.

After constructing a baseline for the background currents for both DPV waveforms (Figure 4.22b), the areas under the DPV peaks were integrated using Origin 9.1. Then, the charge under the DPV peaks at the R_{ext} of 0.7 kΩ and without R_{ext} were calculated using Equation 4.12.

Table 4.4- Charge calculated for DPVs from the integrated area (Figure 4.23a, b) at two different magnitudes of resistance.

R_{ext} magnitude	DPV Charge /C
Without R_{ext}	$(2.40 \pm 0.08) \times 10^{-6}$
$R_{ext} = 0.7$ kΩ	$(2.73 \pm 0.09) \times 10^{-6}$

The calculated charges are given in Table 4.4. Therefore, based on data shown in Table 4.4, the doughnut charts in Figure 4.23a and 4.23b were displayed. This is because we hypothesised that by adding R_{ext} to the working electrode, the loss of some Faradaic charge over the redox reaction of immobilised AQ could be reduced. In the doughnut chart (Figure 4.23a) the red section is measured DPV charge while the blue section is unmeasured DPV charge. The doughnut chart in Figure 4.23b, by contrast, shows the measured DPV charge with the optimised R_{ext}. Based on this doughnut chart, we have made the assumption that, with the presence of a suitable R_{ext}, the charge for redox reactions of AQ could be conserved, despite the fact that under potentiostat conditions the experimental data will not measure 100% of Faradaic charge (ideal reaction).

Increasing charge by R_{ext} added is probably based on two distinct ways. Firstly, when engaging with immobilised redox active at the surface of electrodes, without the presence of diffusion

process, the Faradaic current decays exponentially instead of following $t^{-1/2}$. The presence of R_{ext} in the DPV circuit will slow the decay of the Faradaic current, and increase the generating charge by Faradaic reaction. Therefore, the magnitude of Faradaic current would increase[64,87]. Secondly, the decay rate of the charging and Faradaic currents is entirely dependent on *RC* time constant. In fact, the charging of double layer capacitance can occur in a few milliseconds. Hence, a large non-Faradaic current will be generated in a short time. Consequently, with less *RC* time constant, the Faraday current can be greatly affected by capacitive current due to a slow Faradaic process. However, the R_{ext} added will make *RC* time constant gets icreased[146], forcing the capacitive current to take longer to fall off. This creates an opportunity to increase the Faradaic process[147]. This point will be discussed in great detail in Section 4.25 when we present our results from the DPV simulations.

The determined total of the DPV surface coverages for the covalently immobilised AQ at the surface of the GC electrodes based on Eq. 4.14 was found to be (198 ± 7.5) pmol cm^{-2}. The calculated Γ_{DPV} corresponds to roughness factor (ρ) 1. The procedures for estimating the Γ_{DPV} were used for all our modified electrodes.

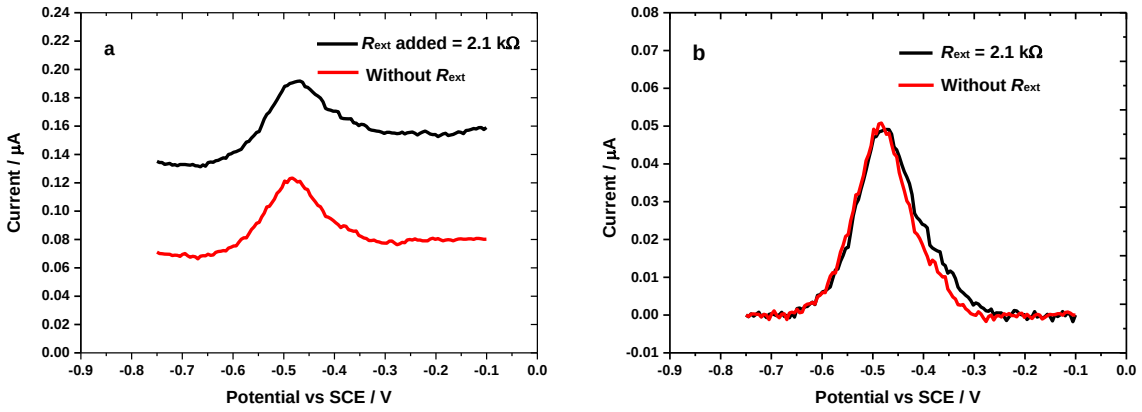

Figure 4.24; a) DPVs for control electrode with the R_{ext} of 2.1 kΩ (black) and without the R_{ext} (red) before background subtraction. The R_{ext} of 2.1 kΩ (red) gives the highest DPV peak current from a plot of DPV current vs R_{ext} b) The DPVs from Fig. 4.24(a) after performing background subtractions using Origin 9.1 software. The DPVs were measured with ΔE_p = 2.5 mV, τ_p = 0.05 s, τ_i = 0.5 s, ΔE_s = 0.005 V and a DPV scan rate of 0.01 V s^{-1} in 0.1 M phosphate buffer solution at pH 7, at 25 º ± 0.5 controlled by using a water bath.

Differential pulse voltammograms for control GC electrodes with an optimised R_{ext} of 2.1 kΩ and without R_{ext}, are shown in Figure 4.24a with the background subtracted DPV waveforms in Figure 4.24b. Performing the same calculations, Γ_{DPV} for the control electrode was found to be 29.8 ± 1.7 pmol/cm^2. The data for two electrodes are presented in Table 4.5.

Table 4.5- The surface coverages from DPV for AQ modified GC electrodes.

Modified electrode	Γ_{DPV} / pmol cm^{-2}
Covalently attached AQ	198 ± 7.5
Control electrode (adsorbed AQ)	29.8 ± 1.7

The calculated Γ_{DPV} using the approximation equation (Eq. 4.14) that we have derived in Section 4.12 was initially compared with Γ_{CV}. Comparisons of the estimated surface coverages for both modified electrodes by CV and DPV can be seen in Figure 4.25.

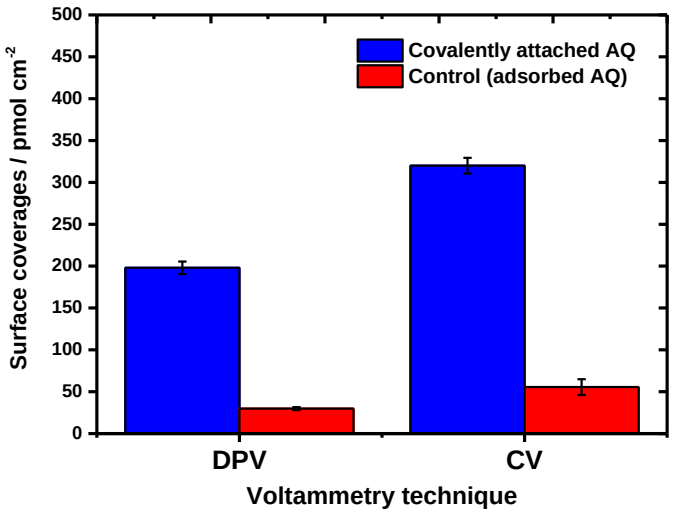

Figure 4.25; Comparison the DPV and CV determined surface coverages for covalently immobilised AQ and control (adsorbed AQ) at the surface of GC electrodes.

The error bars for CV and DPV measurements were obtained from three different modified electrodes. As clearly seen, the obtained DPV surface coverages based on Eq 4.14 are lower than the surface coverages from CV. The data show poor agreement between Γ_{CV} and Γ_{DPV}. This indicates that the surface coverage obtained by DPV from Eq 4.14 are considerably less than the true values as estimated by CV, even though both measurements involved the same Faradaic pseudocapacitance. According to the approximate equations proposed by Anson *et al.*[64] based on Eq. 1.28, the assumption was made that for a small pulse amplitude, C_f remains unchanged during the pulse duration, this leads to the factor of e = 2.718 from the exponentially decay of charging and Faradaic currents that appear in Eq. 1.28. However, this is not true since C_f can undergo a significant change during the duration of the pulse. This is because, at the start of the pulse, none of the pulse potential appears across the electrode/solution interface to drive the redox reaction. The redox reaction, and hence Faradaic pseudocapacitance, only begins to contribute some time into the pulse as the potential the electrode/solution interface build up with the charging of the

double layer. Consequently, C_f will vary during the pulse and can be expressed based on Eq. 4.15. However, as pointed out by Anson *et al.*[64] Eq. 4.15 cannot be solved analytically.

$$\frac{\Delta E - \epsilon}{R_u} = \left[C_{dl} + C_f\right]\frac{\delta \epsilon}{\delta t} \qquad \textbf{Eq. 4.15}$$

In Eq. 4.15 ϵ is the true potential difference across the parallel combination of C_{dl} and C_f.

4.14 Kinetics for covalently immobilised AQ

As one of the main objectives of the study is this result, this chapter aims to give a better insight into DPV experiments based on theory. Thus, a DPV simulation program was developed during this work. This point will be discussed in great detail in Section 4.18. In order to run the simulation, several simulation variables such as the rate of electron transfer (k_s), transfer coefficient (α), total uncompensated resistance in the electrochemical cell (R_t), double layer capacitance (C_{dl}) and surface coverages of immobilised active molecules (Γ) are needed. To avoid guessing initial values, we think that it is better to extract the parameter values from experimental approaches, employing several electrochemical techniques such as CV, chronoamperometry and EIS. The advantage of conducting experiments to obtain the experimental parameters is we could verify our experimental approach. To start the experimental approach, we first measured the kinetic parameters of the modified electrodes using CV. Following this, by varying CV scan rates, the kinetic information of covalently attached AQ could be obtained.

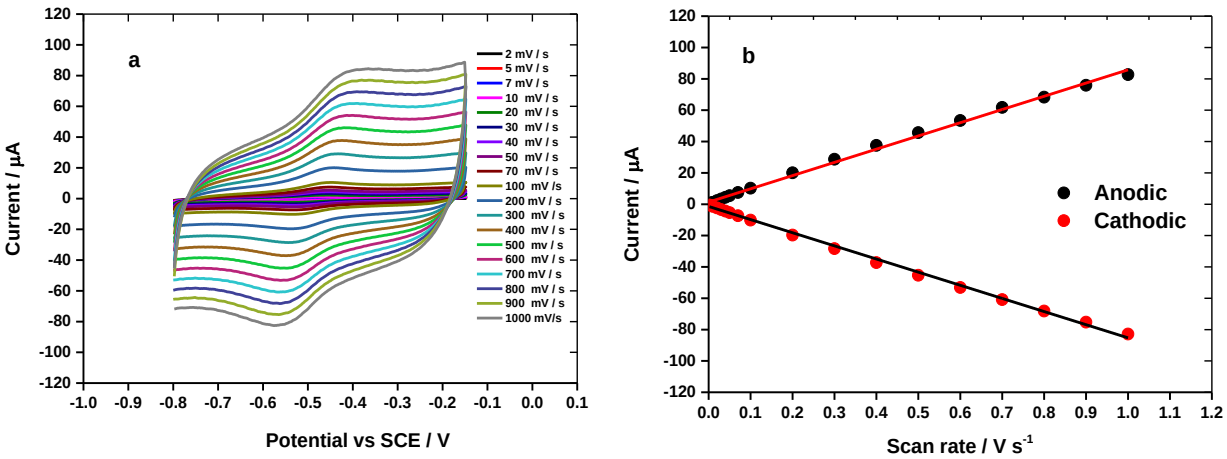

Figure 4.26; a) Cyclic voltammograms for AQ modified GC electrode in 0.1 M pH 7 phosphate buffer at a series of different scan rates (2 mV s^{-1} to 1000 mV s^{-1}). b) Plots of i_p for anodic and cathodic currents (without background subtraction) *vs* scan rate (v). The measurements were carried out at 25 ± 0.5 ° C.

Using the same Laviron formalism as already explained in Chapter 3 (Section 3.16), the electron-transfer kinetics for covalently immobilised AQ at the surface GC electrode were determined. As the first criterion for a surface confined electrochemical process, a plot of anodic and cathodic peak currents against the scan rate (v) shows that the peak currents are linearly proportional to the sweep rate (v). Figure 4.26a shows measured CVs for AQ modified GC electrodes at different scan rates, which starts from 2 mV s^{-1} to 1000 mV s^{-1} in 0.1 M phosphate buffer solution, pH 7. As clearly shown in Figure 4.26b, the anodic and cathodic currents vary linearly with scan rates.

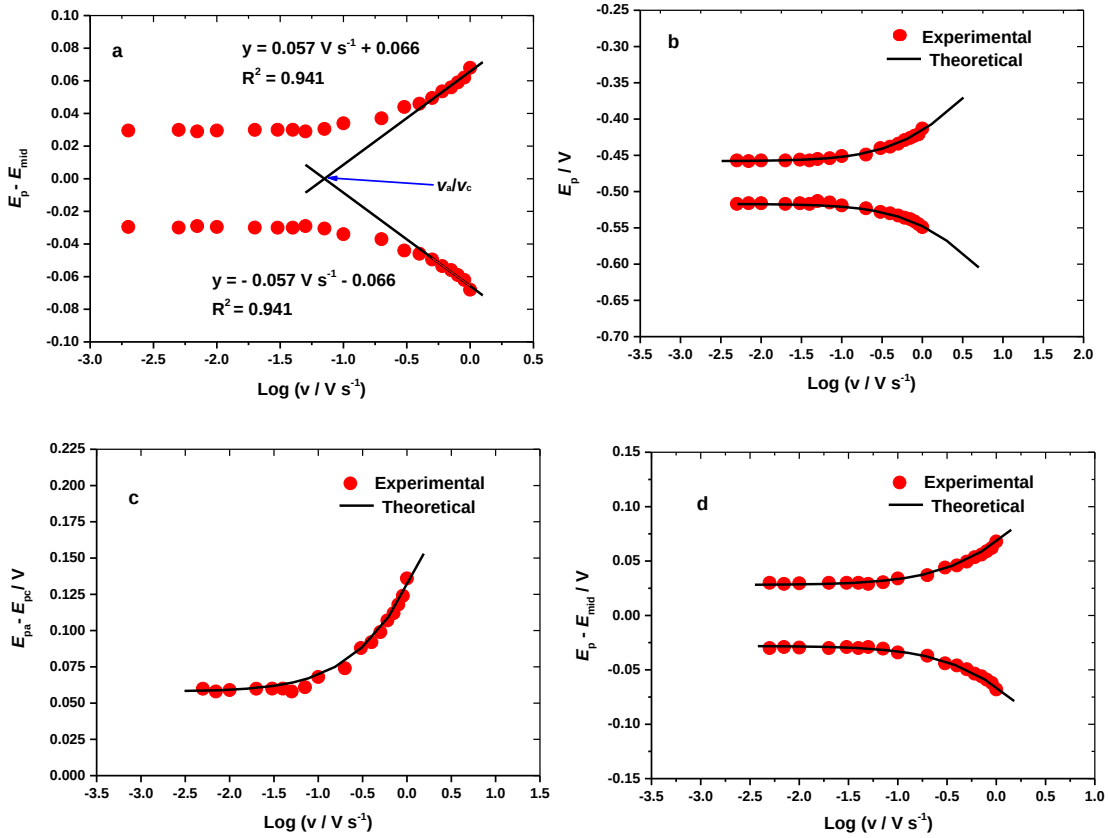

Figure 4.27; a) Laviron plots for the variation of $E_{pa/pc}$ - E_{mid} (overpotential) *vs* the logarithm of the scan rate (v) and the linear fits over the anodic and cathodic branches in order to determine the experimental α and k_s values. b) Plots show the influence of scan rate on peak potential for oxidation and reduction (filled cycles) for AQ modified GC electrode at various scan rate (0.002 to 1.0 V s^{-1}), the theoretical (solid lines) were obtained from the best fitting to the Laviron theoretical plot using the working curve for α = 0.5. c) Plot of experimental data and Laviron theory based on working curve for α = 0.5 for the peak separation (E_{peak}). d) The best fits for experimental data of $E_{pa/pc}$ - E_{mid} (overpotential) to the Laviron theory by employing α = 0.5 for anodic and cathodic curves, respectively.

Based on the Laviron plot of overpotential ($E_{pa/pc}$ - E_{mid}) versus log of scan rate (v) as shown in Figure 4.27a, two branches, anodic and cathodic, were obtained. As can be seen in the plot of E_{peak} vs log v (Figure 4.27c), it is clearly shown that for scan rates 0.6 to 1 Vs^{-1} the peak separations ΔE_{peak} > 200/n or 100 mV. Thus, based on a plot of $E_{pa/pc}$ - E_{mid} vs log v (Figure 4.27a), this range

(0.6 to 1 V s^{-1}) was used in order to estimate α and k_s based upon the two linear best fits. The slopes of the straight lines for anodic and cathodic branches were used to calculate α values using Equations 3.2 and 3.3[61]. Subsequently, extrapolating the linear parts of the anodic and cathodic branches in order to extract v_a/v_c at zero overpotential (shown in Figure 4.27a) on the plot of ($E_{pa/pc}$ - E_{mid}) vs log v, using Equations 3.4 and 3.5, k_s can be determined. The k_s value was found to be 2.83 ± 0.45 cm s^{-1}. Table 4.6 gives the electron transfer coefficients (α) and rate of electron transfer (k_s). From the two different Laviron plots (Figure 4.27a and 4.27b), symmetrically of the anodic curve to the cathodic curve over $E_{pa/pc}$ - E_{mid} *vs* log v and E_{pa}/E_{pc} vs log v were obtained. Therefore, it can be confirmed that the transfer coefficients for anodic and cathodic reactions are α_a, α_c = ~0.5[61].

Table 4.6; Electron transfer coefficients (α) and rate of electron transfer (k_s) for covalently immobilised AQ at the surface of GC electrode, attached through the mono-EDA linker.

AQ modified GC electrode	Transfer coefficient for anodic (α_a)	Transfer coefficient for cathodic (α_c)	Rate of electron transfer (k_s) / s^{-1}
Covalently immobilised AQ	0.505 ± 0.032	0.495 ± 0.025	2.83 ± 0.45

To obtain a better estimate of k_s, three different non-linear plots (Figures 4.27b, c, d) were fitted to the Laviron theoretical plot using the working curve for α = 0.5. Clearly, the fitted plots give a satisfactory fit. The estimated value of k_s from this work is 2.83 s^{-1}. It is noticeable that the estimated k_s in this present work is fairly close to the k_s that was reported by Ghanem *et al.*[55] for the same system was 2.36 s^{-1}.

As clearly observed in Figure 4.27a, the plot of overpotential vs log v at low scan rates, shows that non-zero overpotentials around 35 mV were obtained. This deviates from the ideal Laviron behaviour where the overpotential at low scan rates should go to zero. However, this type of deviations from ideal Laviron behaviour is common in the literature and it is attributed to surface morphology defects, nonideal packing of attached redox probes, rough surfaces or the lateral interaction of redox probes[148]. We believe that the residual peak separation of our data are from Nernstian behaviour mostly due to the lateral interaction of AQ-EDA, defect sites of immobilised AQ-EDA at the surface of GC electrode and nonideal orientation of immobilised AQ as displayed in Figure 4.28. We will return to them when we present our data for a self-assembled monolayer of DNA labelled with AQ at gold electrode surfaces with mercaptohexanol treatment in Chapter 7.

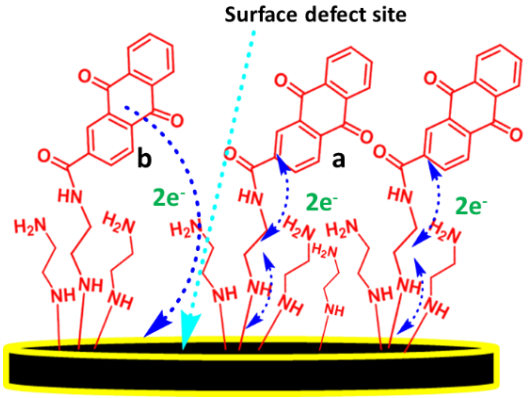

Figure 4.28; Two possibilities for the electrons transfer pathways for AQ covalently immobilised through the EDA linker. a) Electron transfers pathway by hoping mechanism through the EDA linkers. b) Electron transfer pathway by single tunneling mechanism directly to the surface defect site.

4.15 Chronoamperometry at AQ modified GC electrodes

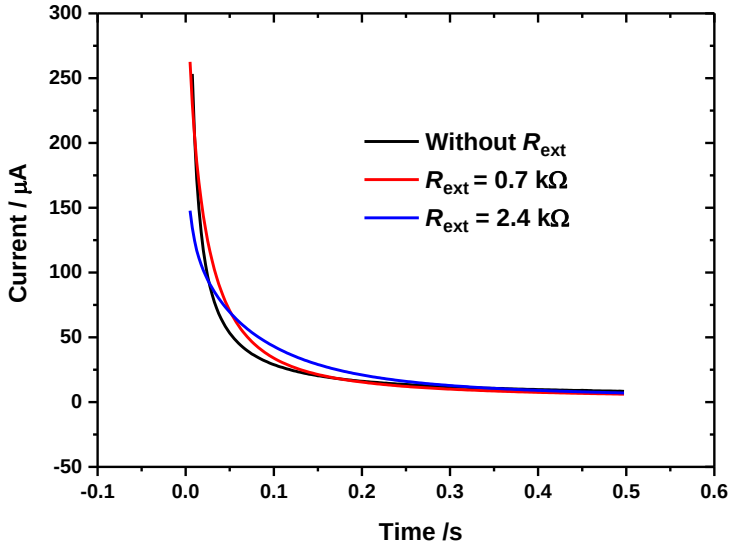

Figure 4.29; Current-time curves for AQ modified GC electrode for three different values of R_{ext} using chronoamperometry by stepping the potential from -0.8 to -0.15 V *vs* SCE for 0.5 s. The time used here is similar to the interval time for DPV. The measurements were carried out in 0.1 M phosphate buffer, pH 7 the electrode area is 0.071 cm^2.

Chronoamperometry for the AQ modified GC electrode was recorded for 3 different R_{ext} values for the covalently attached AQ, Figure 4.29. R_{ext} of 0.7 kΩ corresponds to the maximum DPV peak current condition. In order to obtain the *RC* time constant and rate of electron transfer (k_s), a plot of ln *i* vs *t* was made for each R_{ext} value.

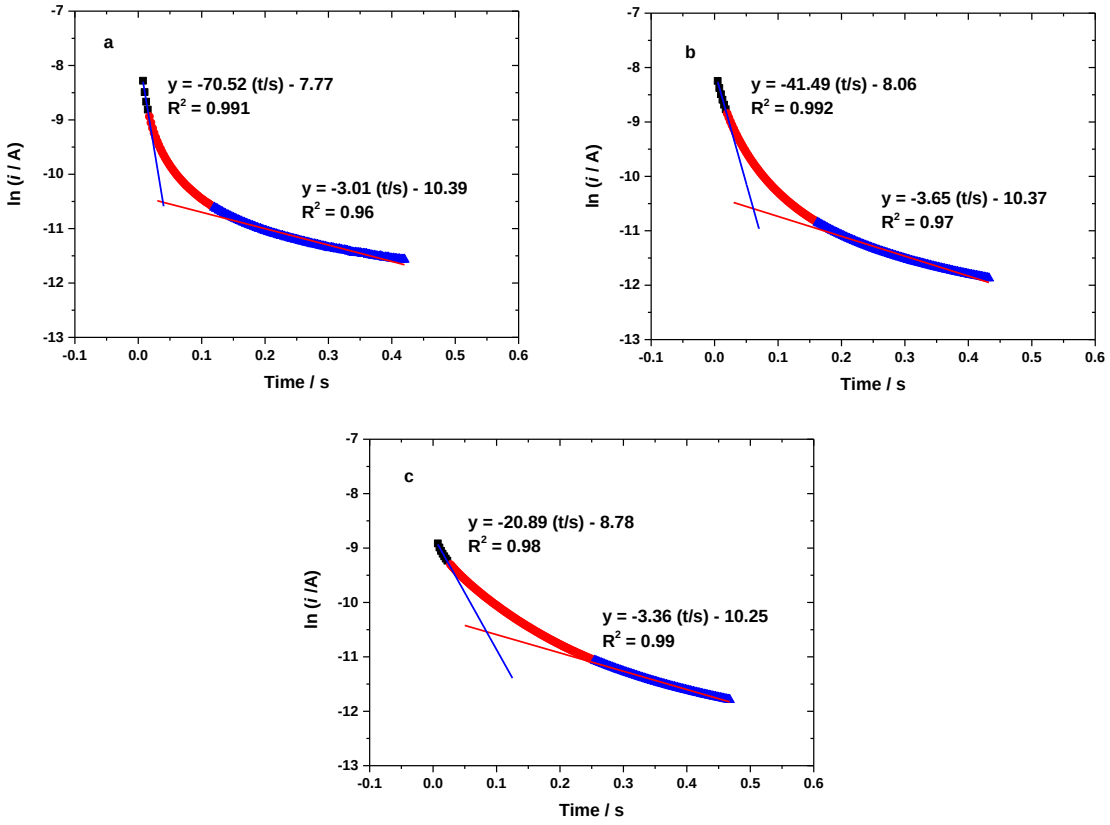

Figure 4.30; Based on Figure 4.29, semilog plots of ln *i vs t* for 3 different magnitudes of R_{ext}. a) R_{ext} = 0 b) R_{ext} = 0.7 kΩ, and c) R_{ext} = 2.4 kΩ.

Figure 4.30 shows the three plots of ln *i* vs *t* for the different values of R_{ext}. A similar approach as previously used in Section 3.12 was used for this analysis. From the graph of ln *i* vs *t* for each value of R_{ext} to get two linear best fits were obtained. Then, using Equations 3.9 and 3.10 as shown in Chapter 3 (Section 3.12), the *RC* time constant and k_s were determined[127]. The calculated *RC* and k_s values are given in Table 4.7. Comparing the value of k_s determined at the different magnitudes of R_{ext} from chronoamperometry to the Laviron method (k_s = 2.83 s^{-1} ± 0.45), we find good agreement.

Table 4.7; *RC* time constant and rate of electron transfer (k_s) obtained from two different linear fits over a plot of ln *i* vs *t*. The *RC* time constant calculated from a slope of linear best fit at short times. By contrast, the k_s was directly determined by a slope of linear best fit at long times.

R_{ext} added in the cell circuit / kΩ	Time constant (*RC*) /s	Rate of electron transfer (k_s) / s^{-1}
$R_{ext} = 0$	0.014 ± 0.001	3.59 ± 0.38
0.7 kΩ	0.026 ± 0.003	3.98 ± 0.31
2.4 kΩ	0.05 ± 0.002	3.28 ± 0.16

Similar trends for the *RC* time constant and k_s are seen here as in for adsorbed 9,10-PQ in Chapter 3. Based on Table 4.7, the estimated *RC* time clearly increases when the magnitude of the R_{ext} is increased. Secondly, the value of k_s determines at R_{ext} of 0.7 kΩ is slightly higher than the determined k_s before adding R_{ext}. As previously mentioned in Section 3.12, this is because the increase in *RC* time may provide a sufficient time scale of an experiment for all redox centres of AQ to undergo rapid-exchange electrons with the electrode surface. Conversely, the determined k_s at R_{ext} of 2.4 kΩ decreased. This is because too large time scale of the experiment may trigger the ohmic drop effect on electrode kinetic as indicated in Equation 4.3[142,143] and depicted in Figure 4.18.

4.15 Kinetics for the control electrodes

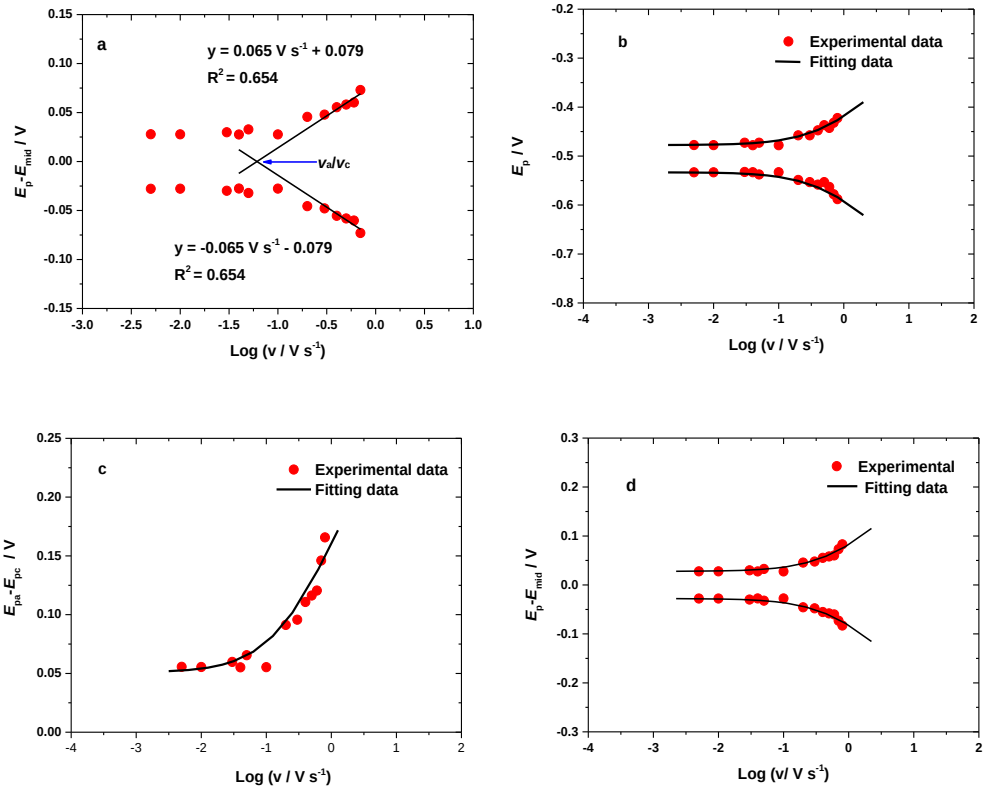

Figure 4.31; a) Laviron plots for experimental data for the variation of $E_{pa/pc}$-E_{mid} (overpotential) *vs* the logarithm of the scan rate (v) and the linear fits over the anodic and cathodic branches in order to determine the experimental α and k_s values. b) Plots show the influence of cyclic voltammetry scan rates on peak potentials oxidation and reduction (filled cycles) for control electrode at various scan rates (0.005 to 1.0 V s^{-1}), the theoretical (solid lines) were obtained from the best fitting to the Laviron theoretical plot using the working curve for α = 0.5. c) Plot of experimental data and Laviron theory based on working curve for α = 0.5 for the peak separation (E_{peak}). d) The best fits for experimental data of $E_{pa/pc}$ - E_{mid} (overpotential) to the Laviron theory employing α = 0.5 for anodic and cathodic curves respectively.

The kinetics of the redox reaction for AQ on control GC electrode were also investigated. It is important to note that the control electrode was obtained by immersing the modified GC electrode with free immobilised EDA for 16 hours in AQ solution without the coupling reagents (NHS and EDC). The control electrode was then washed for three days in DMF. However, the measured CV still shows some oxidation and reduction currents for AQ, but much less than for the covalently immobilised AQ. As we previously shown for the calculated $\Gamma_{cv,}$ AQ for control electrode was found to be 56.4 pmol cm^{-2}. Performing the same analysis using the Laviron procedures, the results for the kinetics of electron transfer between the control electrode were also obtained as shown in Figures 4.31a, b, c, and d. Again, using Equations 3.2, 3.3, 3.4 and 3.5, α_a, α_c and k_s were found to be 0.54 ± 0.007, 0.46 ± 0.007 and 2.25 ± 0.08 s^{-1}, respectively. It is interesting to note that the value k_s for the control electrode was lower than the determined k_s for covalently

coupled AQ (2.83 s^{-1}). As we previously mentioned in Section 4.5, there are two ways for AQ to attach to the surface of the GC electrode. Firstly, the AQ molecules can be directly adsorbed to the surface of GC electrode. Secondly, because we left the control electrode for 16-h in AQ solution, the AQ molecules may react with free EDA by in uncatalysed organic reactions.

4.16 Chronoamperometry for control electrodes

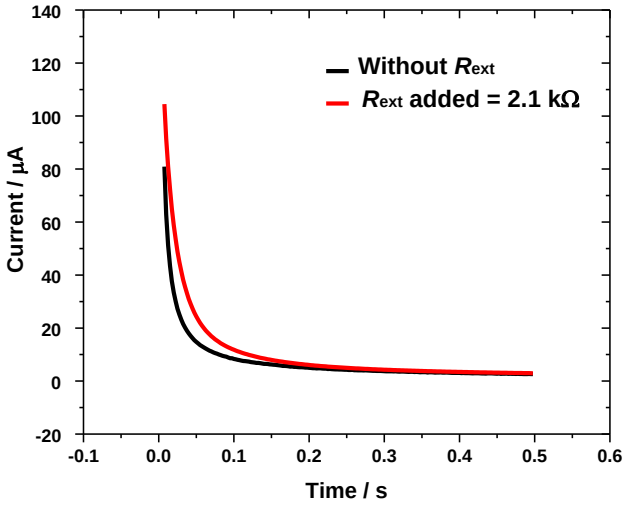

Figure 4.32; Current-time curves for the control electrode at two different magnitudes of R_{ext} for potential step from -0.8 to -0.15 V vs SCE. The time used here is similar to the interval time of DPV. The measurements were carried out in 0.1 M phosphate buffer, pH 7 and the electrode area is 0.071 cm^2.

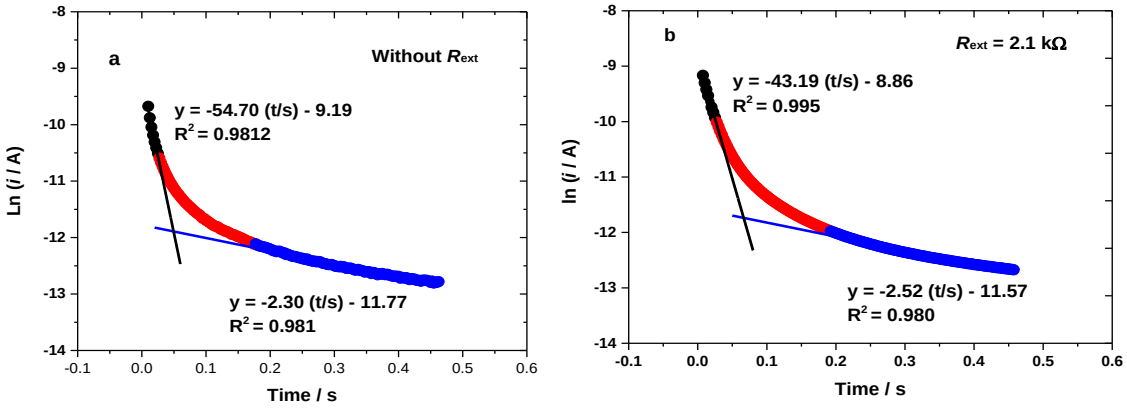

Figure 4.33; Based on Figure 4.32, semilog plots of ln *i vs t* for *RC* time constant and rate of electron transfer (k_s). a) Before adding R_{ext} and b) R_{ext} = 2.1 kΩ.

In order to confirm the k_s from Laviron analysing, the chronoamperometry measurements were also performed for control electrode at two different R_{ext} conditions. The chrononoamperograms at R_{ext} of 2.1 kΩ and without R_{ext} can been seen in Figure 4.32. Chronoamperometry at R_{ext} = 2.1 kΩ was measured because it corresponds to the maximum DPV peak current (Figure 4.16). By plotting ln *i* vs *t* (Figures 4.33a, and b), the two best linear fits were obtained for each plot. Performing the same calculations using Equations 3.9 and 3.10, from each slope, the *RC* time constant and k_s were determined. The results are given Table 4.8. Clearly, the values for k_s determined here agree well with that estimated using the Laviron formalism (k_s = 2.25 s^{-1}).

Table 4.8; *RC* time constant and rate of electron transfer (k_s) obtained by two different linear fits over a plot of ln *i* vs *t*. The *RC* time constant was calculated from a slope of linear best fit at short times. k_s was directly determined from the slope of linear best fit at long times.

Magnitude of R_{ext} added / kΩ	Time constant (*RC*) /s	Rate of electron transfer (k_s) / s^{-1}
R_{ext} = 0	0.019 ± 0.001	2.46 ± 0.15
R_{ext} = 2.1 kΩ	0.023 ± 0.002	2.60 ± 0.08

4.17 Impedance measurements for R_t and C_{dl}

In order to verify our experimental model for estimating the DPV surface coverages using our developed DPV simulation, we have attempted to measure the uncompensated solution resistance (R_u) before and after adding an external resistor (R_u + R_{ext} = R_t) to the DPV cell circuit. Electrochemical impedance spectroscopy (EIS) had been utilised in these measurements. In addition, the double layer capacitance (C_{dl}) at two different potentials (-0.70 and -0.25 V vs SCE) was measured; at these potentials that is negligible contribution from the oxidation and reduction of the AQ. The values of R_u, R_t, and C_{dl} obtained in this work can then be used as simulation variables in our DPV simulation.

In this measurement, we assumed a simple equivalent circuit where resistance and capacitance are connected in series as illustrated in Figure 4.34.

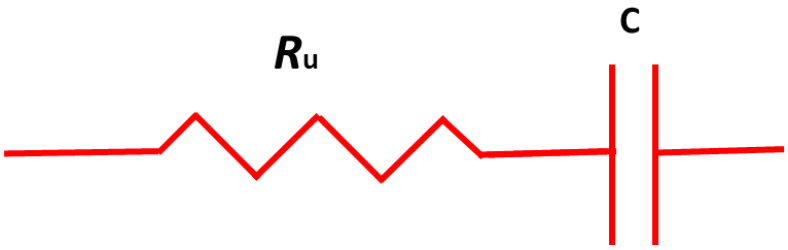

Figure 4.34; Simple equivalent circuit (*RC*) for non-faradaic impedance in measuring resistance solution of the electrochemical cell (R_u) and double layer capacitance of modified electrodes (C_{dl}).

From the plot of DPV peak currents vs R_{ext} for covalently attached AQ (Figure 4.15), an R_{ext} of 0.7 kΩ gave the maximum DPV peak current for the AQ modified GC electrode. In addition, the DPV peak area at R_{ext} = 0.7 kΩ was integrated in order to estimate Γ_{DPV}.

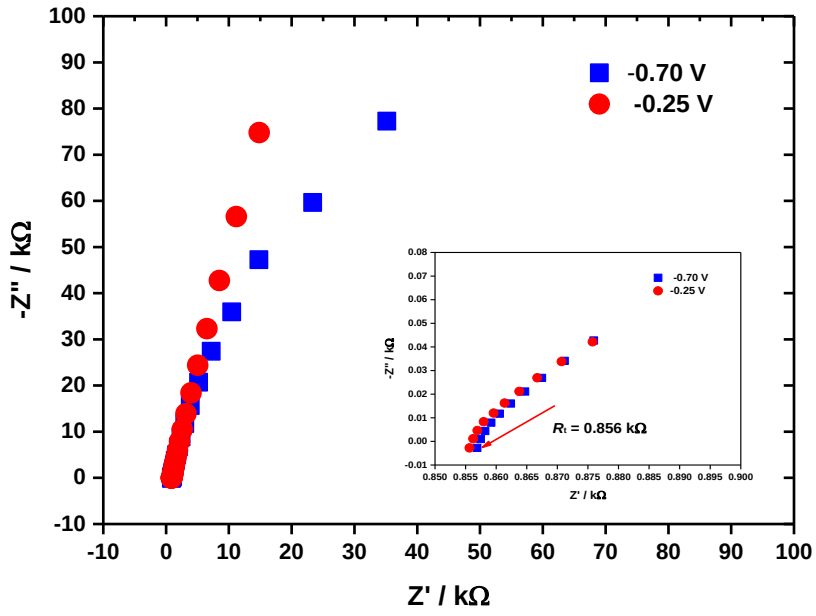

Figure 4.35; Nyquist plots for covalently attached AQ at two different potentials (-0.70 V and -0.25 V vs SCE). The inset figure shows the enlargement of the Nyquist plot in order to show the presence of the total uncompensated resistance (R_t) in the electrochemical cell (R_u + R_{ext} of 0.7 kΩ). The measurements were made on a frequency range from 100 kHz to 0.1 Hz, using 45 frequency and a modulation amplitude of 5 mV in 0.1 M pH phosphate buffer solution.

Figure 4.35 shows the Nyquist plots for the imaginary part of impedance (-Z") as a function of its real component (Z') over the frequency range from 100 kHz to 0.1 Hz. The inset shows the R_u + R_{ext} = R_t value that can directly be determined from the Nyquist plots. From three different data, the average of the R_u +R_{ext} was found to be 0.856 kΩ. The frequency in Figure 4.35 increase top right to bottom. Based on the Nyquist plot, in the presence of AQ film at the surface of the

electrode, the resistance and capacitance are nonuniformly distributed at the surface of GC electrodes.

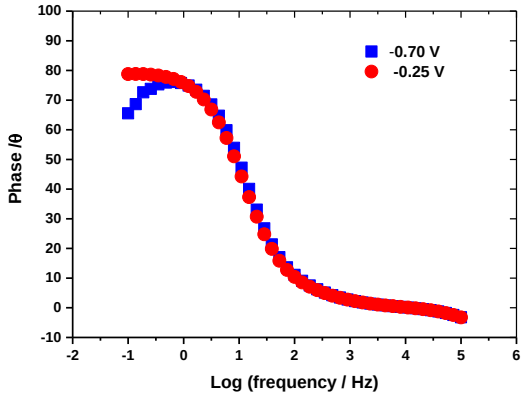

Figure 4.36; Bode plots at two different potentials. These plots were used to differentiate three distinct frequency regions (high, medium and low) in order to determine the C_{dl}. The measurements were made at a frequencies range from 100 kHz to 0.1 Hz, number of frequency = 45 and a modulation amplitude of 5 mV in 0.1 M pH phosphate buffer solution.

Figure 4.36 shows the Bode plots at two different measured potentials and the behaviours of the total uncompensated resistance (R_t) and capacitance (C_{dl}) is clearly shown. The Bode plot is important as it can determine the frequency region of the C_{dl} behaviour because it can give us three different frequency regions. In the high-frequency region, the real impedance (Z') is independent of frequency with the phase angle values near to or at 0. This behaviour contributes to the resistance of the phosphate buffer solution between the working and the reference electrodes. By contrast, in the medium frequency region, a linear relationship can be clearly observed. This region corresponds to the double layer capacitance behaviour of modified electrode/electrolyte interface. Furthermore, a third region can be observed at low-frequency range, where the phase angle reaches a maximum number. Subsequently, it starts to decrease and this parallels to the accumulation of ions at the surface of electrode[149–151].

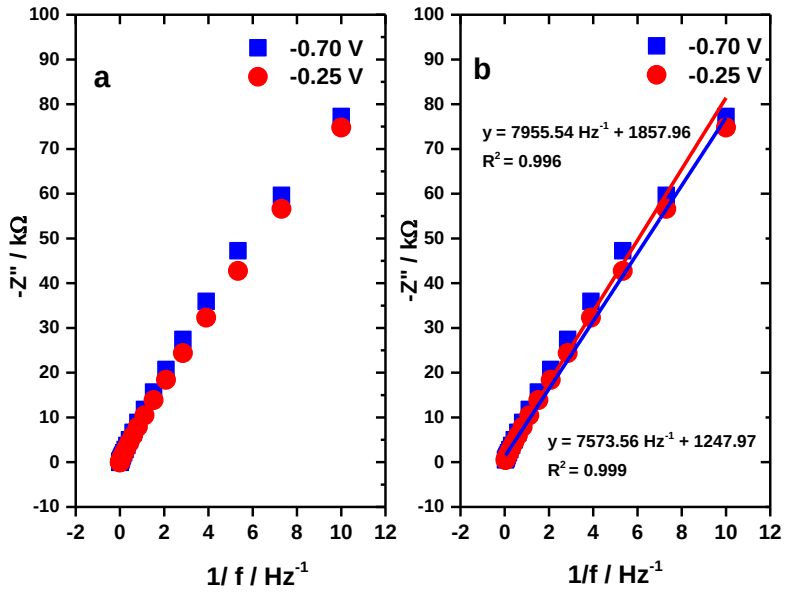

Figure 4.37; a) Plots of imaginary impedance (-Z") *vs* 1/ frequency. b) The best linear fits obtained from the low frequency range over plots of –Z" vs 1/f. The C_{dl} can be calculated from the slope of the linear fitting where m = $1/2\pi C_{dl}$.

We can determine the behaviour of the double layer capacitance for the AQ modified GC electrodes in the low and medium frequency regions by analysing the Bode plots, the C_{dl} for the modified electrode at two different measured potentials (-0.70 V and -0.25 V) vs SCE can be estimated by plotting the imaginary component (-Z") versus 1/ frequency (Figure 4.37a). We then calculate C_{dl} by taking the best fit for the straight lines in the two different frequency regions (low and medium) as shown in Figure 4.37b. A range of frequencies from 0.1 to 21.21 Hz was chosen in order to gain the best linear fit for the plots of -Z" *vs* 1/f. The reason to have the best fits in the range frequencies from 0.1 Hz to 21.21 Hz is because a modulation time (τ_p) of 50 ms was employed in the DPV measurement. Hence, the modulation time of 50 ms may correspond to a frequency of DPV (1/0.05 s) = 20 Hz. The slope of the straight lines is represented in Equation 4.16.

$$-Z'' = R - \frac{j}{2\pi C_{dl}} \qquad \textbf{Eq. 4.16}$$

Where –Z" is an imaginary component, *R* is resistance at high frequency (*Z'* = *R*), *j* is √-1 and C_{dl} is double layer capacitance. C_{dl} for the two measured potentials at -0.70 V and -0.25 V *vs* SCE were found to be 20.0 µF and 21.02 µF, respectively.

Table 4.9; Total uncompensated resistance in the electrochemical cell (R_t) and double layer capacitance (C_{dl}) for two different measured potentials (-0.70 V and -0.25 V) at three different R_{ext} conditions made on the AQ modified GC electrode using EIS.

Magnitude of R_{ext} added /Ω	Total uncompensated resistance in electrochemical cell (R_t) / Ω	C_{dl} measured at -0.70 v vs SCE / µF	C_{dl} measured at -0.25 v vs SCE / µF
Without R_{ext}	149 ± 6.0	19.85 ± 0.36	21.23 ± 0.13
R_{ext} = 700	852 ± 5.5	19.90 ± 0.05	21.91 ± 0.89
R_{ext} = 1600	1753 ± 5.0	19.64 ± 0.60	22.07 ± 1.17

In addition, performing the same analysis on the AQ modified GC electrode with R_{ext} of 1.6 kΩ and without external R_{ext}, the R_t and the C_{dl} was also extracted, as presented in Table 4.9. As shown in that table, the calculated data trends for the C_{dl} at R_{ext} of 1.6 kΩ and without R_{ext} are constant. The errors were calculated based on three different AQ modified GC electrodes.

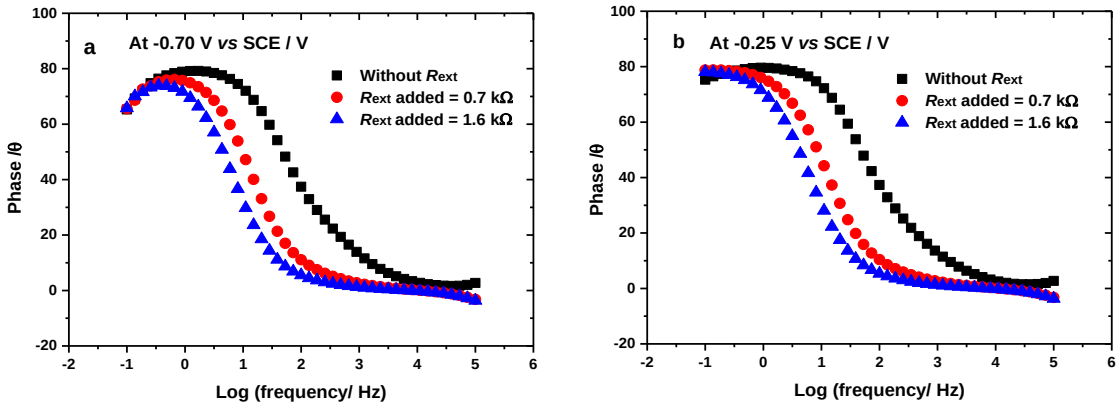

Figure 4.38; Bode plots at three different R_{ext} conditions. a) The measured potential -0.70 V b) Measured potential at -0.25 V.

However, as displayed in the Bode plots at three different conditions of R_{ext} (Figure 4.38), the phase angle for each magnitude of R_{ext} decreased. This was because, with the increasing of the magnitude of R_{ext} in the impedance circuit, the *RC* time increased[151], suggesting that the penetration and accumulation of electrolyte ions to the electrode surface during double-layer charging/discharging are more impeded with the increasing magnitudes of R_{ext} in the electrochemical cell. This can clearly be seen by significantly shifting the medium frequency region (black to red) to lower frequencies when a R_{ext} of 0.7 kΩ is added. In addition, the

maximum value of the phase angle for each R_{ext} condition (0.7 kΩ and 1.6 kΩ) was also shifted to lower frequency. Although the *RC* time increased with increasing magnitude of R_{ext} in the EIS circuit, the calculated C_{dl} using Eq. 4.16 gave constant C_{dl} values for both potentials, as shown in Table 4.9. Hence, based on the EIS measurements, the magnitude of double layer capacitance is largely insensitive to added R_{ext}.

This behaviour has been predicted. According to a paper by Marcio and co-workers[152], decreasing the time constant by decreasing R_u can be distinguished by the Bode plots. In their theoretical study on the SAM-modified electrode, the decreasing magnitudes of R_u did not change the capacitance values. This is because the polar properties of surface modified electrode are constant despite the increased time constant.

Performing a similar analysis for the control electrode (see Appendix 4.5), the R_t and C_{dl} at R_{ext} of 2.1 kΩ were also obtained. The value of R_{ext} of 2.1 kΩ was selected because, based on Figure 4.16, when R_{ext} of 2.1 kΩ was added in the DPV cell circuit, the maximum DPV current for the control electrode was obtained. From the Nyquist plots, R_t was directly found to be 2.26 kΩ. Again, using Equation 4.16, C_{dl} for control electrode at potentials of -0.70 V and -0.25 V can be calculated and were found to be 7.89 ± 0.5 and 9.22 ± 0.2 μF, respectively (Table 4.10). The data were obtained from three different control electrodes. Those values were used in the DPV simulation.

Table 4.10; Total uncompensated resistance in an electrochemical cell (R_t) and double layer capacitance (C_{dl}) from EIS for two different measured potentials (-0.70 and -0.25 V) at R_{ext} added of 2.1 kΩ for the control electrodes.

Potential vs SCE / V	R_t in electrochemical cell / kΩ	C_{dl} for control electrode at R_{ext} added = 2.1 kΩ / μF
-0.70	2.26 ± 0.014	7.89 ± 0.5
-0.25	2.27 ± 0.017	9.22 ± 0.2

In order to evaluate our potentialstat and external resistor box performance, we constructed a dummy cell from resistor and capacitor components to mimic the real electrochemical system at the electrode/electrolyte interface. The constructed dummy cell and the equivalent circuit can be seen in Figure 4.39. The values of resistance and capacitance were chosen to mimic the experimental value. Two different capacitance values (18 ± 3 μF and 20 ± 3 μF) were used. Based on the Nyquist plots, fitting the impedance to the *RC* equivalent circuit in FRA software, the fitted resistance and capacitance values were obtained and compared with the nominal values. The results obtained can be seen in Appendix 4.1 to 4.4.

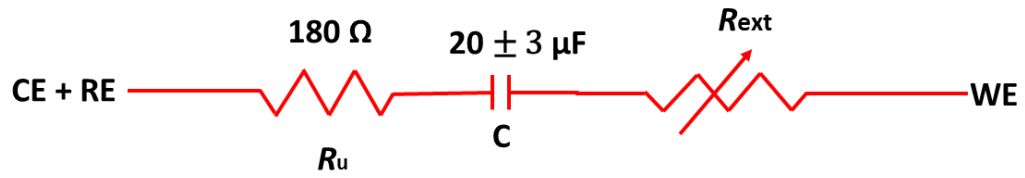

Figure 4.39; *RC* equivalent circuit for the dummy cell connected to three different terminals (counter, reference and working electrodes) and a resistor box.

4.18 Numerical modelling of the DPV response

One of the main objectives of this study was to compare the theoretical DPV response to the experimental DPV. In this section, we use a specially developed DPV simulation program based on numerical algorithms in MATLAB. The DPV simulation was carried out using the explicit finite difference (EFD) approximation using codes written by Dr. Guy Denuault. The script codes for the DPV simulation program can be found in Appendix 4.6. The DPV simulation program went through two stages of development in order to improve the fit to the experimental DPV. The underlying assumptions in the model are;

i) The modified electrode surface is assumed to be covered by a fixed quantity of redox sites.
ii) The double layer charging is described by a simple series *RC* circuit.
iii) The forward and reverse rate constants for the Faradaic reactions are described by the Butler-Volmer kinetics.
iv) At the start of the scan, the surface layer is assumed to be all in the reduced form.
v) The redox sites are considered to be non-interacting and any non-ideal interactions between immobilised redox molecules are ignored.

For the preliminary study, we performed simulations of the experimental DPVs for AQ covalently immobilised through the EDA-linker at the GC electrode surface. Each simulation takes a few minutes to run on Dell computer. The $\Gamma_{DPV,\ exp}$ values obtained from the experiments using our peak integration method were compared with the $\Gamma_{DPV,\ exp}$ values from the best fits of the simulations.

DPV simulations were carried out for a range of values of the simulation parameters such as the redox potential ($E°$), electrode kinetics (k_s and α), total uncompensated solution resistance ($R_u + R_{ext} = R_t$), double layer capacitance (C_{dl}) and the surface coverages from simulation ($\Gamma_{DPV,\ sim}$). The simulated DPVs will be compared to the experimental results and the fit optimised by manually adjusted model parameters.

4.19 DPV Simulation Procedures

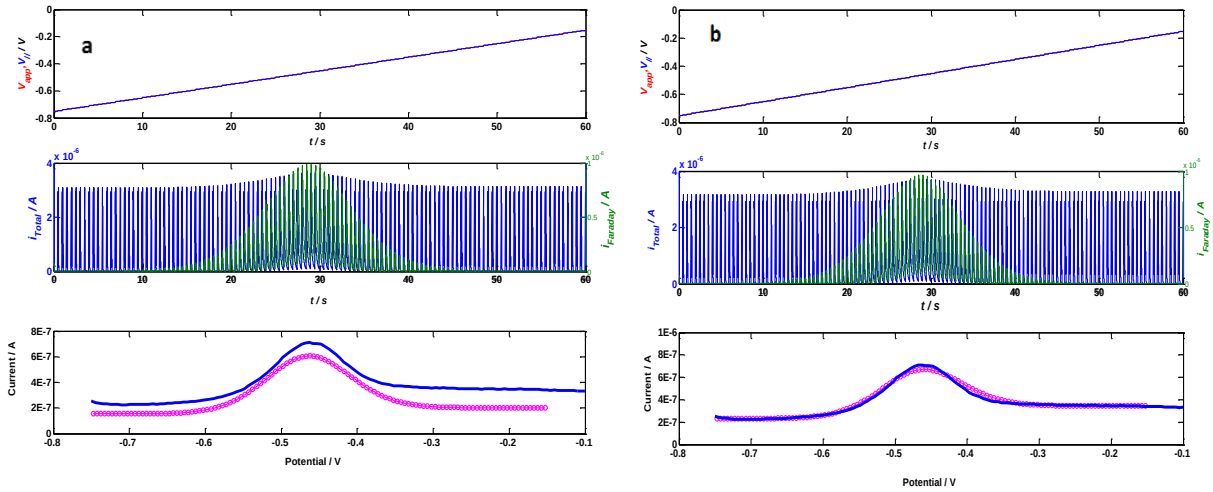

Figure 4.40; DPV simulation data from MATLAB program where the data contributed by three different panels; First panel shows the array of DPV waveforms for 120 periods from potential -0.75 V to -0.15 V. Second panels is current transients for Faradaic and total currents. a) The simulated data from the first step of the simulation procedure, by setting the input parameters that were extracted from the experiments. b) The simulated data from the second step of simulation procedure, by adjusting the parameter values of C_{dl}.

The first step of simulation was done by setting all the parameter values that were extracted from the experiments (R_t, k_s, α, C_{dl} and $\Gamma_{DPV, exp}$). $E°$ is directly extracted from the experimental DPV peak current. k_s values were obtained from CV and chronoamperometry experiments. Both the k_s values were employed in order to get the best simulated DPV current to the experimental DPV. In contrast, α was only obtained from the CV. R_t and C_{dl} were obtained from the EIS measurements. Then, the result as shown in Figure 4.40a was obtained as the output of the simulation. Figure 4.40 shows the DPV simulation results that consist three panels. The first panel displays the generated DPV waveforms at the applied potentials with times for 120 periods of the DPV pulses. In contrast, the second panel shows the total and Faradaic current transients for 120 periods of the DPV pulses. The third panel shows the comparison of the simulated DPV current to the experimental DPV current. If the simulated DPV is not sufficiently fit to the experimental DPV (Figure 4.40a), the parameters of C_{dl} were adjusted until the best fit of capacitive current was gained as displayed in Figure 4.40b.

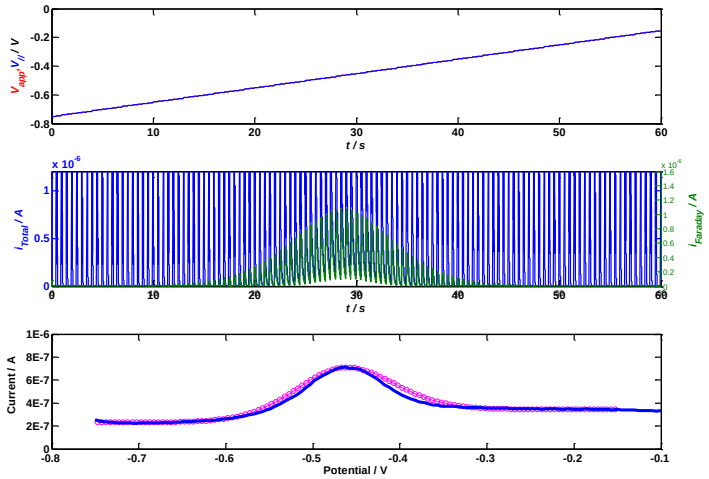

Figure 4.41; The simulated data from the third step of simulation procedure, by adjusting the parameter values of k_s and Γ_{DPV}.

The third step was made by adjusting the k_s experimental value within ± 10%. Subsequently, the final step was performed by forcing the $\Gamma_{DPV, sim}$ value until the best DPV fit was gained as shown in Figure 4.41. Essentially, the third and fourth steps were performed together in order to gain the best DPV fit. The procedures mentioned above were followed for all DPV simulations

4.20 Initial DPV simulation model assuming constant C_{dl}

For the initial DPV simulations, the double layer capacitance (C_{dl}) was estimated from the capacitive current from the CV. The value for C_{dl} determined from CV at a scan rate of 50 mV/s was 16.2 µF and an initial guess was made for the R_t value. Following the procedures described from the previous section, the simulated DPV (pink) shown in Figure 4.42 was obtained.

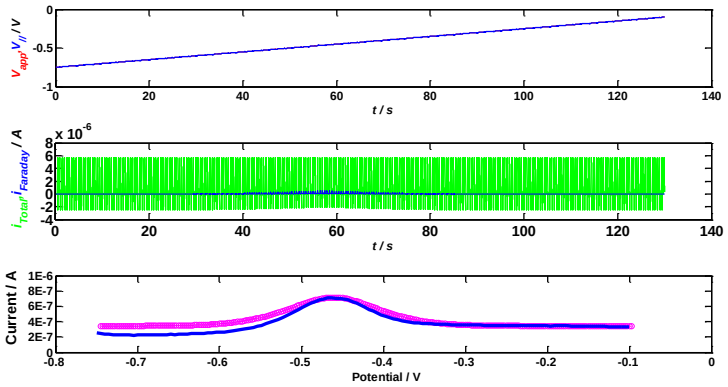

Figure 4.42; DPV simulation data from MATLAB. The first panel shows the DPV waveform for 240 periods from -0.75 V to -0.15 V. The second panel shows the transient currents for 240 periods. The third panel is a comparison of experimental DPV and simulated DPV. The blue curve is the experimental DPV. The pink curve is the best simulated DPV obtained by setting the kinetic rate constant (k_s) = 3.8 s^{-1}, R_u = 0.88 kΩ, transfer coefficient (α) = 0.50, C_{dl} = 16.2 µF and DPV surface coverage ($\Gamma_{DPV, sim}$) = 355 pmol cm^{-2}.

As can be seen in Figure 4.42 the agreement between the simulated DPV and the experimental DPV, in particular on capacitive current from the immobilised AQ layer in the reduced form is poor. In contrast, good agreement is obtained for the capacitive current from the immobilised AQ layer in the oxidised form. This can be observed by a sloping baseline on the experimental DPV for immobilised AQ. It is a common behaviour for electrochemistry quinones where the redox reactions involve accepting and releasing hydrogen ions at different potentials through the monolayer film. Thus, it is unlikely for the electrochemistry of AQ to have a constant double layer capacitance as shown in the pink curve, since the redox reaction of AQ film involves the formation of the reduced form, hydroquinone (AQH_2), and oxidised form, quinone (AQ). To improve this, the second DPV simulation was modified to taking into account the possibility of different C_{dl} for the oxidised and reduced films. In the next section, the DPV simulation data obtained after implementing this improvement are demonstrated.

4.21 DPV Simulation with sigmoidal dependence of C_{dl} on potential

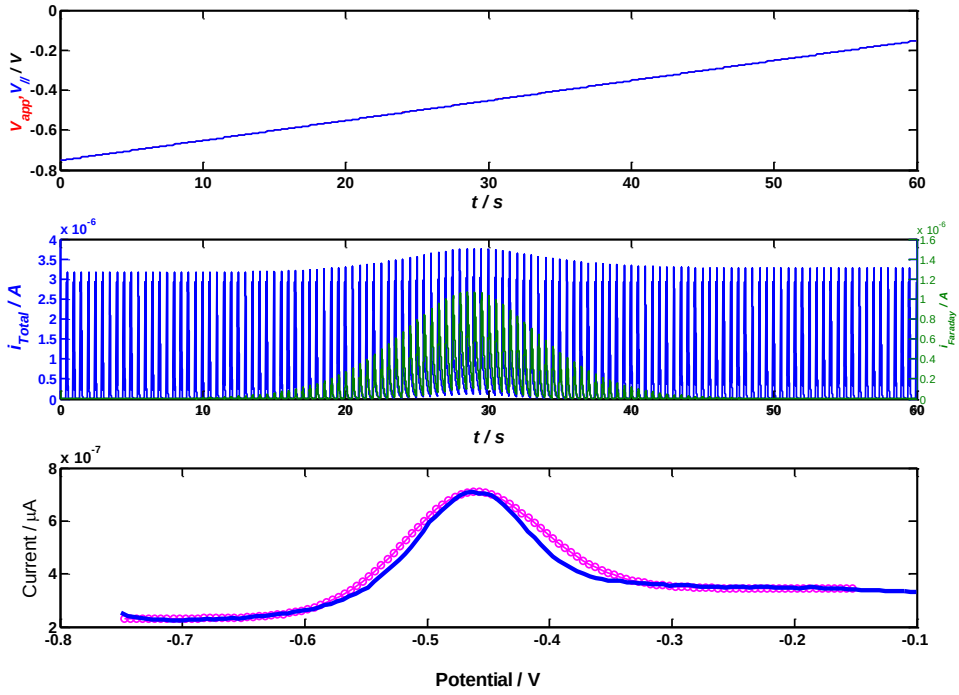

Figure 4.43; Typical DPV simulation data from MATLAB. The first panel shows the array of DPV waveforms for 120 periods from -0.75 V to -0.15 V. The second panel shows the transient currents for 120 periods. The third panel is a comparison of experimental DPV and simulated DPV. This simulated data (pink) is obatained from the third step of the simulation procedure, by adjusting the parameter values of k_s and $\Gamma_{DPV,\ sim}$.

In this section, we compare the experimental DPV results for covalently immobilised AQ with our DPV simulation after implementing different C_{dl} values for the oxidised and reduced forms.

The main interest is to verify the $\Gamma_{DPV,\,exp}$, calculated from Eq. 4.14 and to extract the $\Gamma_{DPV,\,sim}$ for attached AQ through the DPV simulation. In addition, the reliability and errors associated with the parameters determined from the various experiments such as k_s, α, R_u, R_t and C_{dl} can also be shown. Full procedure details explaining how we performed the DPV simulation have been given in Section 4.19.

Looking back at the plot for DPV peak current vs R_{ext} (Figure 4.15) for covalently immobilised AQ, adding R_{ext} of 0.7 kΩ gave the maximum DPV peak current. In addition, the DPV peak at R_{ext} added of 0.7 kΩ was used to integrate the area under DPV peak in order to obtain the DPV charge. Then, by using Eq. 4.14, the $\Gamma_{DPV,\,exp}$ was calculated. The DPV peak at this R_{ext} value was then chosen for the modelling. Figure 4.44a and b show the simulations using the experimentally determined values in the DPV simulation for the two different cases. The simulated DPV current shown in Figure 4.44a was obtained by using the $\Gamma_{DPV,\,exp}$ value that was calculated from Eq. 4.14. Meanwhile, Figure 4.44b shows the simulated DPV current by setting the Γ_{CV} value.

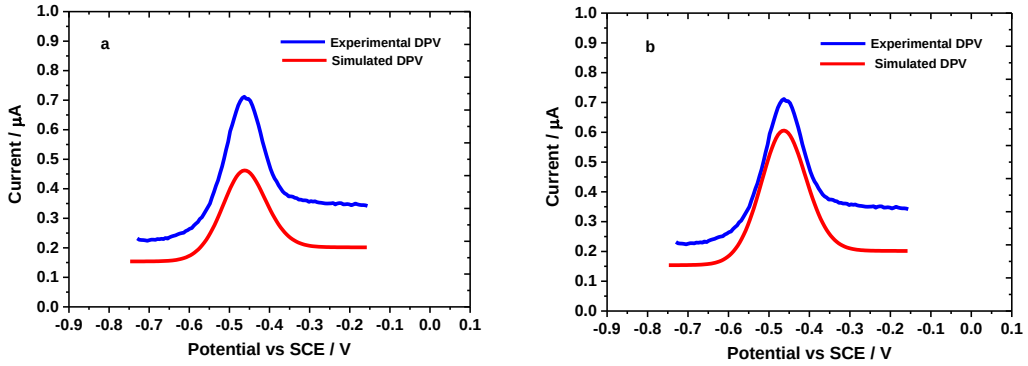

Figure 4.44; Experimental DPVs (blue) and simulated DPVs (red) at R_{ext} added of 0.7 kΩ. a) Simulated DPV obtained by setting $\Gamma_{DPV,\,exp}$ of 198 pmol cm^{-2}, calculated from Eq. 4.14. b) Simulated DPV obtained by setting $\Gamma_{CV,\,exp}$ of 320 pmol cm^{-2}. Other simulation conditions are k_s = 3.97 s^{-1}, R_t = 0.853 kΩ, transfer coefficient α = 0.50, C_{dl} for reduced layer = 19.90 µF, and C_{dl} for oxidised layer = 21.91 µF. The R_t of 0.853 kΩ was directly determined from the Nyquist impedimetric plots.

By performing the second step in fitting the simulation in which the C_{dl} values for the reduced and oxidised layer were adjusted for the two cases, the results shown in Figure 4.45a and b were obtained. Clearly, the use of Γ_{CV} value gave close agreement between the simulated current and the experimental DPV current. Based on Figure 4.45a, the simulation data obtained here provides more support for the idea that the calculated $\Gamma_{DPV,\,exp}$ using Eq. 4.14 is an underestimate. Thus, the simulation based on the Γ_{CV} value was carried further.

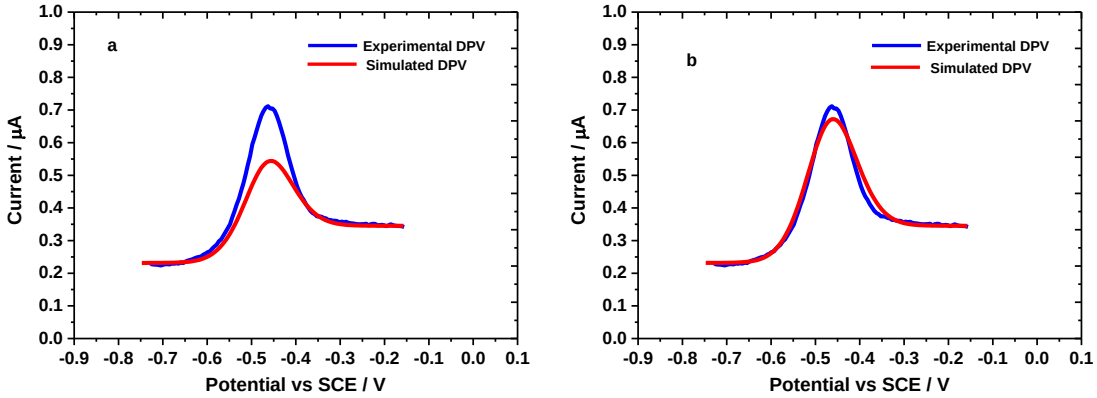

Figure 4.45; a) Simulated DPVs from Figure 4.44a and b, after adjusting the C_{dl} values for the oxidised and reduced layers. a) Simulated DPV obtained by setting $\Gamma_{DPV,\,exp}$ = 198 pmol cm^{-2}, C_{dl} for reduced layer = 23.1 and C_{dl} for oxidised layer = 27.38. b) Simulated DPV obtained by setting $\Gamma_{CV,\,exp}$ = 320 pmol cm^{-2}, C_{dl} for reduced layer = 23.1 and C_{dl} for oxidised layer = 27.38. Other simulation conditions are k_s = 3.97 s^{-1}, R_t = 0.853 kΩ, and transfer coefficient α = 0.50.

In the subsequent steps, by adjusting the k_s and Γ_{CV} values, the best-simulated current to the experimental DPV current was achieved as shown in Figure 4.46. Interestingly, the best $\Gamma_{DPV,\,sim}$ obtained in this simulation was only 12.5% different from the value for Γ_{CV}. It is clear that our simulation model can give a better approximate value to estimate the DPV charge under the DPV peak.

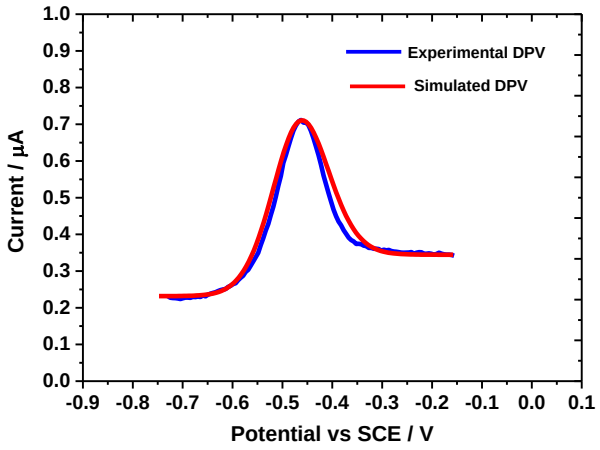

Figure 4.46; Differential pulse voltammograms for the AQ modified GC electrode after adding R_{ext} of 0.7 kΩ corresponding to the maximum DPV peak current. The blue curve is the experimental DPV using ΔE_p = 2.5 mV, τ_p = 0.05 s, τ_i = 0.5 s, ΔE_s = 5 mV and a DPV scan rate at 10 mV s^{-1} in 0.1 M phosphate buffer solution at pH 7. In contrast, the red curve is the best simulated DPV obtained by setting kinetic rate constant (k_s) = 3.97 s^{-1}, R_t = 0.853 kΩ, transfer coefficient (α) = 0.50, C_{dl} for reduced layer = 23.10 µF, C_{dl} for oxidised layer = 27.38 µF and DPV surface coverages (Γ_{DPV}) = 360 pmol cm^{-2}. The R_t of 0.853 kΩ was directly determined from the Nyquist plots. The same DPV parameters entered in the simulation as used in the experimental DPV.

Figure 4.46 shows a comparison of the simulated DPV to the experimental DPV at R_{ext} added of 0.7 kΩ. The best response of the simulated DPV was obtained for a DPV surface coverage of 360 pmol/cm^2. The parameters used in this simulation are given in Table 4.11. It is clear that the experimental DPV gave a reasonable agreement to the theoretical DPV. However, a slight deviation between the experimental and theoretical responses was observed. This is most likely caused by a range of different redox potentials (microenvironments) or a range of rates of electron transfer of individual immobilised AQ. Nevertheless, although we did not consider any non-ideal interactions among immobilised molecules, the simulated DPV current still produced a good fit for covalently immobilised AQ. This suggests that by immobilising AQ through the EDA linker there were less non-ideal interactions between immobilised redox sites.

Table 4.11; Values for MATLAB parameters obtained from the experiments and used in DPV simulation.

MATLAB parameters	Experiment	Simulation
Redox potential ($E°$)	-0.465 V	-0.467 V
Total uncompensated resistance (R_t)	853 Ω	853 Ω
Transfer coefficient (α)	0.50	0.50
Electron transfer coefficient (k_s)	3.98 s^{-1}	3.97 s^{-1}
C_{dl} for reduced surface	20.00 µF	23.10 µF
C_{dl} for oxidised surface	21.90 µF	27.38 µF
$\Gamma_{CV,\ exp}$ vs $\Gamma_{DPV,\ sim}$	320 pmol cm^{-2}	360 pmol cm^{-2}

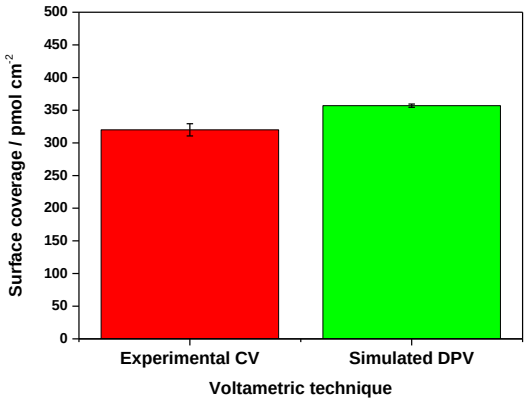

Figure 4.47; Comparison of the DPV surface coverages from experimental calculation (CV) and obtained from the best fit of the DPV simulation to the experimental DPV.

Figure 4.47 shows the comparison of the theoretical Γ_{DPV} and experimental Γ_{CV} of covalently immobilised AQ at the GC electrode surfaces from three replicates modified electrodes. Clearly, the value for Γ_{DPV} obtained from the DPV simulation agrees well with the experimental Γ_{CV}. However, the Γ_{DPV} value is slightly higher than Γ_{CV} with a small error bar. As $\Gamma_{DPV,\ sim}$ obtained

is close to $\Gamma_{CV,\,exp}$, further investigation is needed in order to study the charge by integrating the area under the simulated DPV peak.

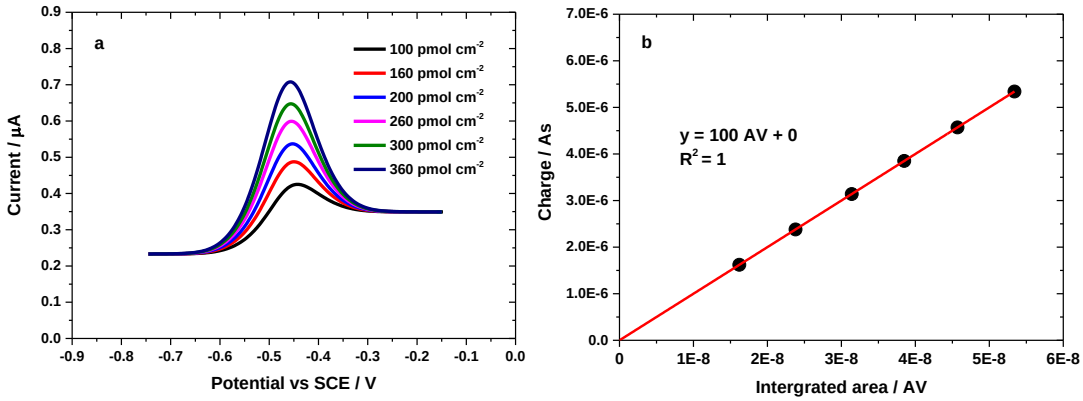

Figure 4.48; a) Simulated DPVs obtained by varying $\Gamma_{DPV,\,sim}$ from 100 to 360 pmol cm^{-2}. b) A linear plot was made by ploting charge vs intergrated area from simulated DPV peaks. Simulation parameters as in Figure 4.46, excluding the $\Gamma_{DPV\,,\,sim}$ values.

As mentioned above, further investigation was carried out by using the simulation model. By varying the surface coverages for $\Gamma_{DPV,\,sim}$ from 100 pmol cm^{-2} to 360 pmol cm^{-2}, the simulated DPVs were obtained as shown in Figure 4.48a. By integrating the area under each simulated DPV peak, the charge from the simulation model was determined. The charge was calculated by dividing the integrated area with a scan rate of DPV. In our experimental design on DPV parameters (Section 4.7), the DPV scan rate of 10 mV/ s was employed. By plotting DPV charge against the integrated area under DPV peak, a straight line with a slope (m) = 100 AV and an intercept = 0 were obtained. Comparing Eq. 4.12, this corresponds to replacing e by a factor of 5. Therefore, a new expression for our approximation method from Eq. 4.12 was obtained.

$$Q_T = \frac{A_{DPV} 5\tau}{\Delta E_1} \qquad \textbf{Eq. 4.17}$$

Where A_{DPV} is the integrated area under DPV peak, τ is the modulation time, and ΔE_1 is the modulation amplitude. Therefore, the final equation for our approximation approach in estimating surface coverages by DPV measurement for covalently immobilised AQ in this work is shown in Equation 4.18.

$$\Gamma_{DPV} = \frac{A_{DPV} 5\tau}{\Delta E_1 nFA} \qquad \textbf{Eq. 4.18}$$

In order to show the application of Eq. 4.18, a comparison of Γ for covalently immobilised AQ by DPV from Eq. 4.14, DPV simulation and Eq. 4.18 is shown in Figure 4.49.

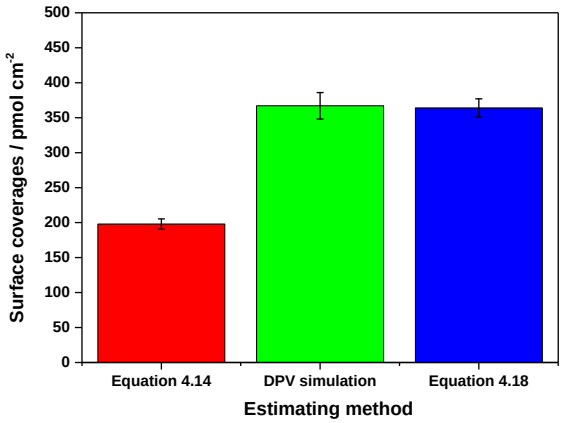

Figure 4.49; Comparison of the estimated surface coverages of the covalently attached AQ by DPV. Red was calculated from Eq. 4.14. Green was extracted from DPV simulation. Blue was calculated from Eq. 4.18.

The error bars in Figure 4.49 are calculated from three different electrodes. Clearly, the value for Γ_{DPV}, extracted from the DPV simulation agrees well with the experimental Γ_{DPV} that has been calculated from Eq. 4.18 rather than Eq. 4.14. Thus, Eq. 4.18 was used for all DPV measurements in this thesis in order to provide an initial estimate the experimental Γ_{DPV} value. For the first attempt, we calculated $\Gamma_{DPV, exp}$ for immobilised AQ using Eq. 4.18 for the control electrodes. The results are shown in Figure 4.50.

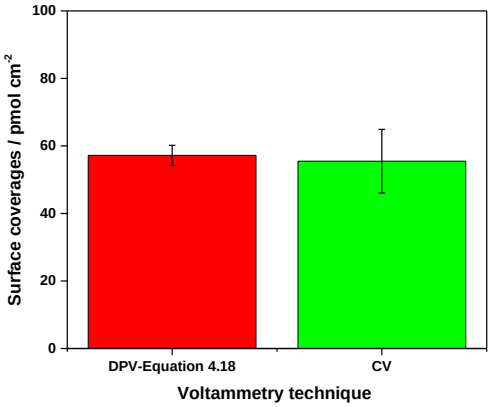

Figure 4.50; Comparison of the estimated surface coverages of attached AQ from the control electrodes by DPV. Red was calculated from Eq. 4.18. Green was obtained from the CV. Results for three replicates are shown.

The bar plots in Figure 4.50 show a comparison of $\Gamma_{DPV, exp}$ calculated using Eq. 4.18 with Γ_{CV}. The DPV peak at 2.1 kΩ was used to obtain the integrated area. This is because R_{ext} of 2.1 kΩ gave the maximum DPV peak current as already shown in a plot R_{ext} vs DPV current (Figure 4.16). Both datasets are in a good agreement. This demonstrates that Eq. 4.18 worked well when the integrated area under DPV peak was used to calculate the surface coverage. We also

performed the DPV simulation on the experimental DPV from the control electrode. This data will be discussed in Section 4.27.

4.22 Typical results for simulated DPV at R_{ext} of 0.7 kΩ

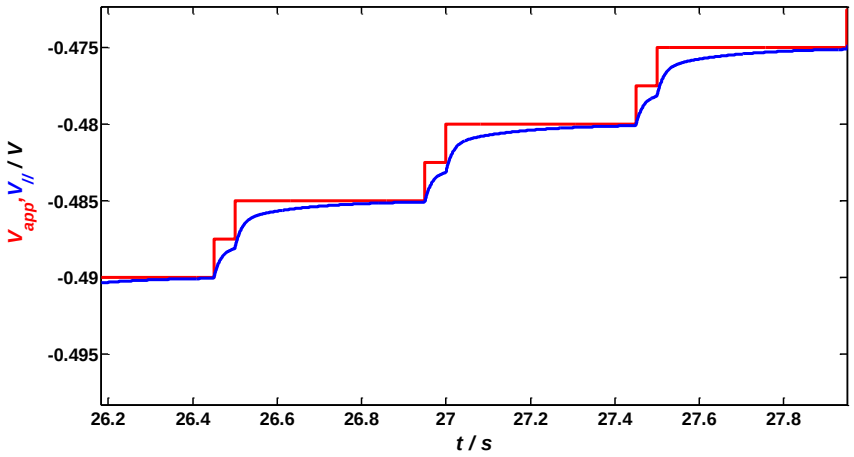

Figure 4.51; The first three periods of the DPV waveform (V_{ap}-red) and the voltage across the parallel part of the circuit (V_p-blue). $\tau_{long} = 450$ ms, $\tau_{short} = 50$ ms, ΔE_p = 2.5 mV, ΔE_i = 5 mV and DPV scan rate is 0.01 V / s. Simulation conditions; E^o = 0.476 V, R_t = 853 Ω, k_s = 3.97 s^{-1}, $\Gamma_{DPV, sim}$ = 360 pmol cm^{-2}, C_{dl} for reduced layer = 23.1, C_{dl} for oxidised layer = 27.38 µF, and A = 0.071 cm^{-2}.

As already demonstrated in Section 4.21 (Figure 4.46), the best simulated DPV to experimental DPV when R_{ext} added of 0.7 kΩ was obtained. Detailed results from the DPV simulation can give us more insight into the DPV waveforms and current transients. Thus, the theoretical DPV waveforms and generated current transients were analysed. As shown previously in Figure 4.43, the first panel shows the theoretical DPV waveform over 120 periods. Figure 4.51 is the enlargement of the DPV waveforms from Figure 4.43. Two different waveforms (red and blue) are clearly observed. The red waveform is the applied potential (V_{app}) whilst the blue waveform is the voltage across the parallel part of the circuit (V_{pa}). In addition, there are two decay components for the Faradaic currents. Clearly, the small potential step produces a small current transient whereas the big potential step generates a big current transient. The two transient currents can be clearly seen in Figures 4.52 and 4.53.

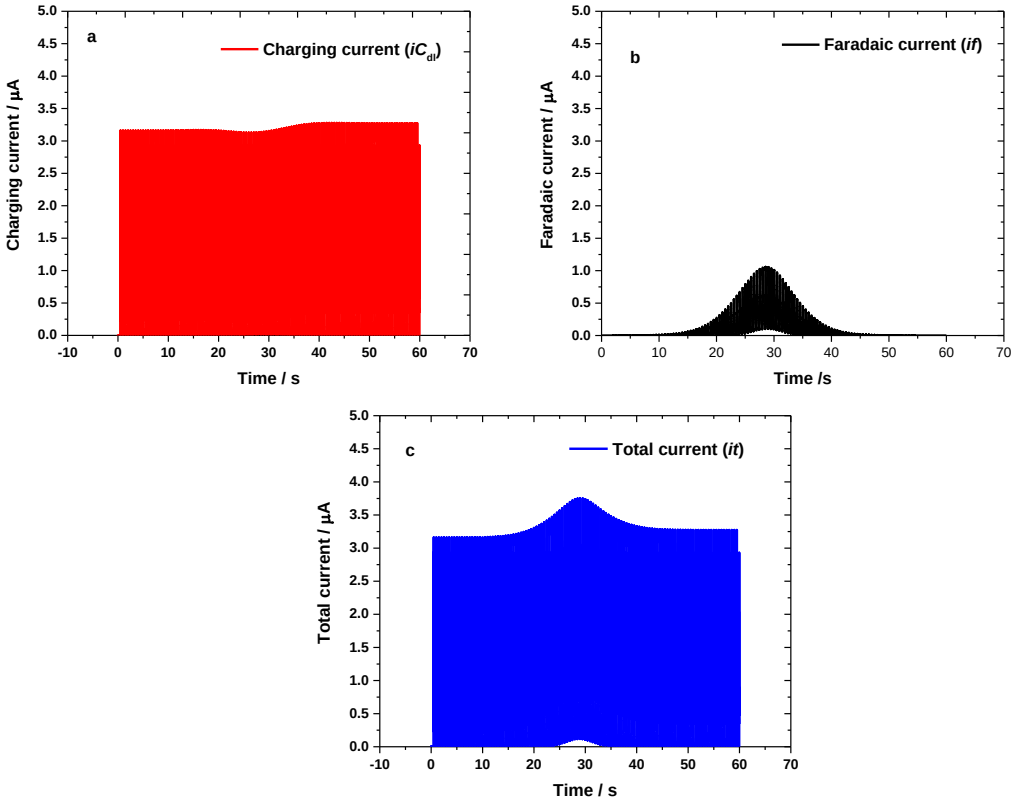

Figure 4.52; Current transients for the 120 periods of the waveform; a) Charging current, b) Faradaic current and c) Total current. The same simulation parameters as in Figure 4.51.

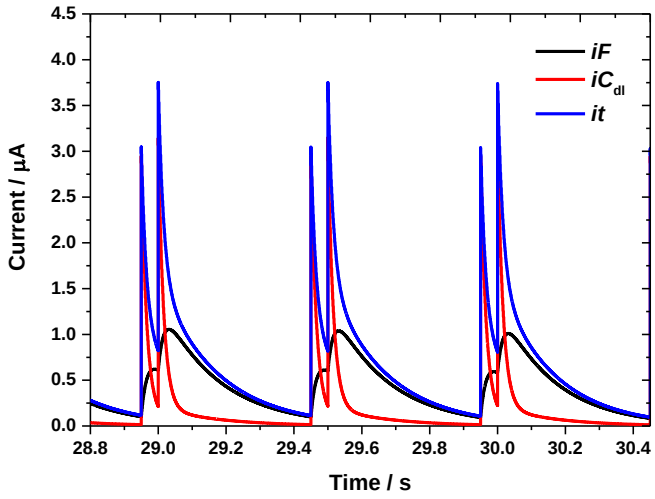

Figure 4.53; Enlargement of the current transients from Figure 4.51 at 28 s to 30 s. The same simulation parameters as in Figure 4.51.

From the survey in Figure 4.52, there are three types of current transient are observed. To clearly see for each feature of the current transients, an enlargement from Figure 4.52 was made as shown in Figure 4.53. Figure 4.53 shows three different types of currents transients from t = 28 s to 29.4 s. The black curve is the Faradaic current, the red curve is the capacitive current, and the blue curve is total current. As can be observed, there are two different features for the currents

transients for each type of current. A small current is produced from the small potential step (ΔE_p). In contrast, the bigger current is generated from the big potential step. Note that the Faradaic current (black curve) rises more slowly as it delayed until the potential has developed across the electrode/solution interface. In contrast, the double layer charging current rises very rapidly. Note also that the Faradaic current peaks about 50 ms after the small potential as expected when the optimum R_{ext} is used.

4.23 The sensitivity of the numerical simulation to the choice of simulation parameters

Although the experimental data agreed qualitatively with the results of the simulations (Figure 4.46), the sensitivity of the simulation to the choice of simulation parameters should be examined. In each case the simulation parameter was varied by ± 10% whilst keeping all the other parameters constants, Figures 4.54a and b show the results for varying R_t.

The same approach was used for C_{dl}, k_s $\Gamma_{DPV,\,sim}$, and α. The results can be seen in Figures 4.55a, b, 4.56a, b, 4.57a, b and 4.58, respectively.

Varying R_t values ± 10%

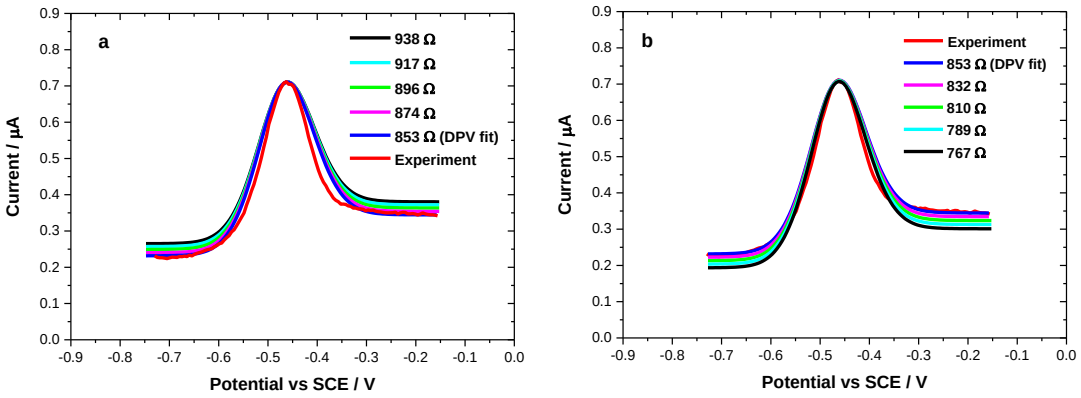

Figure 4.54; Sensitivity of the numerical simulation for DPV to the choice of best fit value (0.853 kΩ) at constant Γ_{DPV} = 360 pmol cm^{-2}, k_s=3.97 s^{-1}, α = 0.5, C_{dl} for reduced surface = 23.1 µF and C_{dl} for oxidised layer = 27.38 µF. a) Simulated DPVs with R_t values (bottom to top) at 0.867 kΩ, 0.893 kΩ, 0.910 kΩ and 0.935 kΩ. b) Simulated DPVs with R_t values (top to bottom) at 0.833 kΩ, 0.808 kΩ, 0.7905 kΩ and 0.765 kΩ. The measured experimental R_t from EIS was found to be 0.853 kΩ.

The effect of varying R_t within ± 10% on the magnitude of the simulated currents are shown in Figure 4.54a and b. As the R_t values increased, the charging current for both the reduced and oxidised layers increased and shifted away from the charging currents for the experimental DPV. In contrast, the magnitudes of the simulated DPV peak currents remain constant. Nevertheless, the height and the size of the peak current decreased. On the contrary, when the R_t values were

decreased, the charging currents on the reduced and oxidised layers decreased. Consequently, the height and size of the peak current increased. Thus, it can be concluded that the simulated peak current is largely sensitive towards R_t.

Varying C_{dl} values ± 10%

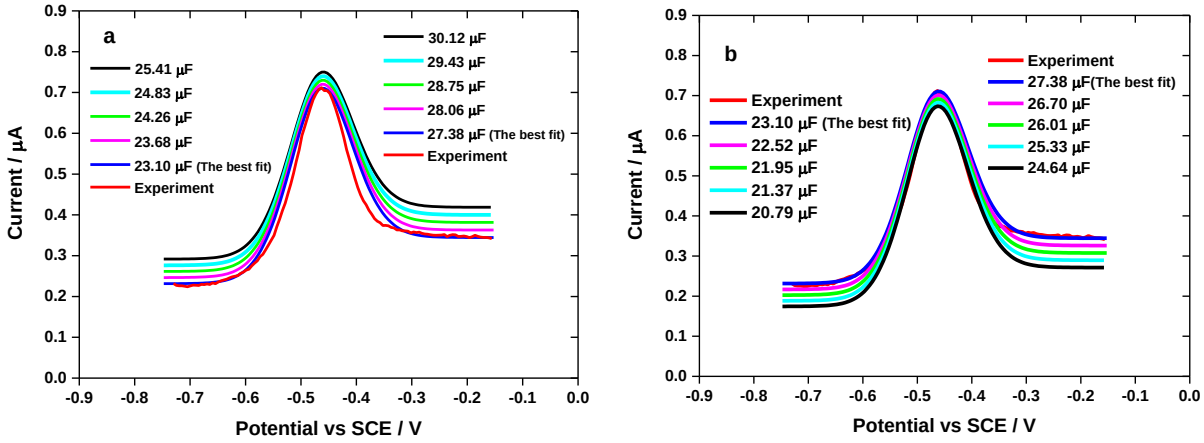

Figure 4.55; Sensitivity of the numerical DPV simulation to varying values of C_{dl} for reduced surface (the best fit value = 23.1µF) and oxidised surface (the best fit = 27.38 µF) at constant Γ_{DPV} = 360 pmol cm^{-2}, R_t = 0.853 kΩ, k_s = 3.97 s^{-1}, and α = 0.5, a) Simulated DPVs with C_{dl} for reduced values (bottom to top) at 23.68 µF, 24.26 µF, 24.83 µF and 25.41 µF. In contrast, on the right side, C_{dl} for oxidised values (bottom to top) at 28.06 µF, 28.75 µF, 29.43 µF and 30.12 µF. b) Simulated DPVs with C_{dl} for reduced values (top to bottom) at 22.52 µF, 21.95 µF, 21.37 µF and 20.79 µF. In contrast, on the right side, C_{dl} for oxidised values (top to bottom) 26.70 µF, 26.01 µF, 25.33 µF and 24.44 µF.

The same data pattern was observed when varying C_{dl} values for the reduced and oxidised layer as shown in Figures 4.55a and b. Clearly, the simulated current is also largely sensitive towards the choice of C_{dl}. However, the simulated current is more sensitive towards a slight change of C_{dl} value compared as compared to a slight change of R_t value.

Varying k_s values ± 10%

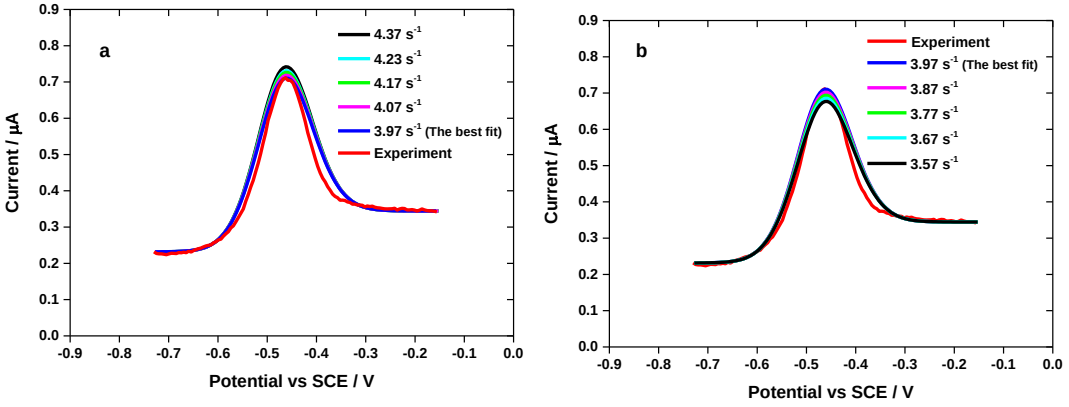

Figure 4.56; Sensitivity of the numerical DPV simulation to k_s (best fit value = 3.97 s^{-1}) at constant Γ_{DPV} = 3.60 pmol cm^{-2}, R_t = 0.853 kΩ, α = 0.5, C_{dl} for reduced layer = 23.1 µF and C_{dl} for oxidized layer = 27.38 µF. a) Simulated DPVs with k_s values (bottom to top) at 4.07 s^{-1}, 4.17 s^{-1}, 4.23 s^{-1} and 4.37 s^{-1}. d) Simulated DPVs with k_s values (top to bottom) at 3.87 s^{-1}, 3.77 s^{-1}, 3.67 s^{-1} and 3.57 s^{-1}. The measured experimental k_s from chronoamperometry was found to be 3.90 s^{-1}.

Figure 4.56a and b show the effect of varying the k_s values on the simulated currents. Clearly, the capacitive current remains unchanged. However, the height of the peak currents increase as the k_s values increase. In terms of the shape of the peak, it gets broader. In contrast, as shown in Figure 4.56b, the reverse effect was obtained when the k_s values were decreased.

Varying Γ_{DPV} values ± 10%

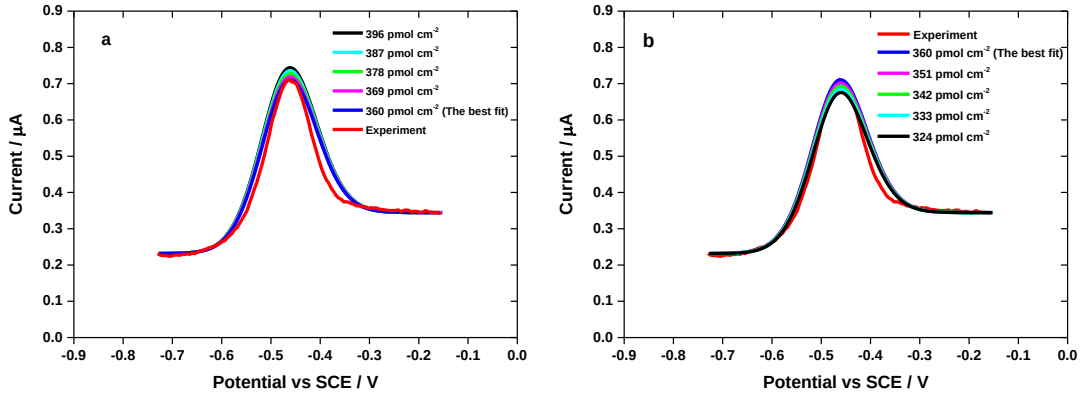

Figure 4.57; Sensitivity of the numerical simulation on varying Γ_{DPV} (best fit value = 360 pmol cm^{-2} at constant R_t = 0.853 kΩ, k_s = 3.97 s^{-1}, α = 0.5, C_{dl} for reduced layer = 23.1 µF and C_{dl} for oxidised layer = 27.38 µF. a) Simulated DPVs with Γ_{DPV} values (bottom to top) at 369 pmol cm^{-2}, 378 pmol cm^{-2}, 387 pmol cm^{-2}, and 396 pmol cm^{-2}. b) Simulated DPVs with $\Gamma_{DPV, sim}$ values (top to bottom) at 351 pmol cm^{-2}, 342 pmol cm^{-2}, 3.33 pmol cm^{-2}, and 324 pmol cm^{-2}.

Figure 4.57a and b present the effect of $\Gamma_{DPV,\,sim}$ on the simulated currents when the $\Gamma_{DPV,\,sim}$ values are increased and decreased. Again, the charging currents remain constant. The height and size of the simulated current increases as the $\Gamma_{DPV,\,sim}$ values are increased. By contrast, when the $\Gamma_{DPV,\,sim}$ values are decreased, the magnitudes of simulated current decreased as shown in Figure 4.57b.

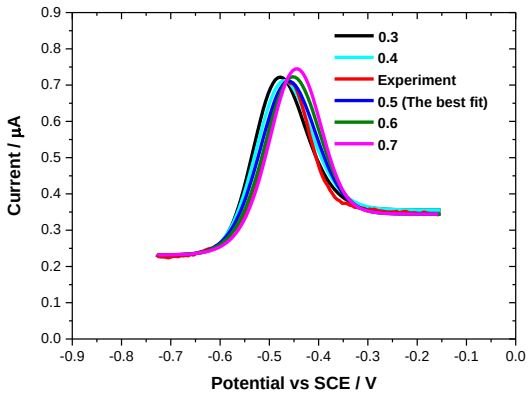

Figure 4.58; Sensitivity of the numerical simulation on varying α, at constant R_t = 0.853 kΩ, k_s = 3.97 s^{-1}, α = 0.5, C_{dl} for reduced layer = 23.1 µF and C_{dl} for oxidised layer = 27.38 µF and $\Gamma_{DPV,\,sim}$ = 360 pmol/ cm^2.

Generally, the transfer coefficient (α) is a property that is inherent for a particular electron transfer process of a redox species. Figure 4.58 presents the effect of α on the simulated currents. As α increases, starting from α = 0.3 and going to α = 0.7, the peak gets shifted to more positive potential. In addition, the magnitude of the simulated currents gradually increases.

In the response to all results above, it can be clearly observed that α demonstrated a significant change in the simulated DPV peak current. In contrast, the variables R_t and C_{dl} gave a significant change on the capacitive currents. However, from the result of varying the C_{dl} values, it is clear that the parameter C_{dl} has a great effect on the simulated currents than R_t.

4.24 DPV simulations for experimental DPVs at R_{ext} = 1.6 kΩ and without R_{ext}

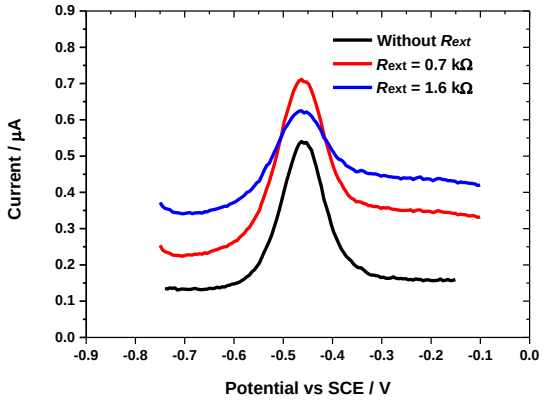

Figure 4.59; Experimental DPV peak currents at three different R_{ext} conditions; before adding R_{ext} (black), R_{ext} of 0.7 kΩ (red) and R_{ext} of 1.6 kΩ (blue). The DPVs were measured over a potential range from -0.75 to -0.15 V vs SCE with a DPV scan rate of 0.01 V s^{-1} in 0.1 M phosphate buffer solution, pH 7. A temperature of 25 º C ± 0.5 was controlled by using a water bath.

Figure 4.59 shows three different experimental DPV curves at three different magnitudes of R_{ext} in an electrochemical cell. DPV simulations were also performed at R_{ext} of 1.6 kΩ and without R_{ext}. It should be noted that the optimised DPV surface coverage that was experimentally obtained from the DPV peak at R_{ext} of 0.7 kΩ, (Figure 4.46) was kept constant for every single simulation. Secondly, the R_{ext} value used in the DPV simulation for each R_t condition was directly obtained from the Nyquist plot. Only two variables, C_{dl} and the k_s, were used to manually find the best DPV fit.

4.24.1 DPV simulation for experimental DPV at R_{ext} of 1.6 kΩ

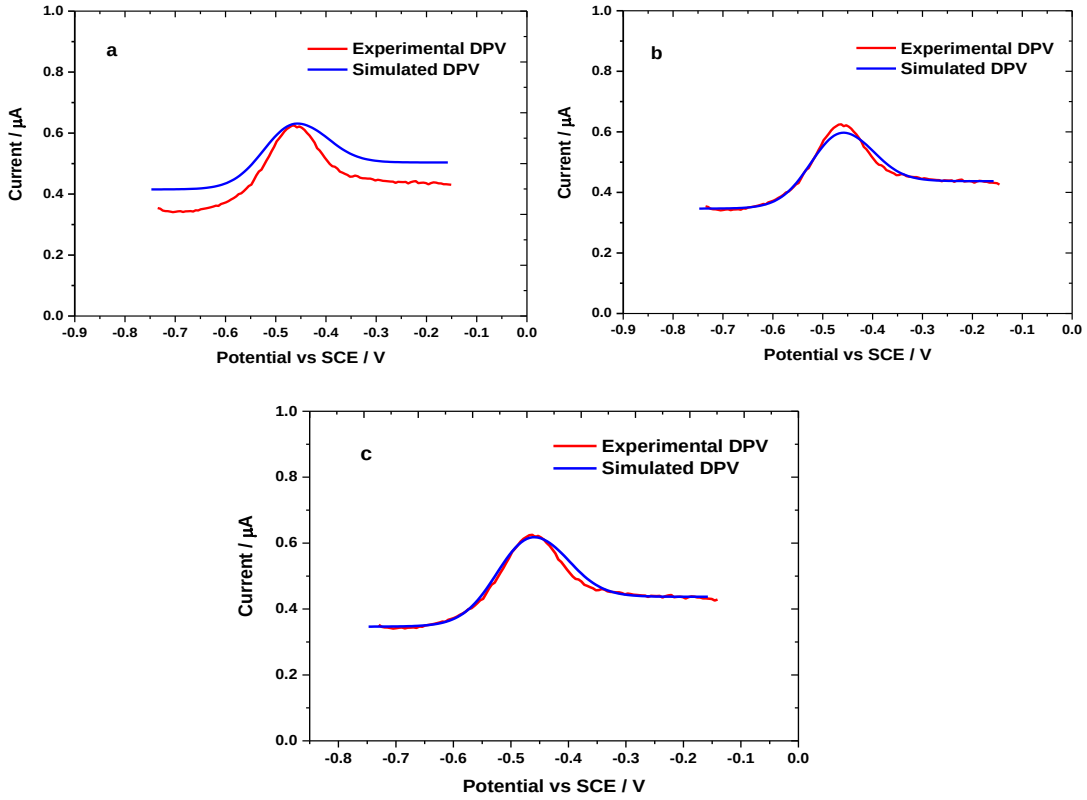

Figure 4.60; a, b, c- Steps in the simulation procedure to obtaining the best fit for the experimental DPV at R_{ext} = 1.6 kΩ. In the first step, the same parameters were entered in the simulation as used in the simulation for experimental DPV at R_{ext} of 0.7 kΩ with the one exception of R_t, which was directly obtained from the Nyquist plots.

a- Simulated DPV (blue) for k_s = 3.97 s^{-1}, R_t = 1753 Ω, transfer coefficient (α) = 0.50, C_{dl} for reduced form = 23.1 µF, C_{dl} for oxidised form = 27.38 µF and $\Gamma_{DPV, sim}$ = 360 pmol cm^{-2}. R_t = 1753 Ω directly determined from the Nyquist plots.

b- Simulated DPV (blue) for k_s = 3.97 s^{-1}, R_t = 1753 Ω, transfer coefficient (α) = 0.50, C_{dl} for reduced form = 20.1 µF, C_{dl} for oxidised form = 24.1 µF and $\Gamma_{DPV, sim}$ = 360 pmol cm^{-2}.

c- Simulated DPV (blue) for k_s = 4.5 s^{-1}, R_t = 1753 Ω, transfer coefficient (α) = 0.50, C_{dl} for reduced form = 20.15 µF, C_{dl} for oxidised form = 24.10 µF and $\Gamma_{DPV, sim}$ = 360 pmol cm^{-2}.

The first step in the DPV simulation was made by keeping all the parameter (from Table 4.11) fixed, but changing R_t. The R_t value of 1753 Ω used was directly determined from the Nyquist plot. As shown in Figure 4.60a, the DPV fit is poor. Following the second step in our simulation procedure, by changing C_{dl} for the reduced layer from 23.1 µF to 20.1 µF and C_{dl} for the oxidised layer form, from 27.38 µF to 24.10 µF, the fit is improved significantly (Figure 4.60b). Finally, by adjusting k_s from 3.97 s^{-1} to 4.5 s^{-1}, good agreement between experimental and simulation was achieved (Figure 4.60c).

4.24.2 DPV simulation for experimental DPV without R_{ext}

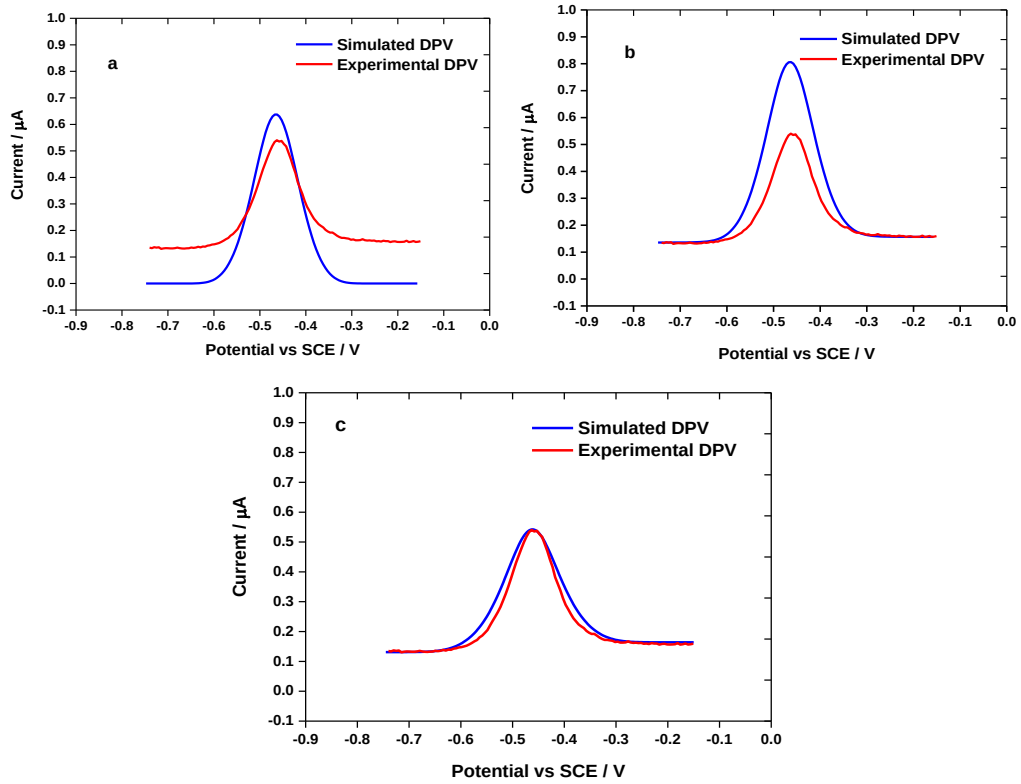

Figure 4.61; a, b, c- Steps in the simulation procedure to obtain the best fit for the experimental DPV before adding R_{ext}. In the first step, the same parameters were entered in the simulation as used in the simulation for experimental DPV at R_{ext} of 0.7 kΩ with the one exception of R_u which was directly obtained from the Nyquist plots.

a- Simulated DPV (blue) for k_s = 3.97 s^{-1}, R_u = 153 Ω, transfer coefficient (α) = 0.50, C_{dl} for reduced layer = 23.10 µF, C_{dl} for oxidised layer = 27.38 µF and $\Gamma_{DPV,\,sim}$ = 360 pmol cm^{-2}. R_u = 153 Ω directly determined from the Nyquist plots.

b) Simulated DPV (blue) for k_s = 3.97 s^{-1}, R_u = 153 Ω, transfer coefficient (α) = 0.50, C_{dl} for reduced layer = 68.4 µF, C_{dl} for oxidised layer = 70.5 µF and $\Gamma_{DPV,\,sim}$ = 360 pmol cm^{-2}.

c) Simulated DPV (blue) for k_s = 2.2 s^{-1}, R_u = 153 Ω, transfer coefficient (α) = 0.50, C_{dl} for reduced layer = 68.4 µF, C_{dl} for oxidised layer = 70.5 µF and $\Gamma_{DPV,\,sim}$ = 360 pmol cm^{-2}.

The same approach was used to fit the experimental DPV for no added R_{ext}. In this case, the R_u value was changed to 153 Ω where the R_u value of 153 Ω was directly extracted from the Nyquist plots.

Figure 4.61a shows the initial fit. Adjusting the C_{dl} values for the reduced and oxidised layers from 23.10 to 68.4 µF and 27.38 to 70.50 µF respectively, drastically improved the fit as shown in Figure 4.61b. Finally, changing the initial k_s value from 3.97 s^{-1} to 2.2 s^{-1} gives the best DPV fit as shown in Figure 4.61c.

4.25 Comparison of the typical simulation results for 3 different experimental DPVs

As discussed in Sections 4.20, and 4.24.1 and 4.24.2, the DPV simulations over three different experimental DPV peaks have been performed. By comparing the DPV peak current generated by simulation to the experimental DPV, setting the best value for each parameter in the DPV simulation, the best DPV fits were obtained. This section presents the typical simulation results for the DPV waveforms (Figure 4.62a, b, and c) and current transients of the waveforms at three different magnitudes of R_{ext} as shown in Figures 4.63a, b and c.

Based on Figures 4.62a, b, and c, for each DPV waveform, a plot of the voltages (V_{app}/V_{pa}) vs time from -0.49 V to -0.475 V and in a period of time from 26 s to 29 s was generated. The idea is to show the first three periods at the voltages from 0.490 V to -0.475 V, because the Faradaic reaction of AQ occurs in the potential range of -0.55 V to -0.43 V. Figures 4.63a, b, and c show the enlargement of the current transients at the three different R_{ext} conditions.

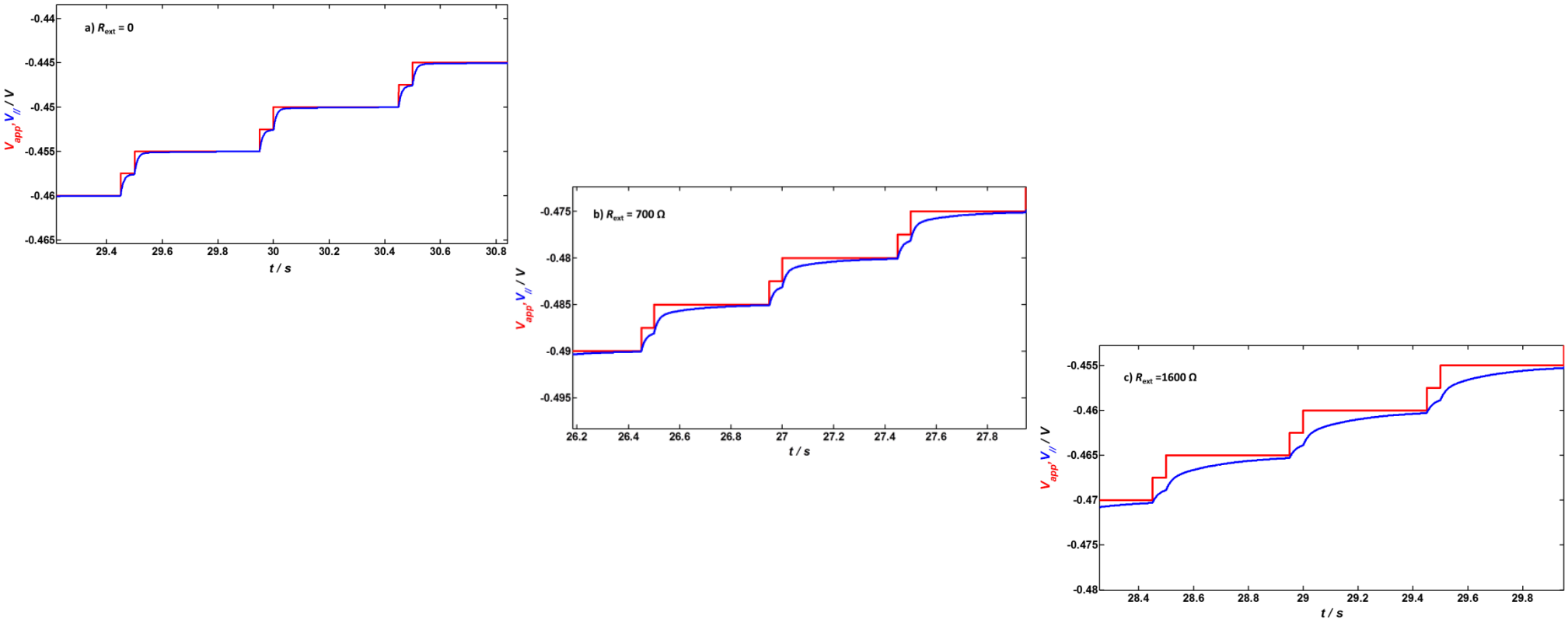

Figure 4.62; a, b, c) Three generated DPV waveforms at 26 s to 30 s. a) R_{ext} = 0 b) R_{ext} = 0.7 kΩ. c) R_{ext} = 1.6 kΩ. Red is the applied voltage (V_{app}) and blue is the voltage across the parallel part of the circuit (V_{pa}).

In Section 4.22, we have shown and explained in detail the waveforms and current transients generated from the DPV simulation. Nevertheless, we only showed the data from the simulation at R_{ext} of 0.7 kΩ. Also, we have shown the simulated DPVs at R_{ext} = 0 and R_{ext} = 1.6 kΩ, respectively. In this section, we compare the theoretical waveforms and generated current transients for the three different R_{ext} conditions (R_{ext} = 0, R_{ext} = 0.7 kΩ and R_{ext} =1.6 kΩ). Based on the DPV waveforms (Figures 4.62a,b and c), by increasing the magnitude of R_{ext} in the cell circuit, the transient period of the voltage across the electrode/solution interface (V_{pa}) in the circuit for both the small and big potential steps takes longer to reach the maximum applied voltage (V_{ap}). It can be clearly observed that at R_{ext} = 0, the transient voltage across (V_{pa}) reached the maximum V_{ap} for both potential steps and almost produced a rectangular input. In contrast, when R_{ext} of 0.7 kΩ was added, V_{pa} takes much longer to reach V_{ap} compared to the the case where R_{ext} = *0*. However, the transient voltage for the small potential step does not reach the maximum V_{ap}. Then, when R_{ext} added was changed from 0.7 kΩ to 1.6 kΩ, the for V_{pa} clearly takes much longer than at R_{ext} of 0.7 kΩ. Also, V_{pa} does not reach the maximum value of V_{ap} for either potential step. This is caused by the increase of the *RC* time constant as the magnitude of R_{ext} added in the circuit is increased. However, when the *RC* time constant becomes too large, the transient for V_{pa} will not reach the actual value of V_{ap}.

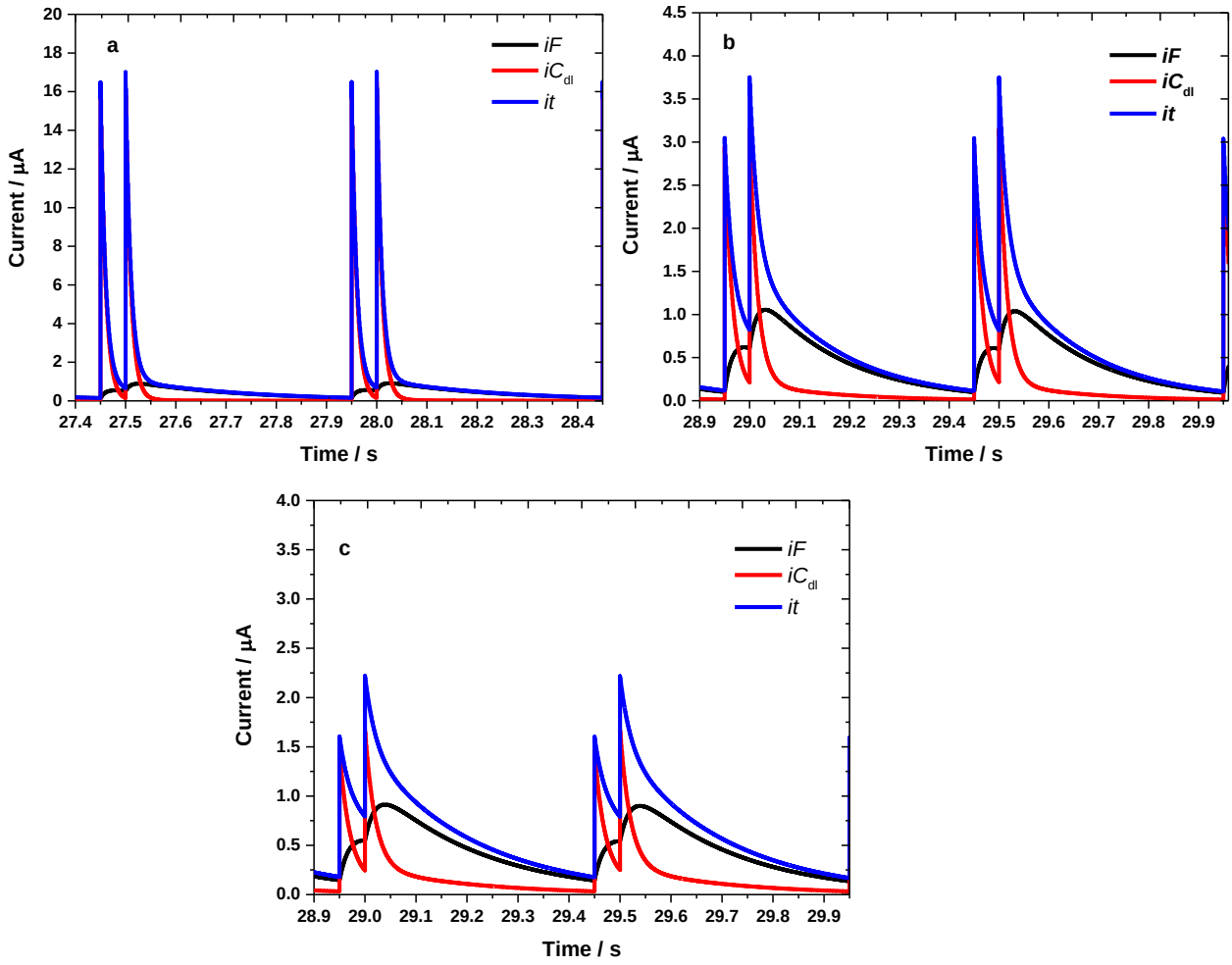

Figure 4.63; Enlargement of the DPV current transients for total, Faradaic and charging currents at a) R_{ext} = 0, b) R_{ext} = 0.7 kΩ and c) R_{ext} = 1.6 kΩ . Only current transients from two generated DPV pulses from 27 s to 30 s are shown.

Further analyses are made for the current transients as shown in Figure 4.63. Figure 4.63 a,b and c shows the three different types of DPV current transient. To note again, red, black and blue demonstrate the current transients for capacitive, Faradaic and total currents. Figures 4.63 a,b and c show the enlargement of current transients from 2 periods of the waveforms, generated at 27 s to 30 s in the Faradaic potential region. We saw before that at R_{ext} added of 0.7 kΩ produced the maximum DPV currents as well as the maximum DPV charge in our DPV experiment, clearly, from Figure 4.63b, the Faradaic current transient is the biggest for R_{ext} of 0.7 kΩ. In contrast, the Faradaic current transients at R_{ext} = 0 and R_{ext} of 1.6 kΩ are smaller.

Second, a prominent feature from Figures 4.63a, b and c when R_{ext} = 0, is that the charging current decays to zero. This would generate the biggest capacitive current and obscures the Faradaic process. As a result, a smaller magnitude of the Faradaic current was produced. Therefore, by adding R_{ext} of 0.7 kΩ, this makes the charging current takes longer to fall off. Consequently, this

would make the charging current obscure the Faradaic process less. This creates an opportunity to enhance the Faradic current as shown in Figure 4.63b. However, when R_{ext} of 1.6 kΩ was added, this makes the charging current transient take much longer to decay as clearly shown in Figure 4.63c. This is because the *RC* time is considerably increased. As a result, a lower magnitude of Faradaic current was generated again (Figure 4.63c). In order to see in greater detail the behaviour of the Faradaic current at the three different R_{ext} conditions, the comparison was made at the maximum Faradaic current as shown in Figure 4.64.

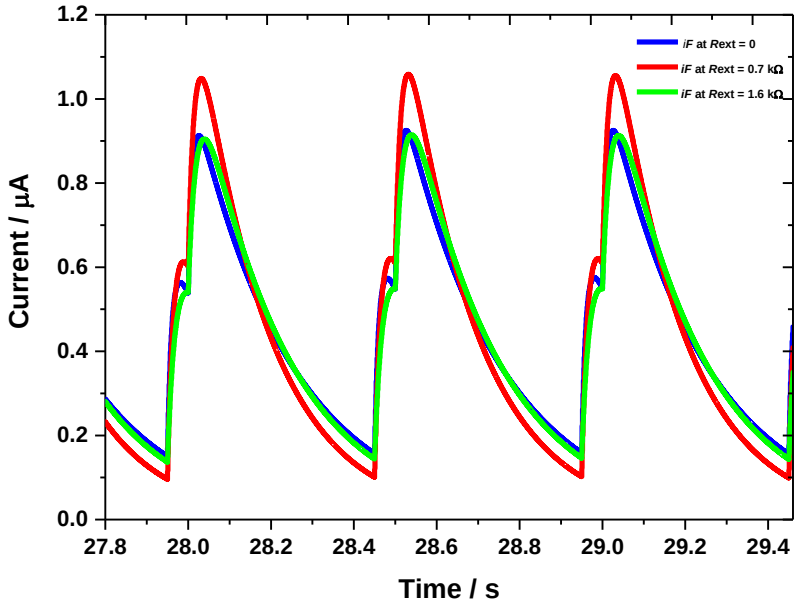

Figure 4.64; Comparison of the generated Faradaic currents; without R_{ext} = blue, R_{ext} added of 0.7 kΩ = red and R_{ext} added of 1.6 kΩ = green.

From Figure 4.64, clearly, the magnitude of the Faradaic current at R_{ext} added of 0.7 kΩ is the highest. This clearly shows that the DPV charge at this magnitude is maximum. As a result, the maximum DPV surface coverages was obtained.

4.26 Comparison of C_{dl} and k_s values extracted from DPV simulations for 3 different values of R_{ext}

The best fit values for C_{dl} and k_s for the fits at the different R_{ext} shown in Sections 4.21, 4.24.1 and 4.24.2 are given in Table 4.12.

Table 4.12; Best fit values for k_s and C_{dl} for three different R_{ext} conditions. $\Gamma_{DPV,\ sim}$ (360 pmol/cm^2) and α (0.5) values were kept constant for all simulations.

Parameters used for obtaining the best DPV fit	DPV simulation before adding R_{ext}	At R_{ext} of 0.7 kΩ	At R_{ext} of 1.6 kΩ
k_s	2.2 s^{-1}	3.97 s^{-1}	4.5 s^{-1}
C_{dl} value for reduced layer	68.4 μF	23.10 μF	20.15 μF
C_{dl} value for oxidised layer	70.5 μF	27.38 μF	24.10 μF

From Table 4.12, we can see key changes in the best fit DPV parameters for the three different R_{ext} values. These are (i) a rise in k_s values and (ii) a decrease in C_{dl} values. As can be observed, the k_s values obtained from the best fits are in the same order of magnitude as the k_s values from the Laviron analysis (Table 4.6) and chronoamperometry measurements (Table 4.7). However, it is notable that the C_{dl} values for the reduced and oxidised films from the DPV fitting are significantly different from the value for C_{dl} obtained by the EIS measurements, assuming an equivalent *RC* circuit (Table 4.9). As shown earlier, the results obtained from the EIS gave a constant C_{dl} value throughout all the experiments and calculations. The data presented for the C_{dl} values from EIS were shown in Section 4.17 (see Table 4.9). Despite the significant change in C_{dl} values over the best DPV fits to the experimental DPVs at R_{ext} of 1.6 kΩ and without R_{ext}, by setting the magnitudes of R_t that were extracted from the Nyquist plots, and keeping the optimised $\Gamma_{DPV,\ sim}$ constant, the best DPV fits are still obtained. Hence, the question that arises from the DPV simulation results presented above is; why do the given C_{dl} data from the DPV simulation decrease with the increased magnitudes of R_t in the electrochemical cell? Here we consider several possible answers.

Firstly, the DPV simulation model employed here assumes a simple ideal series *RC* model to describe the double layer charging. According to this model changing *R* should not effect C.

However, we know that real electrochemical system never follow quite such ideal double layer charging behaviour and the EIS measurements in Section 4.17 already showed that the electrode does not precisely follow the ideal series *RC* circuit behaviour.

The real electrochemical system for the modified electrode may follow a more complex equivalent circuit, as illustrated in Figure 4.65. The circuit is specifically established for the monolayer film at the electrode surface, reported in the literature.

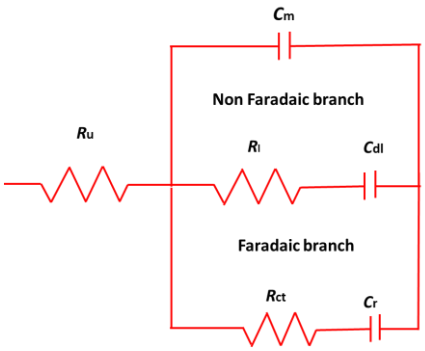

Figure 4.65; Suggested equivalent circuit model for a monolayer film at the electrode surface, R_u is a solution or electrolyte resistance, C_m is an insulating layer capacitance. R_l is AQ adlayer resistance, C_{dl} is the electric double layer from dipolar, polar ions and solvent molecules, C_r is the redox capacitance (pseudocapacitance) and R_{ct} charge transfer resistance[209,210].

We believe that the circuit shown in Figure 4.65 is a reasonable equivalent circuit that might fit to the EIS data. Clearly, it would be possible to incorporate a more complex equivalent circuit model for the double layer into the DPV simulation but it was not felt that this was necessary at this stage. Further recommendations on this concern will be discussed in Chapter 8.

4.27 DPV simulation for control electrode (adsorbed AQ)

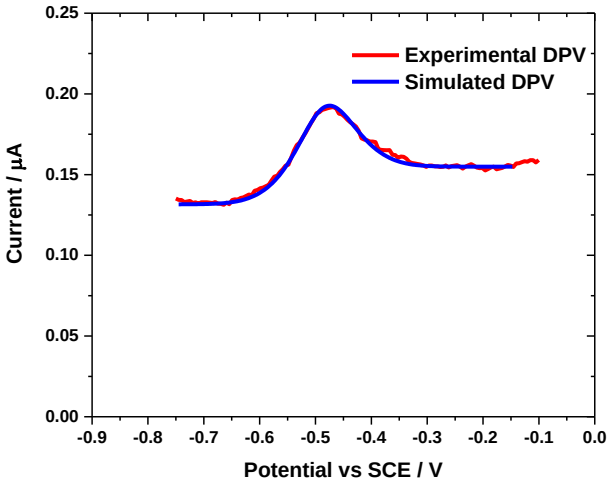

Figure 4.66; DPVs for the control electrode after adding R_{ext} of 2.1 kΩ corresponding to the maximum DPV peak current. The red curve is for experimental DPV, measured at ΔE_p = 2.5 mV, τ_p = 0.05 s, τ_i = 0.5 s, ΔE_s = 5 mV and a DPV scan rate at 0.01 V s^{-1} in 0.1 M phosphate buffer solution, pH 7. The blue curve is the best simulated DPV obtained by setting kinetic rate constant (k_s) = 2.8 s^{-1}, R_t = 2250 Ω, transfer coefficient (α) = 0.5, C_{dl} for reduction 10.45 µF, C_{dl} for oxidation = 11.30 µF and $\Gamma_{DPV, sim}$ = 53 pmol cm^{-2}. The R_t = 2250 kΩ was directly determined from the Nyquist plots.

The DPV response for the control electrode was also modelled by performing the same simulation steps. In this case, R_{ext} added was 2.1 kΩ. Figure 4.66 shows the best fit of the simulated DPV. By contrast, Figure 4.66 shows a bar graph for comparison on the Γ_{DPV} calculated by experiment and from the simulation. The simulation gives satisfactory agreement to the experimental DPV. The parameter values used in this simulation are shown in Table 4.14.

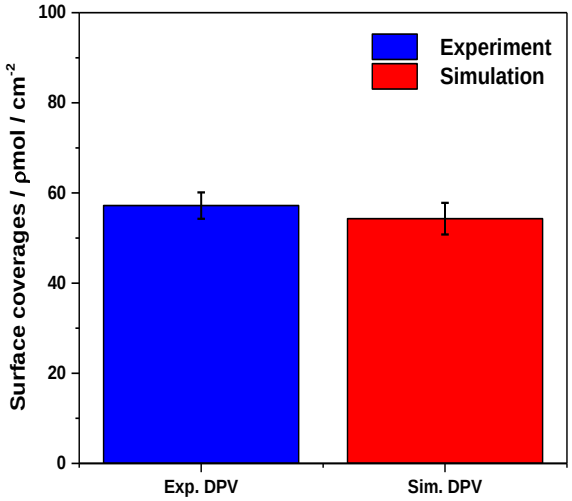

Figure 4.67; Comparison of the surface coverages from experimental calculations and obtained by the best fit of the DPV simulations. Results for three electrodes are shown.

Table 4.14: Parameters used for the DPV simulation of the control electrode experiments.

MATLAB parameters	Experiment	Simulation
Redox potential (E°)	-0.485 V	-0.489 V
Total uncompensated resistance in the electrochemical cell (R_t)	2250 Ω	2250 Ω
Transfer coefficient (α)	0.50	0.50
Rate of electron transferred (k_s)	2.6 s^{-1}	2.8 s^{-1}
C_{dl} for reduced layer	7.89 µF	10.45 µF
C_{dl} for oxidised layer	9.22 µF	11.30 µF
DPV surface coverages; ($\Gamma_{DPV, exp}$) and ($\Gamma_{DPV, sim}$)	56.4 pmol cm^{-2}	53.0 pmol cm^{-2}

4.28 Conclusion

The initial results in this Chapter showed that the covalent immobilisation of AQ to the surface of the GC electrode through the EDA linker produced a more stable and well-behaved redox system than the physically adsorbed 9,10-PQ. Using the stable covalently immobilised AQ modified electrode as a model system, an experimental method for estimating the surface coverage of immobilised redox species by DPV was developed. Moreover, the experimental model developed in this Chapter was accompanied by the theoretical DPV in order to verify the experimental approach.

In addition, the double layer capacitance (C_{dl}), the total uncompensated resistance in the electrochemical cell (R_t), and the kinetic parameters electrodes (k_s and α) were determined from EIS, CV and chronoamperometry experiments. The experimental values obtained from these measurements were used as input parameters for the DPV simulations.

Using DPV simulation, the charge under the simulated DPV peak was calculated. Thus, a simple equation for estimating Γ_{DPV} based on DPV parameters by replacing a factor of e (2.718) by 5 has been proposed. Several assumptions underlay this approach. In the experimental measurements, an external resistance (R_{ext}) was added in series with the modified electrode. By varying R_{ext} the value of R_{ext} that gives the maximum DPV peak current can be found. The coverages $\Gamma_{DPV, exp}$ were then determined by integrating the area under the DPV peak for the maximum DPV peak current case.

The values of $\Gamma_{DPV, exp}$ obtained by our experimental model was compared to the results of simulations of the DPV response and the reliability of the value $\Gamma_{DPV, exp}$ determined based on the experimental model was shown. Overall, good agreement was obtained between the experimental and simulated DPV currents, showing that the experiment can be described by a simple model.

The consistency between the proposed experimental and simulation models presented in this Chapter will be further investigated for a variety of covalently immobilised redox species with different types of the linker in the following chapters. In addition, more complex layer structures such as mixed-monolayers, produced using two different redox molecules have also been investigated. Therefore, in the next chapter (Chapter 5), the DPV models will be applied to covalently immobilised Os and AQ-Os at the surface of GC electrodes immobilised through the hexadiamine linker (HDA).

Chapter 5: Application of the models to the different modified electrodes

5.1 Overview

In Chapter four, the experimental and theoretical models for estimating the surface coverages of immobilised AQ molecules by DPV measurement were developed. This was achieved using AQ covalently immobilised through an EDA linker as a stable and well-behaved model redox system. Both models worked well for estimating the surface coverages of immobilised AQ molecules. However, there is a question raised here, "Do the experimental and theoretical models apply more generally when the conditions at the modified electrode surfaces are varied?" For example, do they work equally well with different attached redox molecules? Therefore, in this chapter, an osmium bipyridine complex was covalently immobilised at the GC electrode employing hexadiamine (HDA) linker and more complex a modified surface was prepared by covalently immobilising both the Os complex and AQ through HDA linkers to generating a mixed monolayer of AQ-Os. These experiments were done in collaboration with Professor Jeremy Kilburn's group from Queen Mary, University of London. Both the Os and AQ-Os modified GC electrodes were kindly prepared and provided by Dr Jessica Groppi, a former PhD student under the supervision of Professor Jeremy Kilburn. By performing the same analyses as made on AQ modified GC electrodes (experiment and simulation), the DPV surface coverages for the immobilised Os and AQ-Os at the surface of GC electrodes were determined.

5.2 Covalently immobilised Os complex at the surface of GC electrode

Complexes of transition metals elements such as ruthenium, osmium, iron, platinum, iridium cobalt, zinc and vanadium, have been successfully immobilised at electrode surfaces as catalysts. Due to their electrochemical reversibility and the different oxidation states of their derivatives, they can be used as electron transfer mediators for the modification of electrode surfaces such as gold, glassy carbon, platinum, and pyrolytic graphite[153]. Using the methodology and procedures described in Section 4.2, an osmium bipyridine complex (Os II/III)[154] has been covalently grafted on the GC electrode using the HDA linker as shown in Figure 5.1.

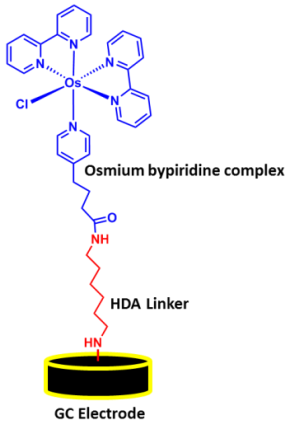

Figure 5.1; Covalent attachment of an osmium bipyridine complex using an HDA linker at the surface of GC electrode.

The HDA linker was used in this work is because attempted grafting of the osmium complex on the EDA linker gave lower surface coverages[92]. It was concluded that the grafting of the EDA linker to the GC electrode surface generates a too densely packed layer to allow the proper coupling of the bulky Os complex, thus resulting in lower surface coverages.

Os complexes are widely reported in electrochemical studies due to the synthetic accessibility from potassium hexachloroosmate (K_2OsCl_6) and their stability upon redox cycling. Moreover, the redox potential of the osmium complex can be tuned by changing the surrounding ligands[118].

5.3 Mixed monolayers of AQ-Os

The modification of electrode surfaces with immobilised binary layers either employing two different redox groups (Figure 5.2) or one redox molecule and an inactive group (Figure 5.3) is one of the challenges in the field of chemically modified electrodes. The main interest in developing mixed-monolayers is related to the development of attractive methods to promote different arrangements on the electrode surface, which enables the control of specific reaction sites thus improving mediated electron transfer, particularly for enzymes [154,155]. In addition, using diluent molecules for composing the mixed-monolayers can be seen as a way to separate redox molecules across a surface with good order principally for their orientation and density[93].

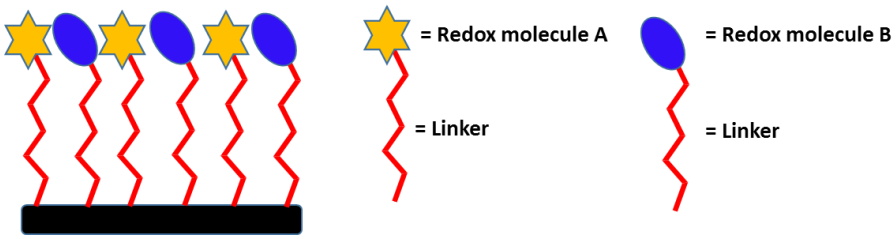

Figure 5.2; General scheme for composing mixed-monolayers at the surface of electrode by using two different redox probes.

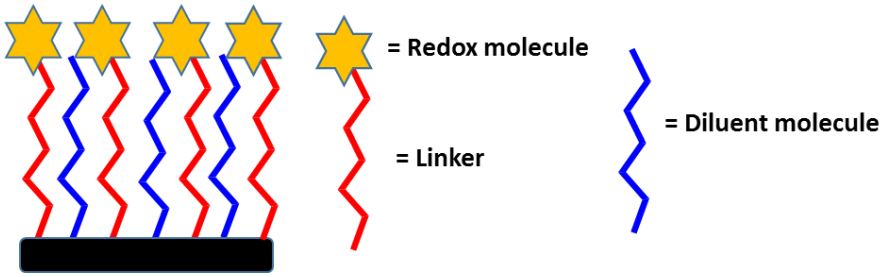

Figure 5.3; General scheme for composing mixed-monolayers at the surface of electrode by using one redox probe incorporated with diluent molecules.

By using a multiple-step approach (described in Chapter 2), the AQ and Os complex were covalently coupled to the HDA linkers to produce the AQ-Os modified GC electrodes as shown in Figure 5.4. This type of modified electrode was prepared by Dr. Jessica Gropi and details of the procedure have been published[154].

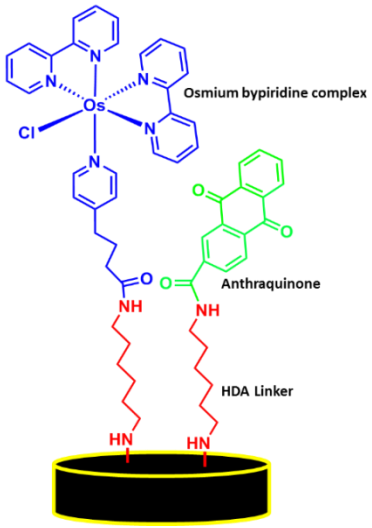

Figure 5.4; Covalent attachment of AQ and osmium bipyridine complex through - HDA linkers to make mixed monolayers.

5.4 Covalently immobilised Os bipyridine complex at the GC electrode surface

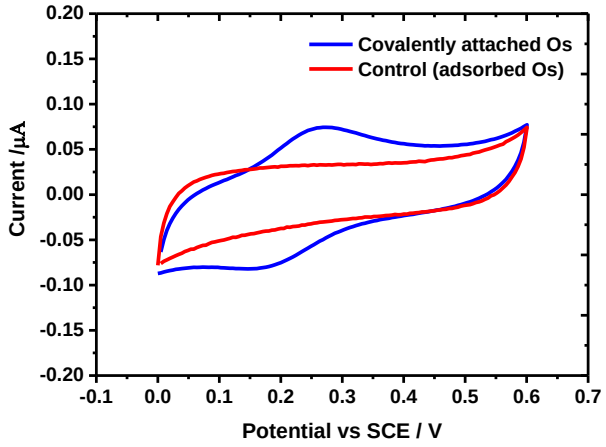

Figure 5.5; CVs for Os modified GC electrode (blue) and control electrode (red). The measurements were carried out at a scan rate of 50 mV s^{-1} in 0.1 M pH 7 phosphate buffer solution. The electrode area is 0.071 cm^2.

Figure 5.5 shows two CVs, recorded for covalently attached Os complex to the HDA linker (blue) and a control GC electrode (red). The CV of the covalently immobilised Os shows well-defined oxidation and reduction peaks for the Os^{2+} and Os^{3+} forms as illustrated in Figure 5.6. To show the stability of the Os modified GC electrodes, ten cycles of CV were run, Figure 5.7.

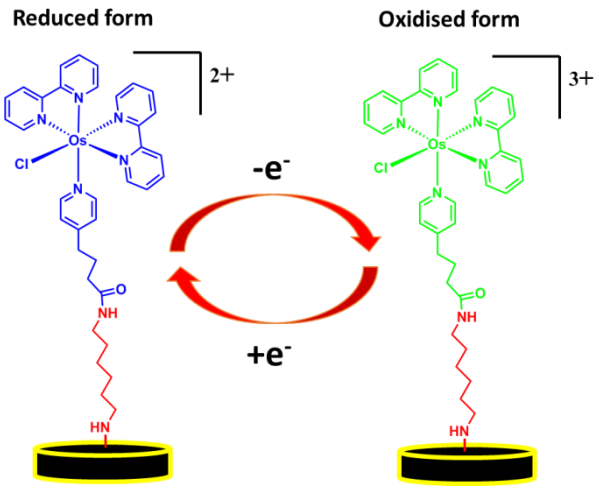

Figure 5.6; Oxidation and reduction of osmium complex involving one electron exchange (Os^{2+}/Os^{3+}).

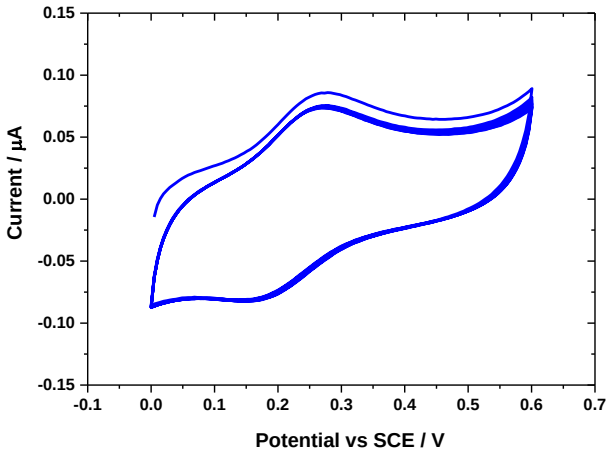

Figure 5.7; Ten cycles of CVs for Os modified GC electrode. The CV measurement was run at a scan rate of 50 mV s^{-1} in 0.1 M pH 7 phosphate buffer solution. The electrode area is 0.071 cm^2.

Based on the CV peaks, performing the same calculation as mentioned earlier in previous chapters using Faraday's law, and assuming again the roughness factor of GC electrode is 1, the surface coverages of Os were calculated to be 13.9 ± 1.5 pmol / cm^2. This calculated value will be compared to the measured DPV surface coverages from our experimental model below. According to the data for immobilised osmium complexes from literature[56,156,157], monolayer surface coverages were found to be between 40 - 100 pmol cm^{-2}. We previously reported that surface coverages osmium pyridine complex could vary between 17- 134 pmol cm^{-2} determined through computational calculations[92,154].

5.5 DPV surface coverages for Os modified GC electrode

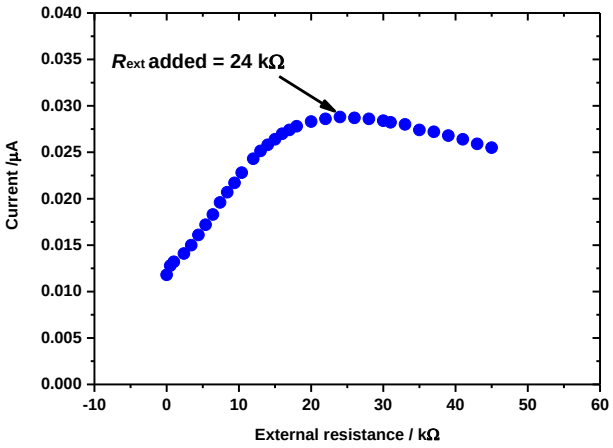

Figure 5.8; DPV peak currents against a series of R_{ext} added (0.5-38 kΩ) to the cell circuit for Os modified GC electrode with ΔE_p = 2.5 mV, τ_p = 0.05 s, τ_i = 0.5 s, ΔE_s = 5 mV and a DPV scan rate of 0.01 V s^{-1} in 0.1 M phosphate buffer solution at pH 7. The measurements were carried out over a potential scan between 0 to 0.6 V *vs* SCE at 25 ± 0.5 ° C. The electrode area is 0.071 cm^2.

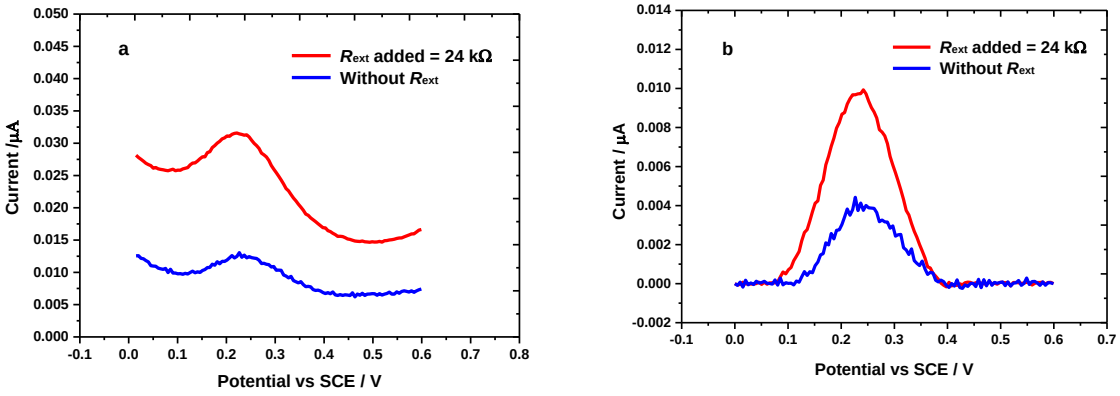

Figure 5.9; a) DPVs for Os modified GC electrode with R_{ext} of 24 kΩ (red) and without the R_{ext} (blue). 24 kΩ gives the highest DPV current for a plot of DPV current vs R_{ext}. b) The DPVs from Figure 5.9a after performing background subtractions. The DPVs were measured at a potential range between 0 to 0.6 V vs SCE with ΔE_p = 2.5 mV, τ_p = 0.05 s, τ_i = 0.5 s, ΔE_s = 5 mV and a DPV scan rate of 0.01 V s^{-1} in 0.1 M phosphate buffer solution at pH 7. The electrode area is 0.071 cm^2.

By adding a series of external resistances to the Os modified GC electrodes, a similar curve relationship of DPV peak currents *vs* R_{ext} as shown for AQ modified GC electrodes was obtained. Figure 5.8 shows a set of DPV peak currents (without background subtraction) plotted against the R_{ext} added. As can be observed from Figure 5.8, the DPV peak currents reach a maximum for R_{ext} of 24 kΩ.

As shown in Figure 5.9a, adding at R_{ext} of 24 kΩ in series with the working electrode produced a DPV current for the Os modified GC electrode that was significantly enhanced. Hence, the Faradaic currents from the DPV become more clearly seen, enhancing the sensitivity in the detection at low surface coverages and providing an excellent evidence for the presence of the small quantities of immobilised redox molecule[64]. Using the equation that we have modelled in this work (Eq. 4.18), the DPV surface coverages of the covalently immobilised Os at the surface of GC electrode were also determined. A background subtraction was performed on the DPV peak current using Origin 9.1 software in order to extract the integrated area under the DPV peak (Figure 5.9b). The calculated DPV surface coverages for the covalently immobilised Os based on our model equation were found to be 22.8 ± 0.39 pmol cm^{-2}.

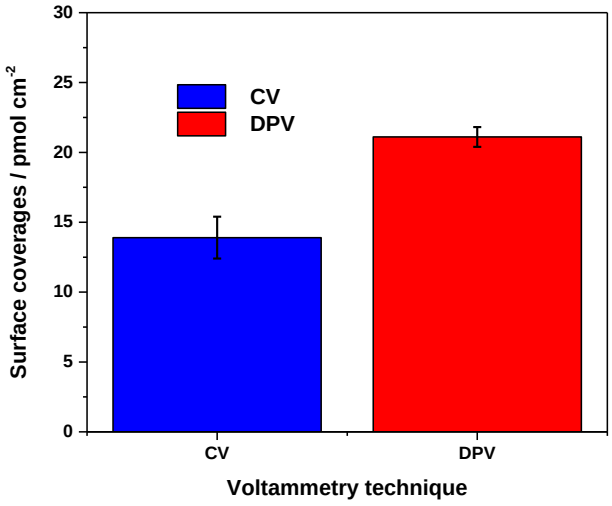

Figure 5.10; Comparison of surface coverages determined by CV and DPV for covalently immobilised Os bipyridine complex at the surface of GC electrodes.

Figure 5.10 show a bar graph comparing the surface coverages determined by CV and DPV techniques. Noticeably, the value for CV is significantly lower than value for CV. Explanations for this difference have been specifically discussed in Section 4.11. As shown in Figure 4.14, on adding different magnitudes of R_{ext} in the CV measurements, the CV redox currents gradually increased, the same behaviour is seen for Os modified GC electrode, as shown in Figure 5.11. It is clearly shown that the oxidation and reduction currents from CV signal were amplified by adding external resistance. Therefore, bigger oxidation and reduction peaks correspond to the increasing of integrated area under CV peaks. Consequently, the measured charge passed during Faradaic reactions also increased. Thus, the calculated CV surface coverages also increased.

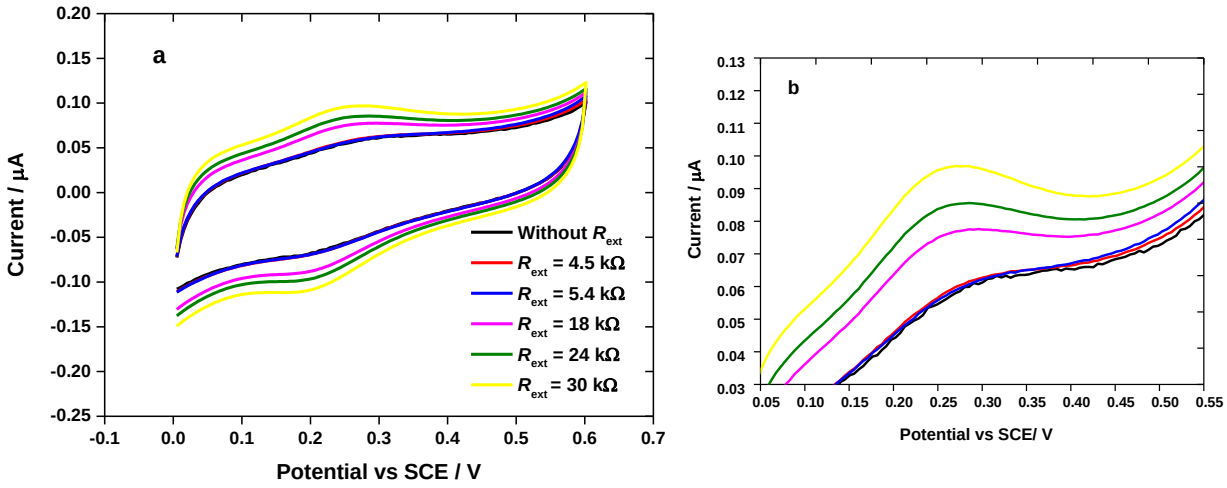

Figure 5.11; a) CVs for Os modified GC electrode with R_{ext} added from 4.5 kΩ to 30 kΩ. Black curve is CV measurement without R_{ext}. The CV measurements were run at a scan rate of 50 mV s^{-1} in 0.1 M pH 7 phosphate buffer solution. The electrode area is 0.071 cm^2. b) Enlargement of oxidation currents from Figure 5.11a.

5.6 Kinetics of covalently attached monolayer Os complex

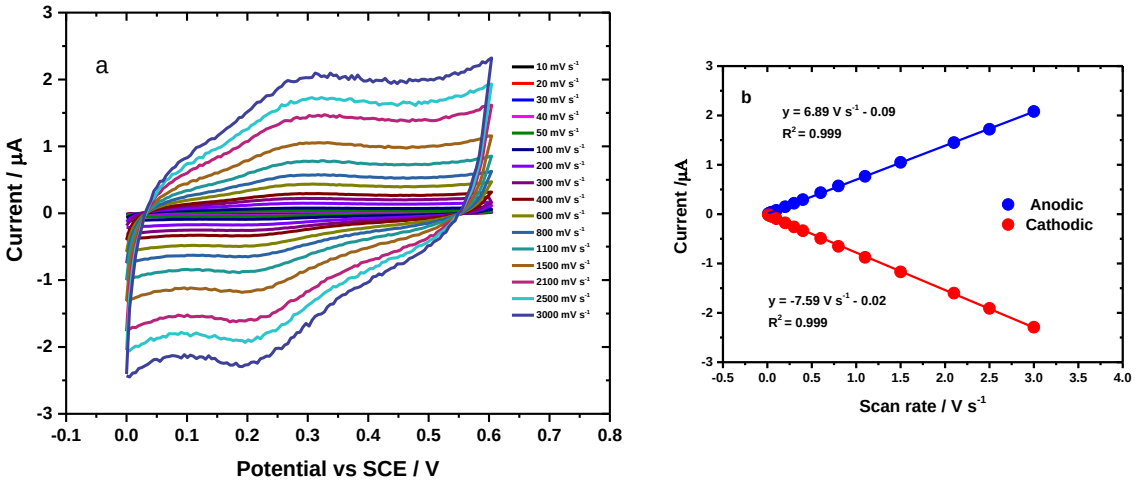

Figure 5.12; a) Cyclic voltammograms of Os modified GC electrode at scan rates from 10 to 3000 mV s^{-1}. b) Dependence of corresponding anodic and cathodic peak currents (raw data) on the scan rate. The measurements were carried out at 25 ± ° C in 0.1 M pH 7 phosphate buffer solution.

Figure 5.12a shows cyclic voltammograms at varying scan rates for Os modified GC electrode from 0.01 V/ s up to 3 V / s. Figure 5.12b shows linear plots for the oxidation and reduction peak currents as a function of scan rate, the linear behaviour is consistent with behaviour expected for an immobilised redox complex. The Laviron model was used to analyse the data. When the peak separation (ΔE_p) is less than 200 mV for a one-electron reaction, the general Laviron equations for determining the α and the k_s as used in the earlier chapter for determining the kinetic electron transfer parameters for covalently immobilised AQ, are not valid. In this case, the α value can be determined from a plot of $\left|(E_{pc} - E_{mid})/(E_{pa} - E_{mid})\right|$ / $n\Delta E_p$ Figure 5.13a. The constant values for $\left|(E_{pc} - E_{mid})/(E_{pa} - E_{mid})\right|$ correspond for α value = 0.5 (Figure 5.13b)[61].

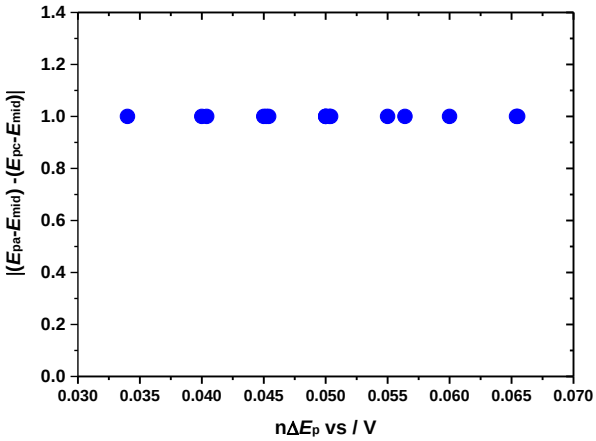

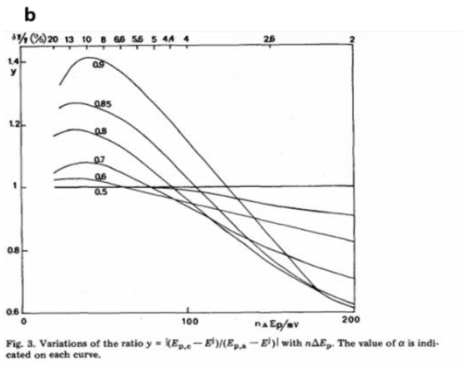

Figure 5.13; a) The plot of the ratio $\left|(E_{pc}\text{-}E_{mid}) / (E_{pa}\text{-}E_{mid})\right|$ against $n\Delta E_p$ for Os modified GC electrode. A horizontal line indicates that the value of α is 0.5 as shown by Laviron. b) The value of α is directly indicated on each curve based on plots of the ratio $\left|(E_{pc} - E_{mid}) / (E_{pa} - E_{mid})\right|$ against $n\Delta E_p$ from Laviron (reprinted with the permission from ref. 113)[61].

The value for k_s was determined based on the tabulated value of m, proposed by Laviron using Equation 5.1[61]

$$m = (\frac{RT}{F})(\frac{k_s}{nV}) \qquad \textbf{Eq. 5.1}$$

where R is the gas constant, T is the temperature in Kelvin, n is the number of electrons transferred, v is the scan rate in V s^{-1} and m values are tabulated and depend on the peak separations (E_{peak}) related to the number of electrons (n) involved in the electron transfer reaction as shown in Figure 5.14.

TABLE 1

m^{-1}	0.5	0.75	1	1.5	2	2.5	3	3.5	4	5
$n\Delta E_p$/ mV ± 0.1 mV	18.8	27	34.8	48.8	61.2	72.2	82.4	91.8	100.6	116.2
m^{-1}	6	7	8	9	10	11	12	13	14	
$n\Delta E_p$/ mV	130	142.4	153.8	164	173.4	182	190	197.6	204.6	

Figure 5.14; Table for values of $n\Delta E_p$ as a function of 1/m for α = 0.5 as proposed by Laviron (reprinted with the permission from ref. 113)[61].

In this analysis, k_s was calculated based on $\Delta E_{peak.}$ The results for two different Os modified GC electrodes are given in Table 5.1.

Table 5.1; Values calculated for k_s for two Os modified GC electrodes.

CV scan rate	k_s from E10	k_s from E11	Average k_s
40 mV /s	0.89 s^{-1}	0.77 s^{-1}	0.83 ± 0.06 s^{-1}
50 mV /s	0.97 s^{-1}	1.11 s^{-1}	1.04 ± 0.07 s^{-1}
70 mV /s	1.55 s^{-1}	1.36 s^{-1}	1.46 ± 0.09 s^{-1}

Because the CV signals at high scan rates are clearly affected by ohmic drop (Figure 5.12a) the appeared k_s values gradually increased, as scan rate increased. From Table 5.1, the average value for k_s at a scan rate of 50 mV /s was 1.04 ± 0.07 s^{-1}. The value for k_s found here is consistent with previous work, reported by Salami and associates[158]. In their work, k_s values for a physically adsorbed osmium (III) complex at the surface of a GC electrode modified with single-wall carbon nanotubes (SWCNTs) for two different deposition times (30 s and 60s) were found to be 4.9 s^{-1} and 6.4 s^{-1}, respectively. In addition to the Laviron procedure, chronoamperometry measurement was also used to estimate k_s.

5.7 Determination of *RC* time constant and k_s by chronoamperometry

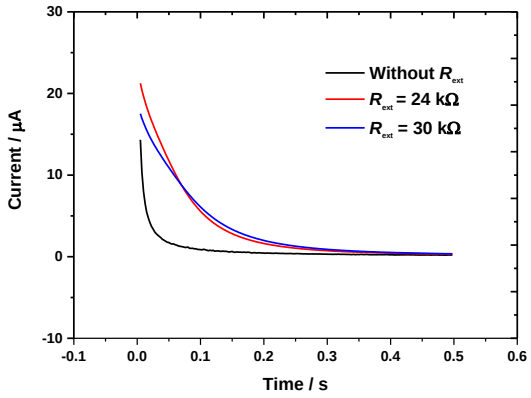

Figure 5.15; Current-time curves for Os modified GC electrode at three different values of R_{ext} using chronoamperometry by stepping the potential from 0 to 0.6 V *vs* SCE for 0.5 s. The time used here is similar to the interval time of DPV. The measurements were carried out in 0.1 M phosphate buffer, pH 7 and the electrode area is 0.071 cm^2.

Chronoamperometric measurements for the Os modified GC electrodes at three different R_{ext} are shown in Figure 5.15. The data were analysed by plotting ln *i* against time (*t*), (Figures 5.16a, b, c). Based on a plot ln *i* vs *t*, the *RC* time constant and k_s can be determined. Full calculation details have been given in Section 3.18, applying Equations 3.10 and 3.11 respectively. The calculated *RC* time constant and k_s are given in Table 5.2. Interestingly, the same data pattern as obtained for the AQ modified GC electrode was observed. The estimated k_s values at different R_{ext} were between 2.45 and 3.70 s^{-1}, slightly higher than k_s determined by the Laviron method.

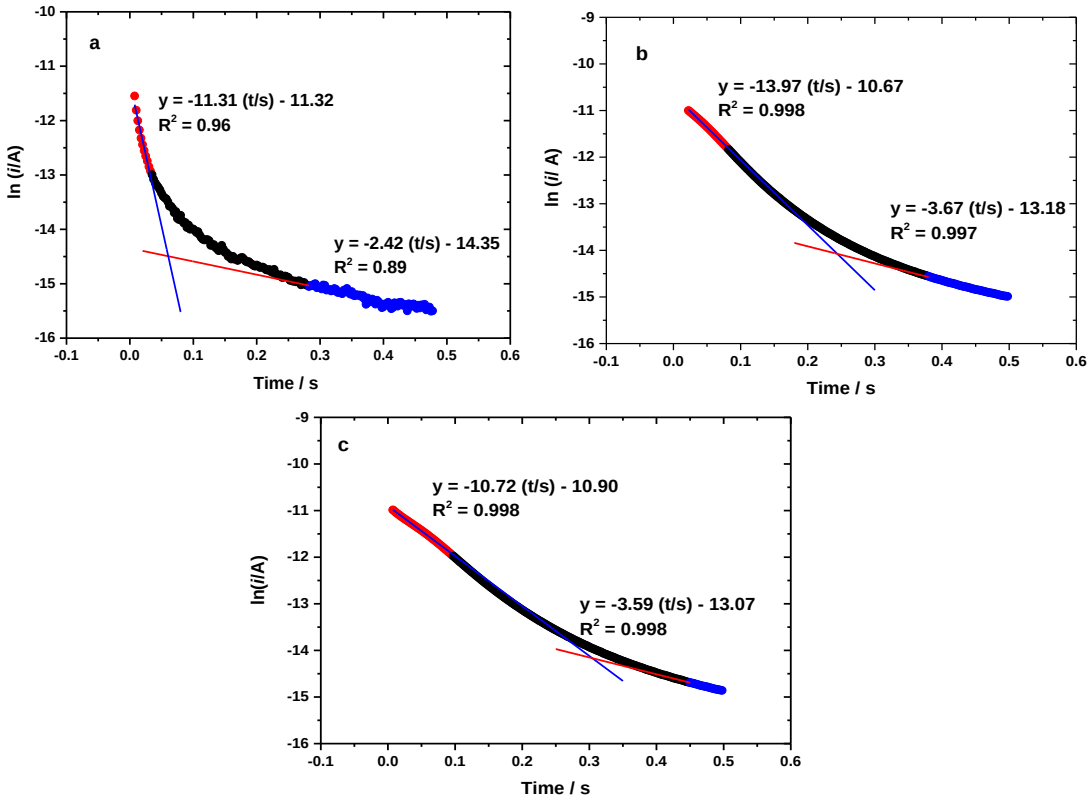

Figure 5.16; Semilog plots of ln *i* vs *t* for 3 different values of R_{ext} for the data from Fig. 5.15. a) Before adding R_{ext}. b) R_{ext} = 24 kΩ and c) R_{ext} = 30 kΩ.

Table 5.2; *RC* time constant and rate of electron transfer (k_s) obtained by linear fits plots of ln *i* vs *t*. The *RC* time constant was calculated from a slope of linear best fit at short times. k_s was directly determined from the slope of linear best fit at long times.

R_{ext} conditions / kΩ	Time constant (*RC*) /s	Rate of electron transfer (k_s) / s^{-1}
Without R_{ext}	0.018 ± 0.001	2.45 ± 0.03
24.0 kΩ	0.074 ± 0.002	3.76 ± 0.13
30.0 kΩ	0.094 ± 0.001	3.66 ± 0.06

5.8 Impendence measurements for R_t and C_{dl} at 24 kΩ

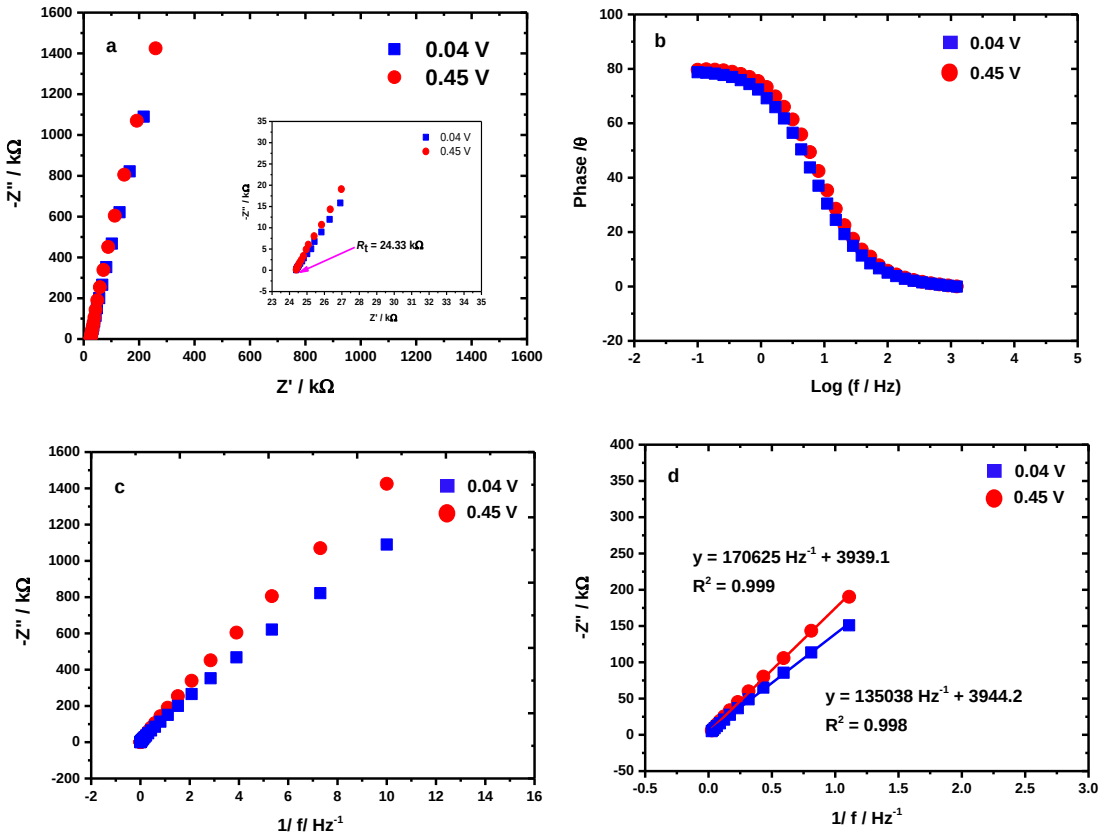

Figure 5.17; Nyquist plots for Os modified GC electrode at two different potentials (0.04 V and 0.45 V). The inset figure shows the enlargement of the Nyquist plot to show the presence of the total uncompensated resistance (R_t) in the electrochemical cell (R_u + R_{ext} of 24 kΩ). b) Bode plots at two different measured potentials. These plots were used to differentiate three distinct frequency regions (high, medium and low) in order to determine C_{dl}. c) Plots of imaginary impedance (-Z") *vs* 1/ frequency. d) The best linear fitting obtained from the low and medium range frequencies over plots of –Z" vs 1/f. The C_{dl} can be calculated from the slope of the linear fitting where m = 1/2πC_{dl}.

By measuring the EIS of the Os modified GC electrode with R_{ext} = 24 kΩ, the total uncompensated resistance (R_t) and C_{dl} for the modified electrode at two different potentials (0.04 V and 0.45 V) were determined. Performing the same data analyses as used for the AQ modified GC electrode, based on the Nyquist, Bode and -Z" vs 1/f plots (Figure 5.17), the R_t and the C_{dl} values at two different potentials were determined, Table 5.3.

Table 5.3; Total uncompensated resistance (R_t) and double layer capacitance (C_{dl}) from EIS for the two different measured potentials (0.04 V and 0.45 V) at R_{ext} of 24 kΩ for the Os modified GC electrodes.

Potential vs SCE / V	Total uncompensated resistance in the electrochemical cell (R_t) / kΩ	C_{dl} for covalently immobilised Os at the R_{ext} = 24 kΩ / μF
0.04	24.34 ± 0.03	1.01 ± 0.18
0.45	24.36 ± 0.02	0.82 ± 0.02

Based on Table 5.3, the C_{dl} data obtained for the monolayer of covalently immobilised Os are significantly lower than C_{dl} obtained from covalently immobilised AQ. Theoretically, the differential capacity of the double layer depends strongly on the electrode potential, surface structure, concentration of immobilised redox molecules and electrolyte composition and concentration[61]. Therefore, we believe all these characteristics contribute to the significant difference of the C_{dl} magnitudes between modified electrodes of AQ and Os. However, the prominent contributing factor in this case is the different surface concentration of immobilised Os to AQ at the GC electrode surfaces. This is because, the difference of the Γ_{CV} and $\Gamma_{DPV,\ sim}$ calculated for monolayer Os is 16 times that for AQ (~ 21:~350 pmol cm^{-2}). In addition, from R_t values, R is independent of the potentials as expected.

5.9 DPV simulation for Os modified GC electrode

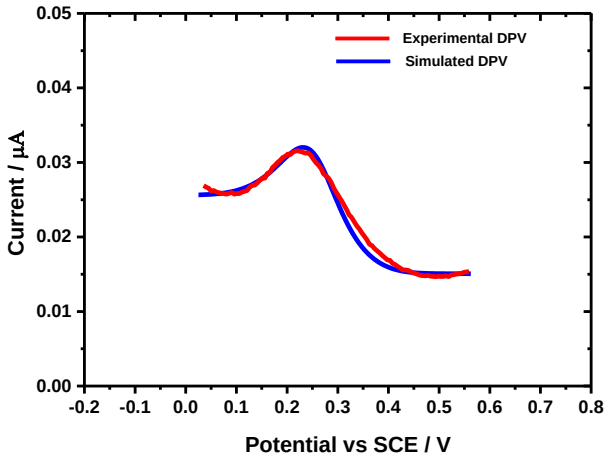

Figure 5.18; DPVs for the Os modified GC electrode with R_{ext} of 24 kΩ corresponding to the maximum DPV peak current. The red voltammogram is the experimental, measured at ΔE_p = 2.5 mV, τ_p = 0.05 s, τ_i = 0.5 s, ΔE_s = 5 mV and a DPV scan rate of 0.01 V s^{-1} in 0.1 M phosphate buffer solution at pH 7. In contrast, the blue curve is the best simulated DPV obtained by setting; k_s = 3.8 s^{-1}, R_t = 24.335 kΩ, α = 0.50, C_{dl} for reduced layer = 1.35 µF, C_{dl} for oxidised layer = 1.03 µF and ($\Gamma_{DPV, sim}$) = 23.1 pmol cm^{-2}. The R_t of 24.335 kΩ was directly determined from the Nyquist plots (Figure 5.17a). The same DPV parameters were used in the DPV simulation as employed in the experimental DPV.

Following the same procedures for the DPV simulation (Chapter 4) the best DPV fit for the Os modified GC electrode at R_{ext} of 24 kΩ was obtained. Figure 5.18 shows the comparison of the best response of the experimental and simulated DPV. All the parameters were extracted from the experimental measurements and the parameter values used in this simulation are given in Table 5.4. The simulated DPV gives an acceptable agreement to the experimental DPV. However, there is a slight deviation between the experimental and simulated responses. In that the experiment DPV peak a slight broader. The deviation could be due to a range of different microenvironments for the Os complex.

Table 5.4; Values for simulation parameters obtained from the experiments and used in the DPV simulation.

Simulation parameters	Experiment	Simulation
Redox potential (E°)	0.235 V	0.239 V
Total uncompensated resistance (R_t)	24335 Ω	24335 Ω
Transfer coefficient (α)	0.50	0.50
Rate of electron transfer (k_s)	3.76 s^{-1}	3.80 s^{-1}
C_{dl} for reduced form	1.12 µF	1.35 µF
C_{dl} for oxidised form	0.97 µF	1.03 µF
$\Gamma_{DPV, exp}$ vs $\Gamma_{DPV, sim}$	2.23 x 10^{-11} mol cm^{-2}	2.30 x 10^{-11} mol cm^{-2}

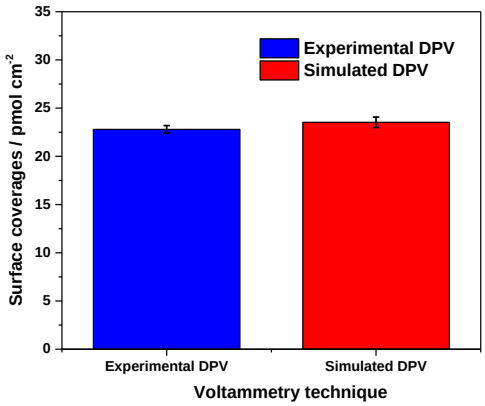

Figure 5.19; Comparison of the DPV surface coverages determined by experimental calculation and obtained by the best fit of the DPV simulations to the experimental DPVs.

The values of Γ_{DPV} from the simulation and experiment are shown in Figure 5.19. The data were obtained from three different modified electrodes. The two values are in good agreement.

5.10 Mixed AQ-Os monolayers modified GC electrodes

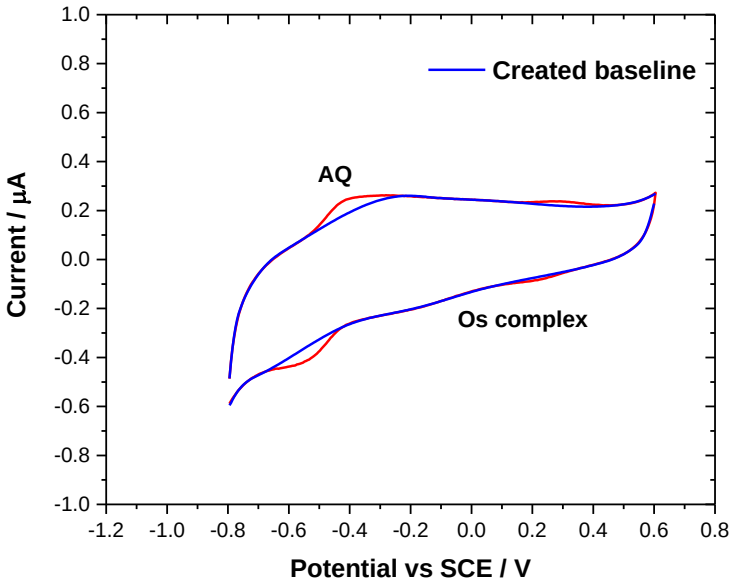

Figure 5.20; Cyclic voltammogram (CV) for AQ-Os mixed-monolayer modified GC electrode and the constructed baseline for the background current (blue). The measurements were carried out at a scan rate of 50 mV s^{-1} in 0.1 M pH 7 phosphate buffer solution. The electrode area is 0.071 cm^2.

The previous work for the individually immobilised AQ and Os show consistency between our experimental and simulation models in determining the surface coverages from DPV measurements. In this experiment, we wanted to verify if our experiment and simulation models could be used for two redox active molecules on the same electrode surface. Figure 5.20 shows the redox peaks for AQ and Os at mid-peak potentials of -0.48 V and 0.25 V vs SCE, respectively. The blue curve is the baseline created for the capacitive currents, constructed by Origin 9.1 software. By performing the same analysis using Origin software on the oxidation and the reduction CV peaks as used in previous chapters, the surface coverages for AQ and Os by CV were calculated, Table 5.4.

Table 5.5; The CV surface coverages for immobilised AQ and Os.

Redox probe	CV surface coverages / pmol cm^{-2}
Covalently immobilised AQ	10.87 ± 0.6
Covalently immobilised Os	5.69 ± 0.5

5.11 DPV surface coverages for AQ-Os mixed monolayers

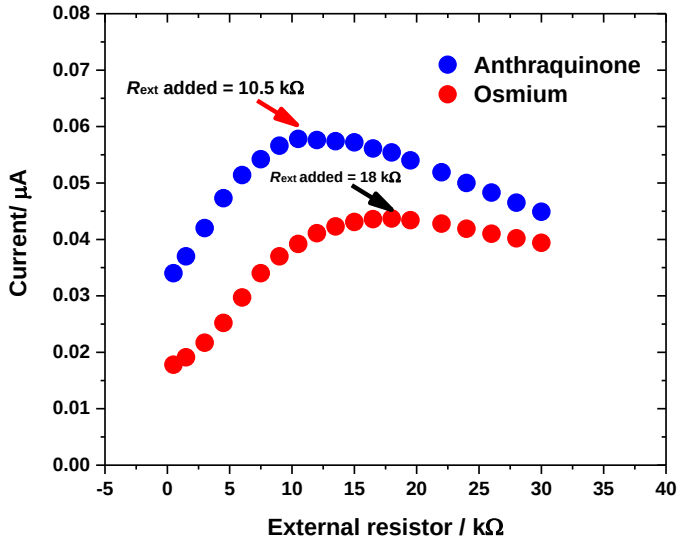

Figure 5.21; Plots of DPV peak currents before performing background subtractions against a series of R_{ext} added (0.5-35 kΩ) to the cell circuit for a mixed AQ-Os monolayer modified GC electrode in 0.1 M pH 7 phosphate buffer solution, measured at ΔE_p = 2.5 mV, τ_p = 0.05 s, τ_i = 0.5 s, ΔE_s = 5 mV and a DPV scan rate of 0.01 V s^{-1}. The measurements were carried out over the potential range between -0.8 to 0.6 V vs SCE at 25 ± 0.5 °C. The electrode area is 0.071 cm^2.

Applying a series of external resistances (R_{ext}) to the AQ-Os modified GC electrode and plotting the magnitudes of the DPV peak currents, curve peak current trends for AQ and Os (Figure 5.21) were obtained. R_{ext} of 10.5 kΩ produced the maximum DPV peak current for AQ, in contrast, R_{ext} of 18 kΩ gave the maximum DPV peak current for the Os complex. Based our experimental model, the DPV peak current responses at those R_{ext} values were integrated in order to calculate the Γ_{DPV} for the two couples.

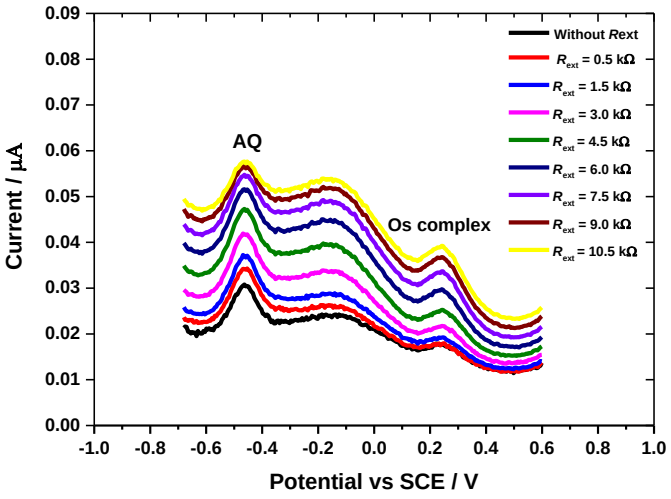

Figure 5.22; DPVs for covalently attached AQ-Os with R_{ext} added from 0.5-10.5 kΩ. The measurements were carried out with at ΔE_p = 2.5 mV, τ_p = 0.05 s, τ_i = 0.5 s, ΔE_s = 5 mV and a DPV scan rate of 0.01 V s^{-1} in 0.1 M pH 7 phosphate buffer solution. The electrode area is 0.071 cm^2.

Based on previous plots of the DPV current peak vs R_{ext} added, a general trend is that the baseline background current and DPV peak current increased together to reach a maximum current. As mentioned earlier for immobilised AQ, since the structure of the reduced and oxidised layers of AQ is different, C_{dl} is different at different potentials. In regard to the DPV currents above, as the potential was scanned from -0.75 to 0.6 vs SCE , the steep change in the background current from -0.1 V to 0.05 V is clearly contributed by a significant change in the double layer capacitance. As the magnitude of charging current is higher at -0.1 V than 0.05, this difference in capacity creates a significant baseline slope on the DPV signal.

The consistent effect of R_{ext} added on the Faradaic process, as observed for monolayers of AQ and Os GC modified electrodes, is not observed for the mixed-monolayer of AQ-Os. Figure 5.22 shows the DPV currents for AQ-Os modified GC electrode from 0.5 kΩ up to 10.5 kΩ. As mentioned above, at R_{ext} of 10.5 kΩ, the optimised DPV peak current for AQ was obtained. However, as noticeably seen in Figure 5.22, despite the DPV current at R_{ext} of 10.5 kΩ giving the maximum DPV peak current, the peak gets smaller. This may be caused by the total capacitance (C_t) of the process being broken down into two parallel components, which are C_{dl}, and C_f. As the *RC* time constant increases when R_{ext} goes from 0.5 to 10.5 kΩ added, the transient voltage across the parallel circuit takes longer to reach the maximum applied voltage. Also, the voltage across will not reach the actual value of applied voltage. Thus, it is believed that the decreasing Faradaic peak starting from R_{ext} = 6 kΩ is most likely to be caused Ohmic drop effects, where the massive *RC* time constant may obscure the Faradaic response by the charging/discharging processes.

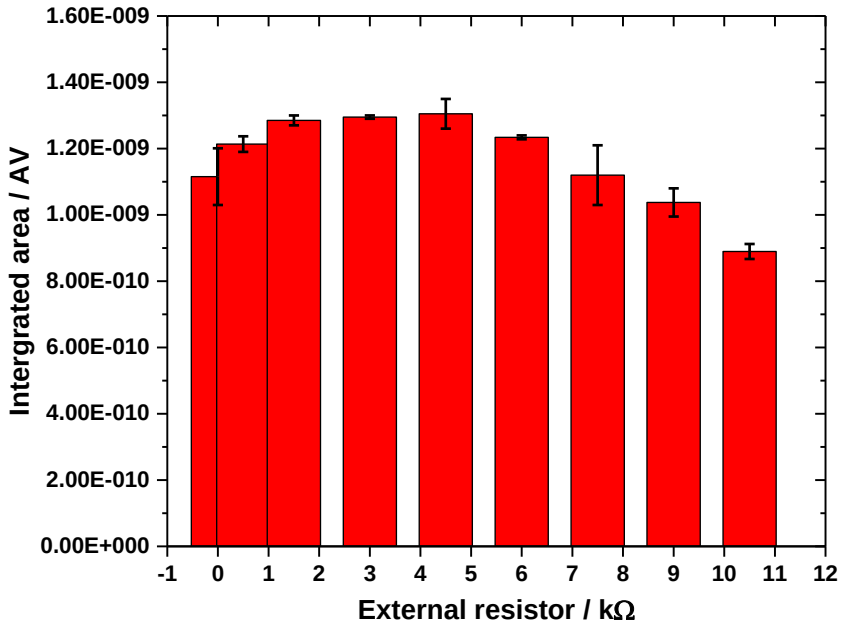

Figure 5.23; The integrated areas under the AQ DPV peaks at different R_{ext} from 0.5 kΩ to 10.5 kΩ obtained after performing background subtractions using Origin 9.1.

To overcome this problem in analysing the DPV surface coverages in the case of AQ in mixed-monolayers, every single DPV peak from 0.5 kΩ to 10.5 kΩ was integrated using Origin 9.1 in order to extract the DPV peak area. According to Equation 4.12, we already found that the area under DPV corresponds to DPV charge. As shown in Figure 5.23 the area under DPV peak at R_{ext} of 4.5 kΩ gave the biggest integrated area value. Thus, the DPV peak current at this R_{ext} value was used to determine the $\Gamma_{DPV,\,exp}$ of AQ with our modelled equation (Eq. 4.18). Meanwhile, the DPV peak current at R_{ext} of 18 kΩ was used to extract the $\Gamma_{DPV,\,exp}$ of the immobilised osmium complex.

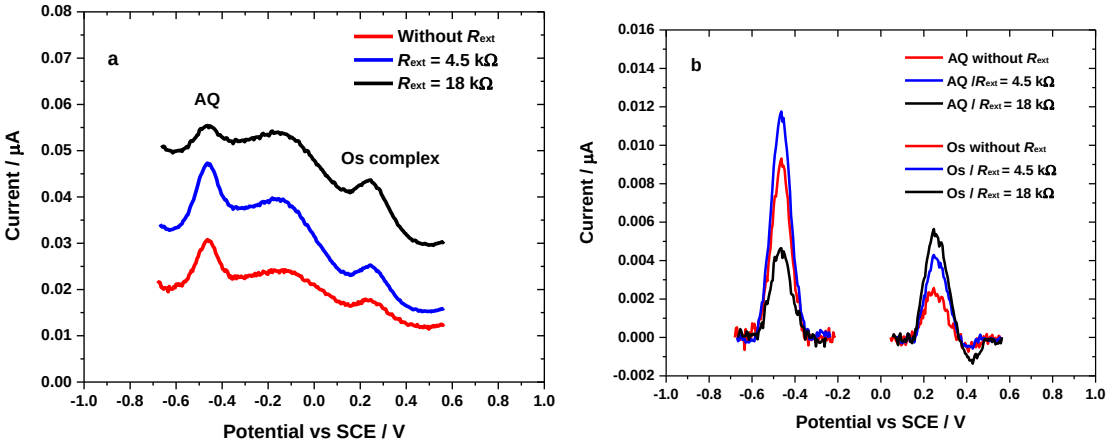

Figure 5.24; a) Differential pulse voltammograms for AQ-Os mixed monolayer modified GC electrode with the R_{ext} at 4.5 kΩ and 18.0 kΩ and without R_{ext}. b) The DPVs after performing background subtractions using Origin 9.1. The DPV baseline-corrected currents were integrated using Origin 9.1 software.The integrated areas were used to determine the Γ_{DPV} surface coverages of covalently immobilised AQ and Os.

Figure 5.24a shows three DPVs at different R_{ext} values in the electrochemical cell (R_{ext} =18 kΩ, R_{ext} = 4.5 kΩ and without external R_{ext}). Figure 5.24b, shows the background subtracted DPV currents. The background subtractions were only performed from -0.7 V to 0.2 V for the DPV peak for AQ and from 0.15 V to 0.6 V for the DPV peak for Osmium. Therefore, the calculated DPV surface coverages are given in Table 5.6.

Table 5.6; The determined DPV surface coverages for AQ-Os from mixed-monolayer.

Redox probe	DPV surface coverage / pmol cm^{-2}
AQ	9.49 ± 0.01
Os	13.87 ± 0.6

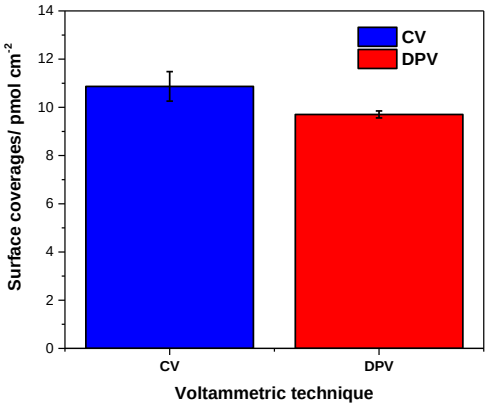

Figure 5.25; Comparison of the surface coverages determined by CV and DPV for covalently immobilised AQ at the surface of AQ-Os modified GC electrodes.

Figure 5.25 shows the bar plots of the surface coverages of AQ by CV and DPV techniques, respectively. The value form CV is slightly higher than Γ_{DPV} and is characterised by a bigger error bar. This could be due to the presence the differential background current as already discussed in Section 5.11 at around -0.2 V as shown in Figure 5.26. This overlaps with the oxidation current from the Faradaic process of AQ. Thus, extracting the area under the oxidation peak of AQ in Origin software is difficult.

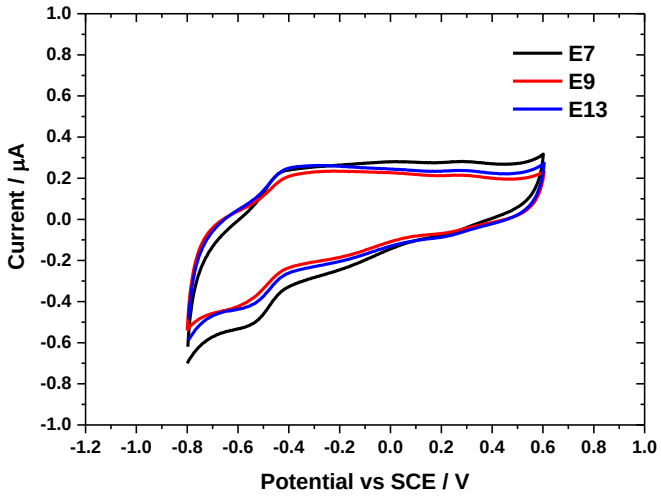

Figure 5.26; CVs for three different AQ-Os modified GC electrodes (sixth cycle shown). The CV measurements were run a scan rate of 50 mV s^{-1} in 0.1 M pH 7 phosphate buffer solution. The electrode area is 0.071 cm^2.

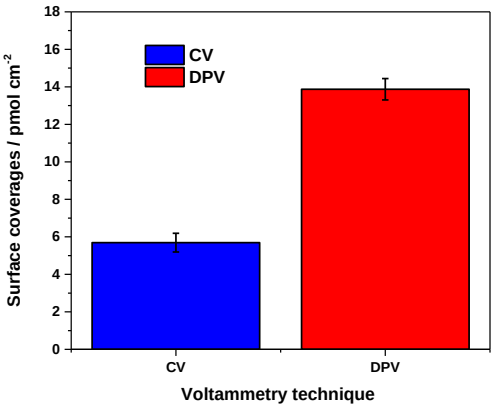

Figure 5.27; Comparison of the surface coverages by CV and DPV for covalently immobilised Os at the surface of GC electrodes.

Figure 5.27 shows bar plots for the surface coverages of immobilised Os from mixed-monolayers calculated from CV and DPV. Interestingly, the same pattern of data as obtained for the individually modified Os electrodes was observed. As shown before in Figure 5.11, by adding external resistance in the CV measurements, the redox currents increased. Figure 5.28 shows the amplification of the CV current by the addition of external resistances. As expected, the surface coverages calculated by CV were lower than those obtained by DPV, as shown in Figure 5.27.

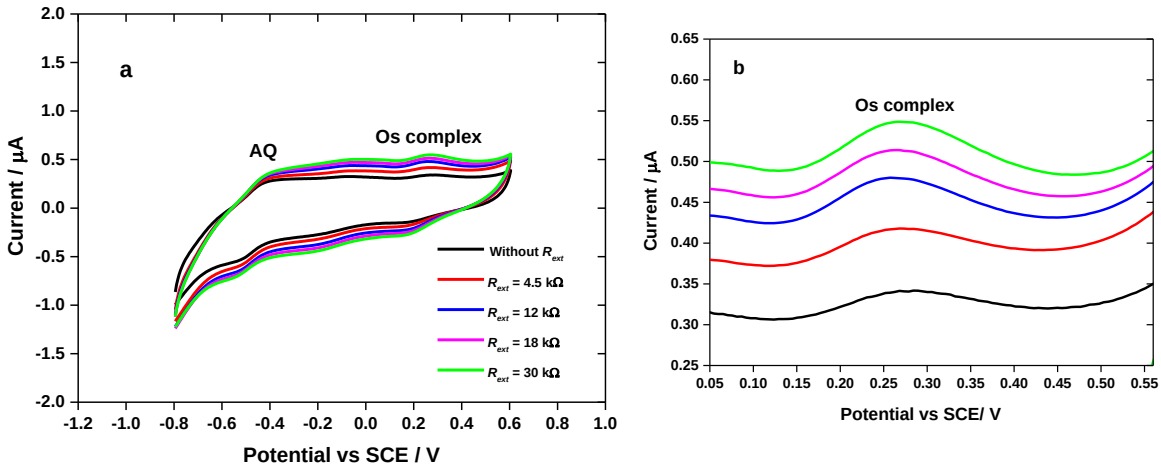

Figure 5.28; a) CVs for AQ-Os modified GC electrode with the R_{ext} added from 4.5 kΩ to 30 kΩ the black curve is the CV measurement without R_{ext}. The CV measurements were run at a scan rate of 50 mV s^{-1} in 0.1 M pH 7 phosphate buffer solution. The electrode area is 0.071 cm^2. b) Enlargement oxidation currents for Os from Figure 5.28a.

5.12 Impedance measurements for R_t and C_{dl} at 4.5 kΩ and 18 kΩ

Since the Γ_{DPV} for the mixed monolayers were determined from the DPV peak currents at R_{ext} of 4.5 kΩ and 18 kΩ, the determination of R_t and C_{dl} impedance was also conducted at these values. The same experimental conditions as employed in measuring R_t and C_{dl} for individually immobilised AQ and Os at the surface of GC electrodes were kept constant. By analysing the Nyquist plots, (the Bode plots and –Z" vs 1/f plots can be found in Appendix 5.1 and 5.2), the R_t and C_{dl} for the mixed-monolayer of AQ-Os were determined, Tables 5.7 and 5.8.

Table 5.7; Total uncompensated resistance in an electrochemical cell (R_t) and double layer capacitance (C_{dl}) from EIS at two different measured potentials (-0.70 V and -0.25 V) at R_{ext} of 4.5 kΩ for the AQ-Os modified GC electrodes.

Potential vs SCE / V	Total uncompensated resistance (R_t) in electrochemical cell / kΩ	C_{dl} for covalently immobilized AQ at R_{ext} = 4.5 kΩ / μF
-0.70	4.69 ± 0.02	2.83 ± 0.16
-0.25	4.70 ± 0.04	3.13 ± 0.14

Table 5.8; Total uncompensated resistance in an electrochemical cell (R_t) and double layer capacitance (C_{dl}) from EIS for two different measured potentials (0.04 V and 0.45 V) at R_{ext} of 18 kΩ for the AQ-Os modified GC electrodes.

Potential vs SCE / V	Total uncompensated resistance (R_t) in electrochemical cell / kΩ	C_{dl} for covalently immobilised Os at R_{ext} =18 kΩ / μF
0.04	18.37 ± 0.06	1.33 ± 0.09
0.45	18.38 ± 0.05	0.97 ± 0.02

5.13 DPV simulation for mixed-monolayer of AQ-Os

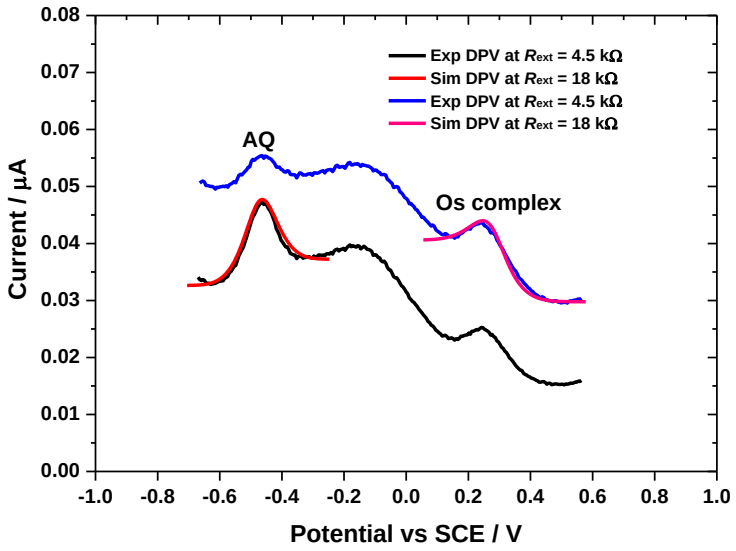

Figure 5.29; Differential pulse voltammograms for the AQ-Os modified electrode at R_{ext} of 4.5 kΩ (black) and 18 kΩ (blue). The black and blue voltammograms are experimental DPVs, measured at ΔE_p = 2.5 mV, τ_p = 0.05 s, τ_i = 0.5 s, ΔE_s = 5 mV and a DPV scan rate of 0.01 V s^{-1} in 0.1 M pH 7 phosphate buffer solution. In contrast, the red line is the best simulated DPV obtained for covalently attached AQ by setting k_s = 3.08 s^{-1}, R_t = 4.695 kΩ, α = 0.50, C_{dl} for reduced layer = 3.81 µF, C_{dl} for oxidized layer = 4.01 µF and $\Gamma_{DPV, sim}$ = 9.39 pmol / cm^2. In addition, the maroon is the best simulated DPV obtained for covalently attached Os by setting k_s = 4.1 s^{-1}, R_t = 18.381 kΩ, α = 0.50, C_{dl} for reduced layer = 2.29 µF, C_{dl} for oxidized layer = 1.80 µF and $\Gamma_{DPv, sim}$ = 14.6 pmol / cm^2 in the MATLAB script. The R_t of 4.695 kΩ for simulated DPV AQ and 18.381 kΩ for simulated DPV Os were directly determined from the Nyquist plots. The same DPV parameters were entered in the DPV simulation as used in the experimental DPV.

Following the same procedures as used in the DPV simulations for individually immobilised AQ and Os, the best DPV fits for mixed-monolayer of AQ-Os were also obtained. Figure 5.29 shows the best simulated DPV for the experimental DPV for AQ at R_{ext} of 4.5 kΩ (black), suggesting that the best fit DPV to experimental DPV was responded at $\Gamma_{DPV, sim}$ value of 9.39 pmol cm^{-2}.

The blue curve is the best simulated DPV for Os at R_{ext} of 18 kΩ, corresponded to the optimal surface coverages of 14.6 pmol cm^{-2}. All the parameters extracted from the experimental measurement and the parameters used in the simulations are shown in Table 5.9. It is clearly that both datasets are in quantitative agreement.

Table 5.9; Values for parameters obtained from the experiments and used in the DPV simulation for mixed monolayers of AQ and Os complex.

	AQ		Os	
Parameters	**Experiment**	**Simulation**	**Experiment**	**Simulation**
Redox potential (E°)	-0.470 V	-0.476 V	0.276 V	0.279 V
Total uncompensated resistance (R_t)	4695 Ω	4695 Ω	18380 Ω	18380 Ω
Transfer coefficient (α)	0.50	0.50	0.50	0.50
Rate of electron transfer (k_s)	3.98 s^{-1}	3.08 s^{-1}	3.76 s^{-1}	4.1 s^{-1}
C_{dl} for reduced form	2.88 µF	3.81 µF	1.42 µF	2.29 µF
C_{dl} for oxidised form	3.13 µF	4.01 µF	0.99 µF	1.80 µF
$\Gamma_{DPV, exp}$ vs $\Gamma_{DPV, sim}$	9.35 pmol cm^{-2}	9.39 pmol cm^{-2}	13.8 pmol cm^{-2}	14.1 pmol cm^{-2}

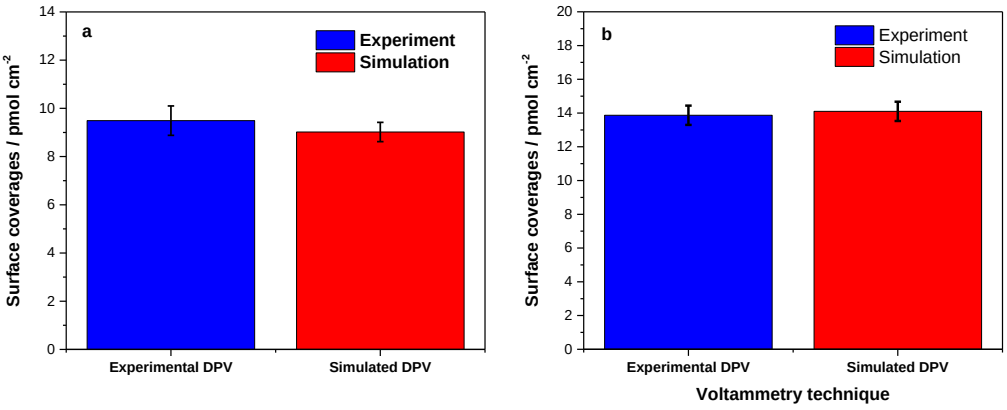

Figure 5.30; Comparison of the DPV surface coverages determined by experimental calculations (blue) and obtained from the best response of the DPV simulations (red) for covalently attached AQ (a) and Os (b).

Figure 5.30 depicts the comparison of DPV surface coverages for AQ from mixed-monolayer that were determined by the experimental model and obtained from the simulation model. By contrast, Figure 5.30b shows the comparison of Γ_{DPV} for the covalently immobilised Os. The trend found here resulted is again consistent, showing that our models are working well, despite two different redox molecules being covalently immobilised at the same surface of GC electrodes.

5.15 Conclusion

The utility and the flexibility of the experimental approach and simulation model was first demonstrated in this Chapter for covalently immobilised Os bipyridine complex at the GC electrode surface. The calculated $\Gamma_{DPV,\,exp}$ data for immobilised Os are in good agreement with the data obtained from the simulation.

In addition, the experimental model was used for AQ and Os co-immobilised at the GC electrode (mixed monolayers). In the first step of analysing the data, a problem was encountered for the AQ redox system due to the size of DPV peak getting smaller as R_{ext} added of 10.5 kΩ. Hence, the determined charge under the DPV peak was significantly smaller. As we have demonstrated earlier in Section 4.12 and 4.13 (Chapter 4), the integrated area under a DPV peak could determine the DPV charge. Hence, in order to overcome this problem, the integrated area under every DPV peak from R_{ext} of 0.5 kΩ to 10.5 kΩ were extracted using Origin 9.1. The maximum area under the DPV peak was obtained at an R_{ext} of 4.5 kΩ. Subsequently, the DPV charge and $\Gamma_{DPV,\,exp}$ for immobilised AQ were calculated. In contrast, this problem did not occur in determining $\Gamma_{DPV,\,exp}$ for Os in the mixed-monolayer. Thus, using the same approach as used for the individual immobilised AQ and Os layers, the surface coverages of Os (in the mixed monolayer) were directly determined. Consistently, the determined $\Gamma_{DPV,\,exp}$ for AQ gave a good correlation with the CV measurement. By contrast, $\Gamma_{DPV,\,exp}$ estimated for the Os complex agreed moderately well with $\Gamma_{CV,}$ but was slightly larger.

To verify our determined $\Gamma_{DPV,\,exp}$ values for the immobilised Os and AQ-Os mixed monolayers from the experimental approaches, DPV simulations were carried out. Overall, based on the simulation best fits, good agreement with the experiments was obtained.

Based on the results presented here, the consistency of the developed models has been demonstrated. The proposed experimental and theoretical models for estimating Γ_{DPV} will be investigated on a different modified electrode surface. For instance, in Chapter 7, in order to show the more utility and flexibility of the experimental and the simulation models, both models will be applied to the immobilised AQ-ssDNA redox system at a surface of gold (Au) electrodes.

Chapter 6: The effect of weak base on the electrochemical attachment of primary amines

6.1 Overview

Chapter 4 described the electrochemical grafting of ethylenediamine (EDA) linker in acetonitrile (ACN) at GC electrodes that have been utilised to covalently attach anthraquinone. In this chapter, the effects of the presence of an aqueous weak base in acetonitrile on the electrochemical attachment of aliphatic primary amine linker at the GC electrode surface is described. The motivation for this research was provided by a piece of work that had been done by Dr. Pinzewska, a former postdoctoral researcher under the supervision of Professor Philip Bartlett and Professor Jeremy Kilburn (Queen Mary, University of London). In her work, she successfully showed that by mixing 20% volume of 0.1 M aqueous sodium hydrogen carbonate ($NaHCO_3$) in acetonitrile (ACN) for electrochemical grafting of EDA-flavin onto GC electrodes, a higher surface coverage (Γ) of covalently immobilised of flavin was obtained. In the present work, a model system of a primary aliphatic amine linker of (EDA) bearing AQ as a redox probe has been used. The simulation on oxidation CVs of the EDA-Boc has been performed using our developed MATLAB script to investigate the theoretical responses of electrochemical grafting of EDA-Boc. Moreover, the CV and DPV surface coverages of covalently immobilised AQ coupled to the EDA linker after attachment in a mixed solvent of ACN/$NaHCO_3$ (method 2) are compared to the surface coverages of AQ coupled to grafted EDA linker in neat ACN (method 1). In order to demonstrate the utility of our model for estimated DPV surface coverages, the DPV simulations have also been performed on experimental DPVs for the immobilised AQ.

6.2 General method for attachment of EDA-Boc (Method 1)

Over the last eight years, our group has reported in the literature results for the modification of electrodes based upon covalent immobilisation of organic redox molecules and redox-active proteins using electrochemical oxidation of primary amine linkers with tert-butyloxycarbonyl (Boc)-protected amino groups at carbon electrodes[54,55]. The electrochemical oxidation of amine enables the formation of a strong covalently bond between nitrogen and the carbon surface. There after an amine-functionalised surface is created after removing the Boc group. This surface modification can then be followed by the use of solid-phase synthesis to couple various redox groups with carboxylic acid functionalities. In this part of my work, a covalently immobilised linker of EDA-Boc subsequently coupled with AQ has been used as a model system as it had previously given the greatest surface coverages of AQ compared to a range of linkers that had been investigated on glassy carbon electrodes[55].

Basically, before coupling of AQ to the EDA linker, we attached the EDA-Boc onto GC electrode by electrochemical oxidation in acetonitrile (ACN) containing tetrabutylammonium tetrafluoroborate (TBATFB) supporting electrolyte as shown in scheme 6.1. After attachment of EDA-Boc, the Boc group was removed with 4 M HCl in dioxane to give an amine functionalized surface.

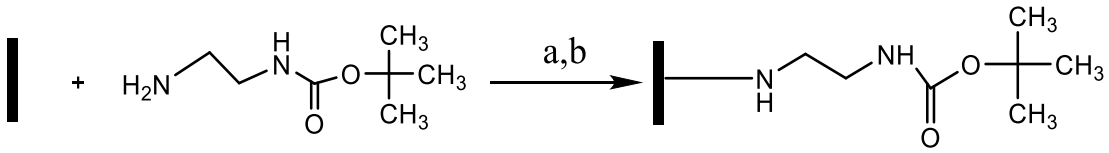

Scheme 6.1; Established method for electrochemical immobilisation of EDA-Boc to a surface of GC electrodes in our research group. a) 10 mM solution of EDA-Boc in ACN with 0.1 M TBATFB, b) cyclic voltammetry 0 -2 V *vs* Ag/AgCl, 50 mV/s for 7 cycles.

As reported in the literature for electrochemical attach of amines onto the carbon surface, the formation of a strong carbon-nitrogen (C-N) bond on the electrochemical grafting of amines to carbon surfaces is driven by the unstable radical cation formed from an oxidation reaction of amines involving a one electron process. Nevertheless, more careful investigations suggested that a C-N bond is formed by a neutral radical that reacts on the surface of carbon [159–161]. The neutral radical is generated after deprotonation of the unstable radical-cation as shown in scheme 6.2. Therefore, one of the main aims of this work is to study in more detail the effect of the chemical deprotonation step of the radical-cation on the overall rate of the covalently immobilisation of EDA-Boc.

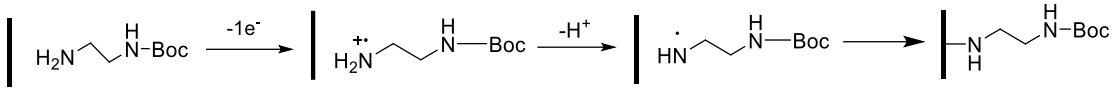

Scheme 6.2; Established mechanistic sequence taking place during the electrochemical oxidation of primary amines in non-aqueous solvents.

ACN was selected as a solvent medium for the oxidation reaction of EDA-Boc rather than DMF and ethanol because it has a good dielectric constant. Moreover, it is electrochemically inactive at the high potential that is usually required for the formation of the amine radical cation. Last but not least, the aliphatic amines are more basic in ACN than in DMF[162]. However, a major interest in this work is to study a new covalent attachment method for N-EDA-Boc at the GC electrodes in the mixed solvent of ACN and a weak base, $NaHCO_3$.

6.3 New method for covalent attachment of EDA-Boc (Method 2)

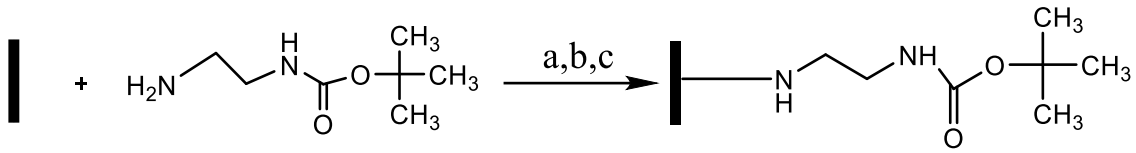

Scheme 6.3; A new method for electrochemical immobilisation of 10 mM EDA-Boc with 0.1 M TBATFB to a surface of GC electrode in the mixed solvents of ACN/$NaHCO_3$ with a ratio of 4:1. a) 8 ml ACN, b) 2 ml of 0.1 M $NaHCO_3$ c) cyclic voltammetry 0 -2 V *vs* Ag/AgCl, 50 mV/s for 7 cycles.

Scheme 6.3 shows sodium hydrogen carbonate employed in a modified method to covalently attach EDA-Boc at the surface of GC electrodes. $NaHCO_3$ is an amphoteric compound. Aqueous solutions of $NaHCO_3$ are very mildly alkaline due to the formation of carbonic acid and hydroxide ion as shown in Scheme 6.4 and could provide more alkaline medium for electrochemical oxidation of EDA-Boc.

$$NaHCO_{3(s)} + H_2O_{(l)} \longleftrightarrow Na^+_{(aq)} + HCO_3^-{}_{(aq)} + H_2O \longleftrightarrow Na^+_{(aq)} + H_2CO_{3(aq)} + OH^-_{(aq)}$$

Scheme 6.4; Equilibrium of sodium hydrogen carbonate ($NaHCO_3$) in water.

As discussed by Oliver and co-workers[163] on the electrochemical attachment of a conjugated amino-ferrocifen complex onto a carbon surface, the presence of a base generally facilitates the deprotonation of the radical-cation to generate neutral radicals as a tool for the formation of the nitrogen-carbon bond. This agreement has been shown with a slight shift of potential redox of amino group and a loss of reversibility CV waveform for the immobilised amino-ferrocifen complex. In addition, Masaichiro *et al.* [164] stated that amines undergo an oxidation process more easily in basic solution rather than in acidic solution. Hence, we believe that with the presence of $NaHCO_3$ solution in ACN as a medium for the attachment EDA-Boc, it should enhance the

generation of neutral radicals of EDA-Boc and improve the efficiency of grafting EDA-Boc to the surface of GC electrodes as compared to neat ACN.

6.4 Simulation for the electrochemical grating EDA-Boc

Electrochemical grafting reactions by adsorbing or electrode derivatizing species to the surface of electrodes lead to passivation of electrode reactions in which the surface is fully covered by electrochemical grafted species after the completion of reaction[165]. Generally, there are two different electrochemical attachment reactions that can be employed to generate radicals for reacting with the surface of electrodes to form stable covalent bonds. The first method is based on amine oxidation and the second method is reduction of aryl diazonium salts[160,166]. Saveant and co-workers[165,167] have provided a theoretical model to analyse self-inhibition reactions from simple repetitive CV data and to predict how the film forms with time in preparative-scale electrolysis. However, this model is only valid for the reaction scheme shown in Scheme 6.5.

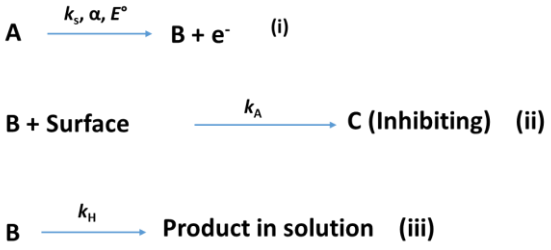

Scheme 6.5; Common mechanism for inhibition of electrode surface reaction.

In their model, the CV waveform on the first cycle and the significant decrease in the subsequent cycles of CV currents is determined by several electrochemical parameters which describe the kinetic competition of radical species at the surface (k_A) to solution reactions (k_H), the diffusion coefficient of the substrate ($D_\circ$) and the coverages of the inhibiting species (Γ). Therefore, it can be deduced that the decreased of currents during repetitive cycling is a convenient way for monitoring the development of either monolayer or multilayer blocking films.

As the Saveant model was developed for electrochemical grafting of the diazonium salt, here, in this experimental Chapter, we were interested to apply the model on electrochemical grafting of the primary amines at the surface of the GC electrode. In this work, a primary amine of the EDA-Boc molecule was used as an experimental model. From previous work reported by previous group members, the immobilisation of aliphatic of primary amines to the surface of carbon electrodes that took place in ACN constantly show the passivation of electrode surface on the responses of irreversible cyclic voltammetry. Noticeably, on the second scan of CV measurement,

the CV current significantly decreased and for the subsequent cycles, it will then totally disappear. Hence, under such conditions, it is hard to determine any significant electrochemical parameters as the reversibility of CV could not be obtained[159]. Therefore, we are really interested to investigate the theoretical analysis over the experimental voltammogram of electrochemical grafting EDA-Boc

As mentioned earlier, we have used simulation codes written in MATLAB software and based on the model described in Saveant's 1995[165] article. The software was written by Associate Professor G. Denuault and the script codes for the MATLAB simulation are given in Appendix 6.1. In the Saveant model[165], he assumed that the homogenous reaction is very fast, hence the B species has no time to diffuse in solution. By contrast, in our simulation model, we assume that the B species can be transported back to the bulk solution by diffusion. From the numerical model, we wish to extract the reaction parameters such as D_o, Γ_{max}, k_A, k_H, and k_S. However, these parameters can not be determined directly by experimental approaches. The one exception is D_o, where we have experimentally attempted to estimate the D_o values using the Randles-Sevcik and the Cottrell equations.

6.5 CV for attached EDA-Boc in neat ACN and ACN/$NaHCO_3$ (4:1)

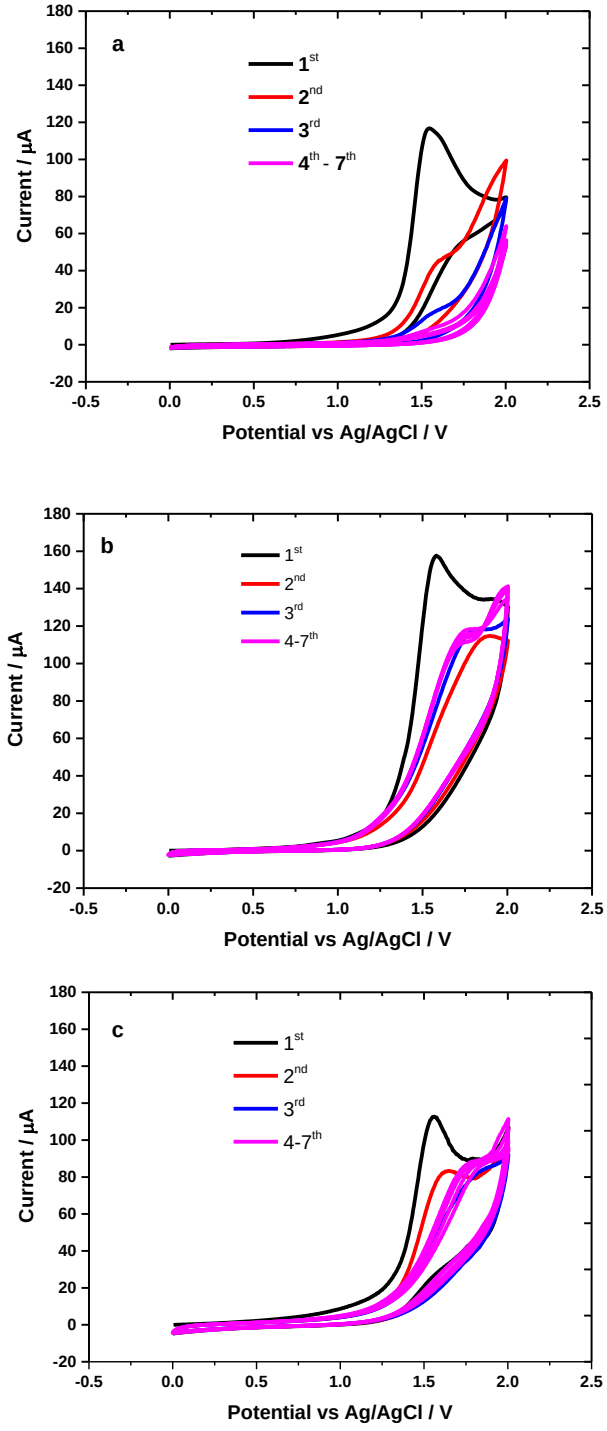

Figure 6.1; Cyclic voltammograms recorded for 10 mM of EDA-Boc with 0.1 M TBATFB carried out in a) neat ACN, b) in 20 % of 0.1 M $NaHCO_3$ in ACN and c) in 20% of water in ACN. All the experiments were recorded at a scan rate of 50 mV/s for 7 cycles. The electrode area was 0.071 cm^2.

The EDA-Boc is an aliphatic primary diamine in which one of amine groups is protected by tert-butyloxycarbonyl (Boc) group. The immobilisation of mono-EDA-Boc in ACN takes place through the unprotected amine group to form a uniform, packed organic monolayers on GC electrode surfaces. The advantage of this linker is that it avoids the formation of bridge or multilayer structures that have been observed with the oxidation of unprotected diamine compounds[168]. Basically, a strong attachment of nitrogen (N) to the glassy carbon surface occurs by reaction of the radical with sp^2 carbon at the electrode surface. The formation of the amine radicals from the electrochemical oxidation of EDA-Boc can be seen as a broad CV peak at around 1.56 V *vs* Ag/AgCl as shown in Figure 6.1(a). The absence of the corresponding cathodic peak on the reverse scan indicates that amine radical cations generated during the forward scan undergo fast chemical reaction, either binding to the GC surface or forming dimer or polymeric species in solution[55]. Moreover, the drastic decrease of the oxidation peak for EDA-Boc on the second and third cycles indicates that the electrode surface is being passivated by EDA-Boc radicals. In the subsequent cycles (4^{th} to 7^{th}) the passivation of the carbon electrode surface by the EDA-Boc layer is complete and blocks the further oxidation of EDA-Boc.

In contrast, Fig. 6.1(b), shows 7 cycles of CV for attachment of EDA-Boc at the carbon surface in a ratio of 1:4 $NaHCO_3$ solution to acetonitrile. Noticeably, there is a very different CV response compared to Fig. 6.1(a), particularly in the shapes of the anodic peaks, the magnitudes of the currents for the first and subsequent cycles and the blocking of electrode surface by EDA-Boc . In terms of blocking the surface, on the 2^{nd} cycle (red line) the carbon surface has been completely passivated by the layer of EDA-Boc. It can be concluded that the passivation of the surface towards amine oxidation in a mixture of ACN/$NaHCO_3$ (method 2) has occurred more rapidly than in neat ACN (method 1). However, on the 4^{th} to 7^{th} cycles, smaller oxidation peaks appeared at around 1.72 V, which may result from the oxidation of water to form oxygen.

In order to verify that the smaller peaks in Fig 6.1(b) correspond to the oxidation of water, a study of electrochemical oxidation EDA-Boc in a mixture ratio of 1:4 water to ACN was conducted. Figure 6.1(c) show that the 3^{rd} scan, the blocking carbon surface had occurred. In contrast, the oxidation peaks are clearly observed on the 4^{th} to 7^{th} cycles, confirming that the peaks around 1.69 V *vs* Ag/AgCl are due to the oxidation of water. Note also from the comparison of Fig. 6.1(a) and 6.1(c) to Fig. 6.1(b), the anodic current that was produced in a mixed solvent of ACN/$NaHCO_3$ is larger than in ACN or in ACN/water. It can initially be concluded that the presence of $NaHCO_3$ can generate more amine radical cations and facilitate the deprotonation process at the GC electrode surface.

Due to the fact that amines are more readily oxidised in more basic solution[164], the pH for three different solvents that had been used as media for electrochemical attachment of EDA-Boc were

also measured. The pH of solutions for neat ACN, ACN/water, ACN/$NaHCO_3$, are 10.20, 10.37 and 11.18, respectively. Hence, it shows that the pH of ACN/$NaHCO_3$ is slightly higher than neat ACN. This is consistent with our initial observation that the presence of base $NaHCO_3$ increases the quantity of amine radical produced as preliminarily results in Fig. 6.1(b). Secondary to this point the deprotonation rate of the substrate is affected by the pK_a of the buffer, hence the deprotonation step of the amine radical cation increases when pK_a (buffer) > pK_a substrate[169]. However, we did not know the pK_a for ACN/$NAHCO_3$, but based upon measured pH values, it indicates that the pK_a value of ACN/$NAHCO_3$ is slightly higher than neat ACN. This results from the presence of a weak base that may alter the pK_a of ACN/$NaHCO_3$ to more alkaline.

Taking into consideration the second scan of the CVs from Figure 6.1a and b, clearly, the turning current of the reverse scan CV for EDA-Boc in neat ACN is considerably higher than in ACN/$NaHCO_3$. We believe that the partial coverages of EDA-Boc were formed after the first cycle. This leads to a non-uniform/ porous layer[170] with some defect sites. Consequently, this generated a higher residual current at more positive potentials. In contrast, the electrode surface was fully blocked by the EDA-Boc film after the fourth scan as the magnitude of the residual current at more positive potential is significantly reduced. However, this is not the case for the coupling of EDA-Boc in ACN/$NaHCO_3$ as the passivation of the electrode surface took place after the first cycle. The residual currents produced during the process will be shown in detail in the next section.

6.6 Residual current after passivation of the electrode surfaces

In the previous section, as shown in Figures 6.1a and b, we have observed that there is a significant different in the CV waveform, particularly the residual currents on the addition of $NaHCO_3$. The residual currents may be generated from the EDA-Boc radicals by forming dimers or polymeric species in the bulk solution[55], and become more significant at more positive applied potential. By contrast, in the case of the electrochemical grafting of EDA-Boc in ACN/$NaHCO_3$, a small peak from the oxidation of water was obtained. In order to confirm these observations, we have investigated the origin of the residual background current. Thus, we have experimentally measured the background solvent currents using a bare GC electrode and a modified GC electrode with EDA-Boc films in several different solutions.

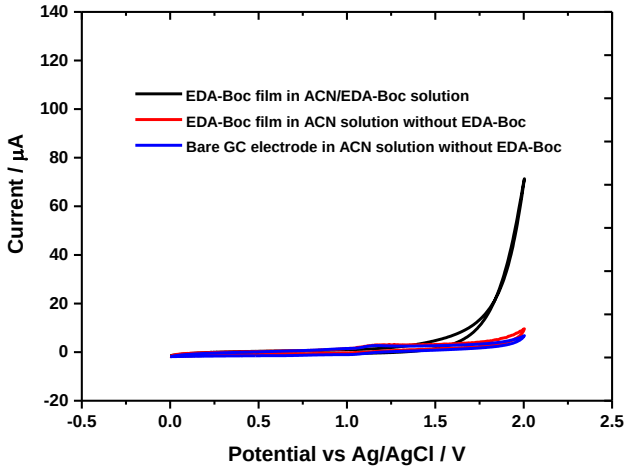

Figure 6.2; CVs showing effect of solvents on bare GC electrode and EDA-Boc modified GC electrodes (third cycle shown). The blue line is a scan taken at bare GC electrode in neat ACN. On the contrary, the red line is a scan taken at EDA-Boc modified GC electrode in neat ACN and the black line is a scan taken from re-measured EDA-Boc modified GC electrode in ACN solution containing EDA-Boc. The scan rate was 50 mV/s and the electrode area was 0.071 cm^2.

In the case of the grafting of EDA-Boc in neat ACN, Figure 6.2 shows the residual currents from two different solutions. The black and the red CVs were obtained when measuring bare and modified GC electrodes in ACN. The modified electrodes were then re-measured in ACN solution in the presence of 10 mM EDA-Boc and the result is shown by the black CV. We believe that the residual current was contributed from EDA-Boc radical species in bulk solution.

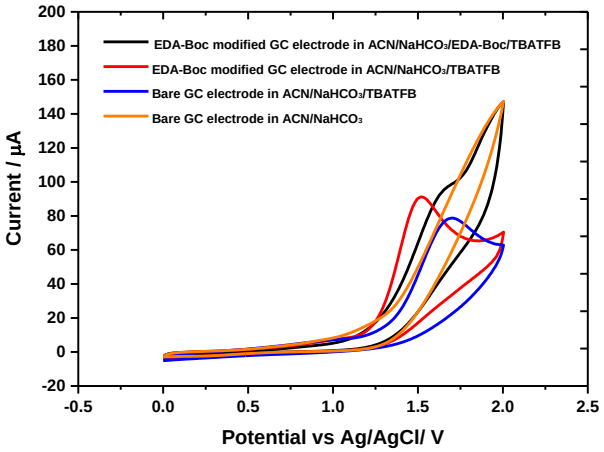

Figure 6.3; CVs showing effect of solvents on bare GC electrode and EDA-Boc modified GC electrodes (third cycle shown). The blue line is a scan taken at bare GC electrode in ACN/$NaHCO_3$ solution containing 0.1 M TBATFB. The orange line is a scan taken at bare GC electrode in neat ACN/$NaHCO_3$ solution without TBATFB. By contrast, the red line is a scan taken at EDA-Boc modified GC electrode in ACN/$NaHCO_3$ solution containing 0.1 M TBATFB and the black line is a scan taken from re-measured EDA-Boc modified GC electrode in ACN/$NaHCO_3$ solution containing 10 mM EDA-Boc and 0.1 M TBATFB. The scan rate was 50 mV/s and the electrode area was 0.071 cm^2.

As can be seen from the CV data for the electrochemical grafting of EDA-Boc in ACN/$NaHCO_3$, on the third cycle of CV, an irreversible peak appeared at around 1.69 V vs Ag/AgCl. The peak is from the oxidation of water. By conducting the same experiment as mentioned above, the residual current from the ACN/$NaHCO_3$ solvent was investigated. Based on Figure 6.3, the blue and the red CVs were obtained when measuring the bare GC and modified electrodes in the blank solvent of ACN/$NaHCO_3$. In contrast, the black CV was obtained when re-measuring the modified electrode in the ACN/$NaHCO_3$ solvent containing EDA-Boc. Thus, it can be concluded that in the absence of EDA-Boc in solution, the oxidation of water in the supporting electrolyte of TBATFB is greatly enhanced. In order to support this statement, we had run a CV measurement on the bare GC electrodes in ACN/$NaHCO_3$ without TBATFB (orange) and it shows no interference of the oxidation of the solvent-supporting electrolyte system.

6.7 Attachment of the EDA-Boc assisted by DBU base

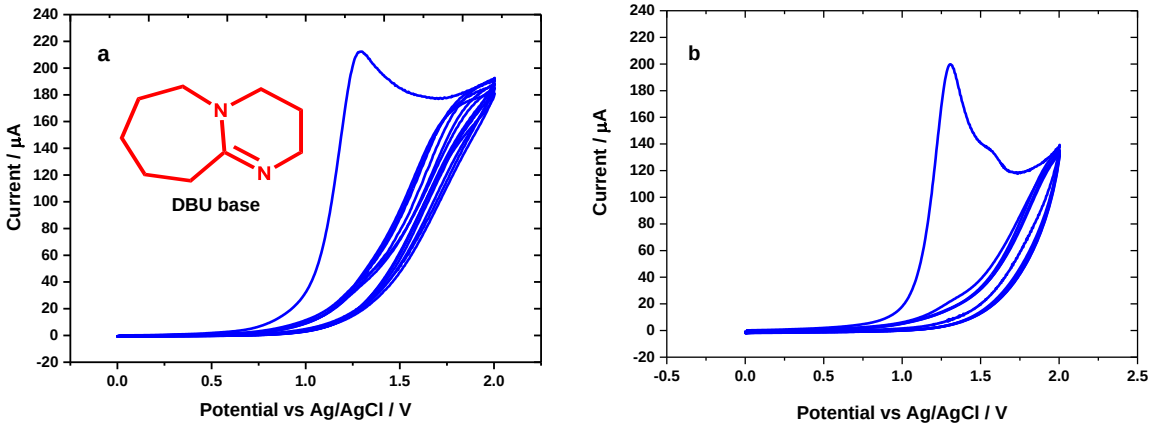

Figure 6.4; a) Cyclic voltammograms recorded for 20% 0.1 M DBU base in ACN with 0.1 M TBATFB. b) Cyclic voltammograms recorded for 20% 0.1 M DBU base in the presence of 10 mM EDA-Boc in ACN with 0.1 M TBATFB. All the experiments were measured at a scan rate of 50 mV/s for 7 cycles.

In the study conducted by Olivier *et al.*[58] on electrochemical grafting of the amino-ferrocifen complex in the presence of the aromatic base 2,4,6-trimethyl-pyridine (collidine), they showed that the successful of deprotonation of aromatic amine radicals where the oxidation peak of the amine on the CV significantly changed. However, the presence of collidine in their experiments did not increase the surface coverages of the amino-ferrocifen complex when compared to the surface coverages of attached amino-ferrocifen complex in the absence of collidine. The same results had been obtained by Tanaka and co-workers[171] where they showed that the presence of collidine did not promote the grafting efficiency of aliphatic amines. This might be related to the relatively weak basic character of the trimethyl-pyridine in comparison to the base properties of the aliphatic primary amine[171]. Therefore, here we attempted to study the effect of a stronger

organic base on the electrochemical grafting of EDA-Boc. The non-nucleophilic, strong base 1,8-diazabicycloundec-7-ene (DBU) is classified as a proton sponge. Figure 6.4 (a), shows the CV for seven cycles in 20 % 0.1 M DBU in ACN in the absence of EDA-Boc. The CV shows a well-defined anodic peak at 1.25 V *vs* Ag/AgCl resulting from the formation of the DBU tertiary amine cation radical. In contrast, Figure 6.4 (b) shows seven cycles of CV for 20% 0.1 M DBU in ACN in the presence of 10 mM EDA-Boc. Clearly, the same potential of oxidation wave around 1.25 V *vs* Ag/AgCl is seen in both cases. However, the normal oxidation peak of EDA-Boc around 1.5 to 1.65 V vs Ag/AgCl disappeared. This results from the oxidation of DBU that took place at lower potential than the oxidation of EDA-Boc, and it completely blocked the electrode surface, forming a DBU film after the first scan of the CV measurement. As a result, the DBU film inhibits the grafting process of EDA-Boc. From this experiment, we can conclude that by using a strong base for electrochemical grafting EDA-Boc to the GC electrode surface, this approach completely halted the electrochemical grafting of EDA-Boc to the GC electrode surface.

6.8 Electrochemical oxidation of EDA-Boc in acidic solution

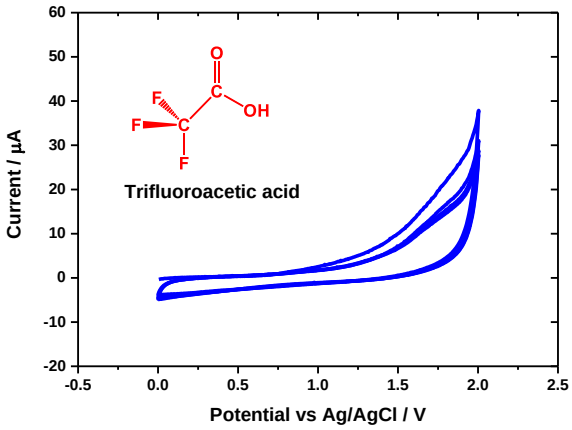

Figure 6.5; Cyclic voltammograms recorded for 10 mM EDA-Boc in ACN with 0.1 M TBATFB in the presence of 20% of trifluoroacetic acid (TFA). All the experiments were measured at potential scans from 0 – 2 V *vs* Ag/AgCl with a scan rate of 50 mV/s for 7 cycles.

In order to show the effect of the deprotonation step and overall efficiency of the attachment of EDA-Boc to the GC electrodes, the electrochemical oxidation of EDA-Boc in the acidic solvent was studied. Figure 6.5 shows the CV for the seven cycles of EDA-Boc in ACN in the presence of 20% trifluoroacetic acid (TFA) 0.1 M. It is clear that the normal oxidation peak EDA-Boc disappeared. This result confirms that the changing of pH to more acidic conditions gives significant effect on the deprotonation step of amine radical cations. The excess protons from the

dissociation of TFA acid might reverse the mechanism of EDA-Boc from the deprotonation step to protonation. This is because amines are completely protonated in the solution of strong acids. The protonation of an amine may lead to the formation of salts of the alkyl ammonium ions. As a result, the excess of protons from TFA completely halted the occurrence of the oxidation process of EDA-Boc. Hence, we conclude that the pH of solvent used for electrochemical grafting of EDA-Boc at the electrode surface plays an important role on the deprotonation step of primary amines.

6.9 Diffusion coefficient measurements for EDA-Boc by CV

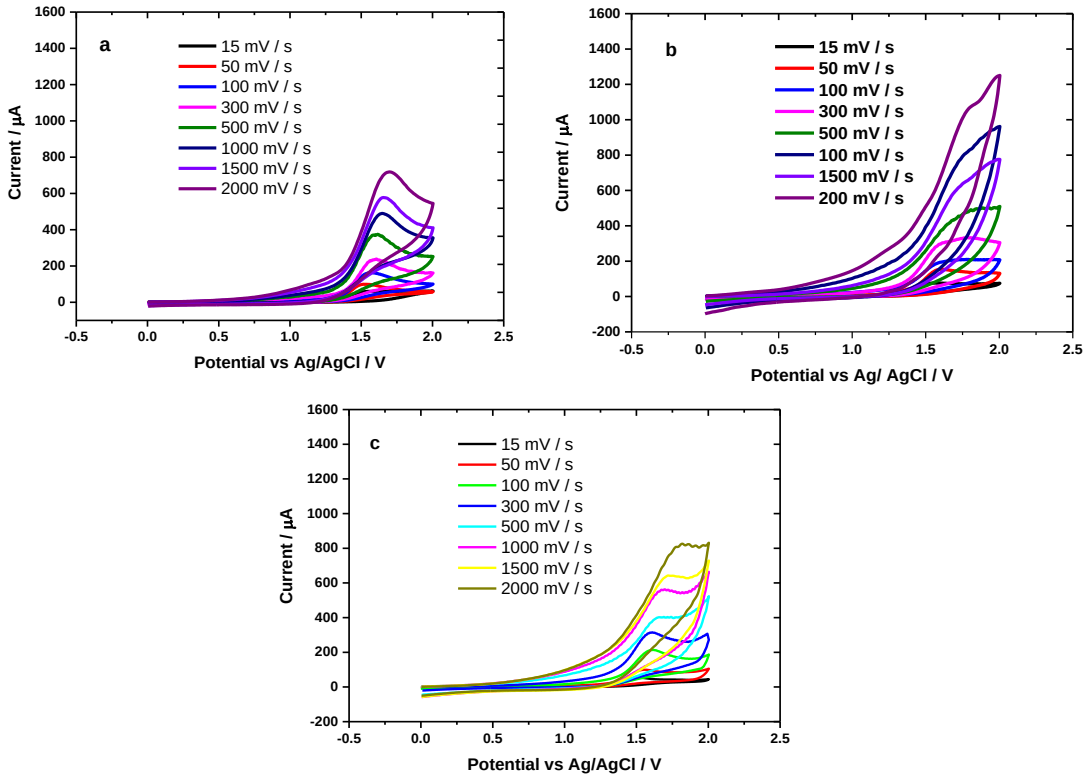

Figure 6.6; First scan cyclic voltammograms for different scan rates of 10 mM EDA-Boc with 0.1 M TBATFB from different modified electrode surfaces. a) In neat ACN, b) In 20% of $NaHCO_3$/ACN and c) In 20% water/ACN. All the experiments were measured at potential scans from 0 – 2 V *vs* Ag/AgCl with a controlled temperature at 25 ± 0.5 ° C using a water bath.

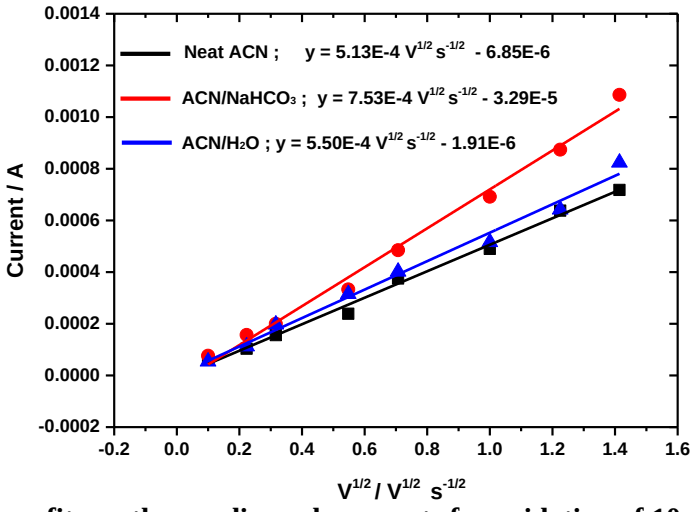

Figure 6.7; Linear fits on the anodic peak currents for oxidation of 10 mM EDA-Boc from the first scan as a function of the square root of the scan rate for different solvents. (Black line) neat ACN; (Blue line) ACN/water (4:1) ; (Red line) ACN/NaHCO$_3$ (4:1).

Diffusion of redox solute molecules in bulk electrolyte is one of the important physical processes for the electrochemical reaction when the solutes moving from the bulk solution to the surface of the electrode and vice versa. However, the knowledge on diffusion at the molecular lever is still very limited because lacking general theories that can satisfactorily describe the diffusion behaviour of wide range of molecules in dense fluids. On the other hand, there are several factors that are influencing the diffusion process such as temperature, solvent densities, dielectric constants and solvation shell[172–174]. Thus, every single factor needs to be considered before measuring the diffusion coefficient of redox molecules. To gain more insight on CV responses during the electrochemical grafting of mono-EDA-Boc to the carbon surface, the diffusion coefficient ($D_\circ$) of EDA-Boc in ACN, ACN/NaHCO$_3$ and ACN/water were attempted to calculate using Randles-Sevcik calculation as shown in Equation 6.1.

$$i_p = (2.69x10^5\, n^{\frac{3}{2}}\, A D_O^{\frac{1}{2}} C_O\, v^{\frac{1}{2}}) \qquad \textbf{Eq. 6.1}$$

Although we know that the application of Randles-Sevcik equation only favours for calculating D_o from reversible electrochemical reactions, but at this moment, it is only the way to try to estimate the D_o of EDA-Boc in the three different solutions by CV measurement.

The generated currents from the first scan of CVs on varying scan rates for the attachment of EDA-Boc in 3 different solutions are shown in Figures 6.6 (a, b and c). Thus, the peak currents on the first scan at around 1.56 V *vs* Ag/AgCl can be plotted against the square root of scan rates ($v^{1/2}$) as shown in Fig. 6.7. Clearly, the I_{pa} was linearly proportional to $v^{1/2}$, indicating that the mass transfer of EDA-Boc to the electrode surface was diffusion-controlled. By getting the slope of the

linear fittings, the diffusion coefficients of the EDA-Boc in three different solvents were calculated using equation 6.1. The D_o calculated for each solvent is shown in Table 6.1.

Table 6.1; Data for diffusion coefficients (D_o) calculated from first cyclic voltammograms for oxidation of 10 mM EDA-Boc in neat ACN, ACN/$NaHCO_3$ and ACN/water.

Solution for EDA-Boc	D_o / cm^2 s^{-1}
Neat ACN	$(7.29 \pm 0.41) \times 10^{-6}$
ACN/water	$(8.14 \pm 0.33) \times 10^{-6}$
ACN/$NaHCO_3$	$(1.79 \pm 0.61) \times 10^{-5}$

From the Table 6.1, it is noticed that the D_o of EDA-Boc in a solution of ACN/$NaHCO_3$ higher than in neat ACN and ACN water. The D_o obtained was $(1.79 \pm 0.61) \times 10^{-5}$ cm^2 s^{-1}, one order of magnitude greater than calculated D_o in neat ACN and ACN/water (10^{-6} cm^2 s^{-1}). Generally, the magnitude of D_o for primary amines in a non-aqueous bulk solvent is (10^{-5} cm^2 s^{-1}). This suggests that the Randles-Sevcik equation for estimating D_o of EDA-Boc in solution may not suitable to apply for irreversible CV case. On the other hand, because the passivation of electrode surfaces for electrochemical grafting EDA-Boc in ACN and ACN/water took place after the second scan of the CV, partial coverage[175–177] of the EDA-Boc formed on carbon surfaces and may lead to the lower rate of the diffusion process. This is not the case for the grafting EDA-Boc in ACN/$NaHCO_3$ in which the electrode surface was passivated after the first scan of CV. In terms of higher D_o value obtained for EDA-Boc in ACN/$NaHCO_3$ than in neat ACN and ACN/water, it is unclear data trend so far. However, it could be due to bigger background current from solvent was generated when electrochemical grafting of EDA-Boc was performed in ACN/$NaHCO_3$. Consequently, the height of peak also increased. In order to validate the diffusion coefficient for the whole system that had been measured by the irreversible CV using the Randles-Sevcik equation, the chronoamperometry measurements had also been made by applying Cottrell equation. The results will be discussed in greater detail later in Section 6.10.

6.10 Diffusion coefficient of EDA-Boc by chronoamperometry

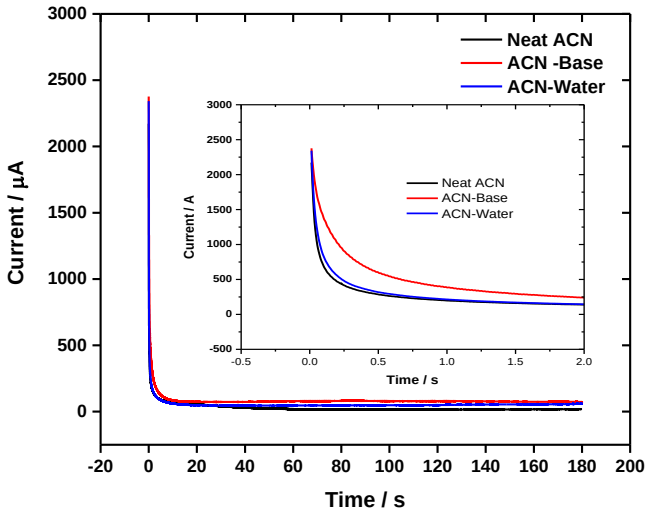

Figure 6.8; Current-time dependencies for oxidation of EDA-Boc in neat ACN (black), ACN/water (blue), and ACN/$NaHCO_3$ (red) by stepping potential from 0 to 2 V vs Ag/AgCl for 180 s. Inset figure shows enlargement of chronoamperograms over time (s) between 0 to 2 s.

In order to further confirm the data trend obtained by CV as shown in the previous section, we calculated the D_o of EDA-Boc in three different solvents using the Cottrell equation by conducting chronoamperometric experiments. Figure 6.8 shows typical chronoamperograms obtained for EDA-Boc in three different solvent electrolytes that were stepped from 0 to 2 V *vs* Ag/AgCl for 180-sec. By stepping the potential, an immediate decrease in current results from the oxidation of EDA-Boc to radical cation or neutral radicals, leading to accumulation of radicals in the electrochemical double layer. By following the Cottrell equation, i is proportional to $t^{1/2}$ as shown in Equation 6.2.

$$i = \frac{nFACD_o^{1/2}}{\pi^{1/2}t^{1/2}} \qquad \textbf{Eq. 6.2}$$

Where, n is the number of electrons transferred, F is the Faraday constant, A is the electrode area, C is the bulk concentration of the redox species and D_o is the diffusion coefficient of redox species.

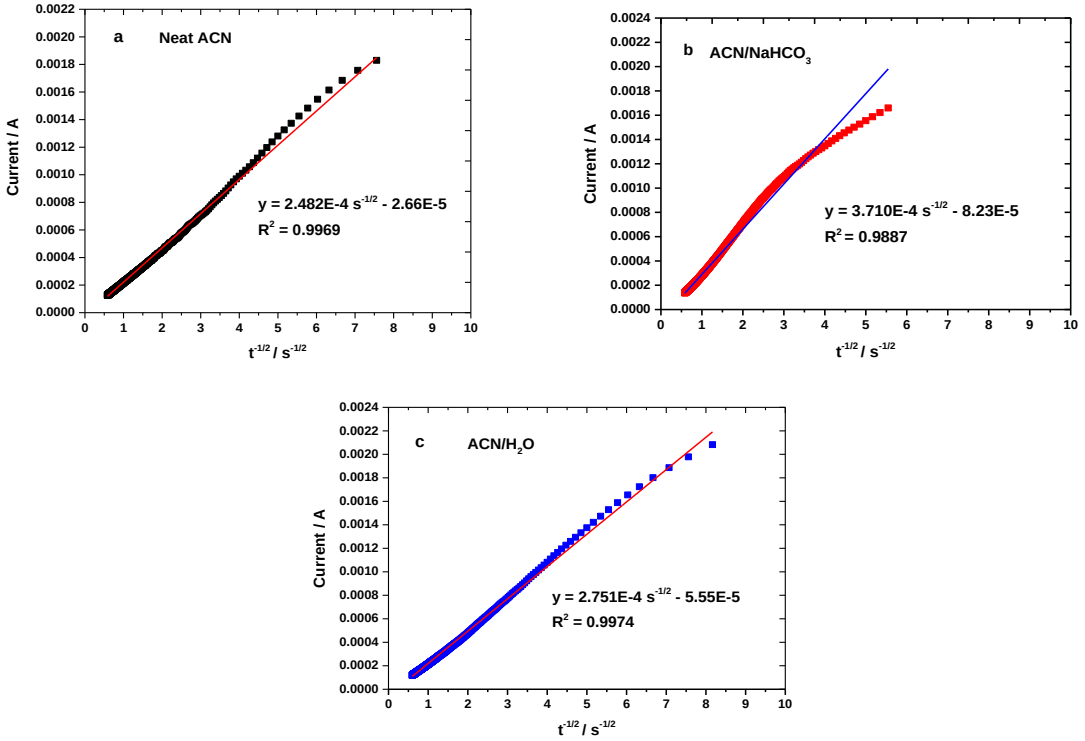

Figure 6.9; Cottrell plots of *i* (t) *vs* $t^{-1/2}$ for the oxidation of EDA-Boc in neat ACN (black), ACN/$NaHCO_3$ (red) and ACN/water (blue) by stepping potential from 0 to 2 V *vs* Ag/AgCl for 180 s.

In order to calculate D_o, using the Cottrell equation, a plot of *i* vs $t^{-1/2}$ should be made and from the straight line, the slope can be obtained[178]. Data from the first 2 s after the potential step with a freshly polished electrode were used to construct the Cottrell plots. In this way the effect of the blocking reaction is minimal. Subsequently, D_o was calculated based on the obtained slope. Figures 6.9 (a, b and c) show plots of *i* vs $t^{1/2}$ with the best linear fits for EDA-Boc in three different electrolyte solutions. Therefore, the D_o of EDA-Boc in three solutions were calculated to be 4.84 x 10^{-5} cm^2 s^{-1} 5.70 x 10^{-5} cm^2 s^{-1} and 7.42 x 10^{-5} cm^2 s^{-1}, respectively, as shown in Table 6.2.

Table 6.2; Diffusion coefficients (D_o) calculated from the Cottrell plots for oxidation of 10 mM EDA-Boc in neat ACN, ACN/$NaHCO_3$ and ACN/water.

Solvent system	D_o / cm^2 s^{-1}
Neat ACN	(4.84 ± 0.14) x 10^{-5}
ACN/$NaHCO_3$	(7.42 ± 0.25) x 10^{-5}
ACN/water	(5.70 ± 0.13) x 10^{-5}

Remarkably, a different trend of results is observed for the D_o than that which had been obtained by CV. Despite there being differences of D_o values from the two methods, however, the D_o

obtained for EDA-Boc in ACN/$NaHCO_3$ is still the same order magnitude with the D_o obtained from CV. Moreover, the D_o obtained in ACN/$NaHCO_3$ is higher than in neat ACN and ACN/water. Comparing the D_o obtained for neat ACN and ACN/water from CV with the D_o obtained by chronoamperometry, gives more support to the idea that applying the Randles-Sevcik equation does not really work for the estimation of D_o from irreversible CV.

Taking into the account for the viscosity of mixture system, as reported by Glen *et al.*[179] on the properties of ACN-water mixtures, the authors showed that the viscosity of the mixture solution gradually increased when the mole fractions of water in ACN were increased. To demonstrate this point, the viscosity of neat ACN at 25º C was reported to be 0.340 x 10^2 poise. By contrast, the viscosity of water mixture-ACN was estimated to be 0.420 x 10^2 poise when the mole fraction of water to ACN was 0.263:0.737. Furthermore, a significant shift of viscosity occurs in a mixture solvent system when the mole fraction of water to ACN is at 0.75, and it was found to be 0.815 x 10^2 poise. This is also supported by Thompson *et al.*[180] on the viscosity measurement of acetonitrile-water using a novel capillary time-of-flight viscometer.

Traditionally, the molecular motion in more viscous liquids is slower than in less viscous liquids as ruled by simple hydrodynamic basis of the Stokes-Einstein equation[178] and is given by the following expression as shown in Equation 6.3.

$$D_o = \frac{k_b T}{6\pi\eta r} \qquad \textbf{Eq. 6.3}$$

Where D_o is the diffusion coefficient. k_B is the Boltzmann constant, T represents the absolute temperature, r is the radius of the diffusing molecule and η is the viscosity of the solvent. Thus, it can be deduced that the D_o of species in a solvent is inversely proportional to the dynamic viscosity of the solvent. This means that the D_o of species in a more viscous solvent is supposedly lower than in a less viscous solvent. Nevertheless, this contradicts our results where the D_o for EDA-Boc in mixture solutions of ACN/water and ACN/$NaHCO_3$ is higher than in neat ACN. The results are not surprising at all because, typically, the Stokes-Einstein (SE) model equation for mutual diffusion is very well suited to large spherical solutes, however, it fails completely for small molecule solutes with comparable size to or smaller than solvent molecules[172,174]. As discussed by Mostinsky[181], by comparing the range of applicability of this equation with experimental data that have been reported in some articles, the discrepancy is moderate and only reached 40% in some cases. In addition, there are some computer simulations that have discovered that the SE relation is inapplicable and inadequate for representing the effect of solvent viscosity on the diffusion coefficient[182–185]. As emphasised by Dabiv and Klass[172], the diffusion of molecules is controlled by local interactions in the bulk solvent such as the solvation shell, steric effects, and dynamic molecules rather than by physical properties of the bulk liquid. Therefore,

there is no simple theory that is able to predict the value of viscosity from molecular properties. Hence, we conclude that in the case of diffusivity of EDA-Boc molecules in neat ACN, ACN/water and ACN/$NaHCO_3$ with a supporting electrolyte of TBATFB, it is not dependent on the viscosity of the solvent. However, because of the complexity of molecular diffusion that is still not well-understood, only detailed molecular dynamics (MD) simulations are likely to be able to predict such a relationship[172,186]. Leaving aside this complexity, as mentioned earlier that the calculated D_o using the Randles-Sevcik equation does not really apply for irreversible CV. Noticeably, the determined D_o by the Cottrell equation is a fair amount higher than CV, however, we believe that the chronoamperometry method yields diffusion coefficients of higher precision than the CV technique. This is because we only used four different cleaned surface GC electrodes to get reproducible results. By contrast, the oxidation of EDA-Boc leads to the passivation of the electrode surface, in CV measurements we had to use more than forty different cleaned surface GC electrodes for each of the diffusion measurements. In the next step, our experimental results on the D_o can be verified by using our specially developed CV simulation for electrochemical grafting EDA-Boc at the electrode surface.

6.11 Simulation for the experimental CVs of immobilised EDA-BOC (Method 1)

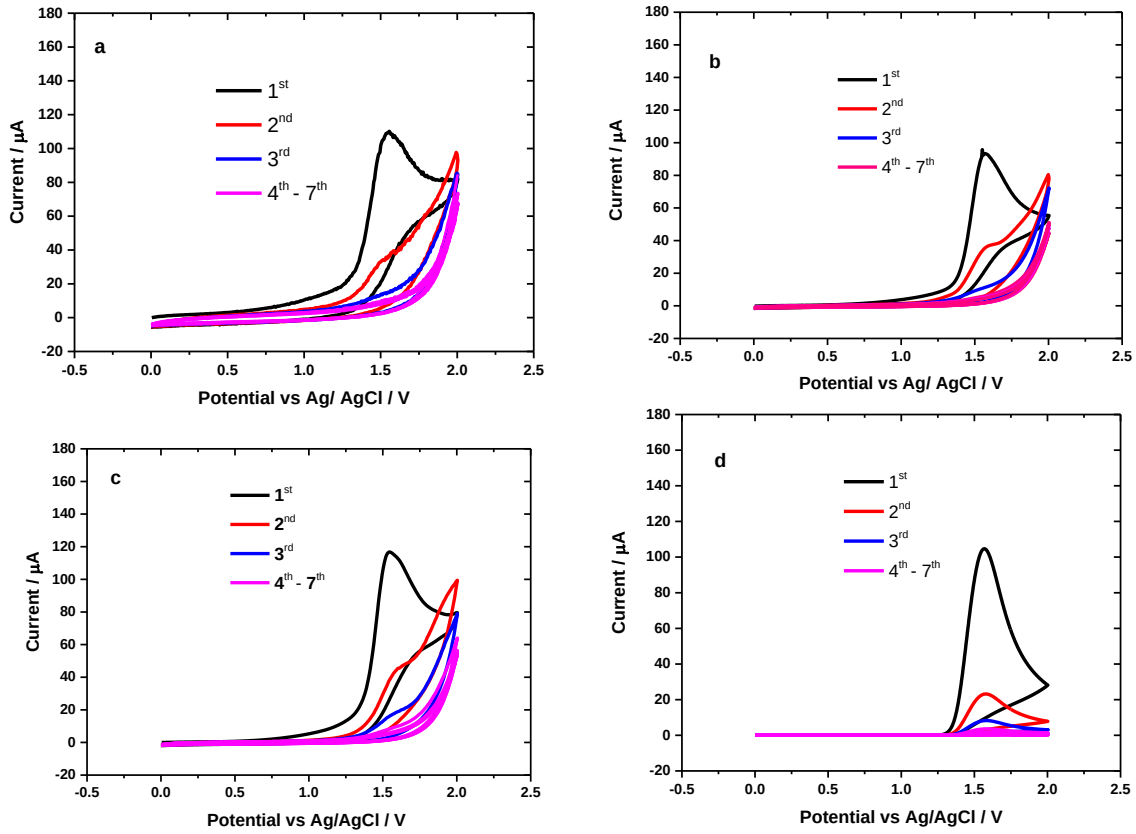

Figure 6.10; a,b,c) First seven scans of cyclic voltammograms from 3 different modified GC electrodes for 10 mM EDA-Boc with 0.1 M TBATFB in neat ACN, d). Simulation fit for the first seven cycles of CV waveforms by setting simulation parameters of $E°$ = 1.45 V, D_o = 4.9 x 10^{-5} cm^2 s^{-1}, Γ_{max} = 2.0 x 10^{-9} mol cm^{-2}, k_S = 1.3 x 10^{-3} cm s^{-1}, k_A = 1.95 x 10^{-5} cm s^{-1}, k_H = 0.6 s^{-1}, α = 0.7 , T = 298 K, v = 50 mV/ s and electrode area = 0.071 cm^2.

In the previous discussion for the experimental results of attachment of EDA-Boc employing method 1 and 2, we have shown the electrochemical behaviour of grafted EDA-Boc in ACN and ACN/$NaHCO_3$ at the GC surface. In addition, the diffusion coefficients (D_o) have been experimentally determined by CV and chronoamperometry. However, as mentioned earlier in Section 6.4, following the theoretical model reported by Saveant and co-workers[165], we wanted to investigate if the model could fit our experimental CVs as previously shown in Figures 6.1a and b. Also, we are interested in understanding and extracting a few more unknown parameters that could not be accessed by experiments using our written simulation codes as in Appendix 6.1. The parameters that we wanted to determine by CV simulation are the rate constant for attachment EDA-Boc (k_A), the rate constant for homogeneous reaction (product formation) k_H, the standard rate constant for electron transfer (k_s) and transfer coefficient (α). Moreover, the D_o values that have been experimentally determined for EDA-Boc could be verified by simulation. Adenier and co-workers[159] stated that it is not possible to determine the thermodynamic and kinetic parameters

by experimental approaches. Hence, they extracted the parameters on attachment amines using digital simulation. The weakness of their article is that they did not show any simulation fit waveform on the CVs for the grafted amines.

Figures 6.10(a, b, c) show the first seven cycles of CVs for electrochemical grafting of EDA-Boc based on procedure 1, for three different modified GC electrodes. In contrast, by setting the best value for each parameter as shown in Table 6.3, the simulated seven repetitive CVs has been obtained (Figure 6.10d). Comparing the simulated CVs (Fig 6.10 d) to the experimental CV, Figure 6.10d shows a reasonable agreement to the experimental CVs, in a particular for the passivation of electrode surfaces by immobilised EDA-Boc. Both of the CVs show the blocking of electrode surface by EDA-Boc film took place after three cycles. The simulation done by Saveant *et al.* [166] on the simulated CV for attachment of diazonium salt at highly oriented pyrolytic graphite (HOPG) electrode surface in ACN shows the simulated peaks decreased significantly faster than the experimental peaks as shown in Figure 6.11. Clearly, the simulated CVs did not give a good match with the experimental CVs, particularly for a degree of the blocking of the electrode surface. This indicates that the electrochemical grafting process gives the passivation of the electrode surface after seven scans of the CV measurements.

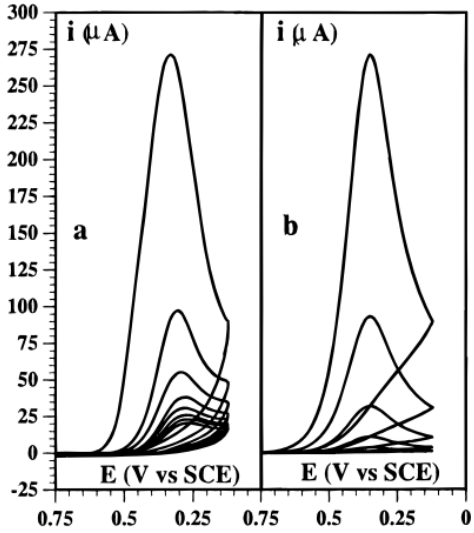

Figure 6.11; Comparison of experimental CV (a) and simulated CV (b) for grafting 4-nitrophenyl diazonium salt at the surface of highly oriented pyrolytic graphite (HOPG) electrodes employing a scan rate of 0.2 V/s, (Adapted from Saveant *et al.*[166] with permission).

Table 6.3: Values for MATLAB parameters obtained from the experiments and used in CV simulation.

Parameter	Determined by experiment	Simulation value
Redox potential ($E°$)	-	1.45 V
Diffusion coefficient (D_o)	4.84 x 10^{-5} cm^2 s^{-1}	4.90 x 10^{-5} cm^2 s^{-1}
Maximum surface coverages (Γ_{max})	-	2.0 x 10^{-9} mol cm^{-2}
Rate constant for electron transfer (k_s)	-	1.3 x 10^{-3} cm s^{-1}
Transfer coefficient (α)	-	0.7
Rate constant for adsorption (k_A)	-	2.15 x 10^{-5} cm s^{-1}
Rate constant for homogenous reaction (k_H)	-	0.6 s^{-1}

Table 6.3 shows the best fit values used for simulation process to generate the simulated CVs as shown in Figure 6.10d. The best fitting between simulation and experimental voltammograms were achieved manually by varying and optimising the parameters values. As the determined D_o value by chronoamperometry experiment was found to be 4.84 x10^{-5} cm^2 s^{-1}, in order to obtain the best fitting the D_o was optimised to be 4.9 x 10 x 10^{-5} cm^2 s^{-1}. Γ_{CVmax} of 2.0 x 10^{-9} mol / cm^2 is used because its the maximum theoretical value for monolayer coverages of EDA-Boc[55] and the value of k_s 1.3 x 10^{-3} cm s^{-1} is the best response for the simulation. Interestingly, the k_s value used is in the same order magnitude that has been reported by Adenier *et al.*[159] for simulation voltammograms for electrochemical oxidation of aliphatic amines. Moreover, they employed α = 0.5 in the CV simulation. In a similar way, as displayed in Figure 6.11b, Saveant *et al.*[166] also used α = 0.45. Nevertheless, in our simulation for experimental CVs, we employed α value of 0.7. To mention generally here, the values of E^0, k_s and α directly affect the position and width of the simulated CV peak. The use of α value smaller than 0.5 would give a narrow CV peak, whereas the α values bigger than 0.5 would produce a broad CV peak. The simulation data patterns when varying these values will be shown and discussed in detail in Section 6.12. Thus, the reason to use α = 0.7 because based on the simulation fits, α value of 0.7 generated close CV shape in terms of the broadening voltammograms, particularly for the first CV cycle. Moreover, the height of peak current for the 1st cycle agreeable with the D_o value that determined by chronoamperometry experiment. However, it is still unclear why the use value of α = 0.7 in the fitting gave us this data pattern, but in order to investigate the more effect of α on the fittings, we have also attempted the fittings using α = 0.5. The data obtained would be discussed more details in Section 6.12 and 6.15 when we investigate the effect of simulation variables on simulated CVs.

To note again, the parameters k_A and k_H also directly affect the height and the relative sizes of the first, second and subsequent peaks. Particularly the relationship both the variables can show the degree of the passivation electrode surface. Therefore, the use of k_A = 2.15 x 10^{-5} cm^2 s^{-1} and k_H =

0.6 s^{-1} gave well agreement with the peak height on the first cycle of CV peak and the blocking features CVs signals.

Despite the height of peak currents and blocking behaviour of the electrode surface is quite satisfactory between two cases, the disagreement on the backward current for each cycle has been clearly observed. On the first scan of simulated CV, the turning point of the backward current is around 35 μA, however, for the experimental CV, it was found to be around 75 μA. According to the article discussed by Saveant *et al*. [165] the reverse scan for the backward current on the first and subsequent cycles can be used to obtain an indication of the degree of blocking of the electrode surface. Moreover, the generated currents on simulated CV relies on the *p* parameter in which *p* describes the competing reactions of species B (radicals) between the surface and solution and the diffusion flux and the area occupied by C as shown in equation 6.4 .

$$p = \frac{k_A C\sqrt{RTD}/\alpha F v}{k_A\sqrt{D_o k_H}\Gamma} \qquad \textbf{E.q 6.4.}$$

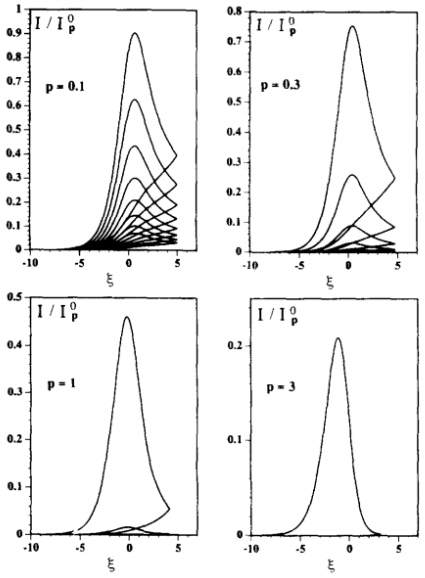

Figure 6.12; The influenced of competition parameter *p* values (0.1, 0.3, 1 and 3) on simulation for self-inhibition reaction, (Adapted from Saveant *et al*.[165] with permission).

As shown in Figure 6.12, they suggested that as *p* increased, the result will be that the grafting process becomes more prominent than diffusion of radicals to the bulk solution. In addition, the peak becomes thinner and the backward current gradually decreases, indicating that the blocking of the surface is more rapidly. Continuing with this trend, it would result in the current reaching zero before the end of the first scan. Hence, it can be assumed that total coverage has been reached[165].

As discussed in the preceding paragraph, the backward currents towards reverse scan of our simulated CV is overestimated by our simulation program. This has contributed to the dissimilarity simulated CV waveform to the experimental CV. Figures 6.13 a and b show the first cycle of experimental and simulated CVs. This dissimilarity is probably contributed from the background currents presence over the experimental CV that could be clearly seen from ~ 0.75 to 2 V *vs* Ag/AgCl.

As shown previously in Figure 6.2, the EDA-Boc in ACN solution contributes significantly to the background current. However, in our simulation program, this type of background process is not included. To include its effect, we treated our simulated current with background current from the experimental CV, where the currents produced after the passivation of electrode surface by EDA-Boc film. We have used the experimental background current measured from the fourth to seventh voltammetric scans. By using Origin 9.1, the interpolated experimental background current could be extracted. Figures 6.13a, b, c and d show an example to illustrate this approach.

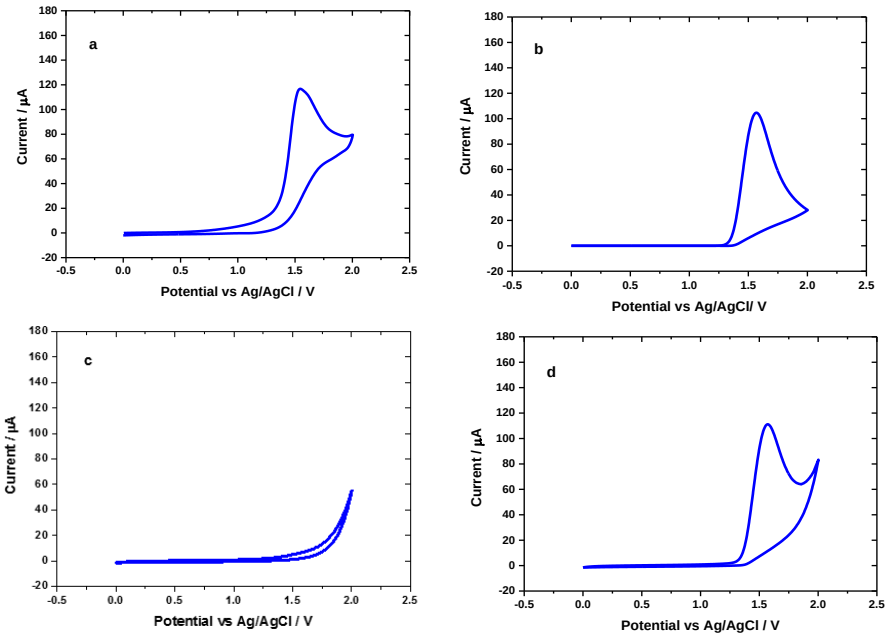

Figure 6.13; a,b) First cycle experimental CV and simulated CV for 10 mM EDA-Boc with 0.1 M TBATFB in neat ACN, c) Interpolated background current used from the fifth cycle of experimental CV d) New simulation CV waveform after adding simulated CV current (6.13b) with interpolated background current (6.13 c) using Origin 9.1.

In order to extract the interpolated experimental background current from Origin 9.1, two different approaches were performed. Firstly, half of the experimental data (potentials and currents) from the forward scan was put into the interpolation template. The potential values obtained from the simulation were also put into the same template. Then, the currents for the potential values

obtained from the simulation can be interpolated. The same procedure was conducted with the other half of the experimental data to make a complete set of interpolated data.

Therefore, by adding the simulated current to the interpolated background current from the experiment in Origin, the simulated CV shape is significantly improved and gave good agreement to the turning current for the reverse scan as depicted in Figure 6.13d. The same approach is employed on the subsequent simulated CV cycles.

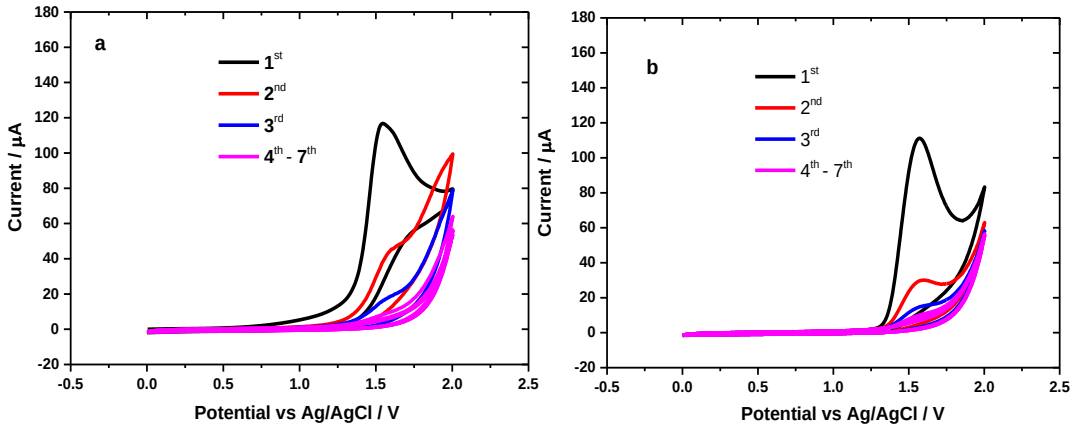

Figure 6.14; New simulated CV waveforms for seven cycles of EDA-Boc after adding the simulated current for each scan to the interpolated background current (b) and comparison of seven repetitive experimental CV (from Figure 6.1a) with the best simulated fit data. Conditions used in simulation were $E°$ = 1.45 V, D_o = 4.9 x 10^{-5} cm^2 s^{-1}, Γ_{max} = 2.0 x 10^{-9} mol cm^{-2}, k_S = 1.3 x 10^{-3} cm s^{-1}, k_A = 2.15 x 10^{-5} cm s^{-1}, k_H = 0.6 s^{-1}, α = 0.7 , T = 298 K, scan rate = 50 mV/ s and electrode area = 0.071 cm^2.

As illustrated in Figure 6.14(b), better agreement of theoretical CV waveforms to the experimental CV could be obtained by adding the simulated CV currents to the experimental background current. Thus, good agreement between the simulation model and experiment was obtained, showing that the simple kinetic scheme adequately describes the process and gave a practical approximation to the experimental data for electrochemical grafting of EDA-Boc in ACN.

6.12 Effect of α = 0.5 on CV simulation

As mentioned earlier in Section 6.11, we used α of 0.7 to obtain the best simulated CVs, as shown in Figure 6.14b. In contrast, Adenier *et al.*[159] and Saveant *et al.*[166] used α = 0.5 in their simulations. To investigate this, we have attempted to simulate the experimental CVs of EDA-Boc using α = 0.5.

Referring back to Equation 6.4 for the competition parameter (ρ), the magnitude of the simulated peak currents (height and width) for the first and subsequent cycles as well as the degree of blocking of the surface is dependent on the collective variable values of D_o, α, k_A, k_H, Γ and C_o rather than the individual values of each variable. Therefore, it is preferable to investigate the generating of the simulated CV currents based on ρ rather than focusing on every single variable. However, in this section, we are interested in investigating the fittings when α of 0.5 is used. Therefore, we will investigate the effect of varying a single variable and keeping all other parameters constant, or varying two variables at the same time, in order to obtain the most accurate fit.

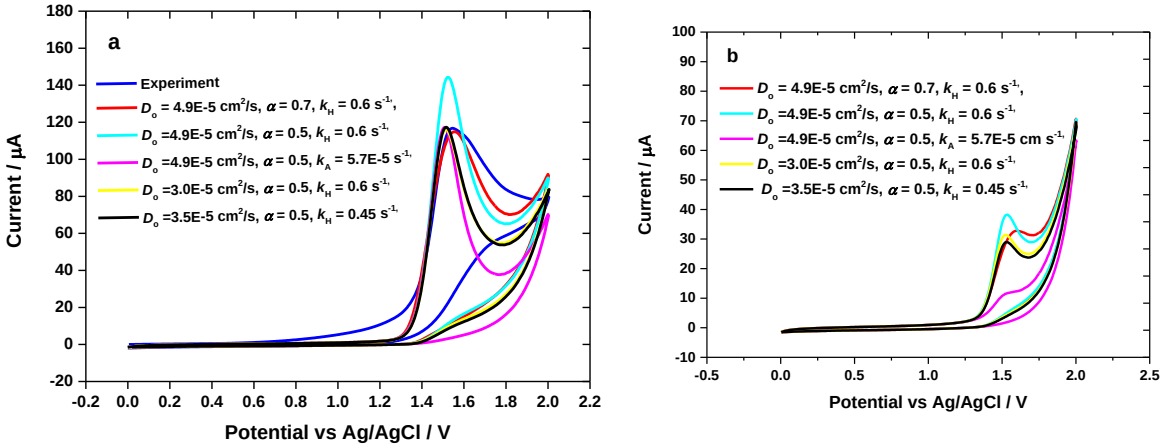

Figure 6.15; a,b) Simulated CVs at 50 mV/s with varying values of D_o, k_A and k_H at α = 0.5 and α = 0.7 (first and second cycles shown). Blue is experimental CV, red is simulated CV from Figure 6.14a and b, light blue; conditions used were D_o = 4.9 x 10^{-5} cm^2 s^{-1}, α = 0.5, and k_H = 0.6 cm s^{-1}, pink; conditions used were D_o = 4.9 x 10^{-5} cm^2 s^{-1}, α = 0.5, and k_A = 5.7 x 10^{-5} cm s^{-1}, yellow; conditions used were D_o = 3.0 x 10^{-5} cm^2 s^{-1} , α = 0.5, and k_H = 0.6 s^{-1}, black; conditions used were D_o = 3.0 x 10^{-5} cm^2 s^{-1}, α = 0.5, and k_H= 0.45 s^{-1}. Other parameters, E_o , k_s and Γ_{max} values were kept constant as in Figure 6.14.

Figures 6.15a shows a comparison of the first scan of experimental CV (blue) to simulated CVs. The simulated CVs were obtained after adding the background current as explained in Section 6.11. The red CV is the simulated CV from figure 6.14b where α = 0.7. By setting α = 0.5, while the other parameters are kept constant, the simulated CV in light blue was obtained. Clearly, the height of the peak current increases significantly and the peak becomes sharper. Using the same approach, but adjusting D_o from 4.9 x 10^{-5} cm^2 s^{-1} to 3.0 x 10^{-5} cm^2 s^{-1}, the height of the peak current again matches the experimental peak (yellow), but produced 53.3 % different value of error when comparing to the experimental D_o. The percent error (%) was calculated based on = [(new input – initial input)/ (initial input)] x 100%.

In addition, the width of the simulated CV peak becomes sharper than when α = 0.7 is used (red). Moreover, a slight shift of the CV peak to more positive potential is observed. In a different case, a similar CV shape and height was obtained (black CV) when changing the D_O input value from

4.9 x 10^{-5} cm^2 s^{-1} to 3.5 x 10^{-5} cm^2 s^{-1} and at the same time, adjusting the k_H from 0.6 s to 0.45 s^{-1}. In this case, comparing the used D_o in the simulation to the experimental D_o, the percent of relative error was calculated to be 31.4 %.

In a different approach, by keeping D_o = 4.9 x 10^{-5} cm^2 s^{-1} constant but changing k_A from 2.15 x10^{-5} cm s^{-1} to 5.7 x 10^{-5} cm s^{-1}, the simulated CV shown in pink was obtained. Clearly, the peak height current matched well with the experimental CV. However, in terms of the peak width, the simulated peak becomes sharper. In addition, the second cycle of the simulated CV (Figure 6.15b) shows that the peak size decreased significantly. Thus, this shows a poor agreement between the experimental and simulated CVs.

This Section clearly shows that by using α = 0.5, it was still possible to obtain a fit to the experimental CV, especially in terms of the height of the peak current. However, the D_o value obtained showed a larger relative error when compared to the experimental D_o values. Moreover, the simulated CV peaks were narrower than the experimental CV peak.

Overall, based on Figures 6.15a and 6.15b, it is now clear that the use α = 0.7 in our fitting produced a better agreement between the simulated CV and the experimental CV, particularly in terms of D_o and the peak width. The electrochemical grafting of EDA-Boc to the surface of a GC electrode involves the deprotonation of the unstable radical-cation. Consequently, the electrochemical grafting of EDA-Boc proceeds by a step wise mechanism (intermediate steps). This could be one of the reasons why α = 0.7 gave a good agreement to the experimental CV and especially produced a small relative error with respect to the experimental D_o. Moreover, as discussed by Sabrina and Favio[187], the electrochemical transfer coefficient (α) is particularly useful in determining the transition between stepwise and concerted electron transfer mechanisms, as illustrated in Scheme 6.6. In their work, experimental and theoretical studies on the role and relevance of α for the electroreduction of perbenzoates, the apparent α values in the range from 0.53 to 0.75 have demonstrated that the process is a stepwise mechanism. By contrast, low α values of less than 0.5, indicated results in agreement with the concerted mechanism.

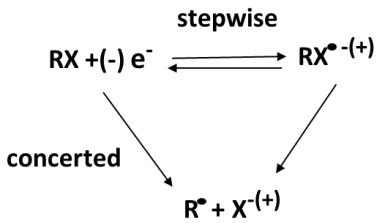

Scheme 6.6; The general reaction scheme for the one electron reductive or oxidative cleavage of neutral molecules when the cleavage follows a concerted or a stepwise pathway. The products could be an ion for the stepwise mechanism or a radical for the concerted mechanism.

6.13 Effect of E and k_s parameters on the simulated CVs

Observably, based on the competition equation as demonstrated by Saveant *et al.*[165,166] the k_s and $E°$ variables are not connected with the competition factor (ρ). Thus we attempted to see a general trend of varying the k_s and $E°$ values in simulated CVs and compared them to the experimental results. Note that only the first cycle is shown in this comparison. Figure 6.16 shows the effect of varying k_s values on the fittings. The other simulation parameter values are kept constant.

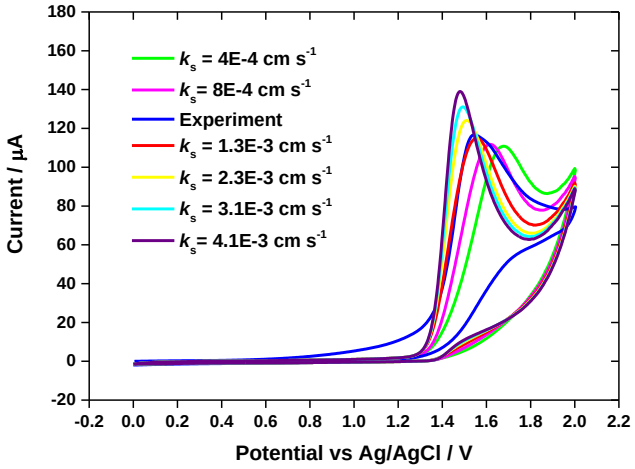

Figure 6.16; Experimental and simulated CVs at 50 mV/s (first cycle shown) with varying values of the rate constant for the homogenous reaction EDA-Boc (k_s). Green = 4 x 10^{-4} cm s^{-1}, pink = 8 x 10^{-4} cm s^{-1}, blue = experiment, red = 1.3 x 10^{-3} cm s^{-1}, yellow = 2.3 x 10^{-3} cm s^{-1}, light blue = 3.1 x 10^{-3} cm s^{-1} and purple = 4.1 x 10^{-3} cm s^{-1}. The other parameters are kept constant as in Figure 6.14.

As can be observed, when varying k_s values from 4 x10^{-4} cm s^{-1} to 4.1 x 10^{-3} cm s^{-1}, the peak shifted to less positive potentials while the peak current gradually increased and the peaks get sharper.

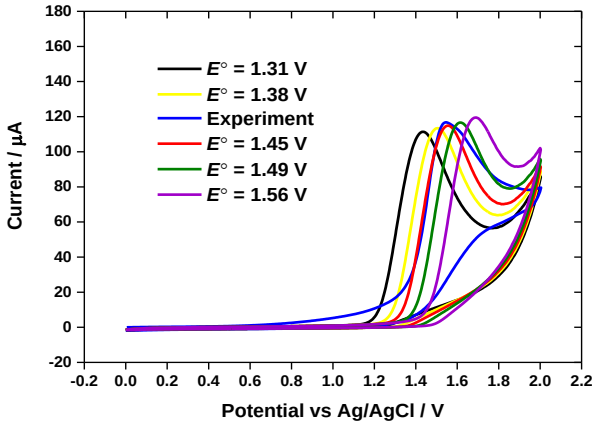

Figure 6.17; Experimental and simulated CVs at 50 mV/s (first cycle shown) with varying $E°$. Black = 1.31 V, yellow = 1.38 V, blue = experiment, red = 1.45 V, green = 1.49 V, purple = 1.56 V. Other parameters are kept constant as in Figure 6.14.

The same approach was used when varying $E°$ and the results are presented in Figure 6.17 were obtained. The data show that the position of the peak current shifted to more positive potentials when $E°$ was increased from 1.31 V to 1.56 V. Overall, these quantitative analyses demonstrated that the shape, size and position of the simulated CVs are sensitive to the parameters k_s and $E°$. However, as seen in Figures 6.16 and 6.17, the peak height is more sensitive to k_s.

6.14 Sensitivity of CV simulation based on competition parameter (ρ)

As demonstrated in Section 6.11, set of fitting values have been used in order to obtain the most accurate simulated CVs compared to the experimental CVs, as shown in Figures 6.14a and b. As explained by Saveant *et al.*[165,166] the degree of passivation of the electrode surface through radical species is determined by the competition of the radical species (ρ) either reacting at the surface or diffusing to the bulk and then reacting in solution. Thus, based on the competition parameter equation (Eq. 6.4), the parameters k_A and k_H directly affect the height and size of the first, second and subsequent peaks, as simplified in Equation 6.5.

$$\rho = \frac{k_A}{k_A + \sqrt{D k_H}} \qquad \textbf{Eq. 6.5}$$

As described by Saveant *et al.*[165] the competition between grafting of the radical species to the electrode surface and homogeneous reaction in solution is described by the ratio of k_A and $(Dk_H)^{1/2}$. In our case, $k_A << (Dk_H)^{1/2}$, thus, the ratio $k_A/\sqrt{k_H}$ determines the fitting rather than the individual values of the two rate constants. Therefore, the fittings for ρ were performed by varying k_A whilst the k_H value is kept constant and vice versa. The data for each case is shown in Figures 6.18 and 6.19.

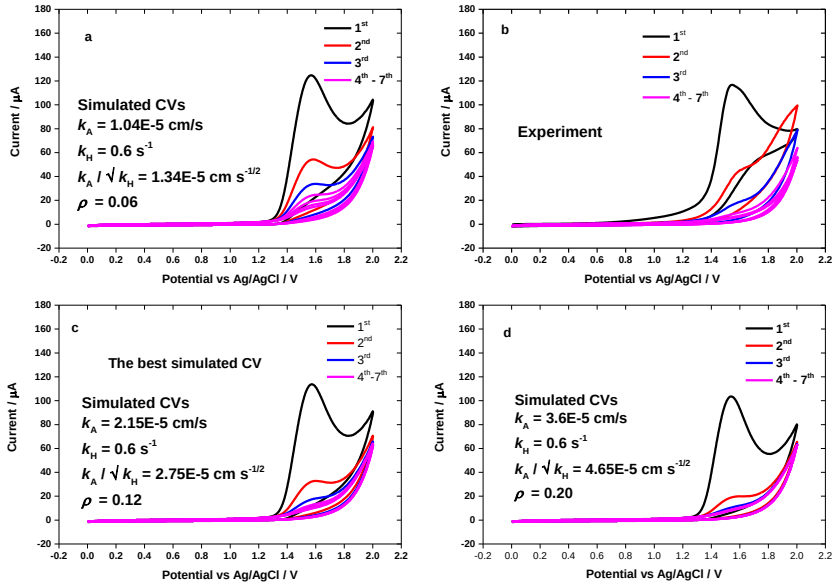

Figure 6.18; Comparison between experimental (b) and simulated CVs. Simulated CVs (a, c and d) were obtained by varying k_A while k_H (0.6 s^{-1}) was kept constant. a) k_A= 1.04 x 10^{-5} cm/s. c) k_A = 2.15 x 10^{-5} cm/s and d) k_A = 3.65 x 10^{-5} cm/s. Other conditions as in Figure 6.14.

Figure 6.18 shows the comparison between experimental CVs (6.18b) and three different simulated CVs. The simulated CVs were obtained by varying k_A using values of 1.04 x10^{-5} cm s^{-1}, 2.15 x 10^{-5} cm s^{-1} and 3.6 x 10^{-5} cm s^{-1} while k_H = 0.6 s^{-1} was kept constant. Based on these values, ρ can be calculated using Eq. 6.4 and the ratio $k_A/\sqrt{k_H}$ can also be determined using Eq. 6.5. ρ for the three simulated CVs was calculated to be 0.06, 0.12 and 0.20. The ratio $k_A/\sqrt{k_H}$ was found to be 1.34 x 10^{-5} cm $s^{-1/2}$, 2.75 x 10^{-5} cm $s^{-1/2}$ and 4.65 x 10^{-5} cm $s^{-1/2}$. Thus, by increasing the k_A, ρ and $k_A/\sqrt{k_H}$ were also increased. Clearly, comparing the simulated CVs from Figures 6.18a, c and d, it can be concluded that the electrode surface is blocked more rapidly and the peak current gradually decreases. In addition, the currents on the second and subsequent cycles gradually decreased until the third peak disappears (Figure 6.18d).

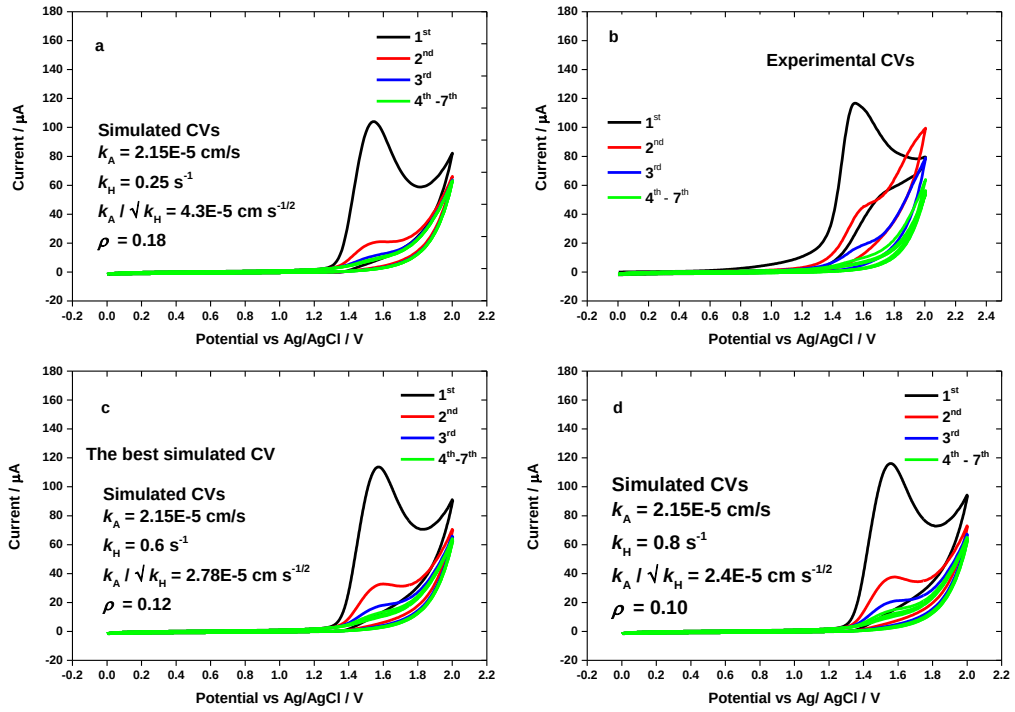

Figure 6.19; Comparison of experimental (b) and simulated CVs. Simulated CVs (a, c and d) were obtained by keeping k_A constant (2.15 x 10^{-5} cm/s) and varying k_H. a) k_H = 0.25 s^{-1}. c) k_H = 0.6 s^{-1} and d) k_H = 0.8 s^{-1}. Other parameters as in Figure 6.14.

The previous discussion has shown that different features were obtained in the simulated CVs when varying k_A while k_H was kept constant. In a different approach, the simulated CVs shown in Figures 6.19a, c, and d were obtained by varying k_H while k_A was kept constant. As before, ρ and the ratio $k_A/\sqrt{k_H}$ were also determined. For the three simulated CVs, ρ was calculated to be 0.18, 0.12 and 0.10. Meanwhile, the ratio $k_A/\sqrt{k_H}$ was found to be 4.3 x 10^{-5} cm s$^{-1/2}$, 2.78 x 10^{-5} cm s$^{-1/2}$ and 2.4 x 10^{-5} cm s$^{-1/2}$. Therefore, by increasing the k_H value, ρ and $k_A/\sqrt{k_H}$ decreased. Clearly, as indicated by the simulated CVs from Figure 6.19a, c and d, the electrode surface is blocked more slowly and the peak currents on the first and subsequent scans increased with increasing k_H.

6.15 Effect of α and D_o on the simulations

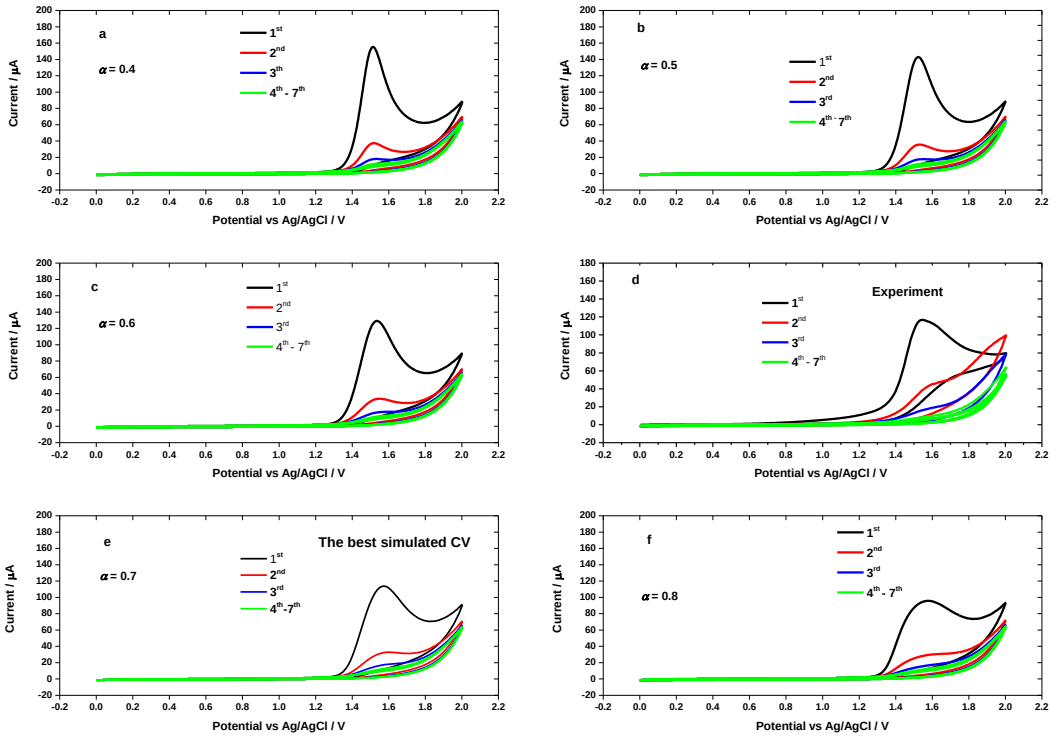

Figure 6.20; Comparison between experimental (d) and simulated CVs. Simulated CVs were obtained from values; a) α = 0.4, b) α = 0.5, c) α = 0.6, e) α = 0.7 and f) α = 0.8. Other parameters as in Figure 6.14.

In order to illustrate the effect of α on the simulations, α values were varied from 0.4 to 0.8. The data are shown in Figures 6.20a, b, c, e and f and compared to the experimental CVs Figure 6.20d. As can be observed, the data pattern shows that the peak gets broader and the peak height of the first and subsequent scans decreases as α increases.

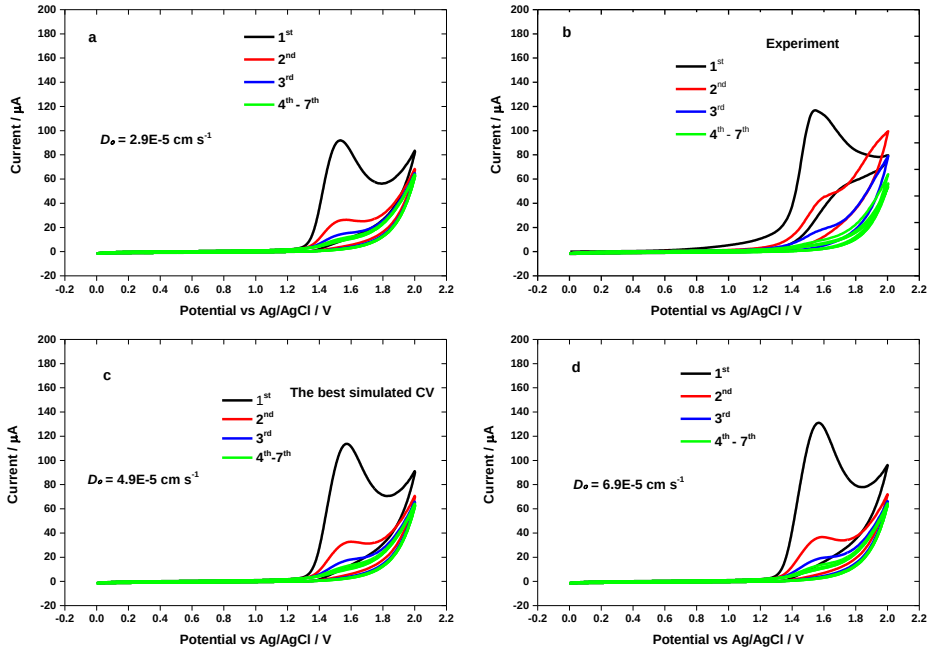

Figure 6.2; Comparison between experimental (b) and simulated CVs. Simulated CVs were obtained by varying D_o; a) D_o = 2.9 x 10^{-5} cm s^{-1} c) D_o = 4.9 x 10^{-5} cm s^{-1}, d) D_o = 6.9 x 10^{-5} cm s^{-1}. Other parameters as in Figure 6.14.

Figures 6.21a, c and d show simulated CVs obtained by varying D_o compared to the experimental CVs (6.21b). The data show that the current increased when D_o increased. The trend is clearly seen for the peak currents of the first scans.

6.16 Simulation for the experimental irreversible CVs of immobilised EDA-Boc (Method 2)

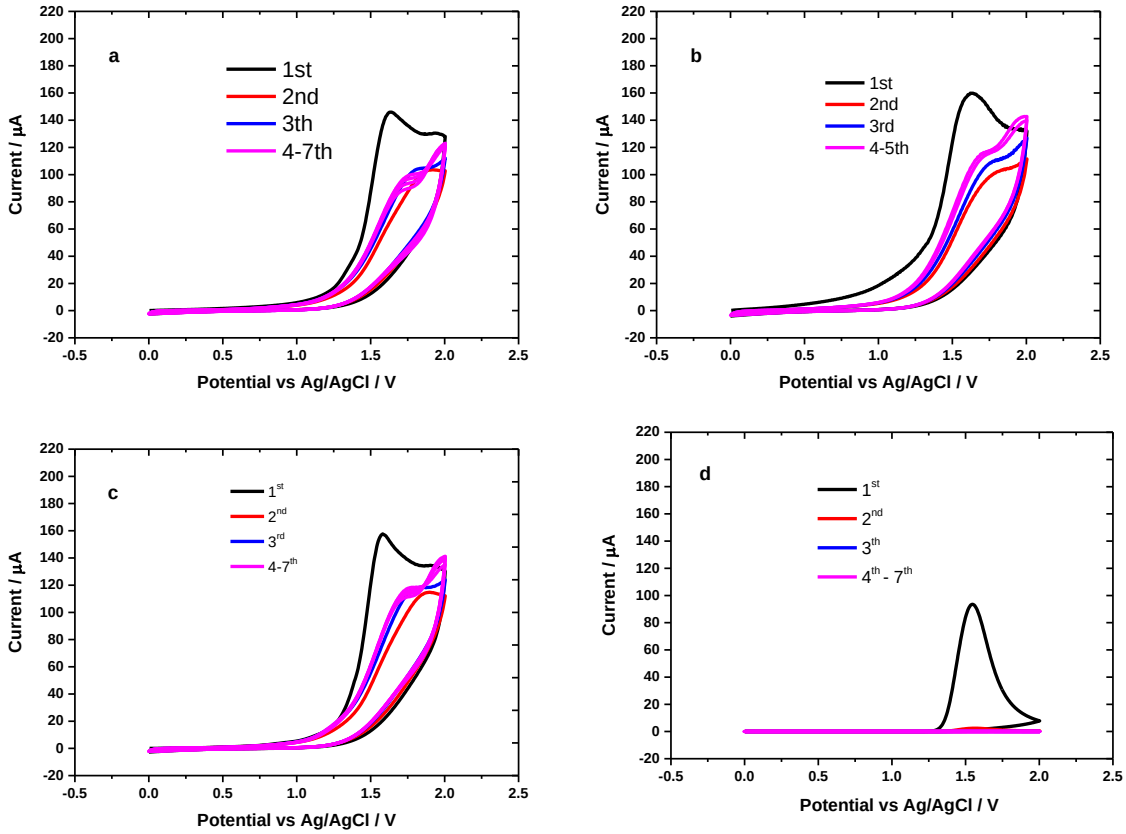

Figure 6.22; a,b,c) Cyclic voltammograms from three different modified GC electrodes for 10 mM EDA-Boc with 0.1 M TBATFB in ACN/$NaHCO_3$, d). Simulation fit for seven cycles of CV by setting numerical parameters of diffusion coefficient (D_o), maximum surface coverages (Γ_{max}), electrode area (A), rate constant for adsorption EDA-Boc (k_A), rate constant for the formation of product (k_H), and rate constant for electron transfer (k_s).

Figures 6.22 (a, b and c) show the CVs for the electrochemical grafting of 10 mM EDA-Boc using method 2 at 3 different electrodes. By using the same procedure for extracting the simulation data from our simulation program, Figure 6.22 (d) depicts the seven repetitive simulated CVs by using the values give in Table 6.4. It is clearly seen that in terms of peak current height, poor agreement between the experimental CV and the simulated CV is seen. As we have shown adding the experimental background current to the simulated current, the CV shapes are greatly improved and are close to the experimental CV. Hence, this deviation of the simulated CVs current is expected. However, the blocking effect of the EDA-Boc film is in good agreement with the experimental results. The experimental CVs indicate that the electrode surfaces have been passivated by EDA-Boc film on the second scan of the CV measurement.

Table 6.4: Values for MATLAB parameters obtained from the experiments and used in the CV simulation.

Parameter	Determined by experiment	Theoretical value
Redox potential (E^o)	-	1.45
Diffusion coefficient (D_o)	7.42×10^{-5} cm^2 s^{-1}	7.5×10^{-5} cm^2 s^{-1}
Maximum surface coverages (Γ_{max})	-	2.0×10^{-9} mol cm^{-2}
Rate constant for electron transfer (k_s)	-	1.3×10^{-3} cm s^{-1}
Transfer coefficient (α)	-	0.7
Rate constant for adsorption (k_A)	-	6.4×10^{-5} cm s^{-1}
Rate constant for homogenous reaction (k_H)	-	0.6 s^{-1}

As we reckoned in the case of simulation of the CV for EDA-Boc in ACN, by treating the simulated current with background solvent current that was generated after blocking of electrode surface by EDA-Boc film, the simulated data has produced a good agreement to the experimental CV. By using the same approach as demonstrated in Figures 6.23a, b, c and d, thus, the new waveform CV as shown in Figure 6.23d was obtained. Interestingly the new shape of the simulated CV is very close to the experimental CV waveform (Figure 6.23a).

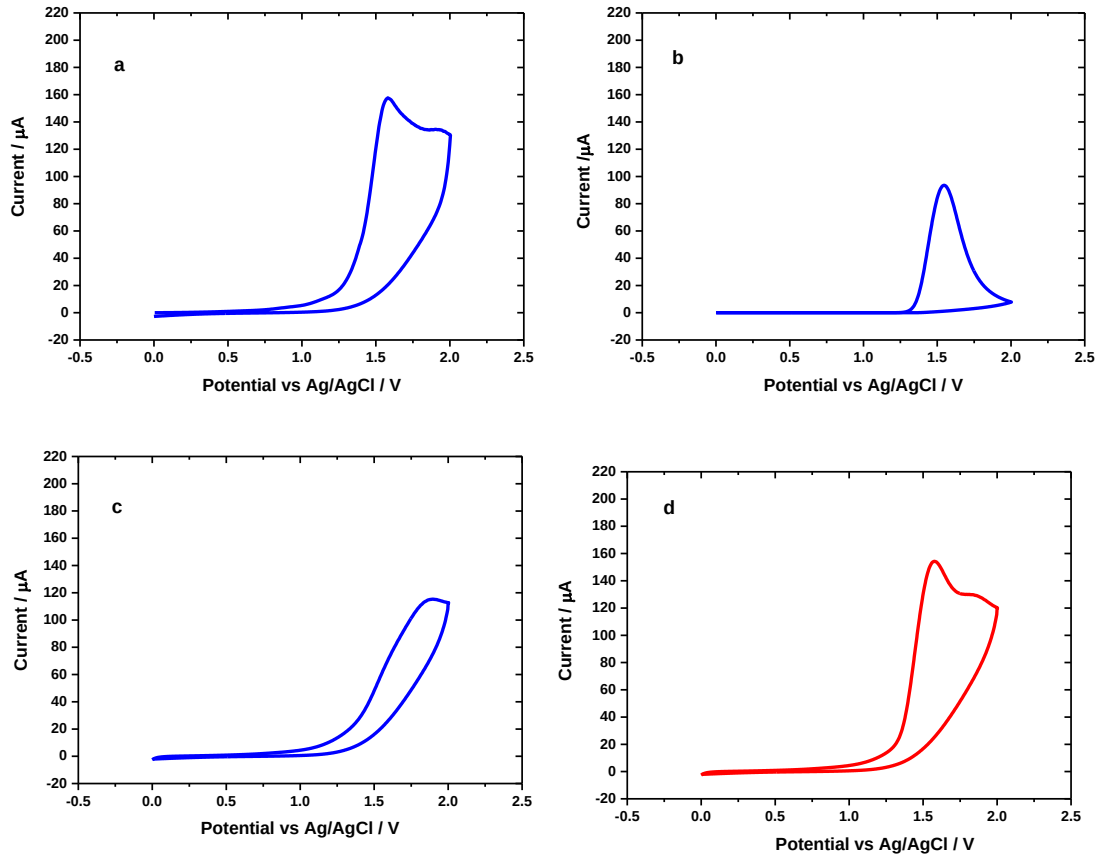

Figure 6.23; a) First cycle of the experimental CV for 10 mM EDA-Boc with 0.1 M TBATFB in ACN/$NaHCO_3$ at 50 mV/s. b) First cycle of simulated CV c) Interpolated background current from the second cycle of the experimental CV d) New simulated CV produced after adding the simulated CV current (6.23b) to the interpolated background current (6.23c) using Origin 9.1. Condition used in simulation were E^o = 1.45 V, D_o = 7.5 x 10^{-5} cm^2 s^{-1}, Γ_{max} = 2.0 x 10^{-9} mol cm^{-2}, k_S = 1.3 x 10^{-3} cm s^{-1}, k_A = 6.4 x 10^{-5} cm s^{-1}, k_H = 0.6 s^{-1}, α = 0.7 , T = 298 K, scan rate = 50 mV/ s and electrode area = 0.071 cm^2.

Referring to the values used in simulation as presented in Table 6.4, as mentioned before, the presence of aqueous $NaHCO_3$ in ACN should enhance the deprotonation rate of amine radical cations, resulting in more neutral amine radicals being produced. Therefore, it should increase k_A, leading to more efficient blocking of the electrode surface as observed in the experimental CVs. Thus, we increased the value of k_A from 2.3 x 10^{-5} cm s^{-1} to 6.4 x 10^{-5} cm s^{-1} for this simulation. By increasing the k_A values while the k_H value is kept constant, we obtained a well-matched simulated CV to the experimental CV. We also believe that when the k_A value is kept constant while the k_H values are reduced, we can still get the best fit but we felt it is unlikely because, too small a value of $k_H < 0.2$ s^{-1}, the CV simulation will generate a reduction peak at around 1.5 V (not shown). Moreover, in validating the value of D_o that had been determined by chronoamperometry experiment, the best value for D_o that was used in this simulation is very close. As we mentioned earlier that ratio $k_A/\sqrt{k_H}$ determines the fitting rather than the individual values of the two rate constants. In the CV simulation for the case of electrochemical grafting of

EDA-Boc in ACN/$NaHCO_3$, we have used the same value of k_H that we used in the simulation for immobilised EDA-Boc in the absence of $NaHCO_3$. Also, the other parameters such as D_o, k_s, α, and $E°$, were kept constant.

The best simulated CV for the attachment of EDA-Boc in the mixed solvent system ACN/$NaHCO_3$ after adding the interpolated background current is shown in Figure 6.24 (b). Figure 6.24 (a) shows the experimental CV. The data only show the two first scans of the CVs since an oxidation peak associated with the solvent system around 1.69 V *vs* Ag/AgCl appeared on the third scan of the experiment. Hence, the simulation procedure was not pursued on the subsequent cycles.

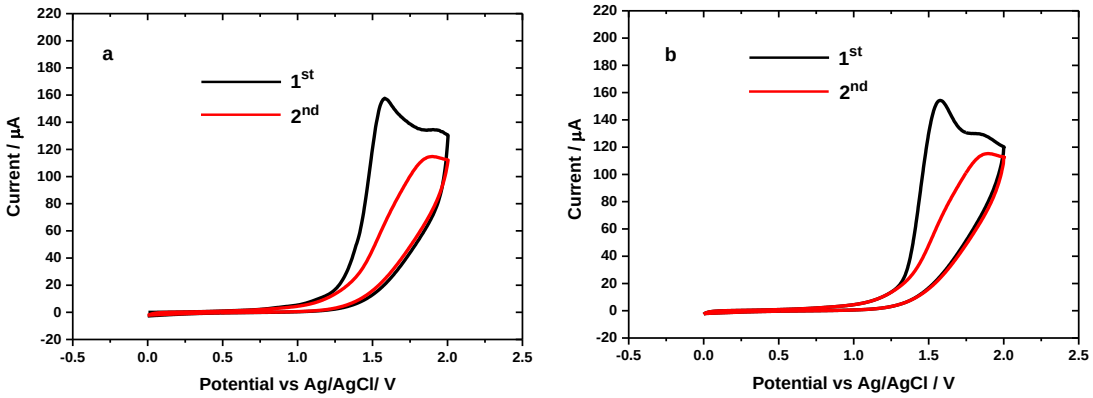

Figure 6.24; Comparison of two repetitive experimental CV (a) (from Figure 6.23 a) with the best simulated fit data (b). Condition used in simulation were $E°$ = 1.45 V, D_o = 7.5 x 10^{-5} cm^2 s^{-1}, Γ_{max} = 2.0 x 10^{-9} mol cm^{-2}, k_S = 1.3 x 10^{-3} cm s^{-1}, k_A = 6.4 x 10^{-5} cm s^{-1}, k_H = 0.6 s^{-1}, α = 0.7 , T = 298 K, scan rate = 50 mV/ s and electrode area = 0.071 cm^2.

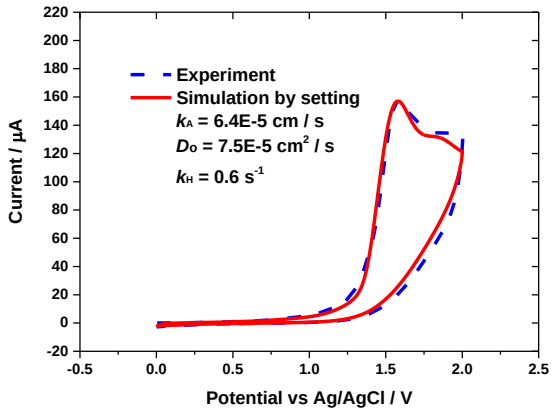

Figure 6.25; The best simulated fit to the experimental CV that has been obtained after adding the interpolated background current for the first scan of the CV. Conditions used in the simulation were $E°$ = 1.45 V, D_o = 7.5 x 10^{-5} cm^2 s^{-1}, Γ_{max} = 2.0 x 10^{-9} mol cm^{-2}, k_S = 1.3 x 10^{-3} cm s^{-1}, k_A = 6.4 x 10^{-5} cm s^{-1}, k_H = 0.6 s^{-1}, α = 0.7 , T = 298 K, scan rate = 50 mV/s and electrode area = 0.071 cm^2.

After performing our simulation procedure for the experimental CV of EDA-Boc in ACN/$NaHCO_3$, it is again evident that by adding the interpolated background solvent current to the simulated CV, the theoretical CV waveform matches the experimental data closely. As reported by Saveant and co-workers[165] the mathematical equations provide a theoretical model for a simple repetitive experimental CV, which is only valid for reactions 1-3 (scheme 6.4). In addition, the proposed model is capable of predicting the growth of film in considering the scan rate. However, for more complex processes in the formation of film, the simulation model should incorporate more knowledge about the growth mechanism.

Therefore, ρ and the ratio $k_A/\sqrt{k_H}$ for two different simulation cases could be determined and compared. Table 6.5 shows a comparison of ρ and $k_A/\sqrt{k_H}$ for the two different fittings. Based on the presented values in Table 6.5, it is clear that ρ and $k_A/\sqrt{k_H}$ for ACN/$NaHCO_3$ are significantly larger than for ACN. Thus, it can be concluded that in the presence of $NaHCO_3$, the rate of attachment of EDA-Boc to the GC electrode surface is enhanced. This is most likely because significantly more intermediate radical species react with the GC electrode surface, rather than in the bulk solution. This leads to more coupling to the electrode surface and as a result, the electrode surface is blocked more rapidly.

Table 6.5; Values calculated for ρ and ($k_A/\sqrt{k_H}$) based on parameters obtained from the best simulated CVs data.

Parameter	Simulation for EDA-Boc in ACN	Simulation for EDA-Boc in ACN/$NaHCO_3$
Competition parameter (ρ)	0.12	0.35
Rate constant ratio ($k_A/\sqrt{k_H}$)	2.8×10^{-5} cm $s^{-1/2}$	8.3×10^{-5} cm $s^{-1/2}$

To conclude, we were able to use the simple kinetic model originally published by Saveant[165] for electrochemical grafting of diazonium at the electrode surfaces. By adding the residual experimental background current to the model, we obtained good agreement between the simulation and the experiment. Because of the complexity of the solvent present in this experiment, as discussed earlier in Section 6.5 (Figure 6.3), more complex chemical equations will not be pursued in this case (in the simulation model).

Based on experimental and theoretical investigations, the efficiency of coupling EDA-Boc to the surface of a GC electrode significantly improved when changing the solvent from neat ACN to ACN/$NaHCO_3$ (4:1). Comparing the ratio $k_A/\sqrt{k_H}$ obtained from the simulations for both methods revealed a significant difference in the ratio $k_A/\sqrt{k_H}$. This is probably due to the slower loss of the radical species in the bulk by reaction in the homogenous solution (lower k_H) in the more basic solution.

6.17 Effect of k_A in the simulation

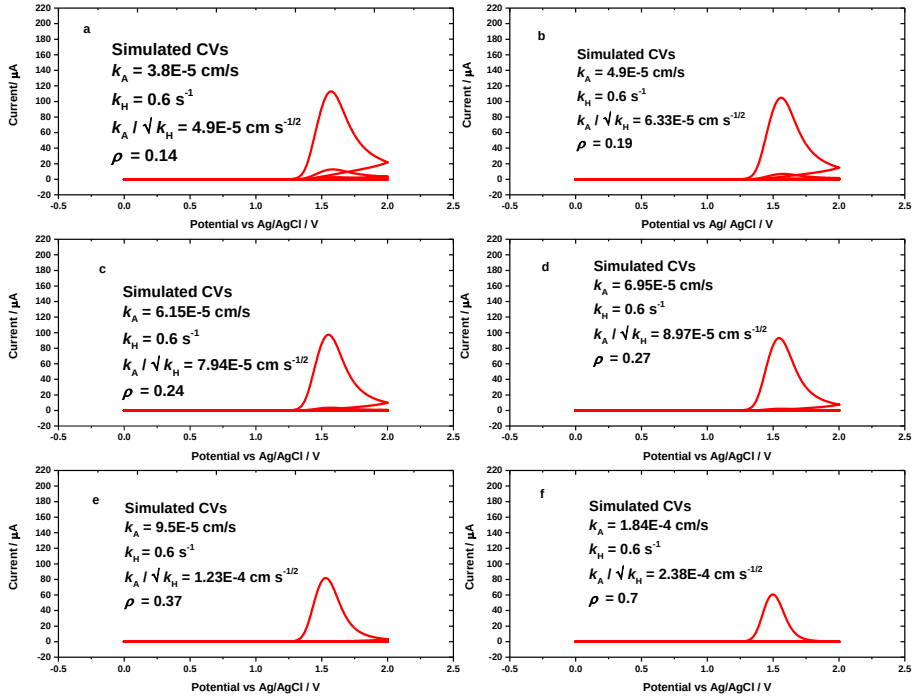

Figure 6.26; Simulated CVs at 50 mV/s with varying values of rate constant for the adsorption of EDA-Boc (k_A) a) 3.85 x 10^{-5} cm s^{-1}, b) 4.9 x 10^{-5} cm s^{-1}, c) 6.1 x 10^{-5} cm s^{-1}, d) 6.9 x 10^{-5} cm s^{-1}, e) 9.5 x 10^{-5} cm s^{-1} and f) 1.8 x 10^{-5} cm s^{-1} while the other parameters are kept constant. Conditions used in simulation were $E°$ = 1.45 V, D_o = 7.5 x 10^{-5} cm^2 s^{-1}, Γ_{max} = 2.0 x 10^{-9} mol cm^{-2}, k_S = 1.3 x 10^{-3} cm s^{-1}, k_H = 0.6 s^{-1}, α = 0.7, T = 298 K, scan rate = 50 mV/s and electrode area = 0.071 cm^2.

In connection with the more rapid blocking effect that was observed experimentally and considering the ratio $k_A/\sqrt{k_H}$, we investigated the variation of k_A values while k_H value is kept constant and the obtained simulated CVs are shown in Figures 6.26 a-f. Clearly, the passivation of the electrode surface, as presented by the simulated CVs, shows that when k_A increased, the current on the second cycle of the simulated CV gradually decreased until the peak disappeared. In addition, another significant phenomenon was observed that corresponded to a more rapid saturation of the electrode surface by immobilised film. The current reaches zero before the turning point of the first cycle, as shown in Figures 6.26e and f. We attempted to fit the first cycle of the simulated CVs to the experimental CV by adding an interpolated background current, as shown previously in Figure 6.23. Thus, by varying k_A while the other simulation parameters are kept constant, setting k_A = 6.4 x 10^{-5} cm / s gave the best response of simulated CV to the experimental CV as can been seen in Figure 6.27.

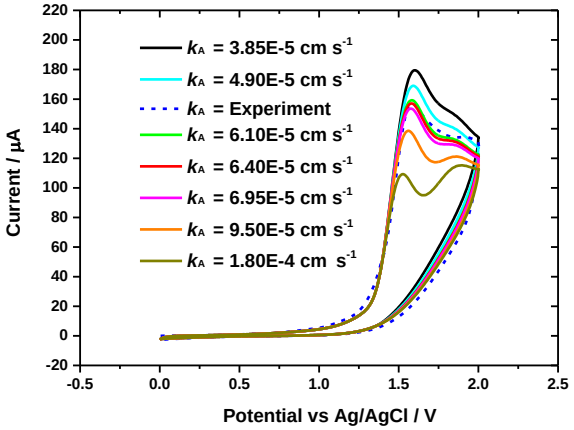

Figure 6.27; The effect varying the kinetic rate constant of adsorption of EDA-Boc (k_A) on the first cycle of simulated CVs (Figure 6.26 a-f) after adding the interpolated experimental background current (Figure 6.23 c) in order to obtain the best fit to the experimental CV waveform.

6.18 Effect of k_H in the simulation

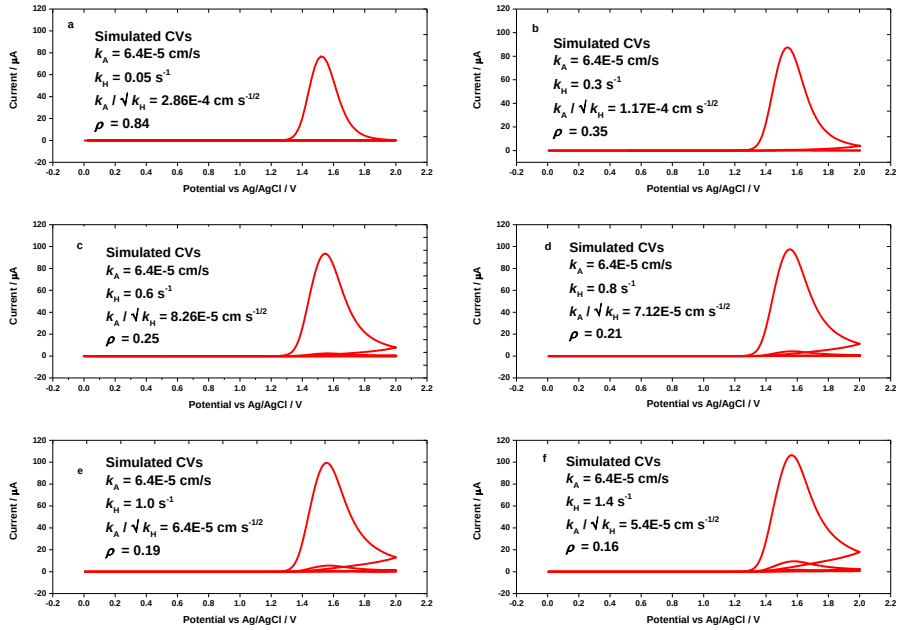

Figure 6.28; Simulated CVs at 50 mV/s with varying values of rate constant for homogenous reaction EDA-Boc (k_H) a) 0.05 s^{-1}, b) 0.3 s^{-1}, c) 0.6 s^{-1}, d) 0.8 s^{-1}, e) 1.0 s^{-1} and f) 1.4 s^{-1} while the others the parameters are kept constant. Conditions used in simulation were $E°$ = 1.45 V, D_o = 7.5 x 10^{-5} cm^2 s^{-1}, Γ_{max} = 2.0 x 10^{-9} mol cm^{-2}, k_S = 1.3 x 10^{-3} cm s^{-1}, k_A = 6.45 cm s^{-1}, α = 0.7, T = 298 K, scan rate = 50 mV/s and electrode area = 0.071 cm^2.

The approach was also applied to varying k_H. k_H were varied between 0.05 s^{-1} and 1.4 s^{-1} while the k_A input was kept constant. The data obtained are shown in Figure 6.28. Clearly, the currents on the first and second peaks increased when increasing k_H. In addition, the peak on the second scan becomes bigger. This is most likely because the radical species react more rapidly in the bulk solution and as a result, the passivation of the electrode surface occurred more slowly. By adding the simulated current from the first cycle to the interpolated background current, new simulated CV currents were obtained as shown in Figure 6.29. From Figure 6.29, clearly, the best fit was obtained when k_H corresponded to 0.6 s^{-1}.

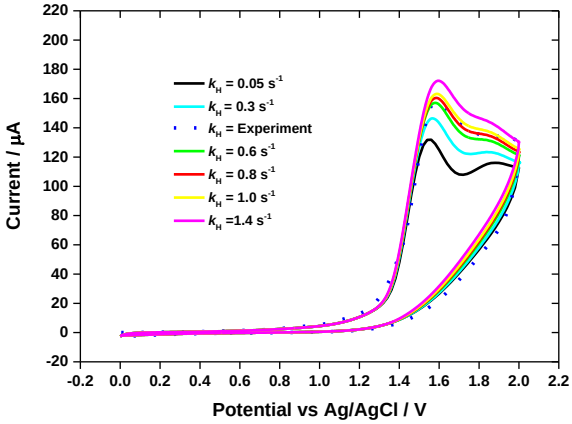

Figure 6.29; The effect of varying the kinetic rate constant for the homogenous reaction of EDA-Boc (k_H) on the first cycle of the simulated CVs (Figure 6.28 a-f) after addition of the interpolated experimental background current (Figure 6.23c).

6.19 Simulations at a scan rate of 100 mV/s

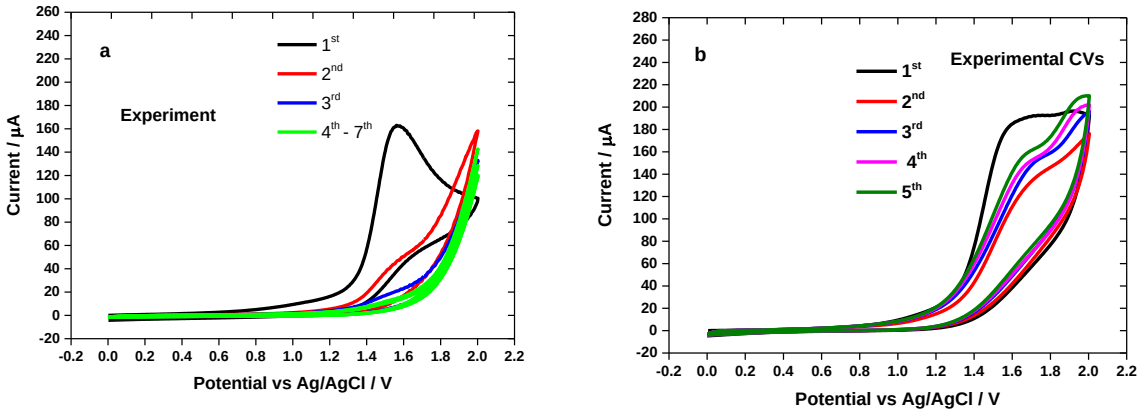

Figure 6.30; Cyclic voltammograms recorded for 10 mM of EDA-Boc with 0.1 M TBATFB carried out in a) neat ACN and b) in 20 % $NaHCO_3$ in ACN. All the experiments were recorded at a scan rate of 100 mV/s for 7 cycles. The electrode area was 0.071 cm^2.

In order to demonstrate the utility and flexibility of our approach, we attempted to simulate experimental CVs of the electrochemical grafting of EDA-Boc at a scan rate of 100 mV/ s. Figure 6.30a shows experimental CVs for coupling EDA-Boc in neat ACN whereas Figure 6.30b presents the experimental CVs for coupling EDA-Boc in ACN/$NaHCO_3$.

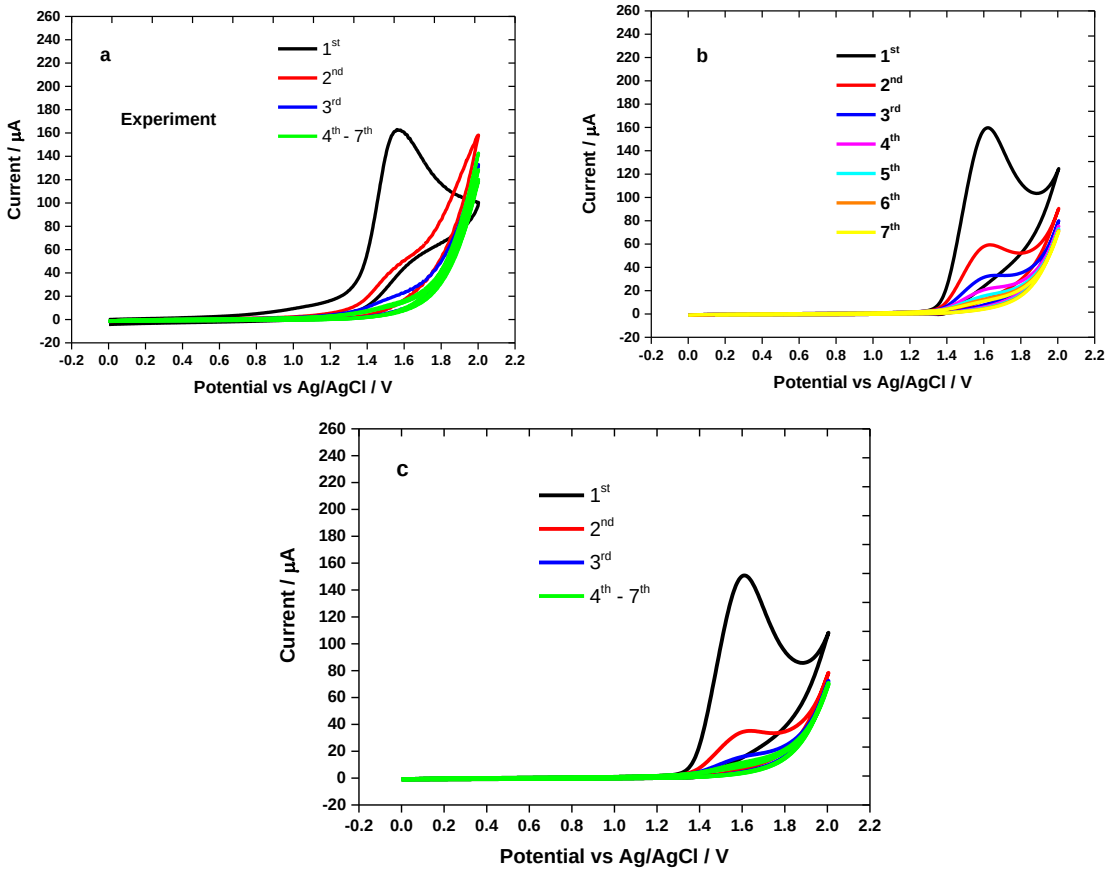

Figure 6.31; **Comparison of seven repetitive experimental CVs (a) with the simulated data (b and c). b) Setting $E°$ = 1.45 V, D_o = 4.9 x 10^{-5} cm^2 s^{-1}, k_A = 2.15 x 10^{-5} cm s^{-1}, k_H = 0.6 s^{-1}. c) Setting $E°$ = 1.45 V, D_o = 5.3 x 10^{-5} cm^2 s^{-1}, k_A = 4.6 x 10^{-5} cm s^{-1} and k_H = 0.8 s^{-1}. Other conditions, Γ_{max} = 2.0 x 10^{-9} mol cm^{-2}, k_S = 1.3 x 10^{-3} cm s^{-1}, α = 0.7, T = 298 K, scan rate = 100 mV/ s and electrode area = 0.071 cm^2 were kept constant.**

For the first step simulation, we used the parameters obtained for the CVs at 0.05 V/s. By using the same approach as previously shown in Figure 6.13, the simulated CVs displayed in Figure 6.31b were obtained. As can be observed, the fit did not correlate well with the experimental CV. The simulated CVs indicate that the passivation of the electrode surface took place after the 5th cycle of CV. The second step of the simulation was performed by reducing the value of k_H in order to simulate a faster passivation of the electrode surface, but the approach failed to achieve any good fit. In addition, a small reduction peak appeared at 1.5 V (not shown). Nevertheless, as shown in Figure 6.31c, good simulated CVs were obtained, especially in terms of blocking features when the k_A and k_H were adjusted from 2.15 x 10^{-5} cm s^{-1} to 4.6 x 10^{-5} cm s^{-1} and from 0.6 s^{-1} to 0.8 s^{-1}, respectively. In order to achieve the best fit on the first scan, the D_o value was slightly increased from 4.9 x 10^{-5} cm^{-2} s^{-1} to 5.3 x 10^{-5} cm s^{-1} increasing the error by 8%.

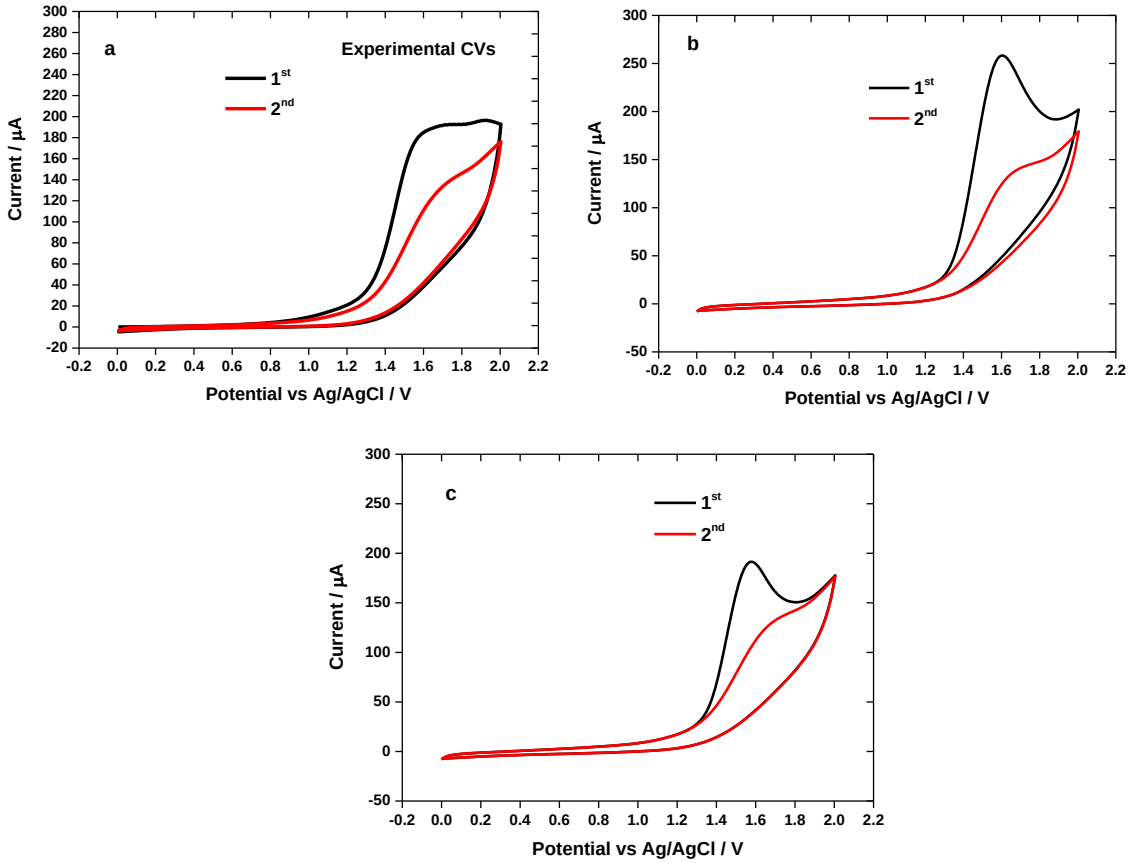

Figure 6.32; Comparison of two repetitive experimental CVs (a) with the simulated data (b and c). b) Setting $E°$ = 1.45 V D_o = 7.5 x 10^{-5} cm^2 s^{-1}, k_A = 6.4 x 10^{-5} cm s^{-1}, k_H = 0.6 s^{-1}. c) Setting $E°$ = 1.45 V, D_o = 7.5 x 10^{-5} cm^2 s^{-1}, k_A = 2.3 x 10^{-4} cm s^{-1} and k_H = 0.8 s^{-1}. Other conditions, Γ_{max} = 2.0 x 10^{-9} mol cm^{-2}, k_S = 1.3 x 10^{-3} cm s^{-1}, α = 0.7 , T = 298 K, scan rate = 100 mV/ s and electrode area = 0.071 cm^2 were kept constant.

For the attachment of EDA-Boc in ACN/$NaHCO_3$, the same simulation approach as for the simulation in ACN was used. Figure 6.32b shows simulated CVs obtained when all the variables determined for 50 mV/s were kept. Clearly, the simulated CVs did not match with the experimental CVs, in particular for the peak height in the first CV scan. The height is higher than for the peak of the experimental CV. By changing the k_A and k_H value from 6.4 x 10^{-5} cm s^{-1} to 2.3 x 10^{-4} cm s^{-1} and from 0.6 s^{-1} to 0.8 s^{-1}, the fitting improved significantly (Figure 6.32c). Interestingly, the k_H value used here is the same value as for the attachment of EDA-Boc in neat ACN. Also, D_o was kept unchanged, and a good agreement between the simulated CV and experimental CV was still obtained. Figure 6.33 compares the first scan of the experimental CV and the simulated CV. Both the CVs are the same CVs as in Figures 6.32a and 6.32c but only the first cycle is shown.

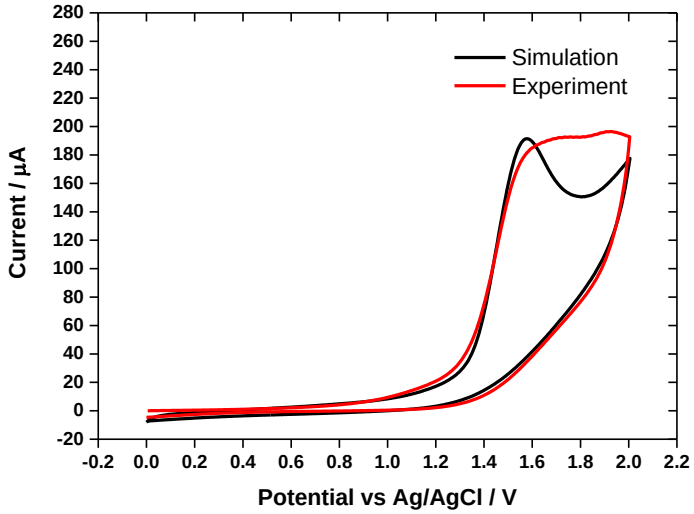

Figure 6.33; The best simulated fit to the experimental CV obtained after adding with the interpolated background current to the first scan of the CV. Condition used in the simulation were D_o = 7.5 x 10^{-5} cm^2 s^{-1}, Γ_{max} = 2.0 x 10^{-9} mol cm^{-2}, k_S = 1.3 x 10^{-3} cm s^{-1}, k_A = 2.3 x 10^{-4} cm s^{-1}, k_H = 0.8 s^{-1}, α = 0.7 , T = 298 K, scan rate = 50 mV/s and electrode area = 0.071 cm^2.

To conclude here, in order to obtain the best-simulated data for the two CVs (Figures 6.31c and 6.32c), there are significantly changing of k_A and k_H from 50 mV/s to 100 mV/s. Comparing k_A and k_H values used in the CV simulations at both the scan rates, the datasets are significantly different. However, a constant D_o value was used for both the simulation cases. We believe that the obtained simulation data provide us with a rational answer. Experimentally, at a slow scan rate, the diffusion layer would grow much further from the electrode surface. As a result, the flux to the electrode surface is considerably small. Thus, it may decrease the rates of k_A and k_H during the electrochemical grafting process. In contrast, when the scan rate was increased from 50 mV/s to 100 mV/s, at a fast scan rate, the diffusion layer would grow much closer to the electrode surface. Thus, the flux to the electrode surface becomes bigger. Consequently, it may increase the rates of k_A and k_H.

6.20 Blocking study of immobilised EDA-Boc by CV

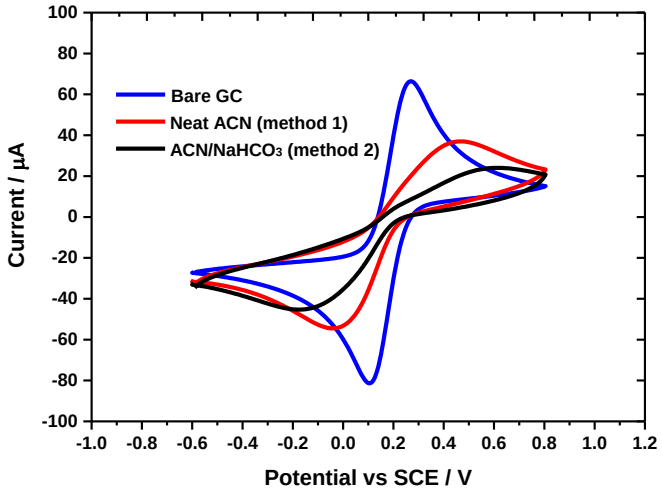

Figure 6.34; CVs showing the blocking effect of EDA-Boc films at surface of EDA-Boc modified GC electrodes in 10 mM $K_3[Fe(CN)_6]$ in 0.1 M KCl (second cycle shown). The blue line is scan taken at bare GC electrode and the red line is a scan taken after grafting EDA-Boc in neat ACN. On the contrary, the black line is a scan taken after grating EDA-Boc in $ACN/NaHCO_3$. The scan rate was 50 mV/s and the electrode area was 0.071 cm^2.

The cyclic voltammogram of solute electroactive species provides a convenient technique to study the presence of the grafted films and their blocking properties on the electrode surface. The covalently attached EDA-Boc at the carbon surfaces prepared by methods 1 and 2 were measured using CV with the presence of 10 mM potassium ferricyanide in 0.1 M KCl in order to study the blocking effect of the grafted EDA-Boc layer. As shown in Figure 6.34, the voltammogram of $[Fe(CN)_6]^{-3}$ exhibits reversible CV signal (blue) at the bare GC electrode with a redox potential around 189 mV. However, the CV signal significantly changed in the presence of the EDA-Boc film on the GC surface. This effect is attributed to the blocking of the modified electrode surface, which gave an increase in the peak separation and a decrease in the peak currents. Greater blocking by the surface film over electron transfer of the redox probe results in a larger ΔE_P value [188].The black and red CVs in Figure 6.34 show the behaviour of the redox reaction of $[Fe(CN)^6]^{-3}$ at two different grated EDA-Boc films. It clears that the EDA-Boc film formed in $ACN/NaHCO_3$ shows more blocking properties towards the electron transfer of the negative redox ions $[Fe(CN)_6]^{-3}$ than the film formed in neat ACN. Based on three replicate experiments (not shown), it could be concluded that the grafting process of EDA-Boc in $ACN/NaHCO_3$ produced a more compact monolayer EDA-Boc film, which leads to grafting behaviour of the electron transfer between the redox species in bulk solution of the carbon surface. As a result, that the $[Fe(CN)^6]^{-3}$ ions are more difficult to diffuse from the bulk solution through the layer to the electrode surfaces. However, the ions are still capable of accessing the electrode surface, probably through

the gap of surrounding EDA-Boc layer (microscopic sites) or underneath the GC electrode[106,166,167], hence the redox peaks are still can be seen, but in small signals. Overall, it can be deduced that the inhibition of $[Fe(CN)^6]^{-3}$ redox current indicates that the electrochemical grafting of EDA-Boc using method 2 produced more compact closely packed film than method 1.

6.21 Electrochemical impedance spectroscopy measurements for blocking EDA-Boc films

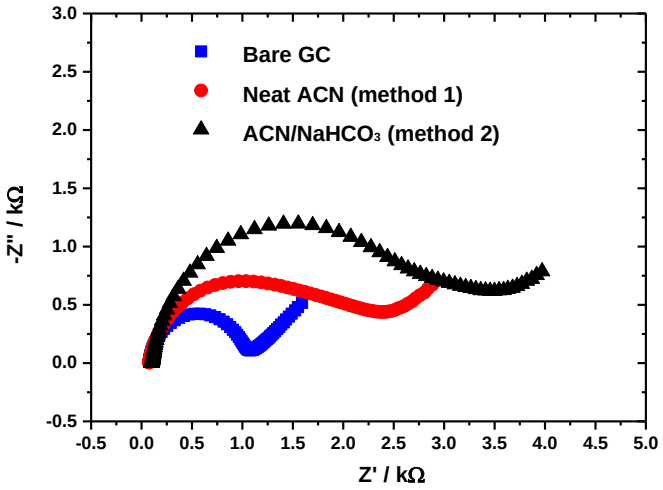

Figure 6.35; Nyquist representations of the impedance spectra at 0.188 V *vs* SCE in 10 mM of $K_3[Fe(CN)_6]$ in 0.1 M KCl for bare GC electrode (blue), modified GC electrode with EDA-Boc film after grafting in ACN (red) and modified GC electrode with EDA-Boc film after grating in ACN/$NaHCO_3$ (black). The measurements were made at a frequency range from 0.1 kHz to 100 kHz, number of frequency = 45 and modulation amplitude = 5 mV.

Electrochemical impedance spectroscopy (EIS) is a complimentary technique to cyclic voltammetry for evaluating the film compactness and the electron transfer resistance across the grafted layer [189]. By keeping the experimental conditions constant for KCl and potassium ferricyanide as used in the CV measurement, the CV data were verified with EIS measurements. Three replicate experiments for each case were conducted and overall, as depicted in Figure 6.35, the impedance spectra (Nyquist plots) show semicircles with the Warburg line, where the semicircle is produced in the high-frequency region, corresponding to the to the interfacial charge-transfer mechanism (R_{ct}) over electron transfer process of redox solute. By contrast, the Warburg line with a slope near unity is produced in the low frequency range, representing a semi-infinite diffusion phenomenon [106,107,155]. The blue semicircle shows the impedance spectrum of $[Fe(CN)^6]^{-3}$ at bare GC electrode. The small diameter semicircle on the Nyqusit plot is resulted from the lower charge transfer resistance (R_{ct}) for the reaction of $[Fe(CN)^6]^{-3}$ at the bare GC electrode. The well-defined Warburg line corresponds to diffusion of $[Fe(CN)^6]^{-3}$ ions from the bulk solution to

the electrode surface[190]. On the contrary, the red and black semicircles depict Nyquist plots of $[Fe(CN)^6]^{-3}$ for modified GC electrodes with 2 different EDA-Boc films that have been prepared employing method 1 and 2. As can be clearly seen the diameter of the semicircle significantly increased from blue to red and gradually increased from red to black. By contrast, the Warburg lines are gradually less apparent. These qualitatively indicate that the electrode kinetic for $[Fe(CN)^6]^{-3}$ ions becomes slower with the presence of EDA-Boc, particularly EDA-Boc film formed by method 2. To conclude, the Nyquist plots show that the grafted EDA-Boc film that had been produced using method 2 inhibits electron transfer of $[Fe(CN)^6]^{-3}$ more strongly than method 1. This result correlates well with the data of the CV experiments.

6.22 Coupling of anthraquinone (AQ) at EDA modified GC electrodes based on method 1 and method 2.

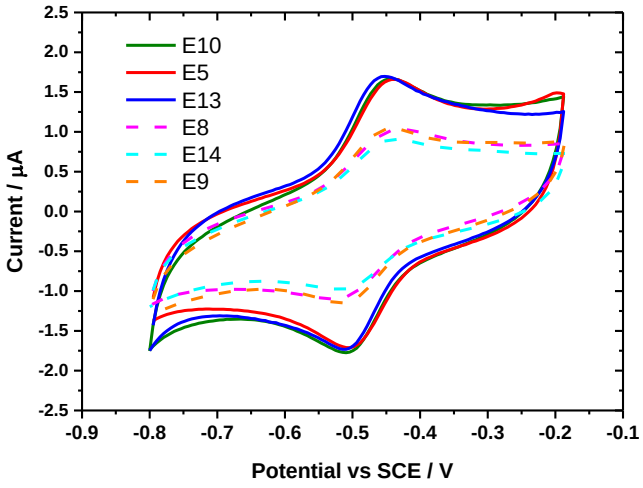

Figure 6.36; Cyclic voltammograms from the six different AQ modified GC electrodes (scan rate 50 mV/s and sixth cycle shown) for two different grafting methods of EDA-Boc. The dashed lines, coupled AQ to the EDA-Boc linker employing method 1 (ACN). The solid lines, coupled AQ to the EDA-Boc linker employing method 2 (ACN/$NaHCO_3$). The AQ modified GC electrodes were measured in 0.1 M phosphate buffer (pH 7) and the electrode area was 0.071 cm^2.

In order to investigate in detail the advantages of using method 2 to produce grafted films of EDA-Boc the BOC groups have removed and the EDA linker was covalently coupled with antraquinone-2-carboxyclic acid (AQ). Figure 6.36 shows the CVs of the AQ covalently attached to the EDA linker in 0.1 M phosphate buffer (pH 7), recorded at a scan rate of 50 mV / s. The solid lines are the CVs of AQ on EDA linkers grafted using method 2. In contrast, the dashed lines are the CVs of AQ on EDA linkers grafted employing method 1. Three different CVs are obtained from three different AQ modified GC electrodes in each case in order to show the reproducibility with replicate experiments. The concentration of AQ was kept constant for each

modification. As can be clearly seen, the oxidation and reduction currents that were generated from the redox reactions of AQ for method 2 are significantly increased over those for method 1. As previously discussed, the grafting of EDA-Boc to the electrode surface in the ACN/$NaHCO_3$ solvent system could produce more compact, dense films than in neat ACN. This could probably lead to the attachment of more AQ molecules at the EDA linker. In order to verify this, the CV surface coverages (Γ_{CV}) of immobilised AQ for each attachment were calculated using equation 1.23, Chapter 1). The results are shown in Table 6.6. The coupling of AQ to the EDA linker that has been grafted using method 2, gave higher surface concentration than method 1.

Table 6.6; Data calculated CV surface coverages of immobilised AQ over two different methods used in electrochemical grafting of EDA-Boc.

Method	CV surface coverages / pmol cm^{-2}
AQ modified GC electrode (method 1)	112 ± 3.54
AQ modified GC electrode (method 2)	181 ± 11.9

6.23 DPV for AQ modified GC electrodes

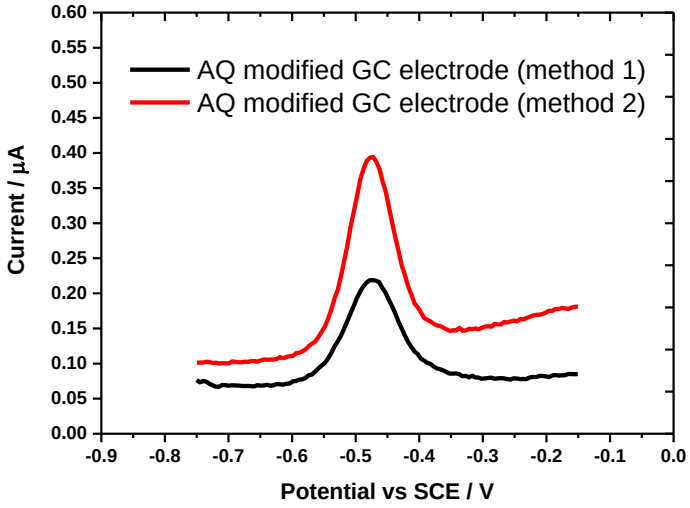

Figure 6.37; Differential pulse voltammograms (DPVs) for AQ modified GC electrodes. The black line, immobilised AQ employing method 1 and the red curve, immobilised AQ employing method 2. The DPVs were measured at ΔE_p = 2.5 mV, τ_p = 0.05 s, τ_i = 0.5 s, ΔE_s = 0.005 V and DPV scan rate = 0.01 V s^{-1} in 0.1 M phosphate buffer solution, pH 7. The area of GC electrode was 0.071 cm^2.

In addition to the CV measurement, the AQ modified electrodes were also measured using DPV before adding the external resistance box in order to more sensitively characterise the covalent immobilised AQ produced with different EDA-Boc grafting methods. By using our non-adjustable DPV parameters that we have modelled, with a modulation amplitude of 2.5 mV, modulation time of 50 ms, interval time of 500 ms and the potential step of 5 mV, the DPV signals for two different AQ modified GC electrodes are shown in the Figure 6.37. It is clearly shown that the coupled AQ on the grafted EDA linker by method 2 gave higher DPV current than method 1. This result is consistent with the data that we had obtained by the CV. However, very well-defined Faradaic currents were obtained from the DPV measurements compared with the CV technique.

6.24 DPV surface coverages of immobilised anthraquinone (AQ)

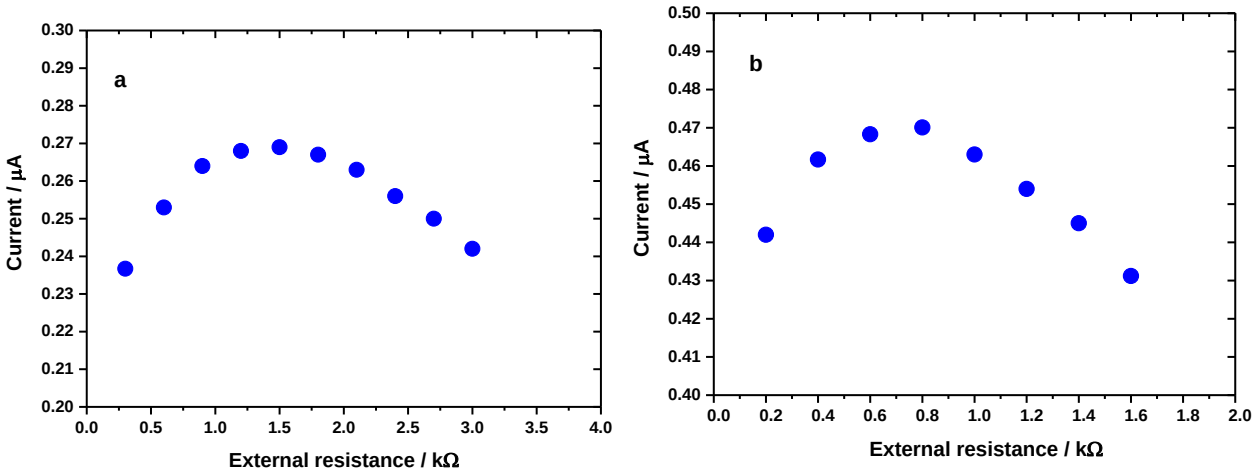

Figure 6.38; Plot of DPVs peak currents against a series of R_{ext} added to the cell circuit over DPV measurements with ΔE_p = 2.5 mV, τ_p = 0.05 s, τ_i = 0.5 s, ΔE_s = 0.005 V and a DPV scan rate of 0.01 V s^{-1} in 0.1 M phosphate buffer solution at pH 7. a) AQ modified GC electrode based upon grafted EDA-Boc by employing method 1. b) AQ modified GC electrode with grafted EDA-Boc by employing method 2. The electrode area was 0.071 cm^2.

Figure 6.38 shows a set of DPV peak currents (without background subtraction) plotted against the added R_{ext} for two different AQ modified GC electrodes. Figure 6.38 (a) shows the data from attached AQ from method 1 whereas Figure 6.38 (b) from method 2. As demonstrated by Anson and co-workers[89] the magnitude of uncompensated resistance on the maximum DPV peak currents shifted to lower R_u values when the surface concentrations of adsorbed species are increased. This resulted when the presence of more adsorbed redox species on the electrode surface gives a larger pseudocapacitance (C_f), where the C_f is in parallel with double layer capacitance (C_{dl}). Hence, the maximum DPV peak current can be obtained based on an approximation relationship of $t = R_u (C_{dl} + C_f)$. Based on this finding, we deduced that more molecules of AQ had been covalently attached on the free EDA linkers in method 2 than method 1. Hence, this means that the monolayer EDA linker provided a number of free EDA linker to be coupled with AQ. This is one piece of evidence that the coupled AQ on the grafted EDA linker using method 2 gave better surface coverages than method 1. As shown in Figure 6.38 (a) and 6.38 (b), by adding R_{ext} of 1.5 kΩ and 0.8 kΩ to the AQ modified GC electrodes, the DPV currents are enhanced for the two modified electrodes. The DPV peak currents are shown in Figures 6.39 and 6.40, respectively.

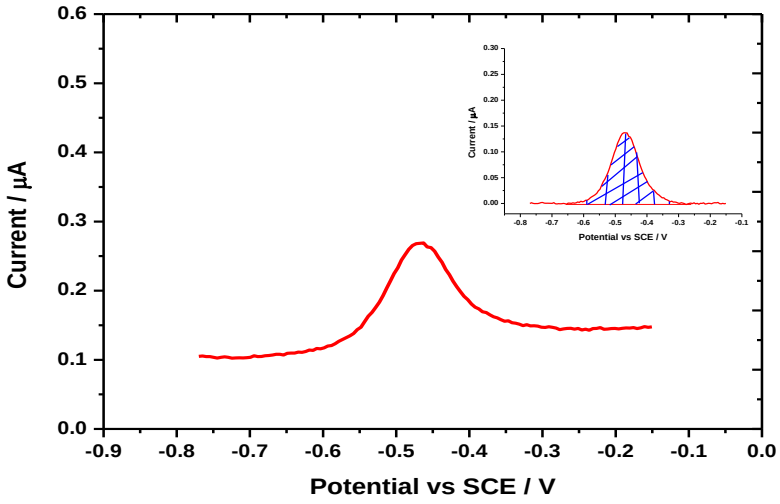

Figure 6.39; DPV for the AQ modified GC electrode (method 1) in 0.1 M pH 7 phosphate buffer solution after adding an R_{ext} of 1.5 kΩ corresponding to the maximum DPV peak current. The inset figure is DPV after performing background subtraction using origin 9.1. DPV paramaters as in Figure 6.39. The electrode area is 0.071 cm^2.

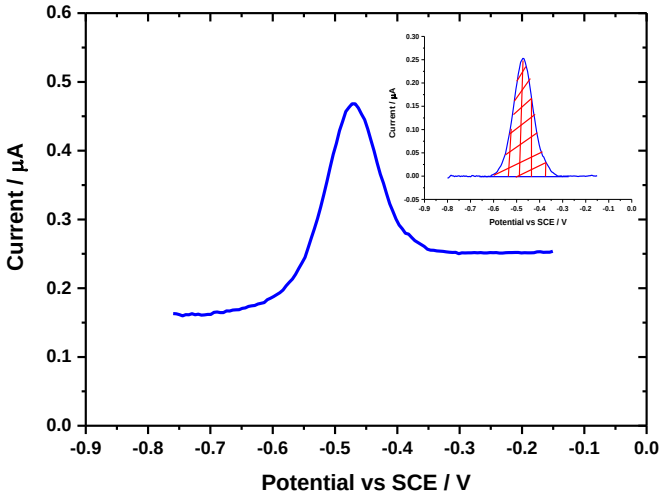

Figure 6.40; DPV for the AQ modified GC electrode (method 2) in 0.1 M pH 7 phosphate buffer solution after adding an R_{ext} of 0.8 kΩ corresponding to the maximum DPV peak current. The inset figure is DPV after performing background subtraction using origin 9.1. DPV parameters as in Figure 6.39. The electrode area is 0.071 cm^2.

Background subtraction was performed on the DPV peak currents using origin 9.1 in order to obtain the integrated area under the DPV peaks as shown in the inset figures. Using the equation that we have modelled (Eq.4.18), the DPV surface coverages for the covalently immobilised AQ at the surface of GC electrodes using the two different attachment methods for grafting EDA-Boc linker was estimated. The results for the two different DPV surface coverages are given in Table 6.7.

Table 6.7; Calculated DPV surface coverages of immobilised AQ for two different methods used in the electrochemical grafting of EDA-Boc.

Method	DPV surface coverage / pmol cm^{-2}
AQ modified GC electrode (method 1)	120 ± 3.40
AQ modified GC electrode (method 2)	205 ± 6.24

There is a similar trend when it comes to comparing the $\Gamma_{DPV,\ exp}$ with the Γ_{CV}, the AQ coupled on the grafted EDA linker (method 2) gave higher surface coverages than method 1. Comparisons of the estimated surface coverages for covalently immobilised AQ by CV and the DPV are illustrated in Figures 6.41 (a) and 6.41 (b), respectively.

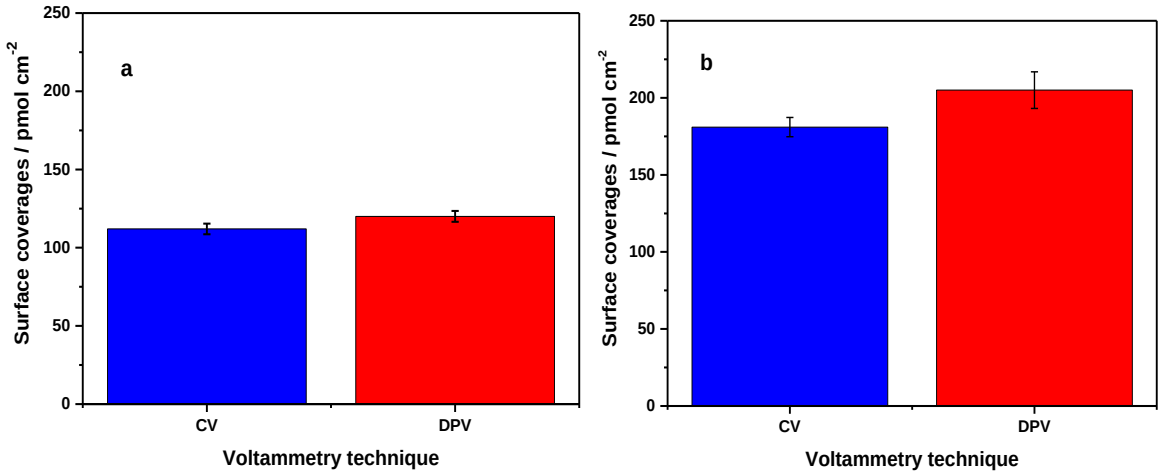

Figure 6.41; Comparisons of the estimated surface coverages (Γ) by CV and DPV techniques for AQ modified GC electrodes for two different of electrochemical grafting methods for EDA-Boc. a) AQ modified GC electrode by grafting EDA-Boc in neat ACN b) AQ modified GC electrode by grafting EDA-Boc in ACN/$NaHCO_3$.

The obtained $\Gamma_{DPV,\ exp}$ compared to the obtained Γ_{CV} for the two different modified electrodes are to close each other. However, the estimated Γ_{CV} is slightly less than $\Gamma_{DPV,\ exp}$ and it has been previously discussed in detail in Chapter 4. Moreover, the experimental $\Gamma_{DPV,\ exp}$ presented here will be verified using our DPV simulation. This will be discussed in detail in Section 6.26.

6.25 Impedance measurements for the R_t and C_{dl} for AQ-modified GC electrodes

In Chapter 4, we analysed and described in detail how to determine the total uncompensated resistance in the electrochemical cell (R_t) and the C_{dl} for the modified GC electrodes. By using the same approach, the C_{dl} for two different types of AQ modified GC electrodes can also be determined. R_t and C_{dl} when R_{ext} of 1.5 kΩ and 0.8 kΩ were introduced to the DPV cell circuit were measured at potentials of -0.7 V and -0.25 V. The magnitudes of R_t (R_u + R_{ext}) in the electrochemical cell can be directly determined from the Nyquist plot as shown in the inset figures in Appendix 6.2a and 6.3a, respectively. A range of frequencies from 0.954 to 21.21 Hz for AQ modified GC electrode (ACN/$NaHCO_3$) and 0.87 to 22.21 Hz for AQ modified GC electrode (neat ACN) were chosen in order to obtain linear fittings on the plots of –*Z*" *vs*. 1/f . C_{dl} can be calculated based on gradients obtained in App. 6.2d and App. 6.3d. The calculated C_{dl} for the two measured potentials (-0.70 V and -0.25 V *vs* SCE) associated with the R_{ext} added of 1.5 and 0.8 kΩ over two different types of AQ modified GC electrodes are presented in Table 6.8. In addition, the determined R_t from the Nyquist plots can also be seen in Table 6.8. The experimentally determined for values of R_t and C_{dl} from the impedance measurements will be used in the DPV simulations.

Table 6.8; Double layer capacitance (C_{dl}) for two different measured potentials, -0.70 V and -0.25 V *vs* SCE, for AQ modified GC electrodes using EIS.

Method	R_t / kΩ	-0.70 V /µF	-0.25 V / µF
AQ modified GC electrode (method 1)	1.66 ± 0.029	9.54 ± 0.76	11.13 ± 0.27
AQ modified GC electrode (method 2)	1.01 ± 0.028	14.09 ± 0.87	18.73 ± 1.97

6.26 Simulation for experimental DPVs

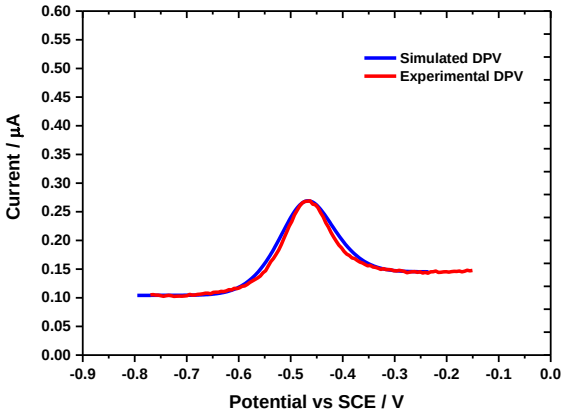

Figure 6.42; DPVs for the AQ modified GC electrode by employing method 1 at R_{ext} added of 1.5 kΩ, corresponding to the maximum DPV peak current. The red voltammogram is the experimental DPV measured with ΔE_p = 2.5 mV, τ_p = 0.05 s, τ_i = 0.5 s, ΔE_s = 0.005 V and a DPV scan rate of 0.01 Vs^{-1} in 0.1 M phosphate buffer solution at pH 7. In contrast, the blue curve is the best simulated DPV was obtained by setting the kinetic rate constant (k_s) = 3.85 s^{-1}, R_t = 1.66 kΩ, α = 0.50, C_{dl} for reduced layer = 11.2 µF, C_{dl} for oxidised layer = 12.6 µF and $\Gamma_{DPV,\,sim}$ = 110 pmol cm^{-2} in our MATLAB script. The R_t of 1.66 kΩ was directly determined from the Nyquist plots. The same DPV parameters were entered in the DPV simulation as used in the experimental DPV.

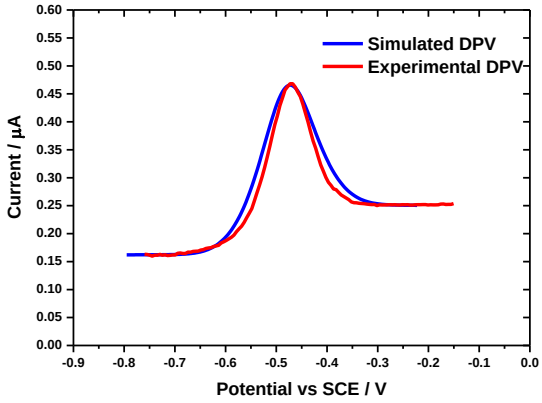

Figure 6.43; DPVs for the AQ modified GC electrode by employing method 2 at R_{ext} added of 0.8 kΩ, corresponding to the maximum DPV peak current. The red voltammogram is the experimental DPV measured with ΔE_p = 2.5 mV, τ_p = 0.05 s, τ_i = 0.5 s, ΔE_s = 0.005 V and a DPV scan rate of 0.01 Vs^{-1} in 0.1 M phosphate buffer solution at pH 7. In contrast, the blue curve is the best simulated DPV obtained by setting k_s = 3.9 s^{-1}, R_t = 1020 Ω, α = 0.50, C_{dl} for reduced layer = 18.2 µF, C_{dl} for oxidised layer = 21.4 µF and $\Gamma_{DPV,\,sim}$ = 197 pmol cm^{-2} in our MATLAB script. The R_t of 1020 Ω was directly determined from the Nyquist plot. The same DPV parameters were entered in the DPV simulation as used in the experimental DPV.

By setting all the variables together as known values that had been extracted out from the experimental work, the DPV simulations on two different types of AQ modified GC electrodes can be performed. By using the same approach, the simulated DPV on the two different type of AQ modified GC electrodes at R_{ext} added of 1.5 kΩ and 0.8 kΩ were obtained as shown in Figure 6.42 and 6.43, respectively. Figure 6.42 shows the best response of the simulated DPV for AQ modified GC electrodes (method 1) is at the optimal $\Gamma_{DPV,\ sim}$ of 110 pmol cm^{-2}. By contrast, Figure 6.43 shows the best response of the simulated DPV is at the optimal $\Gamma_{DPV,\ sim}$ of 197 pmol cm^{-2}. All the parameters were extracted from the experimental work and the used values in these simulations are shown in Table 6.9. Similarly, two different simulated DPVs show slight deviations between the experimental and theoretical responses observed. This is most likely coming from a range of different redox potentials (microenvironments) or the rate constant (orientations) of individual immobilised AQ[191]. However, the results showed that experimental DPVs were in good agreement to the theoretical DPV waveforms.

Table 6.9; Values for MATLAB parameters obtained from the experiments and used in the DPV simulation.

	Method 1		**Method 2**	
Parameters	**Experiment**	**Simulation**	**Experiment**	**Simulation**
Redox potential (E°)	-0.474 V	-0.477 V	-0.477 V	-0.480 V
Total uncompensated resistance in the electrochemical cell (R_t)	1.69 kΩ	1.69 kΩ	1.023 kΩ	1.023 kΩ
Transfer coefficient (α)	0.5	0.5	0.5	0.5
Rate of electron transfer (k_s)	3.98 s^{-1}	3.85 s^{-1}	3.98 s^{-1}	3.90 s^{-1}
C_{dl} for reduced form	9.54 µF	11.20 µF	14.09 µF	14.50 µF
C_{dl} for oxidised form	11.13 µF	12.60 µF	18.01 µF	16.50 µF
$\Gamma_{DPV,\ exp}$ *vs* $\Gamma_{DPV,\ sim}$	120 pmol/cm^2	110 pmol/cm^2	205 pmol/cm^2	197 pmol/cm^2

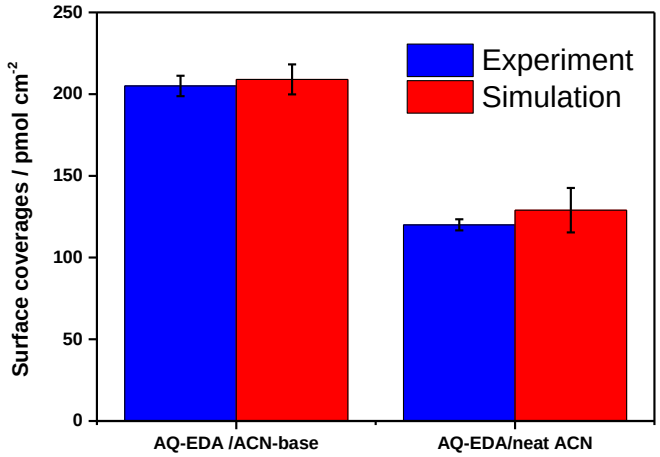

Figure 6.44; Comparison of DPV surface coverages by experimental and simulation approaches for covalently attached AQ over two different electrochemical grafting methods for EDA-Boc linker.

Figure 6.44 shows the comparison of $\Gamma_{DPV,\ exp}$ and $\Gamma_{DPV,\ sim}$ of immobilised AQ on two different methods for the attachment of EDA linkers. It is clearly seen that the obtained $\Gamma_{DPV,\ sim}$ from our DPV simulation and the experimental Γ_{DPV} that had been calculated from our modelled equation (Eq. 4.18) gave similar surface coverages with small errors on three different modified electrodes. It is clearly shown that DPV has offered us better precision measurements in estimating the surface coverages of covalently immobilised AQ at the GC electrode surfaces.

6.27 Conclusion

A new method for electrochemical grafting of EDA-Boc at the surface of GC electrode with the mixed solvents system ACN and a weak base of $NaHCO_3$ in the ratio of 4:1 (method 2) has been performed in this study. Electrochemical behaviours of repetitive CVs were compared to the repetitive CVs for the attachment EDA-Boc in neat ACN (method 1). The CVs show a significant change of CV waveforms, and more rapid blocking of the electrode surface has been observed. In the presence of added $NaHCO_3$, the passivation of the electrode surface took place on the second scan of the measurement.

The diffusion coefficients (D_o) of EDA-Boc in the two different solvent systems were determined. The presence of 20 % of 0.1 M $NaHCO_3$ increased the D_o as experimentally determined by the CV and chronoamperometry techniques. The obtained D_o values from the two methods are not in a good agreement. The chronoamperometry method yields diffusion coefficient of higher precision than CV technique. This is because it is less affected by passivation of the surface by the electrografting reaction.

In order to investigate the effect of protonation and deprotonation of EDA-Boc, the grafting process of EDA-Boc was studied in the presence of a strong base and a strong acid. The results showed that in the presence of non-nucleophilic DBU base, the oxidation peak for EDA-Boc around 1.6 V *vs* Ag/AgCl disappeared. However, strong oxidation peak for the DBU base at 1.25 V *vs* Ag/AgCl was observed. For the oxidation peak of EDA-Boc in the presence of TFA acid, the peak completely disappeared.

The experimental CVs for the attached EDA-Boc at the surface of GC electrodes that have been performed in two different solvent systems were simulated using our simulation model. The mathematical equations have been developed following Saveant's simple model, that modelled the self-inhibition surface reactions. Based upon our simulation program, the determined D_o can be verified. The theoretical voltammograms show that the theoretical D_o is in excellent agreement with experimental D_o that has been measured by chronoamperometry, employing the Cottrell equation. The simulated fit shows satisfactory agreement to the experimental CVs for the attachment of EDA-Boc in ACN, however, in considering the turning current on the reverse scan, the simulation gave a poor fit. Nevertheless, by combining the simulated currents with the experimental background solvent current from the 4^{th} to 7^{th} cycles, the simulated CV was significantly improved, and the new generated CV waveforms are close to the experimental CVs. On the contrary, in the simulation case for the attached EDA-Boc in ACN/$NaHCO_3$, the simulated fit shows good agreement for the blocking effect of the electrode surface, but underestimated the current particularly the peak height. Hence, by using the same approach as discussed on simulated

CV for method 1, the new CV shape is identical to experimental CVs. More complex mathematical equations could be used to describe the background current in the simulation model. However, this was not considered in this study. Furthermore, from the simulation, the kinetic parameters such as k_S, k_A, k_H and α, could be extracted, where those parameters are not directly available from experiments.

In order to investigate the compactness of the EDA-Boc films and the electron transfer resistance across the grafted layers for the two different electrochemical grafting methods, CV and the EIS measurements were made. By measuring the EDA-Boc modified electrodes in the presence of 10 mM of potassium ferricyanide in 0.1 M KCl electrolyte solution, the blocking properties of the grafted EDA-Boc films towards ferricyanide ions can be visualised. As shown by the CV measurements, the EDA-Boc film that was prepared by method 2 gave more blocking film for electron transferred to $[Fe(CN)^6]^{-3}$ ions than EDA-Boc film that was prepared by method 1. Interestingly, the CV data are in good agreement with the EIS results.

More experiments were conducted by coupling anthraquinone (AQ) to the EDA films (after removing the Boc group). The surface coverages (Γ) of the coupled AQ were calculated by CV and our Γ_{DPV} equation (Eq. 4.18). The calculated surface coverages for each technique showed that the Γ_{CV} and Γ_{DPV} of covalently grafted AQ to the EDA linker monolayer prepared by method 2 were higher than the Γ_{CV} and Γ_{DPV} by employing method 1.

In comparing the estimated $\Gamma_{DPV,\ exp}$ using our Γ_{DPV} equation to the Γ_{CV}, the results show that values are close to each other. In order to verify the $\Gamma_{DPV,\ exp}$, DPV simulations were performed. The data showed that the experimental DPVs were in good agreement with the simulated DPVs. The $\Gamma_{DPV,\ sim}$ values gave good agreement to the $\Gamma_{DPV,\ exp}$.

Finally, by showing good agreement between $\Gamma_{DPV,\ exp}$ and $\Gamma_{DPV,\ sim}$ and a good fit the simulated DPVs to the experimental DPVs, we concluded that our Γ_{DPV} equation and developed DPV simulation work well for the new method for the electrochemical grating of EDA-Boc at the surface of GC electrodes.

Chapter 7: Quantification of immobilised ssDNA by DPV based on a DNA labelled system

7.1 Overview

In the previous chapters, the application of experimental models developed to determine the DPV surface coverages of AQ and Os bipyridine complexes covalently attached through amine linkers at the surface of the GC electrode was shown. Using a DPV simulation program, the Γ_{DPV} from the experiment was verified and shown to be in agreement with the theoretical value of Γ_{DPV} obtained. The key objective of this study was to demonstrate flexibility and utility of our models on different surfaces of modified electrodes including a variety of attached redox species. Thus, the models were tested on self-assembled AQ-ssDNA attached to the surface of a gold electrode by thiol groups. In this work, the AQ-ssDNA modified gold electrodes were kindly prepared and provided by a colleague in the same group, Rachel Gao. After conducting the DPV experiments on the modified electrodes, the density of the immobilised ssDNA obtained by using DPV was confirmed using our model Γ_{DPV} equation. Initially, the determined surface coverages of immobilised ssDNA using DPV were compared with the surface coverages determined using CV and chronocoulometry. The AQ-ssDNA modified electrodes were also characterised using CV, chronoamperometry and EIS techniques in order to obtain the information on the kinetics of the electrode reaction (k_s and α), RC time constant, C_{dl} and uncompensated resistance in the electrochemical cell (R_t). By using the values obtained from the experiments to perform the DPV simulation, the experimental Γ_{DPV} for the immobilised ssDNA at the surface of gold was verified.

7.2 Modification of gold electrode surface by self-assembly of DNA monolayers

The immobilisation of DNA using self-assembly of thiol (SAM monolayers) on the surface of gold electrodes is the most common approach used in DNA research for developing DNA sensors[192,193]. ssDNA chains assembled onto the surface of gold electrodes using thiols are widely used in sensors to capture the complementary analyte DNA, or target undergoing hybridization at the surface to form immobilised double stranded DNA (dsDNA)[71].

Typically, DNA probes (ssDNA or dsDNA) are attached to the gold electrode surface using gold-sulfur (Au-S) linkage. The Au-S bond is moderately strong (45 kJ/mol) but the thiol group is easily oxidised and this can weaken the Au-S interaction[46]. Nevertheless, it is more stable than direct physical adsorption, for example as shown earlier in the work on adsorbed 9,10-PQ at the surface of GC electrodes.

As reported in the literature, the immobilised ss-DNA probes can be coiled up on the surface or elongated away from the surface into the bulk solution. As reviewed by Archana[194] and David, this behaviour is influenced by the ionic strength of the bulk solution that is used. Basically, the ss-DNA chains provide a constant negative charge inside the brush region. This provides a local electric field which interacts with the salt ions from the electrolyte. Thus, in the high concentration salt solution, the ssDNA chains will coil up. In contrast, in the low concentration salt solution, the chains will elongate. This is because the flexibility of the immobilised ss-DNA chains is related to the inverse relation of the radius of gyration (R_g) with the ionic strength (Z). In contrast, this is not the case for the immobilised dsDNA, where the dsDNA structure is a rigid duplex. The orientation of the ssDNA chains and the accessibility of the immobilised probes to the complementary target can be enhanced by capping the surface with a small molecule thiol blocking agent, typically 6-mercapto-1-hexanol. The thiol group of MCH quickly displaces the weakly adsorptive ssDNA at the surface, making the conformational of the ssDNA chain more vertical through the thiol end group and elongated further into the solution[192] as shown in Figure 7.1. In the present work, a 24-mer ssDNA sequence was immobilised at the surface of the gold electrode by thiol linkage and treated with MCH in order to cap the non-active sites and to reorientate the ssDNA chains.

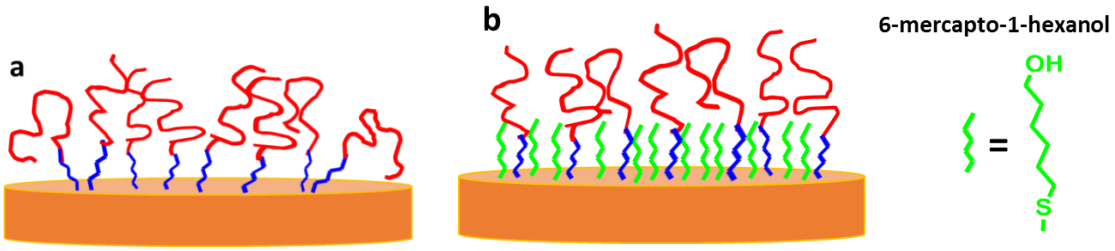

Figure 7.1; a) Self-assembled monolayer of ssDNA by thiols group at the surface of Au electrode. b) After capping the surface with 6-mercapto-1-hexanol.

7.3 Immobilisation of ssDNA labelled with a redox active group

In general, the hybridization process of immobilised ssDNA with its complimentary target is monitored by changes in the current or the electrical potential values using a label. Essentially, in developing genosensors based on immobilised ssDNA, the signal is due to the change in the oxidation or the reduction peak current of the electroactive oligonucleotides themselves, and of an electroactive intercalator in solution. However, the use of bound redox markers such as ferrocene[195] or methylene blue[196] generally attached to the unbound end of ssDNA is gaining in popularity[197]. This is because the electrochemical redox potential and the current for the redox probe attached to the ssDNA chain can be measured based on the electron transfer between the redox centre and the electrode surface before and after the hybridisation process. In terms of choosing suitable redox probes in the literature, generally the redox probe should exhibit a well behaved reversible redox reaction and should be structurally stable during the electrochemical measurement. In addition, the attached redox probe must not disrupt the structure of the DNA. On the basis of the above, AQ was used as a model redox label for the ssDNA in this work. The AQ was attached to the 3' end of the 24-mer single stranded oligonucleotide probe and a hexaethyleneglycol (HEG) spacer with three dithiol phosphoramidities was attached at the 5'. This served as the attachment and linker unit as illustrated in Figure 7.2. A 24-mer single oligonucleotide was employed here, because the 24-mer oligonucleotide chain is less than 80 nm in length when extended. The three dithiol phosphoramidites approximate to a rigid cylinder attached to a gold surface by forming six-sulphur gold bonds[198]. In contrast, the HEG spacer allows the immobilised AQ-ssDNA probes to rotate through a flexible angle on the surface of electrodes.

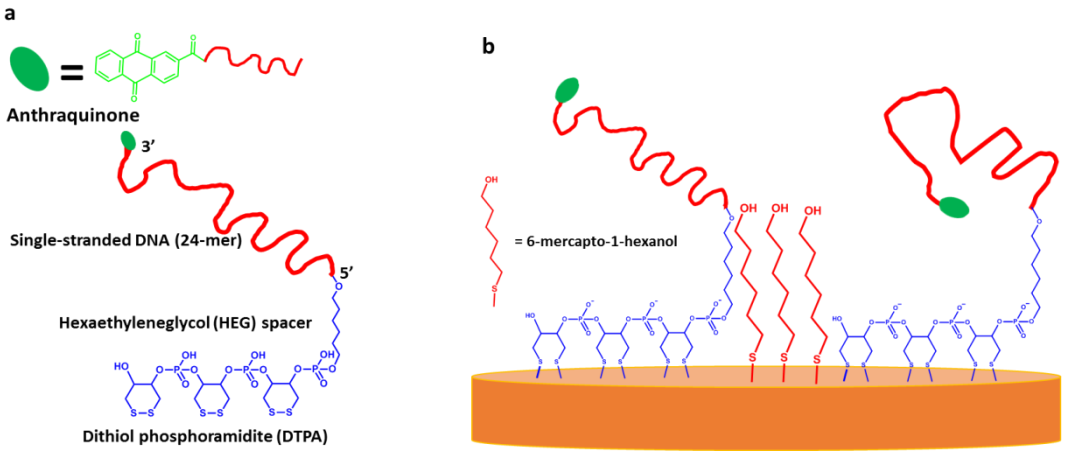

Figure 7.2; Chemical structure AQ-ssDNA with a hexaethyleneglycol (HEG) spacer and three dithiol phosphoramidities (a), providing as an attachment and a linker unit to the surface of Au electrode (b).

An advantage of having the AQ redox probe attached to the ssDNA is that the density of immobilised ssDNA can be quantified by the Faradaic charge for AQ oxidation or reduction. To show the application of our experimental and simulation models in determining the coverages of redox active molecules on modified electrodes, the surface coverages of immobilised ssDNA at the surface of gold electrodes is determined in this Chapter.

7.4 CV for AQ-ssDNA modified Au electrode

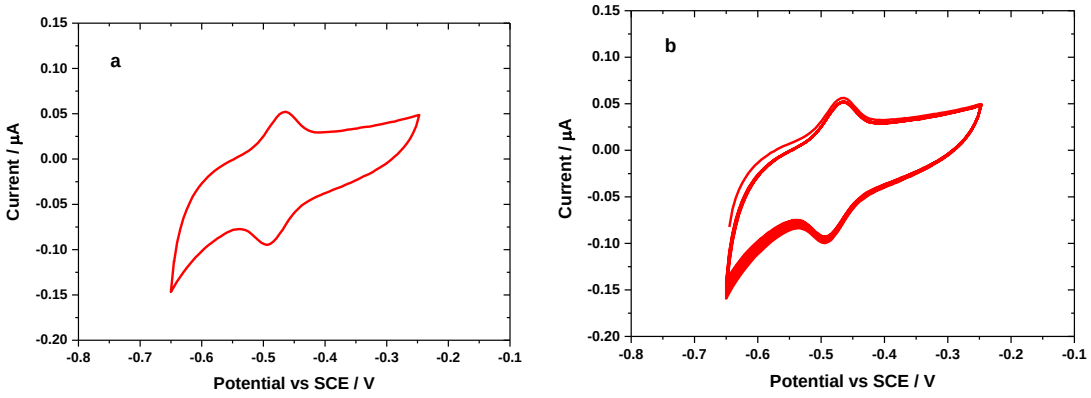

Figure 7.3; a) Cylic voltammograms for AQ-ssDNA modified Au electrode (5th scan shown). b) Ten-cycle cyclic voltammograms for self-assembled monolayer AQ-ssDNA at the surface of a Au electrode. The modified electrode was measured in 0.1 M pH 7 phosphate buffer solution in a range of potential scanned between -0.65 to -0.25 V vs SCE at a scan rate of 50 mV s^{-1}. The electrode area is 0.0341 cm^2.

Initial electrochemical characterisation on self-assembled AQ-single stranded DNA (AQ-ssDNA) at gold electrode was performed by CV. The CV presented in Figure 7.3a shows typical voltammetry data for Faradaic reaction of AQ. The potentials for the oxidation and reduction peaks were found to be at -0.464 V and –0.493 V vs SCE giving a peak separation at 50 mV/s of 0.029 V Figure 7.3b shows 10 consecutive cycles for monolayer AQ-ssDNA in phosphate buffer solution at pH 7 and demonstrates that the system is stable.

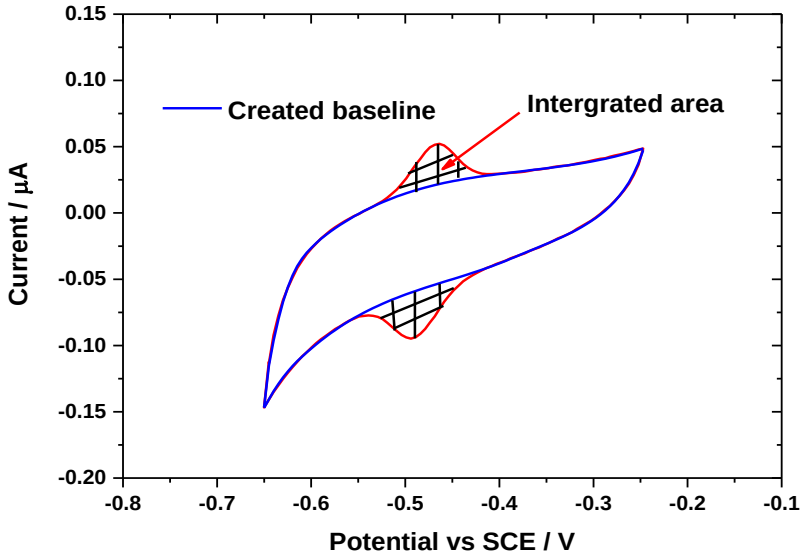

Figure 7.4; A single scan CV for AQ-ssDNA modified Au electrode from Figure 7.3a in order to show the estimated baseline for the capacitive current. The baseline was generated using Origin 9.1.

By integrating the area under redox peaks and using Faraday's law (Eq. 1.23), the surface density of immobilised AQ-ssDNA can be determined. The charge is directly proportional to the number of immobilised ssDNA molecules because every ssDNA molecule was modified with an AQ-2-carboxylic acid at the 3' end (Figure 7.2). Figure 7.4 shows the same CV from Figure 7.3a but the baseline for the capacitive current constructed by using the peak and baseline function in Origin 9.1 as described in Chapter 4. In addition, the crossed-hatched areas can be extracted from Origin software and were used to calculate the coverages of AQ-ssDNA. Assuming that the roughness factor for the electrode gold was 1, the CV surface coverages for AQ-ssDNA were calculated to be 7.45 ± 0.63 pmol cm^{-2}. This value is in agreement with many studies in the literature, reporting values between 3 pmol / cm^2 and 12 pmol / cm^2 for self-assembled monolayers of ssDNA[199]. It is worth mentioning that the roughness factor (ρ) of the cleaned gold surface was determined by cyclic voltammetry in 0.1 M sulphuric acid during the cleaning process of the gold electrode at the scan rate of 0.1 mV / s. Then the ρ for the cleaned surface of the gold electrode was found to

be 1.20 (average between three different electrodes). The same ratio ρ was obtained when we measured the ρ at a scan rate of 50 mV/s. The detailed calculations to determine ρ can be found in Appendix 7.1. Despite the fact that we have experimentally found that ρ is ~ 1.2, we employed ρ = 1 in the $\Gamma_{\text{CV, exp}}$ or the $\Gamma_{\text{DPV, exp}}$ calculations. This is because, from derivation of our simulation model, we assumed that the electrode is initially covered by a monolayer of R and that the DPV waveform drives the oxidation of R to O. The Faradaic charge passed up to time t, Q^t, is given by

$$Q^t = nFA\,\Gamma_R^t \qquad \textbf{Eq. 7.1}$$

where Γ_R^t is the number of moles of R per unit area that have reacted, A is the electrode area and the superscript t indicates that the variable is a function of time. n and F have their usual meaning.

The Faradaic current, i_F^t, is given by

$$i_F^t = \frac{dQ^t}{dt} = nFA\frac{d\Gamma_{\text{R}}^t}{dt} \qquad \textbf{Eq. 7.2}$$

Clearly, based on mathematical expressions from the theoretical model, shown above, the roughness factor (ρ) was not considered. Thus, essentially, the roughness factor for the simulation model is assumed as 1. As a result, by employing the roughness factor of 1 in calculating $\Gamma_{\text{CV, exp}}$ and $\Gamma_{\text{DPV, exp,}}$ this approach gave us a good agreement between the calculated Γ from the experiment and the extracted Γ from the simulation.

7.5 DNA surface coverages by chronocoulometry

In the previous section, the surface coverages for the immobilised AQ-ssDNA was determined by CV. The surface density of AQ –ssDNA was also estimated using the method of Steel et al.[71] but slightly modified /adjusted as reported in by Mahajan *et al.*[200]. For this type of DNA modified electrode system, the charge from the chronoamperometry measurement can be directly obtained without using $[(Ru(NH_3)_6]^{3+}$ and is given by Faradaic reaction of the redox molecule attached on the DNA chain. This is a much simpler and direct determination in which there is no need to determine the isotherm for $[(Ru(NH_3)_6]^{3+}$ binding. Thus, the charge consumed during the AQ redox reaction is directly related to the surface coverage.

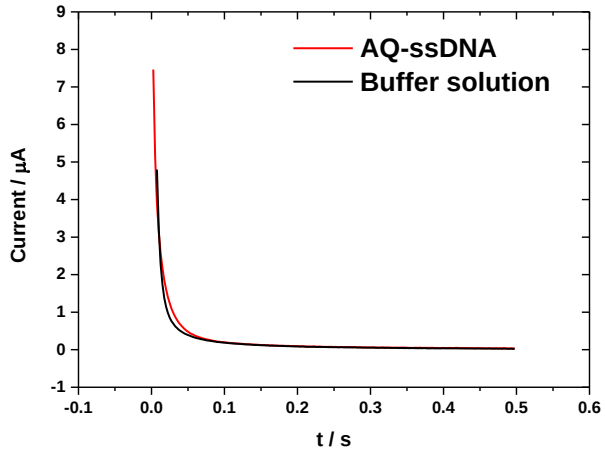

Figure 7.5; Current-time curve for AQ-ssDNA modified Au electrode. Red curve is chronoamprogram of the modified electrode by stepping potential from -0.65 V to -0.25 V vs SCE. In contrast, black curve is the chronoamperogram from the same modified electrode but by stepping the potential outside the potential window for the redox species of AQ which were from -0.65 V to -0.54 V or -0.4 V to -0.25 V vs SCE. Only a chronoamperogram at -0.65 to -0.54 V is shown. The time used here is similar to the interval time of DPV. The electrode area is 0.0341 cm^2.

Figure 7.5 shows chronoamperograms for an AQ-ssDNA modified Au electrode in 0.1 M phosphate buffer (pH 7) for two different potential steps. The chronoamperogram in red corresponds to stepping from -0.65 V to -0.25 V in order to obtain the charge for the AQ redox process (Q_{AQ}). In contrast, the chronoamperogram in black was obtained by stepping the potential outside the potential window of the AQ redox reaction in order to obtain the charge for the buffer solution (Q_{buffer}). Based on the chronoamperograms above, making a plot of current (i) vs $t^{1/2}$ (not shown) and using the integrate function in Origin 9.1, a chronocoulometric plot for the charge (Q) vs $t^{1/2}$ was obtained as shown in Figure 7.6. The chronocoulometric intercepts at $t = 0$ are the charge for the measured electrode at two different potentials. Based on Figure 7.6, for the charge from the buffer solution, a potential scan between -0.65 V to -0.54 V is shown. However, the total

charge for the buffer solution was determined by averaging the charge obtained from the two potential scans of -0.65 V to -0.54 V and -0.4 V to -0.25 V, respectively.

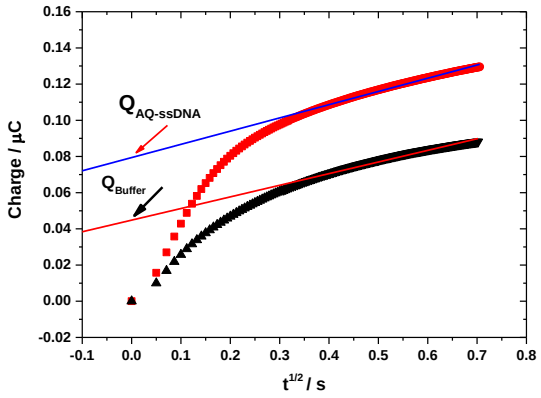

Figure 7.6; Chronocoulometry curves obtained by integrating the chronoamperograms above (Figure 7.5) using Origin 9.1. The red curve is chronocoulometry for the modified electrode by stepping the potential from -0.65 V to -0.25 V *vs* SCE. In contrast, the black curve is the chronocouloumetry from the same modified electrode but by stepping the potential outside the potential window for the AQ redox species from -0.65 V to -0.54 V. The time used here is similar to the interval time of DPV.

Figure 7.6 shows the typical chronocoulometry results for an AQ-ssDNA modified Au electrode. Based on the intercept at t = 0, the charge for the AQ and the buffer solution from AQ-ssDNA modified electrodes can be directly extracted from the plots. Using Equation 7.3, the surface coverages of the immobilised AQ-ssDNA can be calculated.

$$\Gamma_{\mathbf{DNA}} = \frac{Q_{AQ} - Q_{buffer}}{nFA} \qquad \textbf{Eq. 7.3}$$

Where Q_{AQ} is the charge obtained by stepping the potential from -0.65 V to -0.25 V, Q_{buffer} is the average charge obtained by stepping the potential outside the potential window of the AQ redox couple from -0.65 V to -0.54 V and from -0.4 V to -0.25 V vs SCE, n is the number of electrons transferred for AQ (n = 2e-), F is the Faraday constant and A is the electrode area. Thus, the surface coverages of the immobilised DNA based on the attached AQ was determined to be 7.27 ± 0.84 pmol cm^{-2}. As we determined the surface coverages of the immobilised ssDNA to be ~ 7.2 pmol /cm^2, the average distance of the DNA strands are approximately 5.2 nm apart.

7.6 Kinetics of self-assembled monolayer of AQ-ssDNA

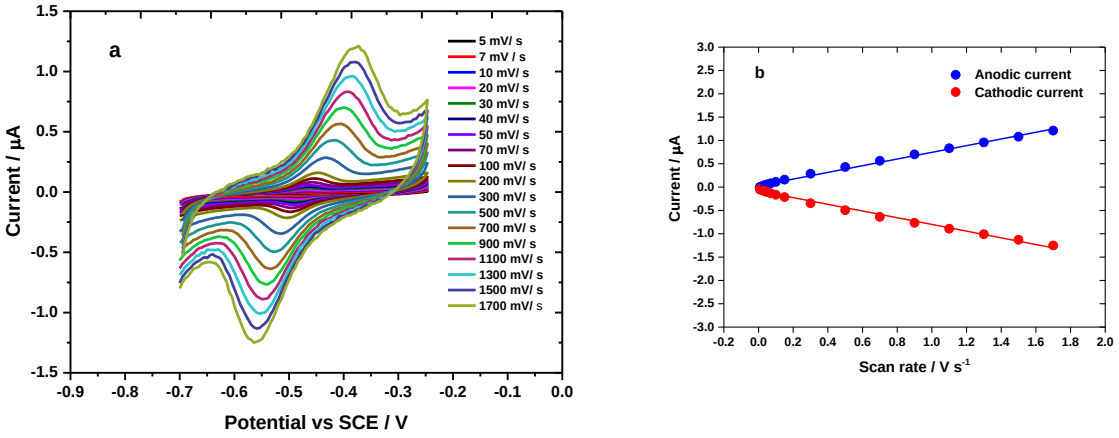

Figure 7.7; a) Cyclic voltammograms of a AQ-ssDNA modified Au electrode in 0.1 M phosphate buffer of pH 7 at a series of different scan rates (0.005 to 1.7 V s^{-1}). b) Plots of i_p for anodic and cathodic currents (without background subtraction) versus scan rate (v). The measurements were conducted over a potential cycle between -0.65 to -0.25 V *vs* SCE as well as a controlled temperature from a water bath at 25 ± 0.5 º C. The electrode area is 0.071 cm^2.

The effect of changing the scan rate on the electrochemical behaviour of AQ-ssDNA modified Au electrodes was investigated in phosphate buffer (pH 7). Figure 7.7a shows a series of cyclic voltammograms recorded at different scan rates from 5 to 1700 mV/ s. In addition, Figure 7.7b clearly shows that the anodic and cathodic peak currents increased linearly with scan rate as expected for a surface immobilised redox species.

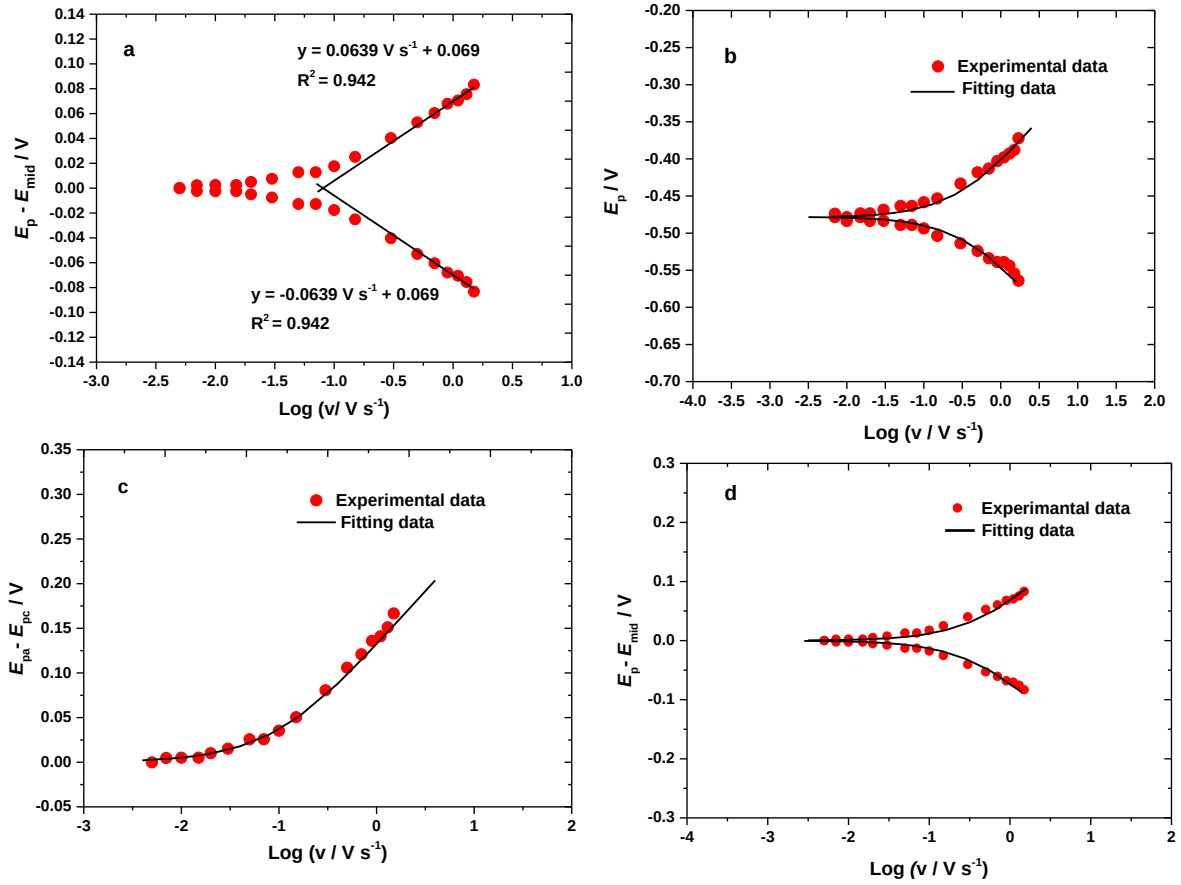

Figure 7.8; a) Laviron plots for experimental data for the variation of $E_{pa/pc}$-E_{mid} (overpotential) *vs* the logarithm of the scan rate (v) and the linear best fittings over anodic and cathodic branches in order to determine the experimental α and k_s values. b) Plots showing the influence of cyclic voltammetry scan rates on peaks of redox potentials for oxidation and reduction (filled cycles) for AQ-ssDNA modified Au electrode at various scan rates (0.005 to 1.7 V s^{-1}), the theoretical (solid lines) were obtained from the best fitting to the Laviron theoretical plot using the working curve for α = 0.5. c) Plot of experimental data and Laviron theory based on working curve for α = 0.5 for the peak separation (E_{peak}). d) The best fits for experimental data of $E_{pa/pc}$-E_{mid} (overpotential) to the Laviron theory by employing α = 0.5 for anodic and cathodic curves respectively.

In further analysis, the Laviron method was applied to determine the α and k_s as previously described in Chapter 3 (Section 3.18). Figures 7.8a, b and c, shows the data obtained for the electron transfer kinetics for an AQ-ssDNA modified Au electrode based on the three different plots (E_p-E_{mid} vs log v, E_p vs Log v and E_{pa}-E_{pc} vs Log v). Essentially, based on a plot of (E_p -E_{mid}) vs log v (Figure 7.8a), extrapolating the linear part of the anodic and cathodic branches in order to extract v_a/v_c at zero overpotential, the α and k_s were determined (Table 7.1).

Table 7.1; Electron transfer coefficient (α) and rate of electron transfer (k_s) for immobilised AQ-ssDNA at the surface of Au electrodes.

AQ-ssDNA	Transfer coefficient for anodic (α_a)	Transfer coefficient for cathodic (α_c)	Rate of electron transfer (k_s) / s^{-1}
Self-assembled AQ-ssDNA	0.45 ± 0.02	0.55 ± 0.02	2.79 ± 0.31

In addition, it is clearly shown that the overpotentials for the AQ-ssDNA modified Au electrode at lower scan rates are almost zero. This is unusual for immobilised AQ redox systems so far. Comparing the experimental data obtained for covalently immobilised AQ attached through the EDA linker, the data obtained here is significantly different. In the case of the immobilised AQ through EDA linker, the overpotential at lower scan rates was found to be around at 35 mV. The almost ideal behaviour obtained for the AQ-ssDNA modified electrode was thought to be due to several factors. Firstly, the surface of AQ-ssDNA modified electrode was capped with mecaptohexanol in order to block non-specific binding sites[201]. This completely blocks, or minimises, the surface defect sites surrounding the dithiol groups. Secondly, the mecaptohexanol may orientate the AQ-ssDNA chains into a more vertical conformation, minimising the lateral interaction between neighbouring grafted ssDNA chains[202]. This favours ideal Nernstian behaviour, where the oxidation and reduction peak potentials are identical to each other. Thus the E_{peak} is equal to $E°'$ (overpotential = ~ 0). In contrast, above 0.1 V / s the peak-to-peak separation start to increase due to the contribution of the rate of heterogeneous electron transfer to the kinetic control of the Faradaic current.

To make a better estimate of k_s, the experimental data points were fitted to the Laviron theoretical curve for α = 0.5 as displayed in Figures 7.8b, c, and d. Clearly, the fits yield a reasonable agreement between the experimental and calculated peak potential variations.

As reported in the literature[196,203], there are three different electron transfer pathways for redox probes immobilised to single stranded DNA, there are illustrated in Figure 7.9. However, a detailed study of the electron transfer for the AQ-ssDNA modified GC electrode was not the aim of this study.

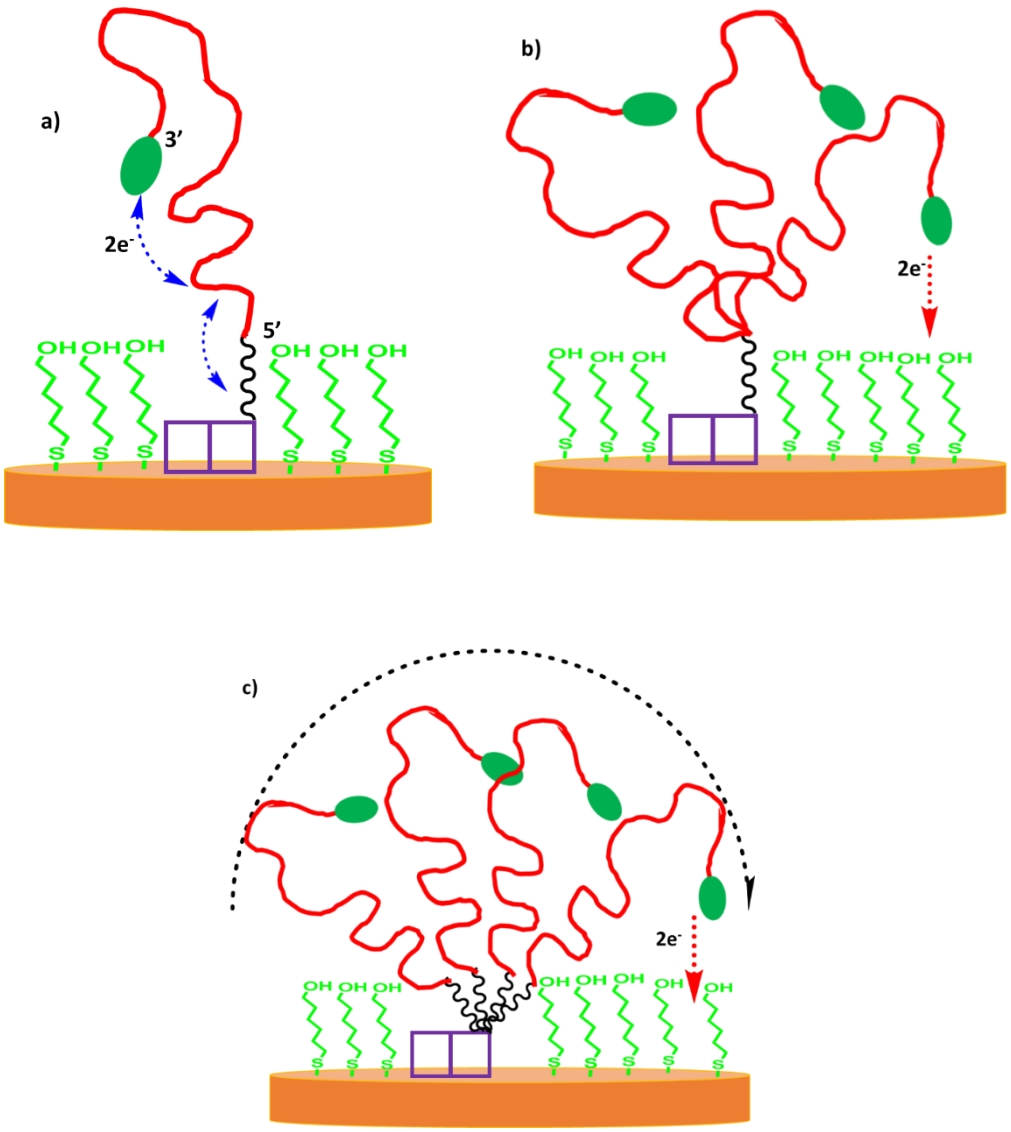

Figure 7.9; Possible pathways of the electron transfer of AQ to the surface of electrode. a) Electrons could transfer through the C6 spacer. b) Electrons could transfer by an elastic bending of the ssDNA chain. c) Electrons could transfer by free rotational motion of the ssDNA chain and C6 spacer.

7.6 Effect of R_{ext} added on DPV for AQ-ssDNA modified Au electrode

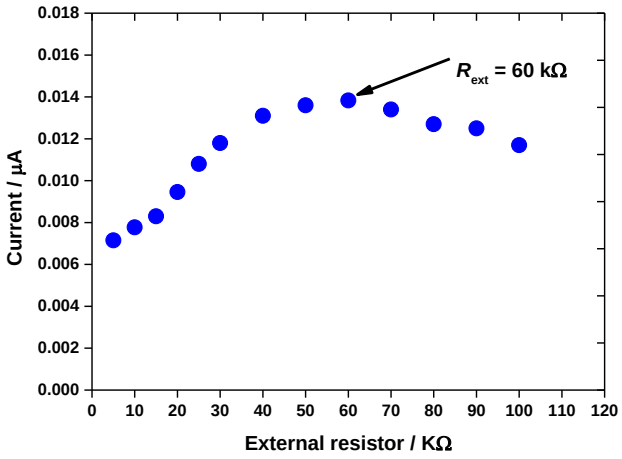

Figure 7.10; Plot of differential pulse voltammogram peak currents against the external resistance (5 - 100 kΩ) added to the cell circuit AQ-ssDNA modified Au electrode in 0.1 M pH 7 phosphate buffer solution at ΔE_p = 2.5 mV, τ_p = 0.05 s, τ_i = 0.5 s, ΔE_s = 5 mV and a DPV scan rate of 0.01 V s^{-1}. The measurements were carried out at potential scanned between -0.65 to -0.25 V with a controlled temperature from a water bath at 25 ± 0.5 ° C.

Scanning a series of external resistance (R_{ext}) for the AQ-ssDNA modified gold electrode from 5 kΩ to 110 kΩ and plotting the magnitudes of the added R_{ext} vs DPV peak currents, as expected a curve of the DPV current trend was obtained (Figure 7.10). As clearly seen, an R_{ext} of 60 kΩ gave the maximum DPV peak current for this electrode. Based on the data trend as shown above, the DPV peak at 60 kΩ should be used to calculate the DPV surface coverages by integrating the area under the DPV peak. However, a similar pattern of DPV curves was obtained as obtained for the mixed-monolayer of AQ attached through the HDA linker at the surface of GC electrode (Chapter 5, Section 5.11) as shown in Figure 7.11.

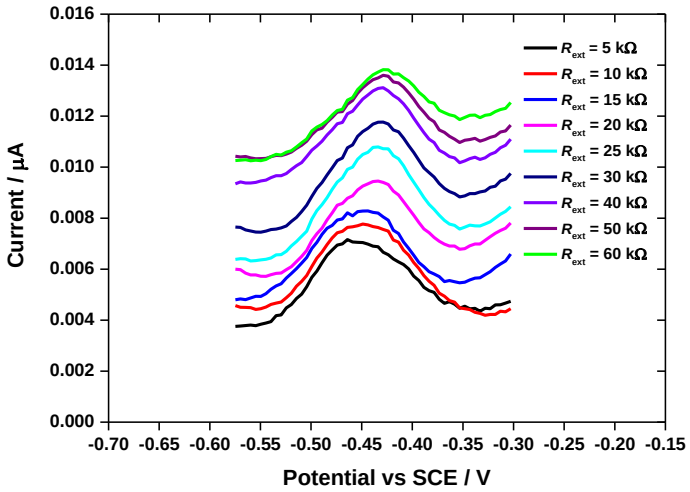

Figure 7.11; DPVs for AQ-ssDNA modified Au electrode with R_{ext} added from 5 kΩ to 60 kΩ. The measurements were carried out between -0.60 V to -0.28 V vs SCE. The DPV parameters were ΔE_p = 2.5 mV, τ_p = 0.05 s, τ_i = 0.5 s, ΔE_s = 5 mV and a DPV scan rate = 0.01 V s^{-1} in 0.1 M pH 7 phosphate buffer solution. The electrode area is 0.0341 cm^2.

Figure 7.11 shows the DPV peaks at different R_{ext} (5 - 60 kΩ), where at R_{ext} = 60 kΩ the optimum DPV peak current was obtained. It can be seen again in the plot of DPV peak current vs R_{ext} (Figure 7.10). Moreover, the prominent feature of the DPV signals presented above is that a shoulder peak appeared at ~ -0.47 V, clearly seen at lower R_{ext} (5 -20 kΩ). Note that as demonstrated in CVs for different scan rates (Figure 7.7a), there is no appearance of a shoulder on the peak. We believe that this feature is not due to contributed abnormal kinetic behaviour of AQ. The origin of this voltammetric feature in DPV is not clear at this moment. However, it seems that the two peaks are generated by the oxidation reaction of AQ that occurred in two different microenvironments. Lawrence *et al.*[204] reported two different peaks at 0.27 V and 0.38 V on the CV for a self-assembled monolayer of the ferrocene with diluent molecules (binary layers) at the gold electrode surface. The feature that appears at 0.27 V was a shoulder peak, generated by an oxidation process of the ferrocene moieties. This shoulder peak was obtained when the surface coverage of immobilised ferrocene was high. In addition, they found that the same electron-transfer process was apparently operative for each peak. In order to better identify the shoulder peak, they performed peak deconvolution using a Gaussian-Lorentzian fitting. The fitting gave them a clear shoulder peak at 0.27 V. Thus, they found that the dual-peak was generated by isolated and clustered ferrocene moieties in the binary SAM layers. For DPV currents of the AQ, therefore, we believe that the shoulder peak at -0.47 is contributed by isolation of the immobilised ssDNA-AQ in binary layer SAMs. Nevertheless, the study of detailed events that occur on the surface of the self-assembled monolayer ssDNA-AQ was not the aim of this study. Hence, no

further work was carried out to confirm this. However, it would be interesting to study in details in future research.

The second feature of the data shown in Figure 7.11 is the slight shift in the potential of the DPV peak to more positive potentials as R_{ext} increased. This could also be due to the microenvironment experienced by the motion dynamics of ssDNA-AQ during the electron transfer process, resulting from either the elastic bending of the ss-DNA chain or the free rotational motion of the ss-DNA by HEG spacer toward the electrode surface. This can be understood from Figure 7.9 as shown earlier in Section 7.6. This may result in dispersion in the global $E^{\circ\prime}$[205], which implies that the formal potentials may not be identical for some AQ redox centres since the local environment around each AQ redox centre is non-uniform.

7.7 DNA surface coverages by DPV

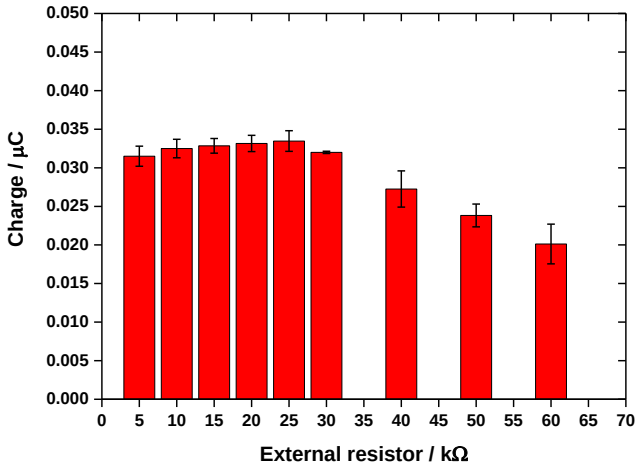

Figure 7.12; Charge measured under each DPV peak for AQ-ssDNA with the R_{ext} added from 5 kΩ to 60 kΩ after background subtractions using Origin 9.1. R_{ext} added of 25 kΩ gave the maximum charge under DPV.

The data obtained here shows a similar pattern to the covalently immobilised mixed-monolayer AQ, and the same analysis procedures were applied in extracting the surface coverages of AQ-ssDNA. Figure 7.12 displays the charge passed under the DPV peak for every DPV peak for the R_{ext} added from 5 kΩ to 60 kΩ. The charge was calculated by dividing the integrated area obtained under the DPV peak using Eq. 4.12. The DPV peak for R_{ext} of 25 kΩ gave the maximum charge.

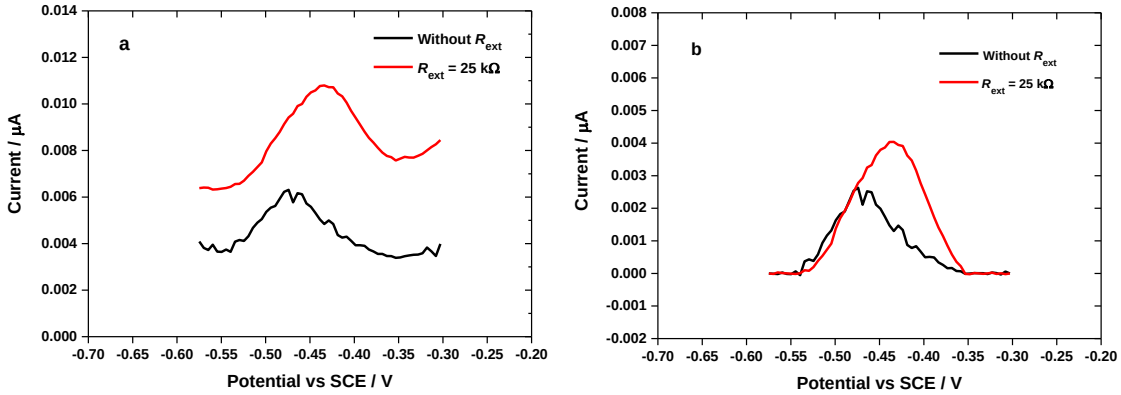

Figure 7.13; Differential pulse voltammograms for AQ-ssDNA modified Au electrode before adding R_{ext} and after adding R_{ext} of 25 kΩ. b) The DPVs after performing background subtractions using Origin 9.1.

Figure 7.13 shows two DPVs for different R_{ext} conditions (R_{ext} = 25 kΩ, and without R_{ext}). By employing Eq. 4.18, the DPV surface coverages for immobilised AQ-DNA from DPV was found to be 7.03 ± 0.52 pmol cm^{-2}.

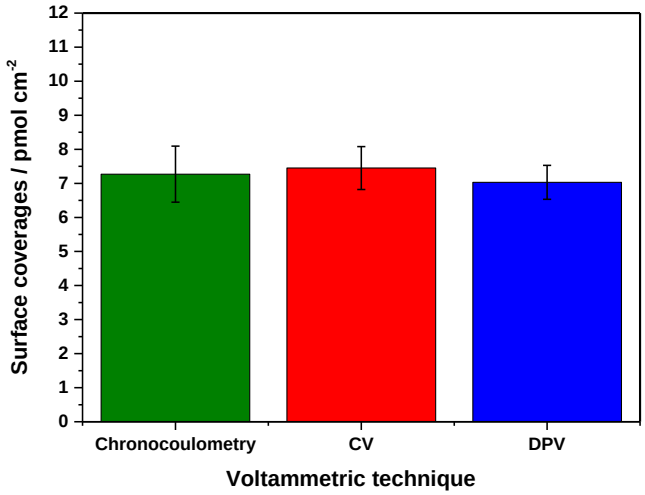

Figure 7.14; Comparison of the surface coverages measured by CV, chronocouloumetry and DPV experiments for self-assembled AQ-ssDNA at the surface of Au electrodes.

Figure 7.14 shows the bar plots of comparison for the surface coverages of self-assembled monolayer AQ-DNA calculated by chronocoulometry, CV and DPV techniques. There is clearly shown that close agreement, within experimental error, between the values. The next step is to verify the determined Γ_{DPV} from an experiment with the DPV simulation ($\Gamma_{DPV,\ sim}$).

7.8 Chronoamperometry measurements for AQ-ssDNA modified Au electrode

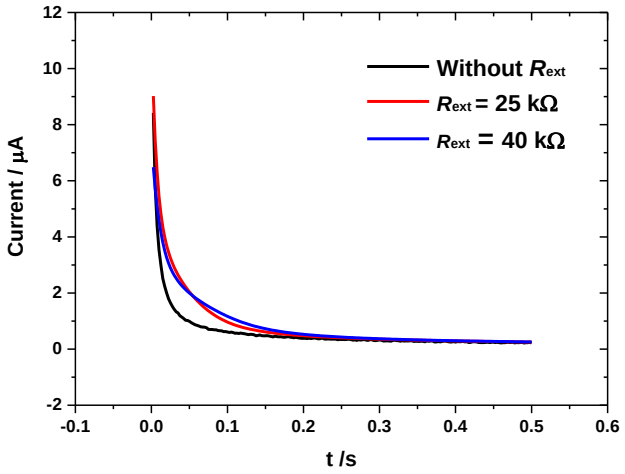

Figure 7.15; Current-time curves for AQ-ssDNA modified Au electrode at three different R_{ext} conditions using chronoamperometry by stepping the potential from -0.65 V to -0.25 V vs SCE for 0.5 s. The time used here is similar to the interval time of DPV.

According to the bar plot of DPV charge vs R_{ext} (Figure 7.12), when the AQ-ssDNA modified Au electrode was measured with R_{ext} of 25 kΩ, the maximum DPV charge was obtained. By performing the same analysis as used for the chronoamperograms from the previous chapters, chronoamperograms for three different R_{ext} conditions for the AQ-ssDNA modified Au electrodes were obtained, Figure 7.15. In order to obtain more qualitative information such as the *RC* time constant and rate of electron transfer (k_s), a plot of ln *i* vs *t* for each R_{ext} condition was created.

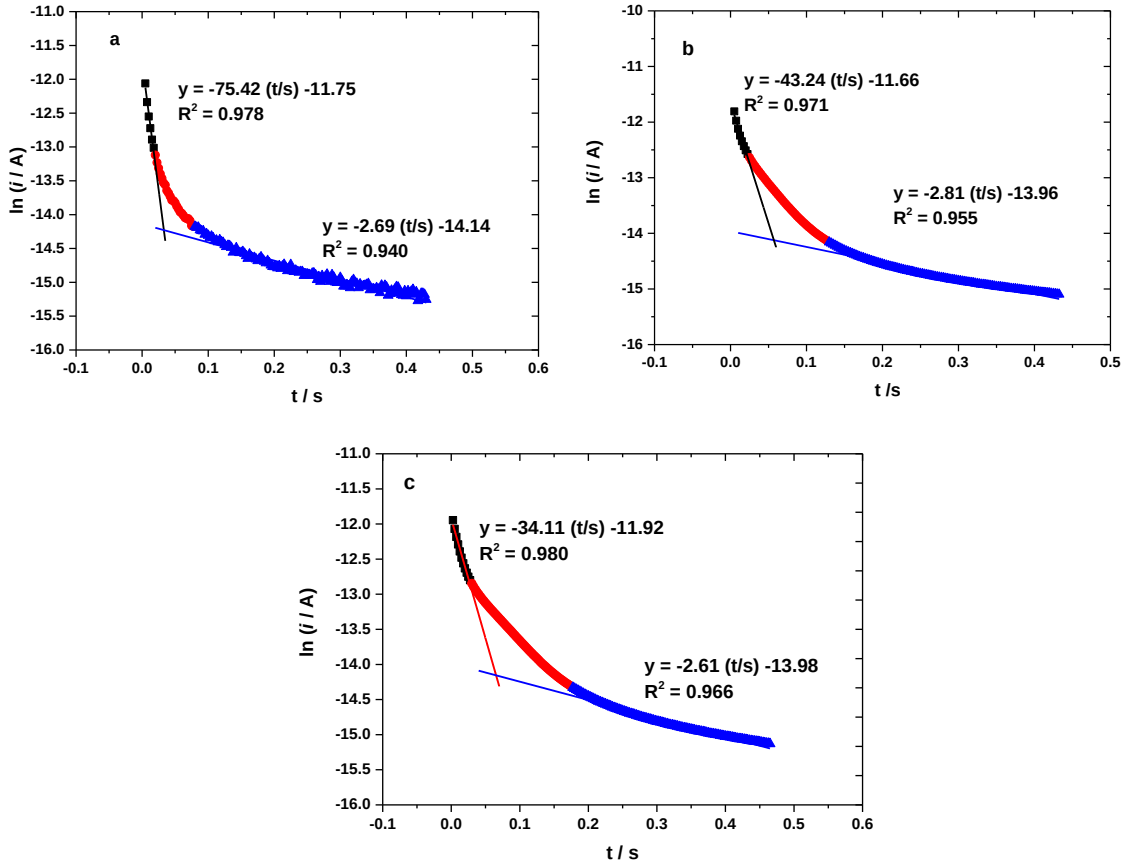

Figure 7.16; Semilog plots of ln *i vs t* for three R_{ext} conditions for data from Figure 7.15 a) Before adding R_{ext}, b) R_{ext} = 25 kΩ, and c) R_{ext} = 40 kΩ.

Figures 7.16a, b and c show three different plots of ln *i* vs *t* from chronoamperometry measurements before adding R_{ext}, after adding the R_{ext} of 25 kΩ and of 40 kΩ. A similar approach as previously used in Section 3.12 was performed for this analysis. By exploiting the graph of ln *i* vs *t* for each R_{ext} condition in order to get two linear best fits, two different slopes were obtained. Using Equations 3.9 and 3.10 as shown in Chapter 3 (Section 3.12), based on the slope for each linear best fit, the *RC* time constant and k_s were determined. The calculated *RC* and k_s are given in Table 7.2. Comparing the determined k_s values at different magnitudes of R_{ext} from chronoamperometry to the Laviron method, we find good agreement with that determined from the Laviron equations (k_s = 2.67 s^{-1}).

Table 7.2; *RC* time constant and rate of electron transfer (k_s) obtained by two different linear fits of a plot of ln *i* vs *t*. The *RC* time constant was calculated from a slope of linear best fit at short time and k_s was directly determined from the slope of linear best fit at long time.

External resistance	Time constant (*RC*) /s	Rate of electron transfer (k_s) / s^{-1}
Without R_{ext}	0.014 ± 0.001	2.96 ± 0.20
25 kΩ	0.022 ± 0.002	3.12 ± 0.31
40 kΩ	0.028 ± 0.001	2.82 ± 0.21

7.9- EIS measurements for AQ-ssDNA modified Au electrode

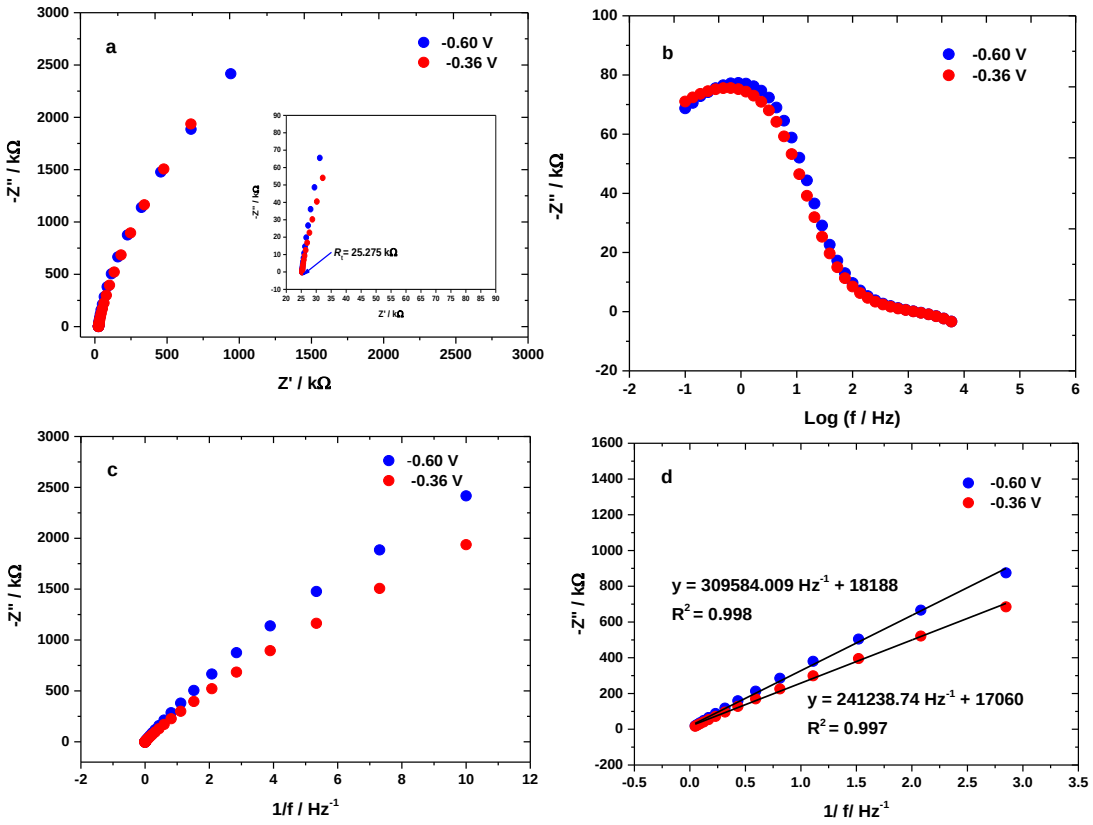

Figure 7.17; a) Nyquist plots for AQ-ssDNA modified Au electrode at two different potentials (-0.60 V and -0.36 V). The inset figure shows the enlargement of the Nyquist plot to show the presence of total uncompensated resistance (R_t) in the electrochemical cell (R_s + R_{ext} at 25 kΩ). b) Bode plots at two different measured potentials. These plots were used to differentiate three distinct frequency regions (high, medium and low) in order to determine the C_{dl}. c) Plots of imaginary impedance (-Z") *vs* 1/ frequency. d) The best linear fitting obtained from the low and medium range frequencies over plots of –Z" vs 1/f. C_{dl} can be calculated from the slope of the linear fitting where m = $1/2\pi C_{dl}$.

Because the Γ_{DPV} for the immobilised AQ-ssDNA was determined from the DPV peak with R_{ext} of 25 kΩ, the impedance measurements were also conducted at R_{ext} of 25 kΩ. The impedance measurements were made at two different potentials, -0.60 V and -0.36 V vs SCE. Figures 7.17a, b, c and d show the Nyquist, Bode and -Z" vs 1/f plots. By performing the same analysis and calculations, R_t in the electrochemical cell and the C_{dl} at two different potentials were determined. Based on the Nyquist plot (Figure 7.17a), R_t was directly determined. In contrast, applying Equation 4.16 (Chapter 4), C_{dl} at potentials of -0.60 V and -0.36 V were also calculated. The results are given in Table 7.3.

Table 7.3; Total uncompensated resistance (R_t) and double layer capacitance (C_{dl}) from EIS for the two different measured potentials (-0.6 V and -0.36 V) at R_{ext} of 25 kΩ for the AQ-ssDNA modified Au electrodes.

Potential vs SCE / V	Total uncompensated resistance in the electrochemical cell (R_t) / kΩ	C_{dl} for AQ-ssDNA at R_{ext} = 25 kΩ / μF
-0.60	25.28 ± 0.001	0.52 ± 0.20
-0.36	25.28 ± 0.005	0.59 ± 0.01

7.9 DPV simulations for the AQ-ssDNA modified Au electrode at R_{ext} = 25 kΩ

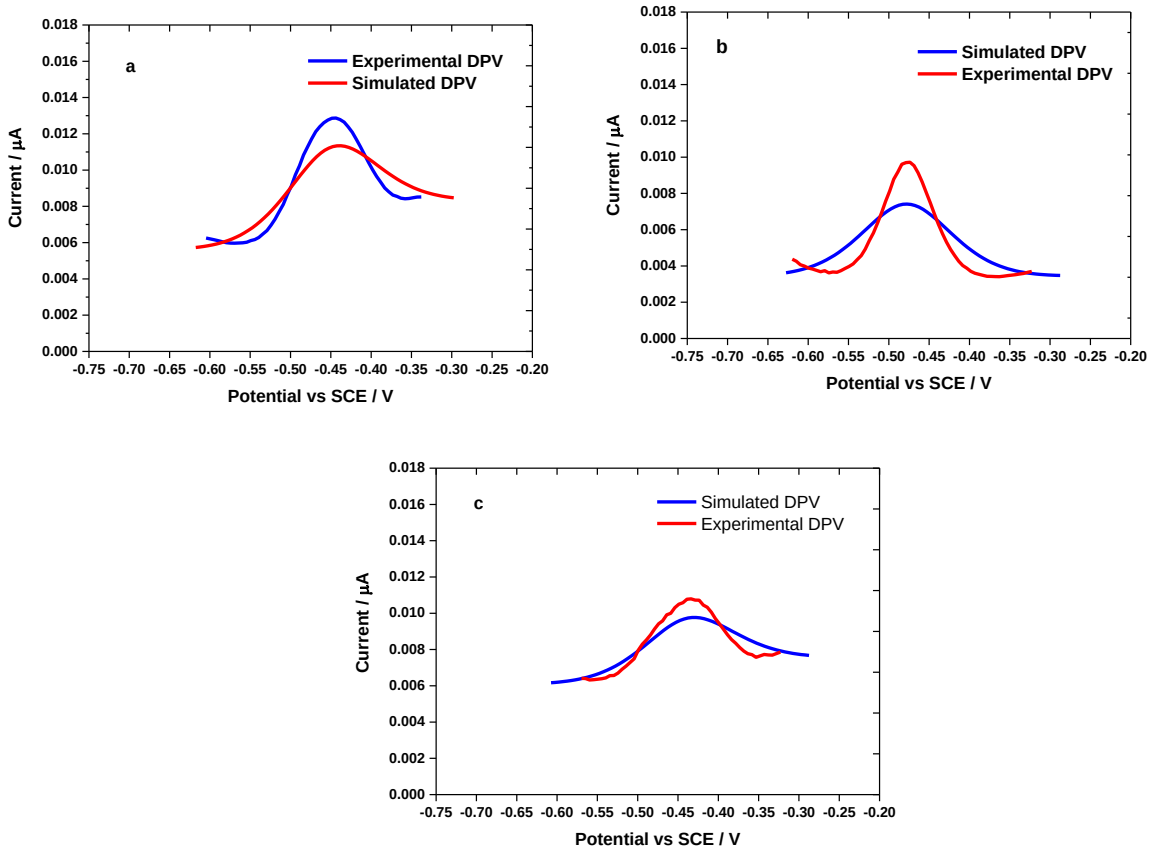

Figure 7.18; The best DPV fits to the experimental DPVs at R_{ext} of 25 kΩ from 3 different AQ-ssDNA modified Au electrodes. Experimental DPV (red) employing a set up parameters with ΔE_p = 2.5 mV, τ_p = 0.05 s, τ_i = 0.5 s, ΔE_s = 5 mV and a DPV scan rate at 0.01 V s^{-1} in 0.1 M phosphate buffer solution at pH 7.

Figure 7.18a- Simulation with k_s = 3.02 s^{-1}, R_t = 25275 Ω, α = 0.50, C_{dl} for reduced layer = 0.69 µF, C_{dl} for oxidised layer = 0.8 µF and $\Gamma_{DPV,sim}$ = 7.64 pmol cm^2 .

Figure 7.18b- Simulation with (k_s) = 2.7 s^{-1}, R_t = 25275 Ω, α = 0.50, C_{dl} for reduced layer = 0.59 µF, C_{dl} for oxidised layer = 0.59 µF and $\Gamma_{DPV,sim}$ = 7.0 pmol cm^{-2} .

Figure 7.18c- Simulation with k_s = 2.65 s^{-1}, R_t = 25275 Ω, α = 0.50, C_{dl} for reduced layer = 0.71 µF, C_{dl} for oxidized layer = 0.77 µF and $\Gamma_{DPV,sim}$ = 5.7 pmol cm^{-2}.

The experimental DPVs were analysed using the DPV simulation to find the best fit between experimental and the simulated DPVs. Following the same analysis procedures for DPV simulation as described earlier, Figures 7.18a, b and c show the experimental DPVs with the best DPV fits from 3 different AQ-ssDNA modified gold electrodes with R_{ext} of 25 kΩ. The results show a reasonable agreement between the simulated DPV and experimental DPV, but generally, the shapes of the DPV peaks observed theoretically were much broader than those obtained experimentally. However, based on the calculated charge under simulated DPV peaks (blue), the

similar charge values to the experimental DPV charge values were obtained. This data pattern was expected, due to non-inclusion of the interactions' surface confined species parameters in our DPV simulation model. In the case of immobilised ssDNA, the ssDNA chains can experience elastic motion or can coil up on the electrode surface. These types of interactions can greatly influence the shape of the experimental voltammogram, particularly in narrowing the peak voltammetry. As demonstrated theoretically by Feldberg[206], by introducing a shape factor (Υ) in the CV simulation, the parameter Υ allows for broadening and narrowing the CV peaks. Interestingly, Υ is denoted for the interactions of the surface-confined species. The same approach has also been reported in detail by Laviron[59] and Anson and Brown[64], as already discussed in Section 1.6. However, the best response of $\Gamma_{DPV,sim}$ values used in these simulations (at R_{ext} = 25 kΩ) are consistent with those calculated by the experimental approach. All the parameter values that were extracted from the experimental work and the DPV simulations are shown in Table 7.4.

Table 7.4; Values for MATLAB parameters obtained from the experiments and used in DPV simulation. The data are shown for different AQ-ssDNA modified Au electrodes.

***The experimental values shown for α and R_t were the average values from Table 7.2 and 7.3. In contrast, the experimental values shown for $E°$, k_s, C_{dl} for reduced layer, C_{dl} for oxidised layer and $\Gamma_{DPV,\,sim}$ were extracted from each DPV peak with R_{ext} added of 25 kΩ.**

	G1		G3			G4		G18
MATLAB parameters	**Experiment**	**Simulation**	**Experiment**	**Simulation**	**Experiment**	**Simulation**	**Experiment**	**Simulation**
Redox potential ($E°$) vs SCE	-0.451 V	-0.456 V	-0.476 V	-0.48 V	-0.439 V	-0.444 V	-0.465	-0.464
Total uncompensated resistance in the electrochemical cell (R_t)*	25275 Ω	25275 Ω	25275 Ω	25275 Ω	25275 Ω	25275 Ω	25275	25275
Transfer coefficient (α)*	0.50	0.50	0.50	0.50	0.50	0.50	0.50	0.50
Rate of electron transfer (k_s)	2.98 s^{-1}	3.02 s^{-1}	3.04 s^{-1}	2.7 s^{-1}	2.40 s^{-1}	2.65 s^{-1}	Unmeasured	3.1
C_{dl} for reduced layer	0.50 µF	0.69 µF	0.56 µF	0.59 µF	0.54 µF	0.71 µF	Unmeasured	0.83 µF
C_{dl} for oxidised layer	0.60 µF	0.80 µF	0.54 µF	0.59 µF	0.57 µF	0.77 µF	Unmeasured	0.75 µF
$\Gamma_{DPV,\,exp}$ vs $\Gamma_{DPV,\,sim}$	7.62 pmol cm^{-2}	7.64 pmol cm^{-2}	7.10 pmol cm^{-2}	7.0 pmol cm^{-2}	5.8 pmol cm^{-2}	5.7 pmol cm^{-2}	6.37 pmol cm^{-2}	6.58 pmol cm^{-2}

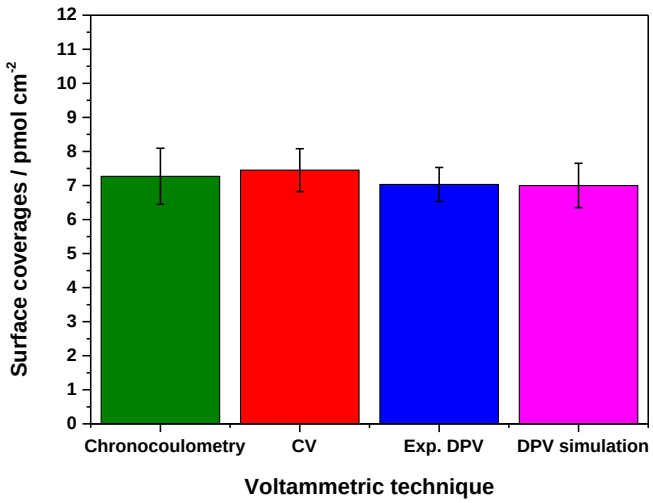

Figure 7.19; Comparison of the DPV surface coverages determined by experimental calculations from chronocoulometry (green), CV (red) and DPV (blue) and obtained by the best response of the DPV simulations (purple) to the experimental DPVs for AQ-ssDNA modified Au electrodes.

The bar plots in Figure 7.19 shows the surface coverages of self-assembled AQ-ssDNA at the surface of gold electrode determined using 4 different approaches. A reasonable agreement was obtained with an experimental error in all cases. As can be observed a small error bar on the estimating Γ of the immobilised ssDNA by DPV than CV and chronocoulometry. This indicates that the DPV technique offers a better precision of measurement than both the methods.

7.10 Conclusion

The determination of DPV surface coverages for immobilised ssDNA with an AQ as a redox marker has been demonstrated in this Chapter. As expected, the determined $\Gamma_{DPV,\,exp}$ gave close agreement to the DNA surface coverages calculated from CV. In addition to the CV measurement, using Steel's method with a slight modification, the surface coverage of immobilised ssDNA was obtained by chronocoulometry. Interestingly, this method also gave a close agreement to the $\Gamma_{DPV,\,exp}$ calculated from our Eq. model (Eq. 4.18). In order to get a better estimate of the DPV surface coverages of immobilised ssDNA in this work, verification of the $\Gamma_{DPV,\,exp}$ using our DPV simulation was made. Through performing the DPV simulation on the experimental DPV peak for AQ-ssDNA, the Γ_{DPV} obtained by the experimental approach was verified. A reasonable agreement of Γ_{DPV} given by simulation to the Γ_{DPV} determined by experiment was achieved. However, deviation of the simulated DPV peak shape from the experimental DPV peak shape was noticed. We believe that our theoretical model may not sensitive to the motional dynamics of ssDNA chains during the Faradaic reaction of AQ, resulting to narrower of the experimental DPV peak and the dispersion of global $E°'$. Nevertheless, this is just a speculation and there is no independent evidence to support this statement. To conclude based on these findings, we believe that DPV offers a new method to determine the surface density of immobilised DNA through attached redox molecules. Moreover, further investigation would be interesting to quantify the density of immobilised double stranded DNA, in particular after the hybridization process of ssDNA. In the future, further research is needed to apply the models in quantifying the hybridised DNA.

Chapter 8: Conclusion

8.1 Conclusion

In this thesis, chemically modified electrodes (CMEs) have been prepared by immobilising organic and inorganic redox molecules, 9,10-PQ, AQ and an Os bipyridine complex, at the electrode surface. The molecules were immobilised by physical adsorption, covalent attachment via amine linkers and self-assembly of a DNA label system. Overall the modified electrodes surface were characterised by CV, DPV, chronoamperometry and EIS measurements. Nevertheless, characterisation of the modified electrodes using DPV in order to estimate the surface coverages of immobilised redox active species was the main aim in this study.

In the first results chapter (Chapter 3), it was concluded that the direct adsorptions of 9,10 PQ at the surface GC electrode was unstable and produced a multilayered film. Consequently, a poorly-behaved quinone redox system was obtained, particularly the abnormality of kinetic behaviour of 9,10-PQ. By using Anson and co-workers' Γ_{DPV} equation for estimating the surface coverages of immobilised 9,10-PQ, the calculated Γ_{DPV} gave results in poor agreement with surface coverages estimated by CV.

The covalently attached AQ at the GC electrode surface via mono EDA linker was presented in the second results chapter (Chapter 4). The covalently attached AQ at the modified surface produced a very stable quinone redox system. Then, an experiment was designed to add the R_{ext} in order to estimate the surface coverages of AQ based on DPV measurements. By following an approximation method from Anson's model, mathematical expressions have been derived in this Chapter providing us an equation that could be used to estimate the Faradaic charge under the DPV peak. By substituting the DPV charge equation in Faraday's law, a simpler equation was obtained, accompanied by a factor of e =2.718 for estimating $\Gamma_{DPV,\,exp}$ using the integrated area under the DPV peak. Comparing the $\Gamma_{DPV,\,sim}$ calculated using Eq. 4.14 with the Γ calculated by CV, the data gave lower surface coverages than Γ_{CV}. Thus we can conclude that Eq. 4.14 based on Anson's approximate method for calculating the surface coverage of the immobilised AQ is an underestimate. Using a special DPV simulation model developed in this study, a very good linear relationship of charge vs integrated area was obtained from the simulated DPV peaks. A plot of charge vs integrated area gave a linear plot with an intercept of 0. Based on the slope of this plot and Eq. 4.14, a factor of 5 was obtained. Interestingly, a good agreement was obtained between the $\Gamma_{DPV,\,exp}$ estimated using Eq. 4.18 with e replaced by a factor of 5 and $\Gamma_{DPV,\,sim}$ extracted from the DPV simulation. Equation 4.18 and DPV simulation were used and compared

in all of the DPV experiments in this thesis in order to provide an estimate the DPV surface coverages of the immobilised redox molecules.

In order to demonstrate the utility and flexibility of the models on various modified electrode surfaces, in the third results chapter (Chapter 5), further testing of Eq. 4.18 and DPV simulation was employed on covalently immobilised Os and mixed layers of AQ-Os. Again, consistency of both the developed models was obtained.

It should be noted that the covalently attached AQ at the GC electrode surface is attached via the primary amine linker of the EDA-Boc, thus the fourth results chapter presented a detailed study on electrochemical grafting of EDA-Boc. In addition, a new method for grafting EDA-Boc was studied in a mixed solvent, ACN and water in the ratio 4:1. Resulting from seven repetitive CV scans, the grafting EDA-Boc in ACN/$NaHCO_3$ shows more rapid passivation of the electrode surface than in neat ACN. Moreover, in the studies of the blocking effect of $[Fe(CN)_6]^{-3}$ ions by monolayer EDA-Boc films in potassium ferricyanide solution, the CV and impedance measurements clearly show more blocking for grafted EDA-Boc films from ACN/$NaHCO_3$ rather than neat ACN. The numerical CV simulation for inhibiting species at the electrode surface was specially developed in order to study the theoretical response on the electrochemical grafting of EDA-Boc. Reasonable agreement was obtained between experiment and simulation. In addition, thermodynamic and kinetic information for the electrochemical grafting that cannot be measured directly by experiment were extracted from the simulation. Furthermore, detailed analysis by coupling AQ to the EDA deprotected monolayer (after removal of the Boc group) showed that higher CV and DPV surface coverages of immobilised AQ were obtained for EDA-Boc grafted in ACN: $NaHCO_3$ as compared to neat ACN. The DPV surface coverages were calculated using our $\Gamma_{DPV,\,exp}$ model. Then, the experimental approach was again verified using DPV simulation. Good agreement between experimental DPV and simulated DPV was achieved.

The fifth results chapter presented a self-assembled monolayer of 24-mer ssDNA labelled with AQ at the gold electrode surface. The DPV surface coverages of immobilised ssDNA were obtained using our experimental model. Reasonable agreement was achieved when comparing the surface coverages of immobilised ssDNA estimated by CV and chronocoulometry. However, the DPV surface coverages estimated by our model produced less error than CV and chronocoulometry. Then, the DPV simulation was performed in order to verify the experimental approach. The simulated DPV peak was broader and the height of the DPV peak current was lower than the experimental DPV peak. However, the charge calculated based on the simulated DPV peak was in good agreement with the calculated charge from experimental DPV. In addition, the best value used for $\Gamma_{DPV,\,sim}$ in the simulation was in good agreement with the calculations for estimating $\Gamma_{DPV,\,exp}$ using the equation we modelled. We believe that the narrower experimental

DPV peak was probably contributed by interactions among immobilised AQ-ssDNA that did not behave ideally. In contrast, non-ideal interaction parameters were not considered in our DPV simulation. Therefore, this data pattern has been expected.

To conclude, it is hoped that the derived equation to estimate the $\Gamma_{DPV,\ exp}$ that has been presented in this work can offer a new solution in the estimation of the DPV surface coverages, particularly for low-level surface concentrations of immobilised redox active species at modified electrode surfaces. By performing electrochemical simulations on the estimated DPV surface coverages and the grafting of the primary amines, both the simulation programs have helped us to verify our experimental approaches.

8.2 Future Outlook

In this study, we have completed our scope of work and all the findings have been discussed in detail in the results' chapters of this thesis. However, further studies need to be conducted in order to show wider applications of the experimental approaches and simulation models that have been developed in this study.

The following recommendations are proposed;

8.2.1 Experimental and theoretical models for estimating DPV surface coverages

The experimental procedure and Γ_{DPV} equation proposed in this study should be employed on any immobilised redox molecules at modified electrode surfaces by various immobilisation techniques in order to show more utility and flexibility of the developed model. In terms of the electrode substrates, it would be interesting to apply on the various solid electrodes surfaces such as platinum and carbon substrates (basal plane, and graphite). Also, it would be much more interesting when surface coverages of immobilised redox molecules at nanomaterials are determined using our model equation.

As mentioned earlier, the DPV simulation program developed in this work did not consider any non-ideal interactions parameter among immobilised redox molecules, in our model, we assumed that the immobilised molecules behave ideally. Figures 8.1a, b, c, and d demonstrate the best DPV fits on experimental DPV currents and all the data have been shown and discussed previously in the thesis. Figure 8.1a, b, and c demonstrate comparisons of the best simulated DPVs to the experimental DPVs for covalently immobilised AQ, osmium complex and mixed monolayers AQ-Os at the GC electrode surfaces. In contrast, Figure 8.1d shows comparisons of the simulated

DPVs to the experimental DPVs self-assembled monolayer ssDNA-AQ at a gold electrode surface.

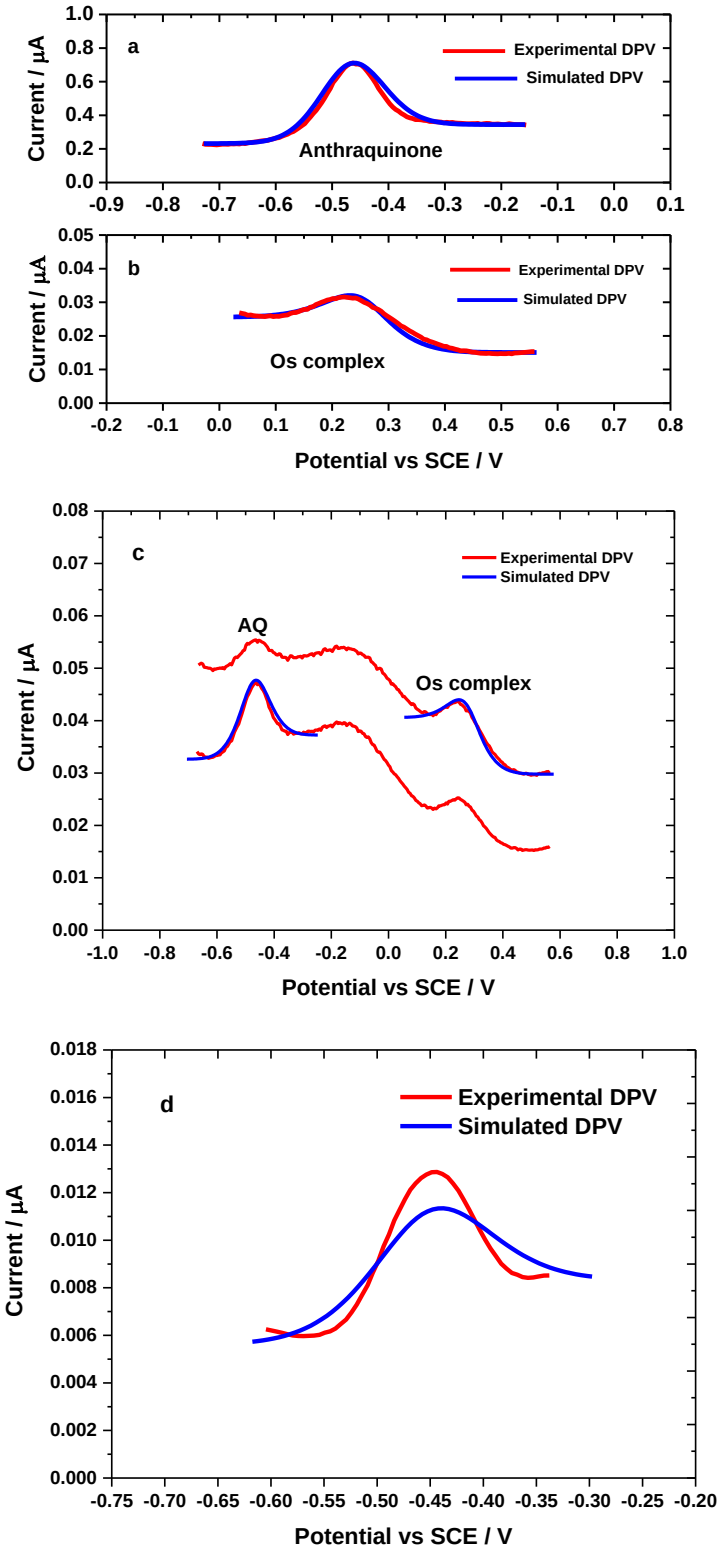

Figure 8.1; The best DPV fits to the experimental DPVs. a) DPVs for covalently immobilised AQ. b) DPVs for covalently immobilised Os bypiridine complex. c) DPVs for covalently immobilised AQ-Os. d) DPVs for self-assembled monolayer ssDNA-AQ. All the data presented here were taken from Chapters 4, 5, and 7 of this thesis.

Obviously, the simulated DPVs obtained for ssDNA-AQ is broader than the experimental DPV peak (red). The main reason that could explain this data pattern is because our DPV simulation did not consider any non-ideal interactions that may occur among attached molecules[64,204]. This behaviour can be attributed to the following causes. Firstly, some immobilised 24-mer ssDNA-AQ chains might be coiled up to the electrode surface. Secondly, referring back to the discussion in Chapter 7, the 24-mer ssDNA chains can experience the phenomenon of dynamic motions, contributed by elastic bending of ssDNA chain or free rotational motion by ssDNA chain and C6 spacer.

Covalently immobilised molecules can produce well-defined organisation and the formation of densely packed structures, as a result, these likely led to the non-ideal interactions between immobilised molecules. To overcome this problem, the DPV simulation may produce the best fit on the self-assembled ssDNA-AQ when the DPV simulation is extended to include the non-ideal parameters for the interactions among immobilised molecules.

In Chapter 4, Sections 4.21, 4.24.1 and 4.26, we have shown that in order to obtain the best fit for experimental DPVs at R_{ext} added of 700 and 1600 Ω, the C_{dl} values used in fittings decreased. This data trend is not similar to the experimental C_{dl} values, measured by EIS. In the case of the experimental EIS measurements, assuming a simple *RC* equivalent circuit, the C_{dl} magnitudes are constant for each R_{ext} condition (see Table 4.9). Thus, we felt that a more complex equivalent circuit model for the double layer capacitance is possible to be incorporated into the DPV simulation and needs further investigations.

8.2.2 Electrochemical grafting of primary amines at the electrode surfaces

In the sixth results chapter, CV simulations have been performed on the experimental CVs for grafting EDA-Boc in ACN and in a mixed solvent of ACN: base. In both cases, good agreement between experimental and simulated CVs was obtained, particularly in terms of the variable values used and the shape of the CV waveform. This was achieved by adding the simulation currents to an experimental background current from the 4th to 7th voltammetric scans. Further experimental and theoretical investigations need to be performed for electrochemical grafting of various primary amines such HDA-Boc, BDA-Boc and a few more.

Furthermore, as we showed that higher surface coverages of covalently immobilised AQ were obtained when grafting of EDA-Boc took place in ACN/$NaHCO_3$, it would be interesting when various redox molecules such as osmium bipyridine complex, nitrobenzene, and ferrocene redox compounds are used to confirm this finding. We expect that the same data pattern would also be obtained.

In order to get good agreement of the simulated CV waveform to experimental CV, every single simulated CV current was manually added to the experimental background current. It would be interesting if the CV simulation was modified by applying a more complex numerical simulation for calculating the background current. Therefore, the manually added simulated current with background current and time-consuming procedure could be avoided. As a result, an easy simulation procedure could be carried out.

Note that from work of previous members of our group, the electrochemical grafting of primary amines has also been performed at GC electrode surfaces coated with carbon nanotubes[139]. It would be interesting if the electrochemical grafting of primary amines in mixed solvent ACN/$NaHCO_3$ was applied on the electrode surfaces coated with nanomaterials.

8.2.3 Quantification of surface coverages of immobilised DNA by DPV

In the seventh chapter of this thesis, we only showed the application of our developed models for estimating the density of the immobilised ssDNA at a gold electrode surface based on a label system. By using the same approaches, further investigations would involve estimating the surface density of immobilised double-stranded DNA at a gold electrode surface.

Appendix A

Appendix 4.1

Table A4.1 – Data measured from the varied R_{ext} magnitudes with a fixed capacitance value (20 ± 3 µF) on our homemade dummy cell by following the *RC* circuit. The determined values of *R* and *C* were extracted by fitting the data with the *RC* circuit FRA software.

R_u/Ω	C/ µF	R_{ext} added / Ω	$R_u + R_{ext} = R_t$ /Ω (From fitting)	Estimate error %	*C* from fitting/ µF	Estimate error %
180	20	Without resistance box (R_{ext} = 0)	179.2	0.051	20.49	0.057
180	20	With resistance box (R_{ext} = 0)	179.3	0.064	20.48	0.072
180	20	100	279.7	0.053	20.49	0.064
180	20	300	480	0.047	20.50	0.061
180	20	500	680	0.239	20.49	0.328
180	20	700	881	0.225	20.49	0.322
180	20	900	1081	0.221	20.48	0.327
180	20	1100	1282	0.222	20.48	0.338
180	20	1300	1484	0.222	20.48	0.346
180	20	1500	1685	0.208	20.48	0.332
180	20	1700	1886	0.215	20.48	0.350
180	20	2400	2.588	0.208	20.48	0.358
180	20	4400	4590	0.172	20.47	0.333
180	20	6400	6600	1.455	20.47	3.035
180	20	8400	8600	1.436	20.47	3.196
180	20	10400	10600	1.365	20.46	3.210
180	20	13000	13200	1.353	20.46	3.386
180	20	15000	15210	1.341	20.45	3.504
180	20	17000	17240	1.333	20.45	3.623
180	20	20000	20240	1.265	20.45	3.634
180	20	22000	22230	1.262	20.46	3.750
180	20	24000	24230	1.266	20.44	3.886
180	20	26000	26.24	1.262	20.44	3.996
180	20	28000	28250	1.259	20.43	4.107
180	20	30000	30240	1.219	20.44	4.097
180	20	33000	33300	1.233	20.44	4.284
180	20	35000	35200	1.208	20.43	4.345

Appendix 4.2

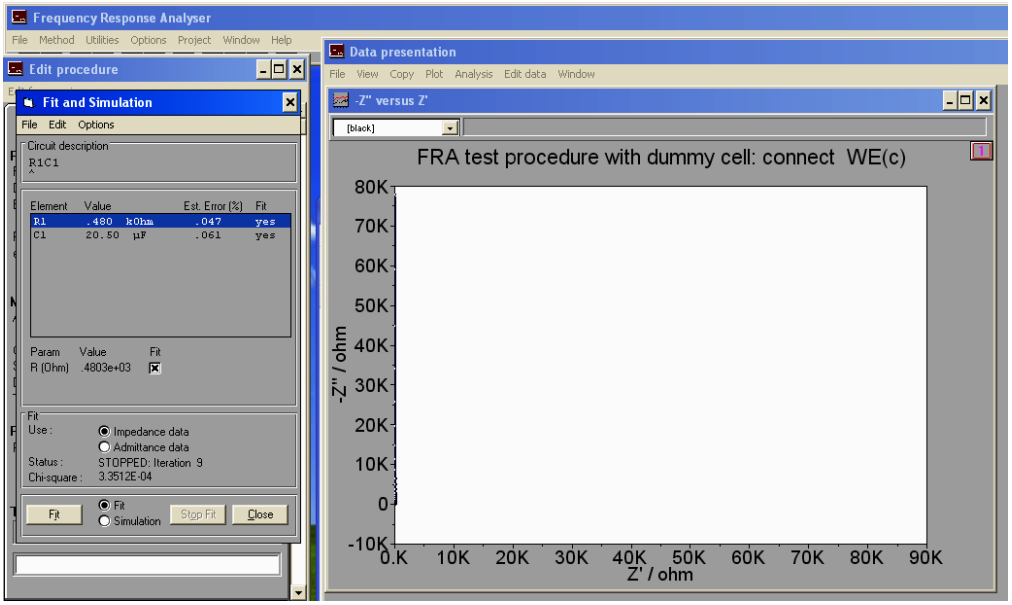

Figure A4.2; Screenshot of image *RC* fitting for our dummy cell carried out by FRA software. The obtained impedance result above when R_{ext} added of 0.3 kΩ from the resistance box with a fixed resistance (0.18 kΩ), connecting in series with a fixed capacitance value of 20 ± 3 µF was measured.

Appendix 4.3

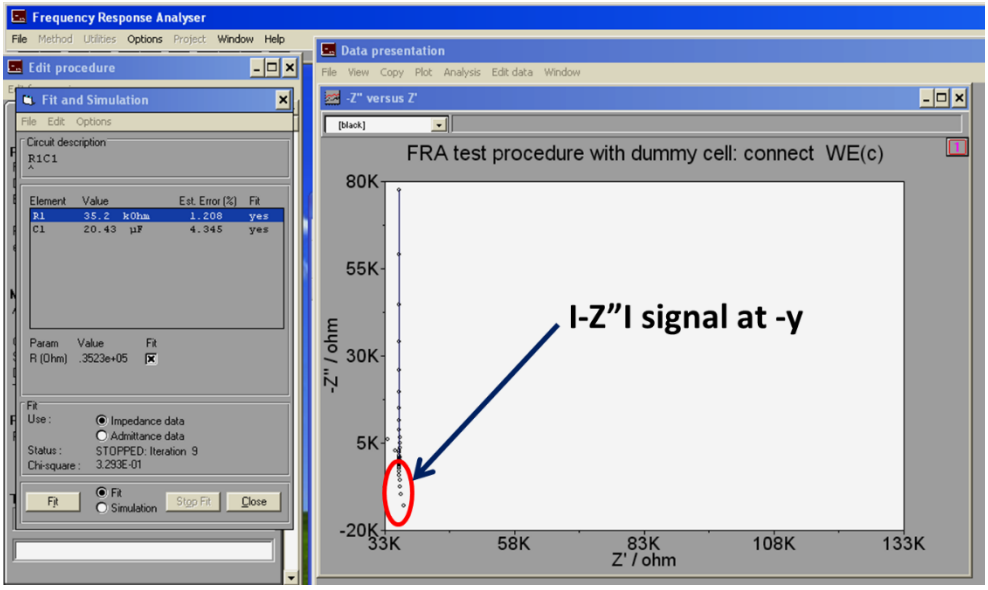

Figure A4.3; Screenshot of image *RC* fitting for our dummy cell carried out by FRA software. The obtained impedance result above when R_{ext} added of 35 kΩ from the resistance box with a fixed resistance (0.18 kΩ), connecting in series with a fixed capacitance value of 20 ± 3 µF was measured.

Appendix 4.4

Table A4.2; Data measured from the varied R_{ext} magnitudes with a fixed capacitance value (18 ± 3 µF) in our homemade dummy cell by following the *RC* circuit. The determined values of *R* and *C* were extracted by fitting the data with the *RC* circuit in the FRA software.

R_u/Ω	C/ µF	R_{ext} added / Ω	$R_u + R_{ext} = R_t$ /Ω (From fitting)	Estimate error %	*C* from fitting/ µF	Estimate error %
180	18	Without resistance box (R_{ext} = 0)	179.3	0.052	18.18	0.057
180	18	With resistance box (R_{ext} = 0)	179.4	0.060	18.18	0.067
180	18	100	279.8	0.051	18.18	0.067
180	18	300	480	0.045	18.18	0.057
180	18	500	680	0.235	18.18	0.318
180	18	700	881	0.227	18.18	0.319
180	18	900	1081	0.222	18.18	0.322
180	18	1100	1282	0.221	18.17	0.329
180	18	1300	1484	0.217	18.18	0.322
180	18	1500	1685	0.217	18.17	0.348
180	18	1700	1886	0.218	18.17	0.340
180	18	2400	2588	0.209	18.17	0.352
180	18	4400	4590	0.185	18.17	0.348
180	18	6400	6600	1.467	18.17	2.978
180	18	8400	8600	1.439	18.17	3.108
180	18	10400	10600	1.374	18.16	3.108
180	18	13000	13220	1.36	18.15	3.287
180	18	15000	15230	1.351	18.15	3.403
180	18	17000	17230	1.346	18.15	3.521
180	18	20000	20230	1.271	18.14	3.503
180	18	22000	22230	1.273	18.15	3.503
180	18	24000	24230	1.273	18.15	3.625
180	18	26000	26240	1.263	18.15	3.818
180	18	28000	28230	1.28	18.14	3.981
180	18	30000	30250	1.233	18.14	3.942
180	18	33000	33300	1.247	18.15	4.145
180	18	35000	35200	1.247	18.15	4.252

From the results in Table A4.1 and A4.2, it is interesting to note that the fitted values for R and C get smaller as the magnitude of R_{ext} added increases. In contrast, the associated errors get bigger. This may be contributed by the effect of -Z" dispersion in the high-frequency region on the Nyquist plots as shown in Figure A4.3. Clearly, at high frequency, the circuit becomes inductance as –Z" changes sign. Generally, in an electrochemical system, inductive behaviour can indicate an error in the EIS measurements due to non-uniform current distribution, potentiostat non-idealities or an inductance from the cable. These types of signals indicate that stray inductance is present and that it very dominates over capacitance at these frequencies when the magnitude of R_{ext} is very large.

Appendix 4.5; EIS measurements of R_t and C_{dl} for control electrode (adsorbed AQ).

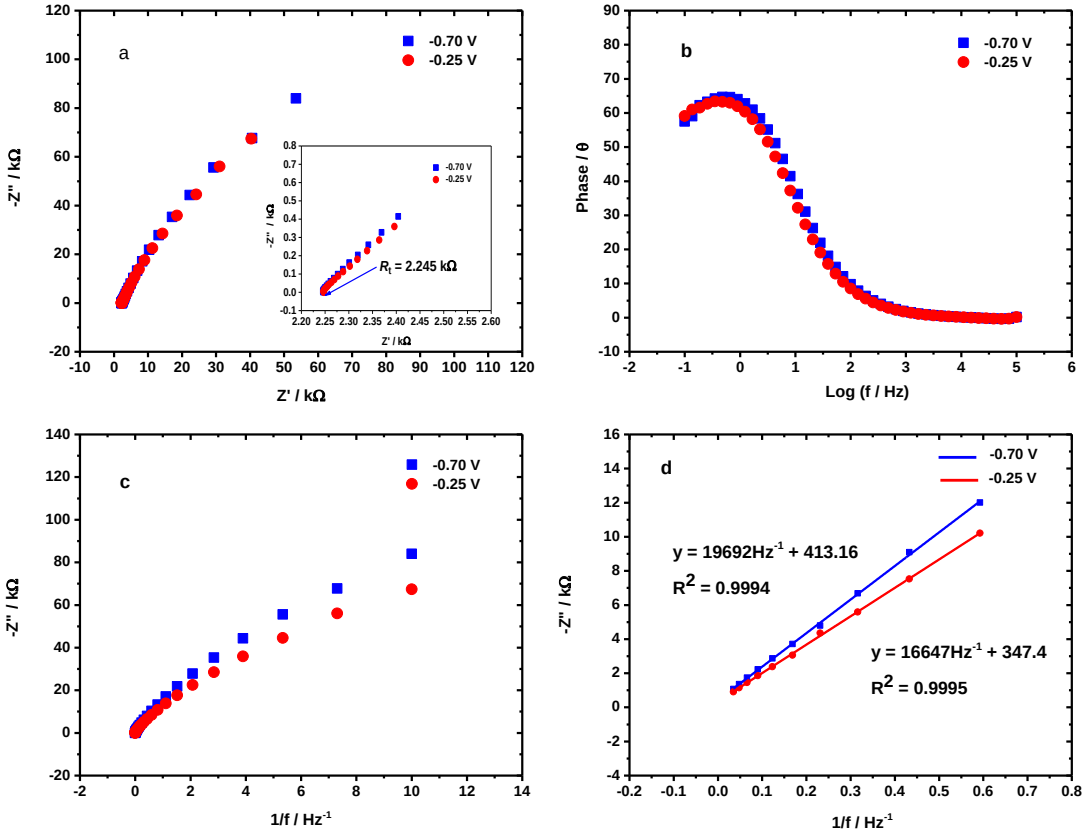

Figure A4.5; a) Nyquist plots for control electrode (adsorbed AQ) at two different potentials (-0.70 V and -0.25 V *vs* SCE). The inset figure shows the enlargement of Nyquist plot to show the presence of total uncompensated resistance (R_t) in the electrochemical cell (R_s + R_{ext} of 2.1 kΩ). b) Bode plots at two different measured potentials. These plots were used to differentiate three distinct frequency regions (high, medium and low) in order to determine the C_{dl}. c) Plots of imaginary impedance (-Z") *vs* 1/ frequency. d) The best linear fitting obtained from the low range frequency over plots of –Z" vs 1/f. The C_{dl} can be calculated from the slope of the linear fitting where m = $1/2\pi C_{dl}$. The measurements were made at a frequency range from 0.1 kHz to 100 kHz, number of frequency = 45 and a modulation amplitude of 5 mV in 0.1 M pH 7 phosphate buffer solution.

Appendix 4.6; MATLAB codes for DPV simulation

```
% Computes the differential pulse voltammogram for the Randles
circuit:
% Ru + (Cdl // CF)
% using finite difference approximation. The Faradaic current is that
for
% an adsorbed redox species assuming Butler-Volmer kinetics. The
double
% layer capacitance varies with potential with a sigmoidal dependence
on
% potential as the adsorbed layer becomes oxidised.
%
% whereas to calculate the total current n can be greater than one.

%======================PARAMETERS=====================================
% reaction parameters
Rt = 853;                % / Ohm
A = 0.071;               % / cm2
n = -2;                  % number of e-, <0 to have >0 oxidation
current
F = 96485;               % / C mol-1
R = 8.314;               % / J K-1 mol-1
T = 298;                 % / K
ks = 3.97;                % / s-1, standard rate constant for e-
transfer
alfa = 0.5;              % transfer coefficient
E0 = -0.468;             % / V
Γ = 3.60e-10;            % / mol cm-2, initial coverage
% double layer dependence on potential
Cdl_re = 23.1e-6;        % / F, capacitance of reduced form
Cdl_ox = 27.38e-6;        % / F, capacitance of oxidised form
Eswitch = E0;            % / V, midway point of the sigmoidal dependence
SigmoSteep = F/R/T;      % / V-1, increase to sharpen the sigmoid
% waveform parameters
Emin = -0.75;            % / V
Emax = -0.1;             % / V
dt = 100e-6;              % / s, time increment for the FD algorithm
tau_long = 450e-3;       % / s, duration of long long plateau
tau_short = 50e-3;       % / s, duration of short plateau
dE1 = 2.5e-3;              % / V, ptl step to short plateau
dE2 = 2.5e-3;            % / V, ptl step from short to long plateau
nperiod = 120;           % number of periods in waveform (minimum 2)
%nperiod = 2*round((Emax-Emin)/(dE1+dE2));
%======================================================================
=====
period = tau_long+tau_short;     % / s
totalduration = nperiod*period; % / s
nu = (dE1+dE2)/period;           % / V s-1, apparent sweep rate
nlong = round(tau_long/dt);      % number of points on long step
nshort = round(tau_short/dt);    % number of points on short pulse
nptotal = nperiod*(nshort+nlong);% total number of points
FRT = F/R/T;
t = zeros(nptotal,1);            % / s, time
Vapp = zeros(nptotal,1);         % / V, voltage applied across circuit
Vpa = zeros(nptotal,1);          % / V, voltage across parallel section
i = zeros(nptotal,1);            % / A, total current
iF = zeros(nptotal,1);           % / A, Faradaic current
iCdl = zeros(nptotal,1);         % / A, double layer charging current
G = G0 * ones(nptotal,1);        % / mol cm-2, coverage
```

```
E_CV = zeros(nperiod,1);        % ptl for CV
i_CV = zeros(nperiod,1);        % current for CV
niCV1 = zeros(nptotal,1);
niCV2 = zeros(nptotal,1);
flag = 0;                       % used to reverse sweep direction
k = 1;
kmax = nptotal;
Eplateau = Emin;
n1 = 1;
n2 = nlong;
n3 = nlong+1;
n4 = nlong+nshort;
for kper = 1 : nperiod          % loop to create waveform
    Vapp(n1:n2) = Eplateau;
    Vapp(n3:n4) = Eplateau+dE1;
    n1 = n1+nlong+nshort;
    n2 = n2+nlong+nshort;
    n3 = n3+nlong+nshort;
    n4 = n4+nlong+nshort;
    Eplateau = Eplateau+dE1+dE2;
    if ((Eplateau >= Emax) && (flag == 0))
        dEtemp = dE1;
        dE1 = -dE2;
        dE2 = -dEtemp;
        flag = 1;
    end
end
Vpa(1) = Vapp(1);
kper = 1;
ni1 = nlong;                    % index for the 1st current reading
ni2 = nlong+nshort;             % index for the 2nd current reading
for k = 2 : kmax;               % differential pulse CV
    t(k) = t(k-1) + dt;
    kfor = ks * exp(alfa * FRT * (Vpa(k-1)-E0));        % / s-1,
forward rate constant
    kbac = ks * exp(-(1 - alfa) * FRT * (Vpa(k-1)-E0)); % / s-1,
backward rate constant
    dGdt = -kfor * G(k-1) + kbac * (G(1) - G(k-1));
    G(k) = G(k-1) + dt * dGdt;
    iF(k) = n * F * A * dGdt;
    % sigmoidal dependence of Cdl on E
================================
    Cdl = Cdl_re+(Cdl_ox-Cdl_re)/(1+exp(SigmoSteep*(Eswitch-Vpa(k-
1))));
    %=================================================================
===
    dVpadt = ((Vapp(k-1) - Vpa(k-1)) / Ru - iF(k-1)) / Cdl;
    Vpa(k) = Vpa(k-1) + dt * dVpadt;
    iCdl(k) = Cdl * dVpadt;
    i(k) = (Vapp(k) - Vpa(k)) / Ru;
    if k == ni1
        i1 = i(k);              % current reading at end of long step
        niCV1(k) = ni1;
    elseif k == ni2
        i2 = i(k);              % current reading at end of short step
        E_CV(kper) = Vapp(k);
        i_CV(kper) = i2-i1;
        niCV2(k) = ni2;
        ni1 = ni1+nlong+nshort;
        ni2= ni2+nlong+nshort;
        kper = kper + 1;
```

```
    end
end
% plot results
figure;
plot(t,Vapp,'-r',t,Vpa,'-b');
xlabel('\bf{\it{t} / s}');
ylabel('\bf{\it{\color{red}V_{app},\color{blue}V_{//}} / V}');
figure;
AX = plotyy(t,i,t,iF,'plot');
xlabel('\bf{\it{t} / s}');
set(get(AX(1),'Ylabel'),'String','\bf{\it{i_{Total}} / A}');
set(get(AX(2),'Ylabel'),'String','\bf{\it{i_{Faraday}} / A}');
figure;
k1 = nptotal-nshort-nlong-nshort-500;
k2 = nptotal-nshort+500;
AX = plotyy(t(k1:k2),iF(k1:k2),t(k1:k2),iCdl(k1:k2),'plot');
xlabel('\bf{\it{t} / s}');
set(get(AX(1),'Ylabel'),'String','\bf{\it{i_{Faraday}} / A}');
set(get(AX(2),'Ylabel'),'String','\bf{\it{i_{Cdl}} / A}');
figure;
plot(E_CV,i_CV,'-mo');
xlabel('\bf{\it{V_{app}} / V}');
ylabel('\bf{\it{i} / A}');
%figure;
%plot(t,iF,'-r',t,iCdl,'-b');
%xlabel('\bf{\it{t} / s}');
%ylabel('\bf{\it{i} / A}');
%figure;
% same plots as above but on one page
%subplot(3,1,1);             % plot1 in a 3x1 array
%plot(t,Vapp,'-r',t,Vpa,'-b');
%xlabel('\bf{\it{t} / s}');
%ylabel('\bf{\it{\color{red}V_{app},\color{blue}V_{//}} / V}');
%subplot(3,1,2);             % plot2 in a 3x1 array
%plot(t,i,'-g',t,iF,'-b');
%AX = plotyy(t,i,t,iF,'plot');
%xlabel('\bf{\it{t} / s}');
%set(get(AX(1),'Ylabel'),'String','\bf{\it{i_{Total}} / A}');
%set(get(AX(2),'Ylabel'),'String','\bf{\it{i_{Faraday}} / A}');
%ylabel('\bf{\it{\color{green}i_{Total},\color{blue}i_{Faraday}} /
A}');
%subplot(3,1,3);             % plot3 in a 3x1 array
%plot(E_CV,i_CV,'-mo');
%xlabel('\bf{\it{V_{app}} / V}');
%ylabel('\bf{\it{i} / A}');

%Ouput DPV to spreadsheet
xlFileOut = 'DPV_CV';
XlsSheet = 'FD_Sim';
xlswrite(xlFileOut,{'Sim_E'},XlsSheet,'A11')
xlswrite(xlFileOut,{'Sim_I'},XlsSheet,'B11')
xlswrite(xlFileOut,E_CV,XlsSheet,'A12');
xlswrite(xlFileOut,i_CV,XlsSheet,'B12');

% %Output current transients to a comma separated text file
TexFileOut = 'DPV_whole_transients';
% OuputTable = table(t,iF,iCdl,i);
% writetable(OuputTable,TexFileOut);

OuputTable =[t iF iCdl i];
dlmwrite('DPV_whole_transients2.txt',OuputTable,'\t')
```

```
name2 = 'DPV_whole_transients2.txt';
X = load(name2);
filename = 'DPV_whole_transients2.xlsx';
xlswrite (filename, X)


hold on

filename = 'AQ E13 2017.xlsx' ;
A = xlsread(filename);

potential=A(:,1);
Current=A(:,2);

plot(potential, Current, 'LineWidth',4, 'color', 'b');
%xlim([0 0.6]);
%ylim([1.1e-8 8.0e-8]);
xlabel('Potential / \Omega'); ylabel('Current / \muA');
```

Appendix 5.1; EIS measurements of R_t and C_{dl} for AQ-Os modified GC electrodes (AQ covalently immobilised).

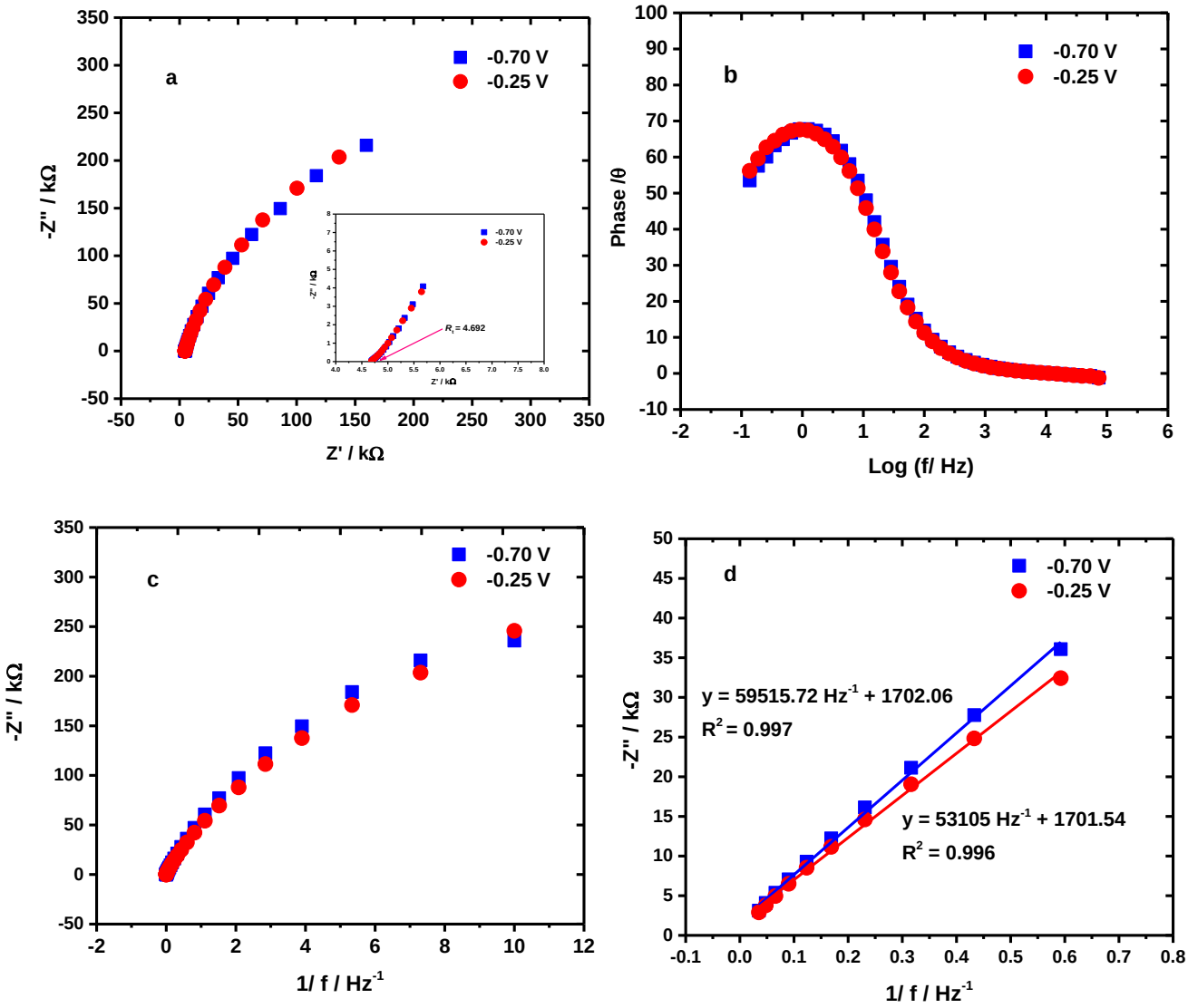

Figure A5.1; a) Nyquist plots for covalently immobilised AQ at two different potentials (-0.70 V and -0.25 V *vs* SCE). The inset figure shows the enlargement of the Nyquist plot to show the presence of the total uncompensated resistance (R_t) in the electrochemical cell (R_s + R_{ext} of 4.5 kΩ). b) Bode plots at two different measured potentials. These plots were used to differentiate three distinct frequency regions (high, medium and low) in order to determine the C_{dl}. c) Plots of imaginary impedance (-Z") *vs* 1/ frequency. d) The best linear fitting obtained from the low range frequency over plots of –Z" vs 1/f. The C_{dl} can be calculated from the slope of the linear fitting where m = $1/2\pi C_{dl}$. The measurements were made at a frequency range from 0.1 kHz to 100 kHz, number of frequency = 45 and a modulation amplitude of 5 mV in 0.1 M pH 7 phosphate buffer solution.

Appendix 5.2; EIS measurements of R_t and C_{dl} for AQ-Os modified GC electrodes (covalently immobilised Os).

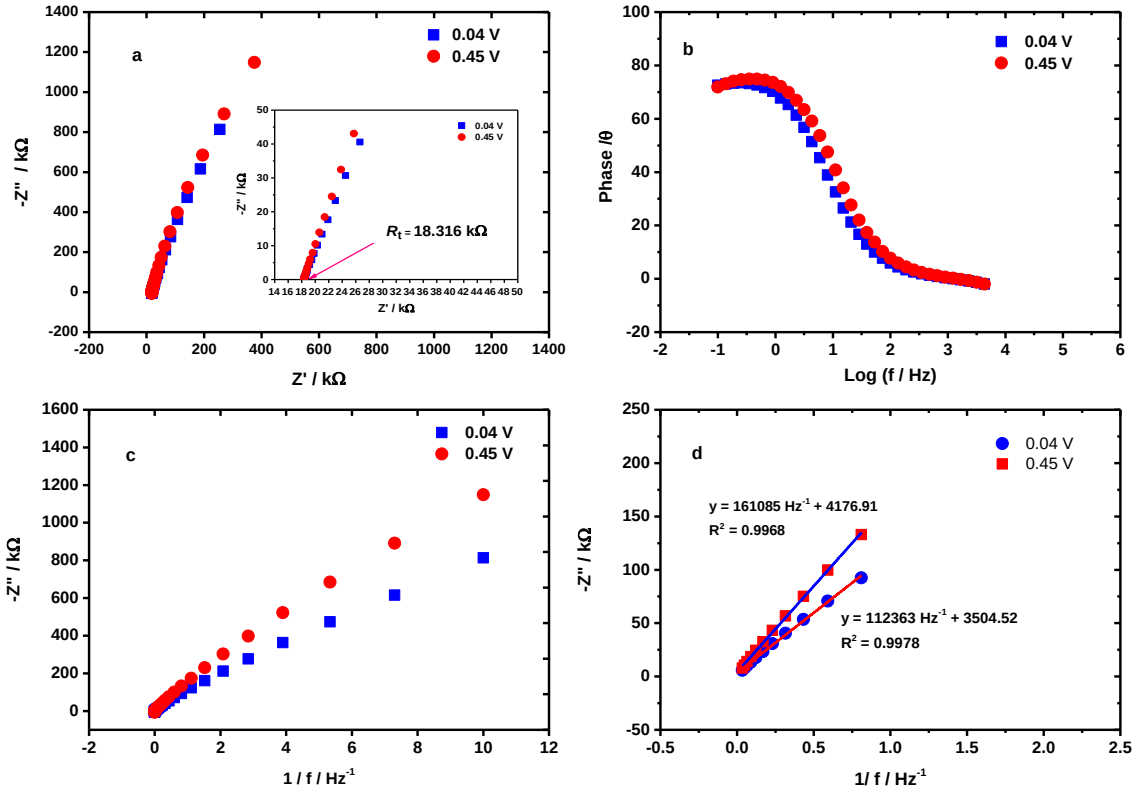

Appendix A5.2; a) Nyquist plots for covalently immobilised Osmium complex (mixed monolayers) at two different potentials (0.04 V and 0.45 V). The inset figure shows the enlargement of the Nyquist plot to show the presence of the total uncompensated resistance (R_t) in the electrochemical cell (R_s + R_{ext} of 18 kΩ). b) Bode plots at two different measured potentials. These plots were used to differentiate three distinct frequency regions (high, medium and low) in order to determine the C_{dl}. c) Plots of imaginary impedance (-Z") *vs* 1/ frequency. d) The best linear fitting obtained from the low range frequency over plots of –Z" vs 1/f. The C_{dl} can be calculated from the slope of the linear fitting where m = 1/2πC_{dl}.The measurements were made at a frequency range from 0.1 kHz to 100 kHz, number of frequency = 45 and a modulation amplitude of 5 mV in 0.1 M pH 7 phosphate buffer solution.

Appendix 6.1; MATLAB codes for CV simulation

```
%
% This program simulates repeated cyclic voltammogramms for the
mechanism
% described by Saveant et al. in articles 1995 and 1997[165,166].
%
% A->B+e, ks, alfa, E0
% B+S->C, kA, S free surface, C sticks on the ede and inhibits further
rxn
% B->P,   kH, homogeneous process
%
% As the coverage of C increases the amount of free surface decreases
%
clear
cAb = 1e-5; % / mol cm-3, bulk cntn of A
cBb = 0;    % / mol cm-3, bulk cntn of B
DA = 7.42e-5;  % / cm2 s-1, diffusion coefficient of A
DB = DA;    % / cm2 s-1, diffusion coefficient of B
GCmax = 2e-9; % / mol cm-2, largest coverage of C
S0 = 0.071;     % / cm2; free ede area available at t=0
kA = 6.4e-5;  % / cm s-1, rate cst for adsorption of B
kH = 0.6;   % / s-1, rate constant for decomposition of B in solution
ks = 0.0013;     % / cm s-1, standard rate cst for e- transfer
alfa = 0.7; % transfer coefficient
Ei = 0;  % / V, start of ptl sweep
Ef = +2;  % / V, end of ptl sweep
E0 = +1.45;     % / V, standard ptl
nu = 0.05;   % / V s-1, sweep rate
F = 96485;  % / C mol-1
R = 8.314;  % / J K-1 mol-1
T = 283;    % K
lambda = 0.45; % used to ensure FD algorithm remains stable
ncycles = 3; % number of voltammetric cycles
kmax = 50;  % number of iterations over forward scan of CV
npinrl = 1;
while npinrl < 2 % ensures at least two points within reaction layer
    dt = abs(Ef-Ei)/nu/kmax;  % / s, time increment
    dx = sqrt(DA*dt/lambda);  % / cm, space increment
    npinrl = sqrt(DB/kH)/dx;  % number of points within reaction layer
    kmax = 2*kmax;
end
kmax2 = 2 * kmax; % number of iterations over forward and reverse
scans
kmaxn = kmax2 * ncycles; % number of iterations for all the cycles
imax = fix(6 * sqrt(kmaxn * lambda)); % converts imax to an integer
cA = cAb * ones(imax,kmaxn); % / mol cm-3, cntn of A
cB = cBb * ones(imax,kmaxn); % / mol cm-3, cntn of B
Cur = zeros(kmaxn,1);        % / A, current
Pot = zeros(kmaxn,1);        % / V, potential
Time = zeros(kmaxn,1);       % / s, time
nC = zeros(kmaxn,1);         % / mol, moles of C on ede
dE = (Ef - Ei) / kmax;       % / V, potential increment
E = Ei;                      % initialises potential
for k=1:kmaxn-1              % start of time loop
    epsi = F/R/T*(E-E0);
    a = -DA; % a,b,c,d,e,f are the coefficients of 2 simultaneous eq.
to
    b = -(DB+dx*kA); % solve for cA(1,k) and cB(1,k)
    c = DA*cA(2,k)+DB*cB(2,k);
    d = -(DA+dx*ks*exp((1-alfa)*epsi));
```

```
    e = dx*ks*exp(-alfa*epsi);
    f = DA*cA(2,k);
    cB(1,k) = (-f+c*d/a)/(e-b*d/a); % electrode boundary condition
    cA(1,k) = -(c+b*cB(1,k))/a;     % electrode boundary condition
    Sfree = S0 - nC(k) / GCmax;     % surface not covered by C
    Cur(k) = F*Sfree*DA*(cA(2,k)-cA(1,k))/dx;
    Time(k) = k * dt;
    Pot(k) = E;
    nC(k+1) = nC(k) + dt * kA * cB(1,k) * Sfree;
    for i = 2 : imax - 1 % diffusion loop
        cA(i,k+1) = cA(i,k) + lambda * ...
            (cA(i+1,k) - 2 * cA(i,k) + cA(i-1,k));
        cB(i,k+1) = cB(i,k) + lambda * ...
            (cB(i+1,k) - 2 * cB(i,k) + cB(i-1,k))- dt * kH * cB(i,k);
    end
    E = E + dE;
    if E > Ef
        dE = -dE; %changes sign of ptl increment at end of scans
    end
    if E < Ei
        dE = -dE;
    end
end
%plot results
x = ones(imax,1);
for i = 1 : imax
    x(i) = i*dx;
end
Emin = min(Ei,Ef);
Emax = max(Ei,Ef);
figure;
for k = 1:2:kmaxn-1 % this loops animates the plots
    subplot(4,1,1) % prepares plot1 in a 4x1 array of plots on the
page
    plot(Time(1:k), Pot(1:k));
    xlabel('Time / s');ylabel('Pot / V');
    xlim([0 max(Time)]);ylim([1.1*Emin 1.1*Emax]);
    subplot(4,1,2); % prepares plot2 in a 4x1 array of plots on the
page
    plot(Time(1:k), Cur(1:k));
    xlabel('Time /  s');ylabel('Cur / A');
    xlim([0 max(Time)]);ylim([1.1*min(Cur) 1.1*max(Cur)]);
    subplot(4,1,3); % prepares plot3 in a 4x1 array of plots on the
page
    plot(Pot(1:k), Cur(1:k));
    xlabel('Pot / V');ylabel('Cur / A');
    xlim([Emin Emax]);ylim([1.1*min(Cur) 1.1*max(Cur)]);
    subplot(4,1,4); % prepares plot4 in a 4x1 array of plots on the
page
    plot(x,cA(:,k),x,cB(:,k));
    ylim([0 1.1*cAb]);xlabel('x / cm');ylabel('c(x,t) / mol cm-3');
    pause(0.01);
end
figure;
plot(Pot(1:k), Cur(1:k));
xlabel('Pot / V');ylabel('Cur / A');
% Ouput results to spreadsheet
FileOut = 'FD_CV_inhibition_A2B_BpS2C_B2P';
XlsSheet = 'FD_Sim';
xlswrite(FileOut,{'E / V'},XlsSheet,'A11')
xlswrite(FileOut,{'i / A'},XlsSheet,'B11')
```

```
xlswrite(FileOut,Pot(1:kmaxn-1),XlsSheet,'A12');
xlswrite(FileOut,Cur(1:kmaxn-1),XlsSheet,'B12');


hold on

filename = 'ACNPURE FOR FITTING.xlsx' ;
A = xlsread(filename);

potential=A(:,1);
Current=A(:,2);

plot(potential, Current, 'LineWidth',2, 'color', 'c');
%xlim([0 2.0]);
%ylim([1.1e-4 5e-4]);
xlabel('Potential / \Omega'); ylabel('Current / \muA')
```

Appendix 6.2; EIS measurements of R_t and C_{dl} for AQ-modified GC electrodes (prepared from method 1).

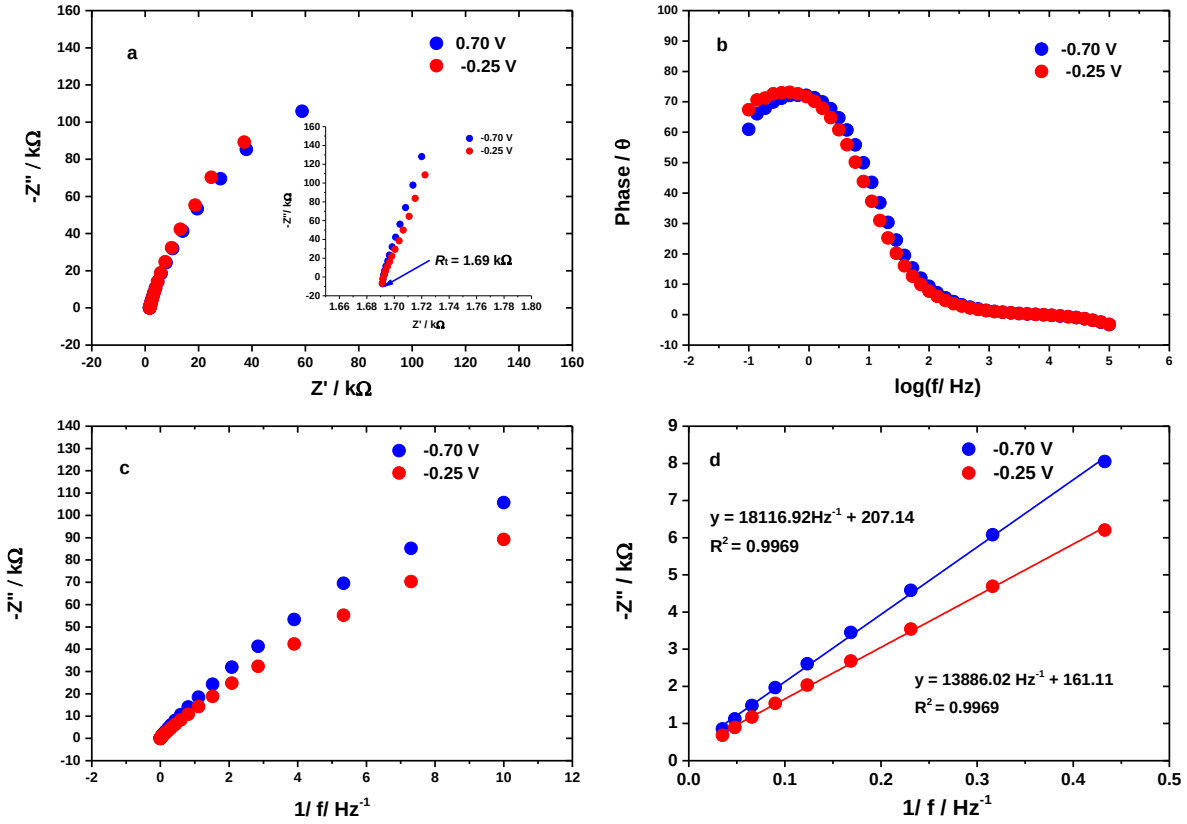

Figure A6.2; a) Nyquist plots for covalently immobilised AQ from neat ACN at two different potentials (-0.70 V and -0.25 V *vs* SCE). The inset figure shows the enlargement of the Nyquist plot to show the presence of the total uncompensated resistance (R_t) in the electrochemical cell (R_u + R_{ext} of 1.5 kΩ). b) Bode plots at two different measured potentials. These plots were used to differentiate three distinct frequency regions (high, medium and low) in order to determine the C_{dl}. c) Plots of imaginary impedance (-Z") *vs* 1/ frequency. d) The best linear fitting obtained from the low range frequency over plots of –Z" *vs* 1/f. The C_{dl} can be calculated from the slope of the linear fitting where m = $1/2\pi C_{dl}$. The measurements were made at a frequency range from 0.1 kHz to 100 kHz, number of frequency = 45 and a modulation amplitude of 5 mV in 0.1 M pH 7 phosphate buffer solution.

Appendix 6.3; EIS measurements of R_t and C_{dl} for AQ-modified GC electrodes (prepared from method 2).

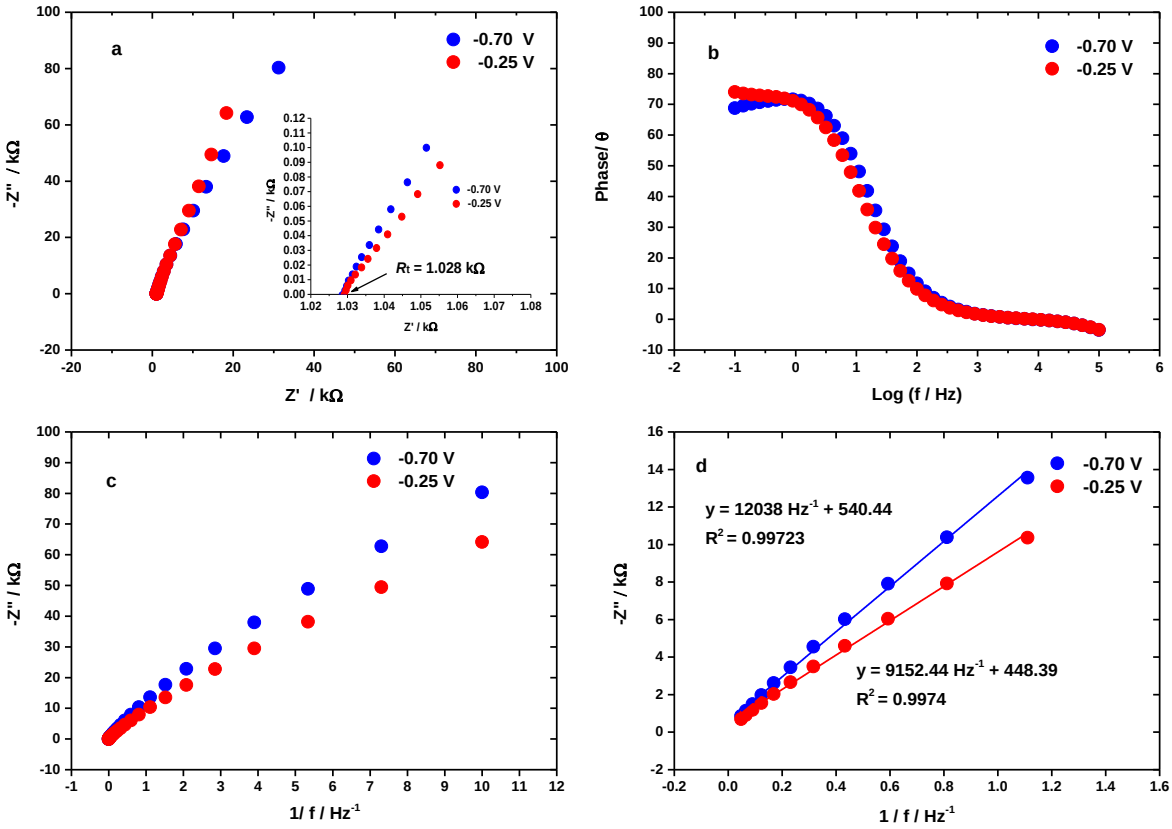

Figure A6.3; a) Nyquist plots for covalently immobilised AQ from ACN/$NaHCO_3$ at two different potentials (-0.70 V and -0.25 V *vs* SCE). The inset figure shows the enlargement of the Nyquist plot to show the presence of the total uncompensated resistance (R_t) in the electrochemical cell (R_u + R_{ext} of 0.8 kΩ). b) Bode plots at two different measured potentials. These plots were used to differentiate three distinct frequency regions (high, medium and low) in order to determine the C_{dl}. c) Plots of imaginary impedance (-Z") *vs* 1/ frequency. d) The best linear fitting obtained from the low range frequency over plots of –Z" *vs* 1/f. The C_{dl} can be calculated from the slope of the linear fitting where m = $1/2\pi C_{dl}$. The measurements were made at a frequency range from 0.1 kHz to 100 kHz, number of frequency = 45 and a modulation amplitude of 5 mV in 0.1 M pH 7 phosphate buffer solution.

Appendix 7.1;

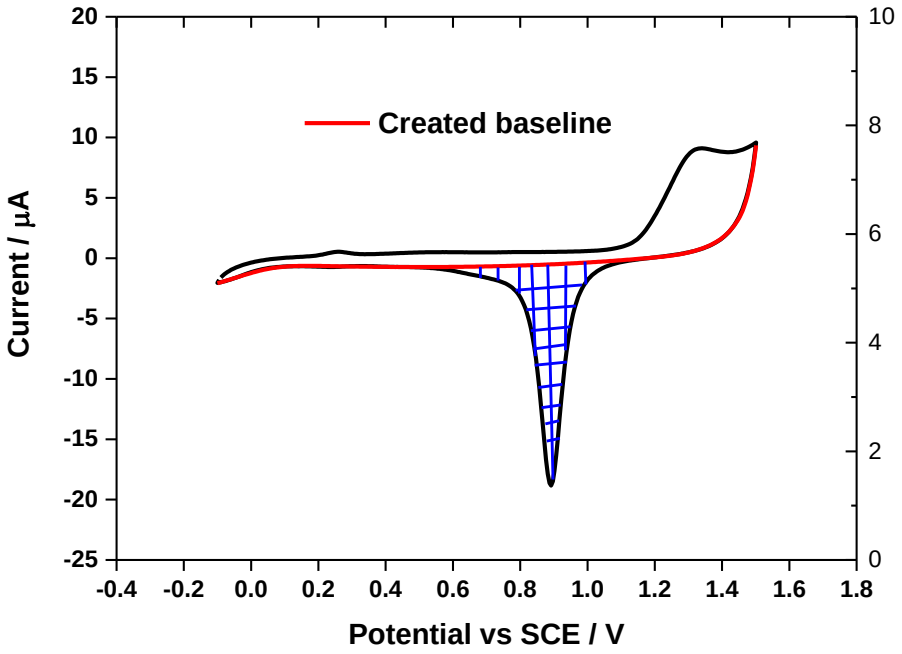

Figure A7.1- Cyclic voltammogram (20th cycle shown) was obtained from the cleaning process of the gold electrode, at 0.1 V / s in 0.5 M sulphuric acid. The area of the electrode is 0.0341 cm^2. The red line is the baseline constructed on Origin 9.1 in order to extract the integrated area under the reduction peak for calculating the real charge (Q_{real}).

Based on CV in Figure A7.1, the roughness factor (ρ) of the cleaned gold electrode was calculated using Equation A7.1. The geometric area (A_{geo}) of the Au electrode employed here was 0.0341 cm^2. In contrast, the real gold surface area (A_{real}) was determined through the total reduction charge (Q_{real}) of the reduction peak using Equation A7.2. The total reduction charge was the total area under the reduction peak. The theoretical charge density of the gold is given in the literature[207,208] as 390 µC cm^{-2}. Hence, for three cleaned surface of the gold electrodes were calculated using Equation A7.3 and were found to be 1.20 ± 0.03. Because the ρ calculated here is close to 1, the roughness factor was approximated as 1 when calculating the CV surface coverages.

$$\rho = \frac{A_{\text{real}}}{A_{\text{geomerty}}} \qquad \textbf{Eq. A7.1}$$

$$\text{Charge } (Q) = \frac{\text{Intergrated area}}{\text{Scan rate of CV}} \qquad \textbf{Eq. A7.2}$$

$$A = \frac{Q_{real}}{Q_{theoretical}} \qquad \textbf{Eq. A7.3}$$

Bibliography

(1) Goyal, R. N.; Bishnoi, S. *Indian J. Chem.* **2012**, *51*, 205–225.

(2) Bartlett, P. N. *Med. Biol. Eng. Comput.* **1990**, *28* (3), B10-7.

(3) Antiochia, R.; Tasca, F.; Mannina, L. *Mater. Sci. Appl.* **2013**, *4* (7), 15–22.

(4) Vyskočil, V.; Barek, J. *Crit. Rev. Anal. Chem.* **2009**, *39* (3), 173–188.

(5) Rifkin, S. C.; Evans, D. H. *Anal. Chem.* **2002**, *48* (14), 2174–2179.

(6) Lennox, J. C.; Murray, R. W. *J. Electroanal. Chem. Interfacial Electrochem.* **1977**, *78* (2), 395–401.

(7) Georgakilas, V.; Otyepka, M.; Bourlinos, A. B.; Chandra, V.; Kim, N.; Kemp, K. C.; Hobza, P.; Zboril, R.; Kim, K. S. *Chem. Rev.* **2012**, *112* (11), 6156–6214.

(8) Ryan R. Moore; Craig E. Banks, A.; Compton, R. G. *Anal. Chem.* **2004**, *76* (10), 2677–2682.

(9) Jiang, L.; Nelson, G. W.; Abda, J.; Foord, J. S. *ACS Appl. Mater. Interfaces* **2016**, *8* (42), 28338–28348.

(10) Xie, M. S.; Xia, B. Y.; Li, Y.; Yan, Y.; Yang, Y.; Sun, Q.; Chan, S. H.; Fisher, A.; Wang, X. *Energy Environ. Sci.* **2016**, *9* (5), 1687–1695.

(11) Lupu, S.; Lete, C.; Marin, M.; Totir, N.; Balaure, P. C. *Electrochim. Acta* **2009**, *54* (7), 1932–1938.

(12) Niedziółka-Jönsson, J.; Barka, F.; Castel, X.; Pisarek, M.; Bezzi, N.; Boukherroub, R.; Szunerits, S. *Langmuir* **2010**, *26* (6), 4266–4273.

(13) Uslu, B.; Ozkan, S. *Comb. Chem. High Throughput Screen.* **2007**, *10* (7), 495–513.

(14) Gaál, F. F.; Guzsvány, V. J.; Bjelica, L. J. *J. Serb. Chem. Soc.285+615* **2007**, *7245135* (543).

(15) Zittel, H. E.; Miller, F. J. *Anal. Chem.* **1965**, *37* (2), 200–203.

(16) Nuzzo, R. G.; Allara, D. L. *J. Am. Chem. Soc.* **1983**, *105* (13), 4481–4483.

(17) Xu, Y. *Int. J. Hydrogen Energy* **2009**, *34* (1), 77–83.

(18) Lane, R. F.; Hubbard, A. T. *J. Phys. Chem.* **1973**, *77* (11), 1401–1410.

(19) Lane, R. F.; Hubbard, A. T. *J. Phys. Chem.* **1973**, *77* (11), 1411–1421.

(20) Watkins, B. F.; Behling, J. R.; Kariv, E.; Miller, L. L. *J. Am. Chem. Soc.* **1975**, *97* (12), 3549–3550.

(21) Moses, P. R.; Wier, L.; Murray, R. W. *Anal. Chem.* **1975**, *47* (12), 1882–1886.

(22) Desimoni, E.; Brunetti, B. *Electroanalysis* **2012**, *24* (7), 1481–1500.

(23) Zen, J.-M.; Senthil Kumar, A.; Tsai, D.-M. *Electroanalysis* **2003**, *15* (13), 1073–1087.

(24) Soriaga, M. P.; Hubbard, A. T. *J. Am. Chem. Soc.* **1982**, *104* (10), 2742–2747.

(25) Shannon, C.; Frank, D. G.; Hubbard, A. T. *Annu. Rev. Phys. Chem.* **1991**, *42* (1), 393–

431.

(26) McCreery, R. L. *Chem. Rev.* **2008**, *108* (7), 2646–2687.

(27) Stergiou, D. V.; Prodromidis, M. I.; Veltsistas, P. G.; Evmiridis, N. P. *Electroanalysis* **2004**, *16* (11), 949–954.

(28) Gilardi, G.; Fantuzzi, A. *Trends Biotechnol.* **2001**, *19* (11), 468–476.

(29) Putzbach, W.; Ronkainen, N. J. *Sensors* **2013**, *13* (4), 4811–4840.

(30) Šljukić, B.; Banks, C. E.; Compton, R. G. *J. Iran. Chem. Soc.* **2005**, *2* (1), 1–25.

(31) Kumar, A. S.; Swetha, P. *Colloids Surfaces A Physicochem. Eng. Asp.* **2011**, *384* (1–3), 597–604.

(32) Li, G.; Miao, P. *Electrochemical Analysis of Proteins*; Springer: New York, 2013.

(33) Abdualla, M. Sythesis and characterisation of ferrocenyl monolayers on silicon surfaces, PhD Thesis,Newcastle University, 2013.

(34) Porter, M. D.; Bright, T. B.; Allara, D. L.; Chidsey, C. E. D. *J. Am. Chem. Soc.* **1987**, *109* (12), 3559–3568.

(35) Häkkinen, H. *Nat. Chem.* **2012**, *4* (6), 443–455.

(36) Akiba, U.; Fujihira, M.; Akiba, U.; Fujihira, M. In *Encyclopedia of Electrochemistry*; Wiley-VCH Verlag GmbH & Co. KGaA: Weinheim, Germany, 2007.

(37) Rao, A.; Chaitanya Kumar, K.; Iqbal, Y.; Sreedhar, & B. *Indian J. Chem. Technol.* **2009**, *16*, 25–31.

(38) Shimura, T.; Aramaki, K. *Corros. Sci.* **2006**, *48* (11), 3784–3801.

(39) Kaur, I.; Zhao, X.; Bryce, M. R.; Schauer, P. A.; Low, P. J.; Kataky, R. *Chemphyschem* **2013**, *14* (2), 431–440.

(40) Love, J. C.; Estroff, L. a.; Kriebel, J. K.; Nuzzo, R. G.; Whitesides, G. M. *Chem. Rev.* **2005**, *105*, 1103–1169.

(41) Fragoso, A.; Laboria, N.; Latta, D.; Ciara K. O'Sullivan. *Anal. Chem.* **2008**, *85* (5), 1712–1719.

(42) Subramanian, A.; Irudayaraj, J.; Ryan, T. *Sensors Actuators B Chem.* **2006**, *114* (1), 192–198.

(43) Nakamura, F.; Ito, E.; Hayashi, T.; Hara, M. *Colloids Surfaces A Physicochem. Eng. Asp.* **2006**, *284*, 495–498.

(44) Gobi, K. V.; Iwasaka, H.; Miura, N. *Biosens. Bioelectron.* **2007**, *22* (7), 1382–1389.

(45) Papadopoulou, E.; Gale, N.; Thompson, J. F.; Fleming, T. A.; Brown, T.; Bartlett, P. N. *Chem. Sci.* **2016**, *7*, 386–393.

(46) Madaan, N.; Terry, A.; Harb, J.; Davis, R. C.; Schlaad, H.; Linford, M. R. *J. Phys. Chem. C* **2011**, *115* (46), 22931–22938.

(47) Nuzzo, R. G.; Allara, D. L. *J. Am. Chem. Soc.* **1983**, *105* (13), 4481–4483.

(48) Sheridan, M. V.; Lam, K.; Sharafi, M.; Schneebeli, S. T.; Geiger, W. E. *Langmuir* **2016**,

32 (6), 1645–1657.

(49) Nimse, S. B.; Song, K.; Sonawane, M. D.; Sayyed, D. R.; Kim, T. *Sensors* **2014**, *14* (12), 22208–22229.

(50) Moses, P. R.; Wier, L.; Murray, R. W. *Anal. Chem.* **1975**, *47* (12), 1882–1886.

(51) Bard, A. J. *J. Chem. Educ.* **1983**, *60* (4), 302.

(52) Watkins, B. F.; Behling, J. R.; Kariv, E.; Miller, L. L. *J. Am. Chem. Soc.* **1975**, *97* (12), 3549–3550.

(53) Downard, A. J. *Electroanalysis* **2000**, *12* (14), 1085–1096.

(54) Chrétien, J.-M.; Ghanem, M. A.; Bartlett, P. N.; Kilburn, J. D. *Chemistry* **2008**, *14* (8), 2548–2556.

(55) Ghanem, M. A.; Chrétien, J.-M.; Pinczewska, A.; Kilburn, J. D.; Bartlett, P. N. *J. Mater. Chem.* **2008**, *18* (41), 4917.

(56) Boland, S.; Barrière, F.; Leech, D. *Langmuir* **2008**, *24* (12), 6351–6358.

(57) Lee, L.; Brooksby, P. A.; Leroux, Y. R.; Hapiot, P.; Downard, A. J. *Langmuir* **2013**, *29* (9), 3133–3139.

(58) Buriez, O.; Podvorica, F. I.; Galtayries, A.; Labbé, E.; Top, S.; Vessières, A.; Jaouen, G.; Combellas, C.; Amatore, C. *J. Electroanal. Chem.* **2013**, *699*, 21–27.

(59) Laviron, E. *J. Electroanal. Chem.* **1979**, *100*, 263–270.

(60) Laviron, E.; Roullier, L. *J. Electroanal. Chem. Interfacial Electrochem.* **1980**, *115* (1), 65–74.

(61) Laviron, E. *J. Electroanal. Chem. Interfacial Electrochem.* **1979**, *101*, 19–28.

(62) Laviron, E. *J. Electroanal. Chem. Interfacial Electrochem.* **1974**, *52*, 355–393.

(63) Bard, A. J.; Faulkner, L. R. *Electrochemical methods : fundamentals and applications*; Wiley: New York, 2001.

(64) Brown, A. P.; Anson, F. C. *Anal. Chem.* **1977**, *49* (11), 1589–1595.

(65) Blaedel, W. J.; Mabbott, G. A. *Anal. Chem.* **1981**, *53* (14), 2270–2274.

(66) Ramírez, P.; Mano, N.; Andreu, R.; Ruzgas, T.; Heller, A.; Gorton, L.; Shleev, S. *Biochim. Biophys. Acta - Bioenerg.* **2008**, *1777* (10), 1364–1369.

(67) Poppe, J.; Gabriel, S.; Liebscher, L.; Hickey, S. G.; Eychmüller, A. *J. Mater. Chem. C* **2013**, *1* (7), 1515.

(68) Chen, D.; Tao, Q.; Liao, L. W.; Liu, S. X.; Chen, Y. X.; Ye, S. *Electrocatalysis* **2011**, *2* (3), 207–219.

(69) Fragkou, V.; Ge, Y.; Steiner, G.; Freeman, D.; Bartetzko, N.; Turner, A. P. F. *Int. J. Electrochem. Sci* **2012**, *7*, 6214–6220.

(70) Sharp, M.; Petersson, M.; Edström, K. *J. Electroanal. Chem. Interfacial Electrochem.* **1979**, *95* (1), 123–130.

(71) Adam B. Steel, Tonya M. Herne, A.; Tarlov, M. J. *Anal. Chem.* **1998**, *70* (22), 4670–

4677.

(72) Koval, C. A.; Anson, F. C. *Anal. Chem.* **1978**, *50* (2), 223–229.

(73) Stutts, K. J.; Dayton, M. A.; Wightman, R. M. *Anal. Chem.* **1982**, *54* (6), 995–998.

(74) Hussam, A. *Compr. Anal. Chem.* **2006**, *47*, 661–689.

(75) Li, Q.; Mathur, G.; Gowda, S.; Surthi, S.; Zhao, Q.; Yu, L.; Lindsey, J. S.; Bocian, D. F.; Misra, V. *Adv. Mater.* **2004**, *16* (2), 133–137.

(76) Antuch, M.; Abradelo, D. G.; Cao, R. *Electroanalysis* **2015**, *27* (8), 1939–1943.

(77) Blanchard, P.-Y.; Alévêque, O.; Breton, T.; Levillain, E. *Langmuir* **2012**, *28* (38), 13741–13745.

(78) Imahori, H.; Taku Hasobe; Hiroko Yamada; Nishimura, Y.; Iwao Yamazaki, F. S. *Langmuir* **2001**, *17* (16), 4925–4931.

(79) Leroux, Y. R.; Hui, F.; Noël, J.-M.; Roux, C.; Downard, A. J.; Hapiot, P. *Langmuir* **2011**, *27* (17), 11222–11228.

(80) Parry, E. P.; Osteryoung, R. A. *Anal. Chem.* **1964**, *36* (7), 1366–1367.

(81) Osteryoung, R. A.; Osteryoung, J.; Albery, W. J.; Rogers, G. T. *Philos. Trans. R. Soc. London A Math. Phys. Eng. Sci.* **1981**, *302* (1468).

(82) Wang, J.; Freiha, B. A. *Talanta* **1983**, *30* (5), 317–322.

(83) Sokol, W. F.; Evans, D. H. *Anal. Chem.* **1981**, *53* (4), 578–580.

(84) Ortuño, J. A.; Serna, C.; Molina, A.; Gil, A. *Anal. Chem.* **2006**, *78* (23), 8129–8133.

(85) BASi Your Scientific Connection, Pulse Voltammetry Techniques https://www.basinc.com/manuals/EC_epsilon/Techniques/Pulse/pulse (accessed Jul 11, 2016).

(86) Martínez-Ortiz, F.; Laborda, E.; Limon-Petersen, J. G.; Rogers, E. I.; Serna, C.; Rees, N. V.; Molina, A.; Compton, R. G. *J. Phys. Chem. C* **2009**, *113* (39), 17215–17222.

(87) Price, J. F.; Baldwin, R. P. *Anal. Chem.* **1980**, *52* (12), 1940–1944.

(88) Osteryoung, J. *J. Chem. Educ.* **1983**, *60* (4), 296.

(89) Flanagan, J. B.; Takahashi, K.; Anson, F. C. *J. Electroanal. Chem. Interfacial Electrochem.* **1977**, *81* (2), 261–273.

(90) Wei, H. Z.; van de Ven, T. G. M.; Omanovic, S.; Zeng, Y. W. *Langmuir* **2008**, *24* (21), 12375–12384.

(91) Oldham, K. B.; Myland, J. C. *Electrochim. Acta* **2011**, *56* (28), 10612–10625.

(92) Groppi, J. Toward the Control of Partial Covalent Modification of Glassy Carbon Surfaces, PhD Thesis, Queen Mary, University of London, 2016.

(93) Groppi, J.; Bartlett, P. N.; Kilburn, J. D. *Chemistry* **2016**, *22* (3), 1030–1036.

(94) Ishioka, T.; Uchida, T.; Teramae, N. *Anal. Chim. Acta* **2001**, *449* (1), 253–260.

(95) Chen, L.; Lv, C.; Chen, J.; Bi, S. *Electrochim. Acta* **2013**, *93*, 222–229.

(96) Shi, K.; Shiu, K.-K. *J. Electroanal. Chem.* **2004**, *574* (1), 63–70.

(97) Neumann, C. C. M.; Batchelor-McAuley, C.; Downing, C.; Compton, R. G. *Chem. - A Eur. J.* **2011**, *17* (26), 7320–7326.

(98) Muddasir Hanif, LU Ping, GU Cheng, WANG Zhi-ming, YANG Shu-min, YANG Bing, W. C. and M. Y. *Chem. Res. Chinese Univ.* **2009**, *25* (6), 960–956.

(99) Surya Prakash Rao, H.; Vijjapu, S. *RSC Adv.* **2012**, *2* (17), 6773.

(100) Snyder, C. H.; Gutierrez-Cirlos, E. B.; Trumpower, B. L. *J. Biol. Chem.* **2000**, *275* (18), 13535–13541.

(101) Zhang, Q.; Piro, B.; Ramsay, S.; Noël, V.; Reisberg, S.; Pham, M.-C. *Electrochim. Acta* **2012**, *85*, 588–593.

(102) Susan, M. A. B. H.; Begum, M.; Takeoka, Y.; Watanabe, M. *J. Electroanal. Chem.* **2000**, *481* (2), 192–199.

(103) Prodromidis, M. I.; Veltsistas, P. G.; Karayannis, M. I. *Anal. Chem.* **2000**, *72* (17), 3995–4002.

(104) McDermott, M. T.; McCreery, R. L. *Langmuir* **1994**, *10* (11), 4307–4314.

(105) Kano, K.; Uno, B. *Anal. Chem.* **1993**, *65* (8), 1088–1093.

(106) Baranton, S.; Bélanger, D. *J. Phys. Chem. B* **2005**, *109* (51), 24401–24410.

(107) Saby, C.; Ortiz, B.; Champagne, G. Y.; Bélanger, D. *Langmuir* **1997**, *13* (25), 6805–6813.

(108) Guin, P. S.; Das, S.; Mandal, P. C. *Int. J. Electrochem.* **2011**, *2011*, 1–22.

(109) Jürmann, G.; Schiffrin, D. J.; Tammeveski, K. *Electrochim. Acta* **2007**, *53* (2), 390–399.

(110) Manisankar, P.; Gomathi, A. *Bull. Chem. Soc. Jpn.* **2005**, *78* (10), 1783–1790.

(111) Manisankar, P.; Gomathi, A.; Velayutham, D. *J. Solid State Electrochem.* **2005**, *9* (9), 601–608.

(112) Salimi, A.; Mousavi, M. F.; Sharghi, H.; Shamsipur, M. *Bull. Chem. Soc. Jpn.* **1999**, *72* (9), 2121–2127.

(113) Nagata, M.; Kondo, M.; Suemori, Y.; Ochiai, T.; Dewa, T.; Ohtsuka, T.; Nango, M. *Colloids Surfaces B Biointerfaces* **2008**, *64* (1), 16–21.

(114) Leventis, H. C.; Streeter, I.; Wildgoose, G. G.; Lawrence, N. S.; Jiang, L.; Jones, T. G. .; Compton, R. G. *Talanta* **2004**, *63* (4), 1039–1051.

(115) Yang, Z.; Wang, P.; Zhang, W.; Zhu, G. *Fresenius. J. Anal. Chem.* **2001**, *371* (3), 337–341.

(116) Wardman, P. *J. Phys. Chem. Ref. Data* **1989**, *18* (4), 1637.

(117) Motulsky, H. J.; Ransnas, L. A. *FASEB J.* **1987**, *1* (5), 365–374.

(118) Eckermann, A. L.; Feld, D. J.; Shaw, J. A.; Meade, T. J. *Coord. Chem. Rev.* **2010**, *254* (15–16), 1769–1802.

(119) Hay, S.; Westerlund, K.; Tommos, C. *J. Phys. Chem. B* **2007**, *111* (13), 3488–3495.

(120) Campos, R.; Ferapontova, E. E. *Electrochim. Acta* **2014**, *126*, 151–157.

(121) Mulas, A.; Hervault, Y.-M.; He, X.; Di Piazza, E.; Norel, L.; Rigaut, S.; Lagrost, C. *Langmuir* **2015**, *31* (25), 7138–7147.

(122) March, G.; Reisberg, S.; Piro, B.; Pham, M. C.; Delamar, M.; Noel, V.; Odenthal, K.; Hibbert, D. B.; Gooding, J. J. *J. Electroanal. Chem.* **2008**, *622* (1), 37–43.

(123) Batchelor-McAuley, C.; Kozub, B. R.; Menshykau, D.; Compton, R. G. *J. Phys. Chem. C* **2011**, *115* (3), 714–718.

(124) Razzaq, H.; Qureshi, R.; Schiffrin, D. J. *Electrochem. commun.* **2014**, *39*, 9–11.

(125) Smith, E. T.; Davis, C. A.; Barber, M. J. *Anal. Biochem.* **2003**, *323* (1), 114–121.

(126) Bleda-Martínez, M. J.; Maciá-Agulló, J. A.; Lozano-Castelló, D.; Morallón, E.; Cazorla-Amorós, D.; Linares-Solano, A. *Carbon N. Y.* **2005**, *43* (13), 2677–2684.

(127) Forster, R. J. *Anal. Chem.* **1996**, *68* (18), 3143–3150.

(128) Forster, R. J.; Faulkner, L. R. *Anal. Chem.* **1995**, *67* (7), 1232–1239.

(129) Zhang, D.; Wilson, G. S.; Niki, K. *Anal. Chem.* **1994**, *66* (22), 3873–3881.

(130) Holt, K. B.; Caruana, D. J.; Millán-Barrios, E. J. *J. Am. Chem. Soc.* **2009**, *131* (32), 11272–11273.

(131) McDermott, M. T.; McDermott, C. A.; McCreery, R. L. *Anal. Chem.* **1993**, *65* (7), 937–944.

(132) Pinczewska, A.; Sosna, M.; Bloodworth, S.; Kilburn, J. D.; Bartlett, P. N. *J. Am. Chem. Soc.* **2012**, *134* (43), 18022–18033.

(133) Celiktas, A.; Ghanem, M. A.; Bartlett, P. N. *J. Electroanal. Chem.* **2012**, *670*, 42–49.

(134) Ligaj, M.; Jasnowska, J.; Musiał, W. G.; Filipiak, M. *Electrochim. Acta* **2006**, *51* (24), 5193–5198.

(135) Li, F.; Feng, Y.; Yang, L.; Liu, S. *Talanta* **2010**, *83* (1), 205–209.

(136) Alonso-Lomillo, M. A.; Domínguez-Renedo, O.; Hernández-Martín, A.; Arcos-Martínez, M. J. *Anal. Biochem.* **2009**, *395* (1), 86–90.

(137) Löfås, S.; Johnsson, B. *J. Chem. Soc., Chem. Commun.* **1990**, *4* (21), 1526–1528.

(138) Lai, T.; Hou, Q.; Yang, H.; Luo, X.; Xi, M. *Acta Biochim. Biophys. Sin. (Shanghai).* **2010**, *42* (11), 787–792.

(139) Ghanem, M. A.; Kocak, I.; Al-Mayouf, A.; AlHoshan, M.; Bartlett, P. N. *Electrochim. Acta* **2012**, *68*, 74–80.

(140) Pelzer, J.; Scholz, F.; Henrion, G.; Nitschke, L. *Electroanalysis* **1989**, *1* (5), 437–440.

(141) Lovrić, M. *J. Electroanal. Chem. Interfacial Electrochem.* **1984**, *175* (1–2), 33–52.

(142) Lauer, G.; Osteryoung, R. A. *Anal. Chem.* **1966**, *38*, 1106–1112.

(143) Richtering, W.; Doblhofer, K. *Electrochim. Acta* **1989**, *34* (12), 1685–1688.

(144) Heering, H. A.; Mondal, M. S.; Armstrong, F. A. *Anal. Biochem.* **1998**, *71* (174–182).

(145) Drake, K. F.; Van Duyne, R. P.; Bond, A. M. *J. Electroanal. Chem. Interfacial Electrochem.* **1978**, *89* (2), 231–246.

(146) Aberg, S. *J. Electroanal. Chem.* **1996**, *419* (1), 99–103.

(147) Rizal, B.; Archibald, M. M.; Connolly, T.; Shepard, S.; Burns, M. J.; Chiles, T. C.; Naughton, M. J. *Anal. Chem.* **2013**, *85* (21), 10040–10044.

(148) Abhayawardhana, A. D.; Sutherland, T. C. *J. Phys. Chem. C* **2009**, *113* (12), 4915–4924.

(149) Moulton, S. E.; Barisci, J. N.; Bath, A.; Stella, R.; Wallace, G. G. *Langmuir* **2004**, *21* (1), 316–322.

(150) Kim, C.-H.; Pyun, S.-I.; Shin, H.-C. *J. Electrochem. Soc.* **2002**, *149* (2), A93.

(151) Lee, G.-J.; Pyun, S.-I.; Kim, C.-H. *J. Solid State Electrochem.* **2004**, *8* (2), 110–117.

(152) Góes, M. S.; Rahman, H.; Ryall, J.; Davis, J. J.; Bueno, P. R. *Langmuir* **2012**, *28* (25), 9689–9699.

(153) Salimi, A.; Kavosi, B.; Hallaj, R.; Babaei, A. *Electroanalysis* **2009**, *21* (8), 909–917.

(154) Groppi, J.; Bartlett, P. N.; Kilburn, J. D. *Chem. - A Eur. J.* **2016**, *22* (3), 1030–1036.

(155) Mossanha, R.; Ramos, M. K.; Santos, C. S.; Pessoa, C. A. *J. Electrochem. Soc.* **2015**, *162* (7), B145–B151.

(156) Acevedo, D.; Abruna, H. D. *J. Phys. Chem.* **1991**, *95* (23), 9590–9594.

(157) Casero, E.; Darder, M.; Takada, K.; Abruña, H. D.; Pariente, F.; Lorenzo, E. *Langmuir* **1999**, *15* (1), 127–134.

(158) Salimi, A.; Kavosi, B.; Babaei, A.; Hallaj, R. *Anal. Chim. Acta* **2008**, *618* (1), 43–53.

(159) Adenier, A.; Chehimi, M. M.; Gallardo, I.; Pinson, J.; Vilà, N. *Langmuir* **2004**, *20* (19), 8243–8253.

(160) Nasraoui, R.; Bergamini, J.-F.; Ababou-Girard, S.; Geneste, F. *J. Solid State Electrochem.* **2010**, *15* (1), 139–146.

(161) Deinhammer, R. S.; Ho, M.; Anderegg, J. W.; Porter, M. D. *Langmuir* **1994**, *10* (4), 1306–1313.

(162) Ross S.D, Finkelstein M, Rudd E.J. *Anodic Oxidation*; Academic Press: New York, 1975.

(163) Buriez, O.; Labbé, E.; Pigeon, P.; Jaouen, G.; Amatore, C. *J. Electroanal. Chem.* **2008**, *619–620*, 169–175.

(164) Masui, M.; Sayo, H.; Tsuda, Y. *J. Chem. Soc. B Phys. Org.* **1968**, 973.

(165) Bhugun, I.; Savéant, J.-M. *J. Electroanal. Chem.* **1995**, *395* (1–2), 127–131.

(166) Andrieux, C. P.; Gonzalez, F.; Savéant, J.-M. *J. Am. Chem. Soc.* **1997**, *119* (18), 4292–4300.

(167) Allongue, P.; Delamar, M.; Desbat, B.; Fagebaume, O.; Hitmi, R.; Pinson, J.; Savéant, J.-M. *J. Am. Chem. Soc.* **1997**, *119* (1), 201–207.

(168) Barbier, B. *J. Electrochem. Soc.* **1990**, *137* (6), 1757.

(169) Pastore, P.; Badocco, D.; Zanon, F. *Electrochim. Acta* **2006**, *51* (25), 5394–5401.

(170) Menanteau, T.; Dias, M.; Levillain, E.; Downard, A. J.; Breton, T. *J. Phys. Chem. C* **2016**, *120* (8), 4423–4429.

(171) Tanaka, M.; Sawaguchi, T.; Sato, Y.; Yoshioka, K.; Niwa, O. *Langmuir* **2011**, *27* (1), 170–178.

(172) Turton, D. A.; Wynne, K. *J. Phys. Chem. B* **2014**, *118* (17), 4600–4604.

(173) Chan, T. C.; Lee, I.; Chan, K. S. *J. Phys. Chem. B* **2014**, *118* (37), 10945–10955.

(174) Chan, T. C.; Li, H. T.; Li, K. Y. *J. Phys. Chem. B* **2015**, *119* (51), 15718–15728.

(175) Kullapere, M.; Mirkhalaf, F.; Tammeveski, K. *Electrochim. Acta* **2010**, *56* (1), 166–173.

(176) Koiry, S. P.; Aswal, D. K.; Saxena, V.; Padma, N.; Chauhan, A. K.; Joshi, N.; Gupta, S. K.; Yakhmi, J. V.; Guerin, D.; Vuillaume, D. *Appl. Phys. Lett.* **2007**, *90* (11), 113118.

(177) Kanyong, P.; Sun, G.; Rösicke, F.; Syritski, V.; Panne, U.; Hinrichs, K.; Rappich, J. *Electrochem. commun.* **2015**, *51*, 103–107.

(178) Lovelock, K. R. J.; Ejigu, A.; Loh, S. F.; Men, S.; Licence, P.; Walsh, D. A. *Phys. Chem. Chem. Phys.* **2011**, *13* (21), 10155–10164.

(179) Cunningham, G. P.; Vidulich, G. A.; Kay, R. L. *J. Chem. Eng. Data* **1967**, *12* (3), 336–337.

(180) Thompson, J. W.; Kaiser, T. J.; Jorgenson, J. W. *J. Chromatogr. A* **2006**, *1134* (1–2), 201–209.

(181) Mostinsky, I. L. Diffusion Coefficient: ThermopediaTM, A to Z Guide to Thermodynamics, Heat and Mass Transfer and Fluids Engineering, Posted 2 February 2011. http://www.thermopedia.com/content/696/ (accessed Dec 8, 2015).

(182) Ould-Kaddour, F.; Levesque, D. *Phys. Rev. E. Stat. Nonlin. Soft Matter Phys.* **2001**, *63* (1 Pt 1), 11205.

(183) Kumar, S. K.; Szamel, G.; Douglas, J. F. *J. Chem. Phys.* **2006**, *124* (21), 214501.

(184) Walser, R.; Mark, A. E.; van Gunsteren, W. F. *Chem. Phys. Lett.* **1999**, *303* (5–6), 583–586.

(185) Walser, R.; Hess, B.; Mark, A. E.; van Gunsteren, W. F. *Chem. Phys. Lett.* **2001**, *334* (4–6), 337–342.

(186) Wang, J.; Hou, T. *J. Comput. Chem.* **2011**, *32* (16), 3505–3519.

(187) Antonello, S.; Maran, F. *J. Am. Chem. Soc.* **1999**, *121* (41), 9668–9676.

(188) Lee, L. Modification of Glassy Carbon Electrodes with Diazonium Cation Terminated Films: “Sticky Surfaces,” Master Thesis, University of Canterbury, 2011.

(189) Liu, J.; Cheng, L.; Liu, B.; Dong, S. *Langmuir* **2000**, *16* (19), 7471–7476.

(190) Liu, J.; Dong, S. *Electrochem. commun.* **2000**, *2* (10), 707–712.

(191) Yaqub, M.; Walsh, J. J.; Keyes, T. E.; Proust, A.; Rinfray, C.; Izzet, G.; McCormac, T.; Forster, R. J. *Langmuir* **2014**, *30* (15), 4509–4516.

(192) Steel, A. B.; Levicky, R. L.; Herne, T. M.; Tarlov, M. J. *Biophys. J.* **2000**, *79* (2), 975–981.

(193) Zhang, J.; Song, S.; Wang, L.; Pan, D.; Fan, C. *Nat. Protoc.* **2007**, *2* (11), 2888–2895.

(194) Rao, A. N.; Grainger, D. W. *Biomater. Sci.* **2014**, *2* (4), 436.

(195) Pheeney, C. G.; Barton, J. K. *J. Am. Chem. Soc.* **2013**, *135* (40), 14944–14947.

(196) Anne, A.; Demaille, C. *J. Am. Chem. Soc.* **2008**, *130* (30), 9812–9823.

(197) Grabowska, I.; Singleton, D. G.; Stachyra, A.; Góra-Sochacka, A.; Sirko, A.; Zagórski-Ostoja, W.; Radecka, H.; Stulz, E.; Radecki, J. *Chem. Commun.* **2014**, *50* (32), 4196.

(198) Papadopoulou, E.; Gale, N.; Thompson, J. F.; Fleming, T. A.; Brown, T.; Bartlett, P. N. *Chem. Sci.* **2016**, *7* (1), 386–393.

(199) Bosco, A.; Bano, F.; Parisse, P.; Casalis, L.; DeSimone, A.; Micheletti, C. *Nanoscale* **2012**, *4* (5), 1734–1741.

(200) Mahajan, S.; Richardson, J.; Gaied, N. B.; Zhao, Z.; Brown, T.; Bartlett, P. N. *Electroanalysis* **2009**, *21* (20), 2190–2197.

(201) Kowalczyk, A.; Nowicka, A. M.; Jurczakowski, R.; Niedzialkowski, P.; Ossowski, T.; Stojek, Z. *Electroanalysis* **2010**, *22* (1), 49–59.

(202) Campos, R.; Kotlyar, A.; Ferapontova, E. E. *Langmuir* **2014**, *30* (40), 11853–11857.

(203) Eckermann, A. L.; Feld, D. J.; Shaw, J. A.; Meade, T. J. *Coord.Chem.Rev.* 2010, pp 1769–1802.

(204) Lawrence Yoon Suk Lee; Sutherland, T. C.; Simona Rucareanu, A.; Lennox, R. B. *Langmuir* **2006**, *22* (9), 4438–4444.

(205) Mullenix, A. Electrochemical Investigation of Anthraquinone tagged Oligonucleotides and Electrodes, PhD Thesis, University of Tennessee - Knoxville, 2004.

(206) Feldberg, S. W. *Anal. Chem.* **2011**, *83* (15), 5851–5856.

(207) Trasatti, S.; Petrii, O. A. *Pure Appl. Chem.* **1991**, *63* (5), 711–734.

(208) Ressine, A.; Vaz-Domínguez, C.; Fernandez, V. M.; De Lacey, A. L.; Laurell, T.; Ruzgas, T.; Shleev, S. *Biosens. Bioelectron.* **2010**, *25* (5), 1001–1007.

(209) Bueno, P. R.; Fabregat-Santiago, F.; Davis, J. J. *Anal. Chem.* **2013**, *85* (1), 411–417.

(210) Santos, A.; Davis, J. J.; Bueno, P. R. *J. Anal. Bioanal. Tech.* **2014**, *S7* (12), 1–15.